Energy Pathways of the Internal Gravity Wave Field in the Ocean driven by Wave–Mean Flow and Wave–Wave Interactions

Dissertation zur Erlangung des Doktorgrades der Naturwissenschaften (Dr. rer. nat.) an der Fakultat für Mathematik, Informatik und Naturwissenschaften im Fachbereich Erdsystemwissenschaften der Universitat Hamburg

vorgelegt von

Pablo Sebastia Saez

aus Valencia, Spanien

Hamburg, 2025

Universität Hamburg

DER FORSCHUNG | DER LEHRE | DER BILDUNG

Fachbereich Erdsystemwissenschaften

Datum der Disputation:	09.04.2026
Gutachter:innen der Dissertation:	Prof. Dr. Carsten Eden Dr. Manita Chouksey
Zusammensetzung der Prüfungskommission:	Prof. Dr. Carsten Eden Dr. Manita Chouksey Prof. Dr. Dirk Olbers Prof. Dr. Hermann Held PD. Dr. Thomas Pollmann
Vorsitzender des Fach-Promotionsausschusses Erdsystemwissenschaften:	Prof. Dr. Hermann Held
Dekan der MIN Fakultät:	Prof. Dr. Ing. Norbert Ritter

Eidesstattliche Versicherung | Declaration on Oath

Hiermit versichere ich an Eides statt, die vorliegende Dissertationsschrift selbst verfasst und keine anderen als die angegebenen Hilfsmittel und Quellen benutzt zu haben. Sofern im Zuge der Erstellung der vorliegenden Dissertationsschrift generative Künstliche Intelligenz (gKI) basierte elektronische Hilfsmittel verwendet wurden, versichere ich, dass meine eigene Leistung im Vordergrund stand und dass eine vollständige Dokumentation aller verwendeten Hilfsmittel gemäß der Guten wissenschaftlichen Praxis vorliegt. Ich trage die Verantwortung für eventuell durch die gKI generierte fehlerhafte oder verzerrte Inhalte, fehlerhafte Referenzen, Verstöße gegen das Datenschutz- und Urheberrecht oder Plagiate.

I hereby declare and affirm that this doctoral dissertation is my own work and that I have not used any aids and sources other than those indicated. If electronic resources based on generative artificial intelligence (gAI) were used in the course of writing this dissertation, I confirm that my own work was the main and value-adding contribution and that complete documentation of all resources used is available in accordance with good scientific practice. I am responsible for any erroneous or distorted content, incorrect references, violations of data protection and copyright law or plagiarism that may have been generated by the gAI.

Hamburg, den 30.11.2025 Unterschrift: 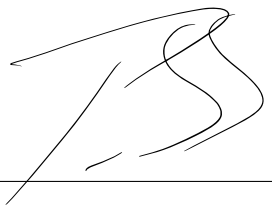

Zusammenfassung

Interne Schwerewellen (ISWn) vermitteln wichtige Wege im Energiekreislauf des Ozeans und verteilen Energie über eine große Bandbreite von Skalen aufgrund von Wechselwirkungen mit ihrer Umgebung, die inter alia durch mittlere Strömungen, andere Wellen, Topografie und Turbulenzen geprägt ist. Durch diese Wechselwirkungen ISW übertragen Energie auf kleine Skalen und induzieren Dichtemischung, die für die Aufrechterhaltung der globalen Umwälzströmung erforderlich ist. Die Diagnose und Quantifizierung dieser Wege bleibt jedoch aufgrund komplexer Entstehungs-, Wechselwirkungs- und Dissipationsprozesse von ISWn eine Herausforderung. Diese Dissertation untersucht Energiewege, die durch Wellen-mittlerer Strömungen und Wellen-Wellen Wechselwirkungen unter repräsentativen ozeanischen Bedingungen angetrieben werden. Theorie, numerische Modellierung und beobachtungsgestützte Analysen werden integriert, um ein einheitliches Verständnis der ISW-Dynamik zu ermöglichen.

ISW breiten sich in einer inhomogenen Umgebung aus; je nach der relativen Skalentrennung zwischen ISWn und ihrer Umgebung entstehen dynamisch unterschiedliche Wechselwirkungsregime. Wenn schnelle, kleinräumige ISWn mit langsam variierenden Hintergrundströmungen interagieren, entwickeln sich ISWn gemäß der WKBJ-ray tracing theory (Strahlverfolgungstheorie). Innerhalb dieses Regimes untersucht der erste Teil der Dissertation die Entwicklung von ISWn in einem kohärenten mesoskaligen Wirbel unter Verwendung des neuen Internal Wave Energy Model (Modell zur Energie interner Schwererwellen), das auf der sechsdimensionalen Strahlungstransportgleichung basiert. Simulationen, die mit dem Garrett-Munk Spektrum (GM76) und einem aus Beobachtungen abgeleiteten Wirbel- und Schichtungsprofil aus dem Kanarenstromsystem initialisiert werden, zeigen, dass vertikale Scherung einen Energieverlust des ISW-Spektrums am Rand verursacht, während laterale Scherung aufgrund einer sich entwickelnden Anisotropie einen Energiegewinn außerhalb des Wirbels bewirkt. Vertikale Refraktion verursacht oberflächenverstärkte Dissipation am Rand des Wirbels mit einer Diffusion von $O(10^{-7})$ bis $O(10^{-5})\,\mathrm{m^2 s^{-1}}$.

Wenn die Skalentrennung abnimmt und Wellen Wechselwirkungen mit ähnlichen Skalen eingehen, dominieren schwach nichtlineare Wechselwirkungen die Entwicklung von ISWn. Der zweite Teil der Dissertation entwickelt eine einheitliche theoretische Grundlage für Welle-Welle und Welle-Wirbel Triadenwechselwirkungen. Die kinetischen Gleichungen (auch Streuungsintegral genannt) werden sowohl aus Euler- als auch aus Lagrange-Formulierungen des rotierenden, geschichteten, nicht-hydrostatischen Boussinesq Systems abgeleitet. Beide Formulierungen unterscheiden sich im Allgemeinen, da die Energie im Euler-Rahmen streng quadratisch ist, jedoch im Lagrange-Rahmen eine unendliche Reihe in Amplitudenpotenzen ist. Unter Resonanzbedingungen reduzieren sich beide kinetischen Gleichungen auf quadratischer Form und sind gleich. Unter horizontal isotropen Bedingungen tragen nur resonante Wechselwirkungen zum Energietransfer bei, während unter anisotropen Bedingungen bisher nicht berücksichtigte nichtresonante Wechselwirkungen über den Imaginärteil der Zeitantwortfunktion beitragen können.

Aufbauend auf dieser theoretischen Grundlage wird im dritten Teil der Dissertation die neue numerische Methode Scattering Integral for Nonlinear Energy Transfers (Streuintegral für nichtlineare Energieübertragungen) entwickelt, um das Streuintegral über typische ozeanische ISW-Spektren auszuwerten. Diese Methode löst langbestehende Probleme hinsichtlich der Konsistenz schwacher Wechselwirkungen und der Konvergenz des Streuungsintegrals. Bei Anwendung auf das GM76-Spektrum divergiert das Streuungsintegral, sofern keine Modifikationen wie spektral steilere Steigungen oder ein Übergang zu Turbulen-

zen eingeführt werden, was darauf hindeutet, dass das kanonische GM76-Spektrum unter nichtlinearen Energieübertragungen nicht universell selbstkonsistent ist. Die berechneten Energieübertragungen werden eher durch nichtlokale Wechselwirkungen dominiert als durch lokale Wechselwirkungen. Parametrische subharmonische Instabilität steuert die inverse Energiekaskade in der Frequenz, induzierte Diffusion treibt frequenz-bidirektionale Energieübertragungen an und elastische Streuung trägt zu schwachen Vorwärtsübertragungen bei. Es werden zwei bisher unbekannte Mechanismen identifiziert: Die dritte parametrische Erzeugung ist der Haupttreiber für Vorwärtsenergiekaskaden, und horizontale Diffusion treibt starke Energieübertragungen bei hohen Frequenzen an.

Zusammen bietet diese Dissertation einen integrierten Überblick, wie die Energie der ISWn durch mesoskalige Strömungen und schwach nichtlineare Wechselwirkungen umverteilt wird. Durch die Kombination von theoretischen Entwicklungen, numerischen Fortschritten und beobachtungsbasierten Konfigurationen liefert die Dissertation eine quantitative Beschreibung der komplexen Energiepfade des gesamten ISW-Feldes in bisher höchster Auflösung. Die Ergebnisse schaffen eine solide physikalische Grundlage für die Parametrisierung von ISW-Prozessen in Ozeanzirkulationsmodellen und eröffnen neue Wege für die zukünftige Forschung zur ISW-Energetik.

Abstract

Internal gravity waves (IGWs) mediate key pathways in the ocean's energy cycle, redistributing energy across a broad range of scales due to interactions with their environment shaped by, inter alia, mean flows, other waves, topography, and turbulence. Through these interactions, IGWs transfer energy to smaller scales, inducing density mixing that is essential to maintain the global overturning circulation. Yet diagnosing and quantifying these pathways remains challenging due to complex IGW generation, interaction, and dissipation processes. This thesis examines energy pathways driven by wave-mean flow and wave-wave interactions under representative oceanic conditions. Theory, numerical modeling, and observation-based analyses are integrated to provide a unified understanding of IGW dynamics.

IGWs evolve within an inhomogeneous environment; their scale separation gives rise to dynamically distinct interaction regimes. When fast, small-scale IGWs interact with slowly varying background flows, IGWs evolve according to WKBJ-ray tracing theory. Within this regime, the first part of the thesis investigates IGW evolution in a coherent mesoscale eddy using a novel Internal Wave Energy Model based on the six-dimensional radiative transfer equation. Simulations initialized with the Garrett–Munk spectrum (GM76) and an observation-inspired eddy and stratification from the Canary Current System show that vertical shear drives wave energy loss at the rim, whereas lateral shear drives wave energy gain outside the eddy through anisotropy development. Vertical refraction produces surface-intensified dissipation at the eddy rim with diffusivities of $O(10^{-7})$ to $O(10^{-5})\,\mathrm{m^2 s^{-1}}$.

As scale separation diminishes and waves interact with similar scales, weakly nonlinear effects dominate their evolution. The second part of the thesis develops a unified theoretical foundation for wave-wave and wave-vortex triad interactions. The kinetic equations or scattering integrals are derived from both Euler and Lagrange formulations of the rotating, stratified, non-hydrostatic Boussinesq system. Both formulations generally differ, as energy is strictly quadratic in the Eulerian framework but is an infinite series in amplitude powers in the Lagrangian. However, under resonant conditions, both kinetic equations reduce to quadratic form and are equal. In horizontally isotropic conditions, only resonant interactions contribute to energy transfers, while in anisotropic conditions, so far unconsidered non-resonant interactions may contribute through the imaginary part of the time response function.

Based on this theoretical framework, the third part of the thesis develops the novel numerical framework Scattering Integral for Nonlinear Energy Transfers to evaluate the scattering integral across typical oceanic IGW spectra. These methods resolve long-standing issues regarding weak-interaction consistency and convergence of the scattering integral. When applied to the GM76 spectrum, the scattering integral diverges unless modified by steeper slopes or smooth transitions to turbulence, suggesting that the canonical GM76 spectrum is not universally self-consistent. The computed energy transfers are dominated by non-local interactions rather than local interactions. Parametric subharmonic instability drives an inverse energy cascades in frequency; induced diffusion drives bidirectional energy transfers in frequency; and elastic scattering weak forward transfers. Two new mechanisms are identified: Third parametric generation is the main driver of forward energy cascades, and horizontal diffusion drives strong energy transfers at high frequencies.

Together, these studies offer an integrated view of how IGW energy is redistributed by mesoscale flows and weakly nonlinear interactions. By combining theoretical and numerical advances with observation-based configurations, the thesis provides a quantitative description of the complex energy pathways of the full IGW field at unprecedented high resolution. The findings establish a robust physical foundation for parameterizing IGW processes in ocean circulation models and open new paths for future research on IGW energetics.

Publications related to this dissertation

Sebastia Saez, P., Eden, C., Chouksey, M., (2024): "Evolution of internal gravity waves in a meso-scale eddy simulated using a novel model", published in *Journal of Physical Oceanography*

Sebastia Saez, P., Chouksey, M., Eden, C., Olbers, D., (2025): "Wave-wave interactions of internal gravity waves. Part A: Comparison of Eulerian and Lagrangian frameworks", submitted to *Journal of Physical Oceanography*

Sebastia Saez, P., Chouksey, M., Eden, C., Olbers, D., (2025): "Wave-wave interactions of internal gravity waves. Part B: Spectral energy transfers in a typical internal gravity wave field", submitted to *Journal of Physical Oceanography*

Contents

Zusammenfassung **iv**

Abstract **vi**

Publications related to this dissertation **viii**

1 Introduction **1**
1.1 Internal gravity waves in the ocean . . . 3
1.2 Modeling internal gravity waves . . . 8
1.2.1 Linear internal gravity waves and their interactions with the large-scale mean flow . . . 10
1.2.2 The wave field as statistical ensemble - The Radiative Transfer Equation 13
1.2.3 Nonlinear interactions within the internal gravity wave spectrum . . . 14
1.3 Thesis overview . . . 17

2 Evolution of internal gravity waves in a meso-scale eddy simulated using a novel model **19**
2.1 Introduction . . . 20
2.2 Energetics of IGWs . . . 21
2.2.1 Spectral energy balance . . . 22
2.2.2 Wave breaking and dissipation . . . 23
2.2.3 The Garrett-Munk model spectrum . . . 24
2.2.4 Instability at wavenumber thresholds . . . 24
2.3 Numerical simulations . . . 25
2.3.1 Waves in a coherent eddy . . . 27
2.3.2 Wave-mean flow interaction . . . 29
2.3.3 Wave propagation . . . 34
2.3.4 Vertical wave refraction and wave dissipation . . . 35
2.3.5 Comparison to observations . . . 37
2.4 Summary and discussion . . . 39
A The Internal Wave Energy Model (IWEM) . . . 43
B Observed velocities . . . 44
C Idealized velocities . . . 44

3 Wave-wave interactions of internal gravity waves. Part A: Comparison of Eulerian and Lagrangian frameworks **46**
3.1 Introduction . . . 47
3.2 The Eulerian framework . . . 49
3.3 The Lagrangian framework . . . 53
3.3.1 The Lagrangian equations of motion . . . 53
3.3.2 The Lagrangian density functional . . . 54

3.3.3 Lagrangian interaction coefficients . . . 55
3.4 Energy conservation and the fundamental relation . . . 57
3.4.1 The fundamental relation . . . 57
3.4.2 Relations between the coupling coefficients . . . 58
3.4.3 Eulerian and Lagrangian energies . . . 60
3.5 Kinetic equation . . . 61
3.5.1 Resonance and non-resonance . . . 63
3.6 Conclusions . . . 64
A The Lagrangian polarization vector . . . 66
B The Lagrangian interaction coefficient . . . 66

4 Wave-wave interactions of internal gravity waves. Part B: Spectral energy transfers in a typical internal gravity wave field 68
4.1 Introduction . . . 69
4.2 Methods to evaluate the scattering integral . . . 71
4.3 Evaluations of resonant and non-resonant interactions . . . 74
4.3.1 Evaluations including all interactions . . . 75
4.3.2 Evaluations including only resonant interactions . . . 76
4.3.3 Resonant interactions in (m, k, ϕ)- and (m, ω, ϕ)-space . . . 78
4.4 Convergence of the scattering integral . . . 80
4.5 Local and Non-local interactions . . . 83
4.5.1 Induced diffusion and horizontal diffusion . . . 86
4.5.2 Elastic scattering . . . 88
4.5.3 Parametric subharmonic instability . . . 89
4.5.4 Third parametric generation TPG . . . 90
4.5.5 Relative importance between local and non-local interactions . . . 91
4.6 Conclusions . . . 92
A The Garrett-Munk model - GM76 . . . 96
B Resonant condition in (ω, m, ϕ)-space as in Olbers (1974) . . . 97

5 Supplemental Material to Wave-wave interactions of internal gravity waves. Part B: Spectral energy transfers in a typical internal gravity wave field 99
5.1 Dependence of the energy transfers by a gradual transition from a -2 to a -3-slope in vertical wavenumber and a changing roll-off wavenumber m_r^* . . . 100
5.2 Comparison of different filters for triad interaction mechanisms . . . 101

6 Conclusions and perspectives 103
6.1 Synthesis and perspectives across the three main chapters . . . 103
6.1.1 How do interactions between internal gravity waves and a mesoscale eddy shape the internal gravity wave spectrum? . . . 104
6.1.2 How do nonlinear interactions among internal gravity waves govern energy transfers within the oceanic internal gravity wave field? . . . 108
6.1.3 How do interactions within the internal gravity wave field affect variations of the universal oceanic internal gravity wave spectrum? . . . 109
6.2 An integrated picture . . . 113

1

Introduction

Legends tell of Cleopatra's fleet escaping through the mists of the *Ionian Sea* in a final bid for freedom. The desperate escape failed not just in the hands of Octavian's fleet but perhaps before the sea itself. Her vessels were said to be held back by the remora (suckerfish) attached to the hulls, slowing them down for them to face the defeat before Octavian's fleet. Yet some now theorize about an invisible grip – a layering of fresh water above salt water, where the water stands, the vessel's speed decreases, and the rudders fail. It has been hypothesized that such "dead waters" explain an alternative theory for Cleopatra's defeat during the *Battle of Actium* (31 BC); see Fourdrinoy et al. (2020)[1]. Nearly two millennia later, in the frozen Arctic, the explorer Fridtjof Nansen would unknowingly encounter the same haunting stillness aboard the *Fram* (Nansen, 1902). It was Nansen that coined the term "dead waters" for this quiet adversary, but its presence had already written itself into the story of an empire lost. But the story continues as some years later the Swedish physicist and oceanographer Vagn Walfrid Ekman explained the formation of internal waves at the interface between the salt water and freshwater layers with experimental and theoretical studies (Ekman, 1904). Such waves would interact with the ship and slow it down by the exerted drag. Since then, internal gravity waves have stirred more than just the sea – they have stirred our curiosity, urging us to uncover the deep and quiet forces that still move beneath the surface.

What began as an oddity observed by Nansen – the dead water phenomenon – turned out to have larger implications beyond just maritime navigation. Internal gravity waves, now understood as essential to both oceanic and atmospheric systems, have since become one of the central foci of geophysical research. Internal gravity waves are wave motions arising in fluids in which density is stratified and gravity is acting. In the ocean, stratification is primarily governed by vertical gradients in temperature and salinity, leading to variations in the fluid's density with depth. When the stratified equilibrium is perturbed, buoyancy forces drive an oscillatory motion that restores the displaced fluid to its original position. These motions may manifest as interfacial waves at sharp density transitions similar to the waves that Cleopatra's fleet or Nansen may have encountered or as a more familiar phenomenon at the air-sea interface in the form of surface waves. However, as the name indicates, internal gravity waves exist in the interior of the ocean, where density is continuously stratified. Compared to surface gravity waves, the density contrasts over the water column are much smaller, and the restoring force of gravity is weaker compared to the air-sea interface, resulting in substantially

[1] https://www.cnrs.fr/en/press/behind-dead-water-phenomenon

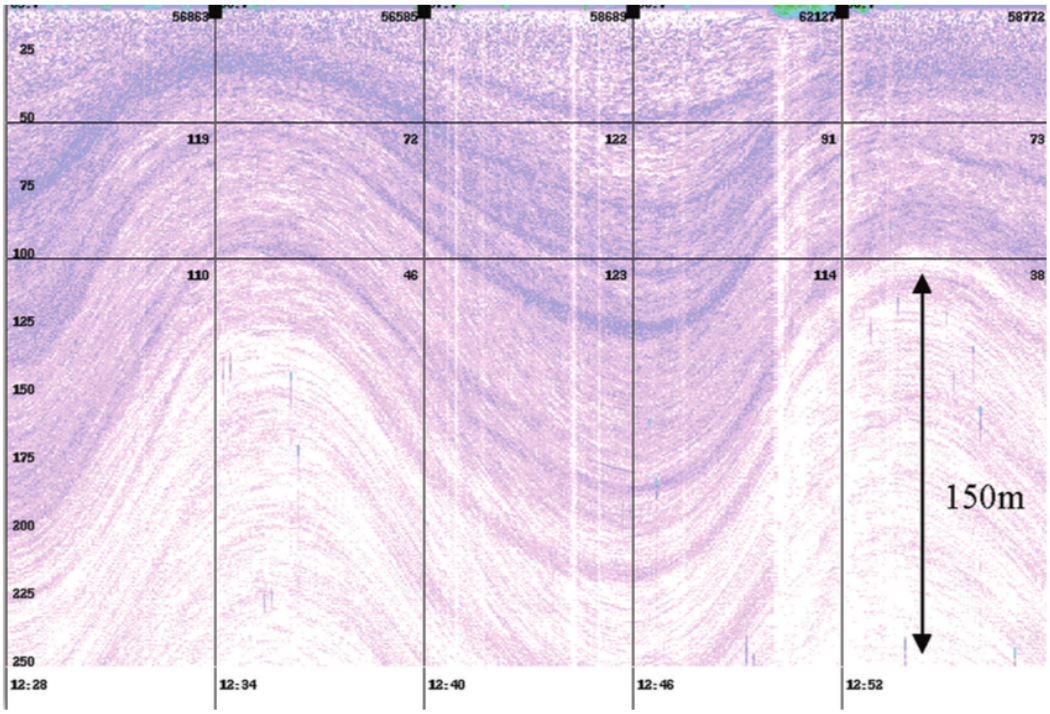

Figure 1.1: A spectacular echogram of the water column obtained by an EK500 echosounder operating at a frequency of 38 kHz during the 2005 INSTANT Indonesian Throughflow cruise, covering the upper 250 m of the water column. The ship was on standby when waves with a wavelength of about 1.8 km passed under the ship with a speed of roughly 1.5 m/s. The wave amplitude (peak to trough) exceeds 100 m. Higher backscatter values indicate higher plankton concentration or large schools of fish. The vertical axis is depth in meters. The horizontal axis is time; the spacing between two vertical lines is 6 minutes. From Susanto et al. (2005).

longer periods and wavelengths of IGWs. In a rotating system, internal gravity waves are bounded between the inertial period $2\pi/f$, where f is the Coriolis parameter that arises from the rotational period of Earth, and the local buoyancy period $2\pi/N$, where N is the buoyancy or Brunt-Väisälä frequency. Their horizontal scales range from a few meters to some tens of kilometers, and their vertical scales range from about one meter to one kilometer. Generally, their vertical displacements are about 10 m and velocities of 5 cm/s. These representative values can, however, vary substantially, as we see in Fig. 1.1, where the wave's amplitude and velocity are more than ten times larger. Internal gravity waves cover thus a vast range of spatial and temporal scales, which makes them central to the spectrum of oceanic processes connecting the large scales with the small ones. Fig. 1.2 shows the space-time spectrum of processes in the ocean. Oceanic processes are divided into three major dynamical regimes: the large-scale geostrophic-balanced motion, the internal gravity wave field, and the small-scale turbulence. Internal gravity waves bridge, therefore, the gap between the large-scale flow of the ocean, like geostrophically balanced motions, and the small-scale three-dimensional turbulence.

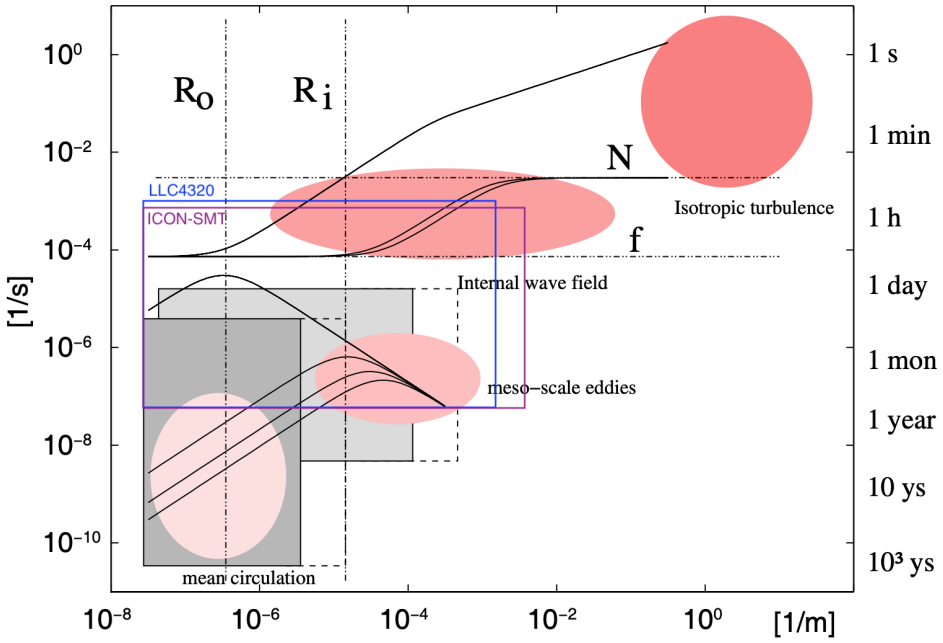

Figure 1.2: Space-time scales of important oceanic processes (pink areas) and scales explicitly resolved by ocean models (grey rectangular areas). Also shown are dispersion curves (solid lines) for linear gravity waves (upper set) and planetary waves (lower set). Vertical dotted lines indicate the external (Ro) and the first internal (Ri) Rossby radii. Two last-generation high-resolution global ocean models are indicated as examples of the present-day state-of-the-art in ocean modeling: LLC4320 (LLC, latitude–longitude–polar cap) $\frac{1}{48^\circ}$ global-ocean MITGCM simulation with hourly output (blue box), see Gallmeier et al. (2023); ICON-SubMesoscale-Telescope (ICON-SMT) with horizontal resolution finer than 1 km over the telescoped area and two-hourly output (purple box), see Korn et al. (2022). The figure is adapted from Olbers et al. (2012)

1.1. Internal gravity waves in the ocean

Internal gravity waves (IGWs) are omnipresent in the ocean and play a fundamental role in the ocean's energy cycle. By linking large and small scales through complex energy transfers, they are crucial to sustaining the global overturning circulation. IGWs inject energy into the ocean's interior through mixing, which helps maintain the large-scale flow of water masses (e.g., Munk, 1966; Garrett and Munk, 1972; Wunsch and Ferrari, 2003; Talley, 2013, and references therein).

Understanding how this mixing is supplied leads us back to the dynamics of IGWs themselves. As IGWs propagate through the ocean and shift toward higher frequencies and shorter wavelengths, they can become unstable and break, see Staquet (2004). This wave breaking initiates a transfer of energy into the turbulent regime, triggering a forward cascade toward progressively smaller scales, ultimately reaching the Kolmogorov scale (see Olbers et al., 2012). Through this cascade, energy is transferred from waves into turbulence, where viscous forces dominate and enable mixing that alters the density structure of the ocean. This mixing reduces local stratification and increases the ocean's mean potential energy by redistributing mass: dense water is lifted upward, and lighter water is displaced downward. This energy transformation provides a reservoir of potential energy that supports the large-scale circulation.

The energy input required to sustain this mixing is estimated by Munk's "abyssal recipe" Munk (1966), which postulates that deep and intermediate water upwelling must be balanced by the downward diffusion of surface heat. The energy balance can be expressed as $\kappa N^2/b \approx wN^2$, where κ is the vertical (diapycnal) diffusivity and $b = 1.3 \times 10^3$ m is the vertical depth scale of the density stratification. This must hold in a global average – with a global upwelling rate of $wA = 30\,\mathrm{Sv}$ ($1\,\mathrm{Sv} = 10^6\,\mathrm{m^3 s^{-1}}$) for the meridional overturning circulation and the global ocean area $A = 360 \times 10^{12}\,\mathrm{m^2}$ – we recover Munk's canonical value for the mean diffusivity $\kappa = 10^{-4}\,\mathrm{m^2 s^{-1}}$. The corresponding energy conversion rate through turbulence and mixing is $\rho\kappa N^2 \times HA$, assuming a mean ocean depth $H = 3800\,\mathrm{m}$ and an estimated Brunt-Väisälä frequency $N = 5 \times 10^{-3}\,\mathrm{s^{-1}}$. A re-evaluation by Munk and Wunsch (1998) suggests a value closer to 2.1 TW. Despite its importance, the physical mechanisms driving this energy conversion, like IGW breaking, are still not fully understood and are often misrepresented in numerical models, which in turn leads to energetic inconsistencies and thus inaccurate model predictions.

Accurately representing IGW-induced mixing is critical for realistic predictions of large-scale ocean circulation and climate. However, current global general circulation models resolve only limited spatial and temporal scales. Since Olbers et al. (2012), where the resolved regimes by the model generation of that time are indicated by the grey boxes in Fig. 1.2, there have been significant advancements in ocean modeling. The highest resolution global ocean models today, such as the LLC4320 MITGCM-simulation (Gallmeier et al., 2023) and ICON-SMT (Korn et al., 2022) shown by the blue and purple boxes in Fig. 1.2, can resolve scales down to approximately 1 km horizontally and a few meters vertically, with temporal resolutions of hours. Even these are far from capturing the full spectrum of IGWs and turbulence scales due to applied filtering techniques, such as Reynolds decomposition. In Reynolds decomposition, a field variable is split into a mean and a fluctuating component. Averaging the governing equations introduces turbulent flux terms into the momentum balance for the mean flow. Further, the evolution of these fluxes depends on higher-order moments, which require fourth-order correlations, and so on. This highlights not only the multiscale nature of turbulence but also the absence of a closed analytical theory, necessitating parameterization of these unresolved motions.

A common simplification in ocean models is to prescribe a fixed vertical diffusivity, e.g., Munk (1966), to represent the dissipation of unresolved IGWs. However, this overlooks the complex dynamics involved in the generation and propagation of IGWs, and especially their interactions with the background environment and final dissipation (Müller and Briscoe, 2000; Natarov and Müller, 2005; Olbers and Eden, 2013, 2017; Eden and Olbers, 2017; Musgrave et al., 2022). Observational and theoretical studies (Polzin, 2004, 2009) show that this approach fails to capture the variability in vertical and horizontal mixing structures. Alternatives have been proposed. For instance, Bryan (1979) introduced a depth-dependent diffusivity with a prescribed function, while others (Cummins et al., 1990) suggested making it a function of stratification N. However, these methods did not account for the energy source driving mixing, such as IGW breaking. To realistically represent mixing, it is thus crucial to understand not only how much energy is supplied by the IGW field, but also from where it originates, how it propagates, interacts, and ultimately dissipates. This calls for a comprehensive understanding of the entire intricate life cycle of IGWs sketched in Fig. 1.3 – from generation, through nonlinear interactions and spectral energy cascades, to eventual dissipation.

Several estimates have been proposed for the energy input into the IGW field from

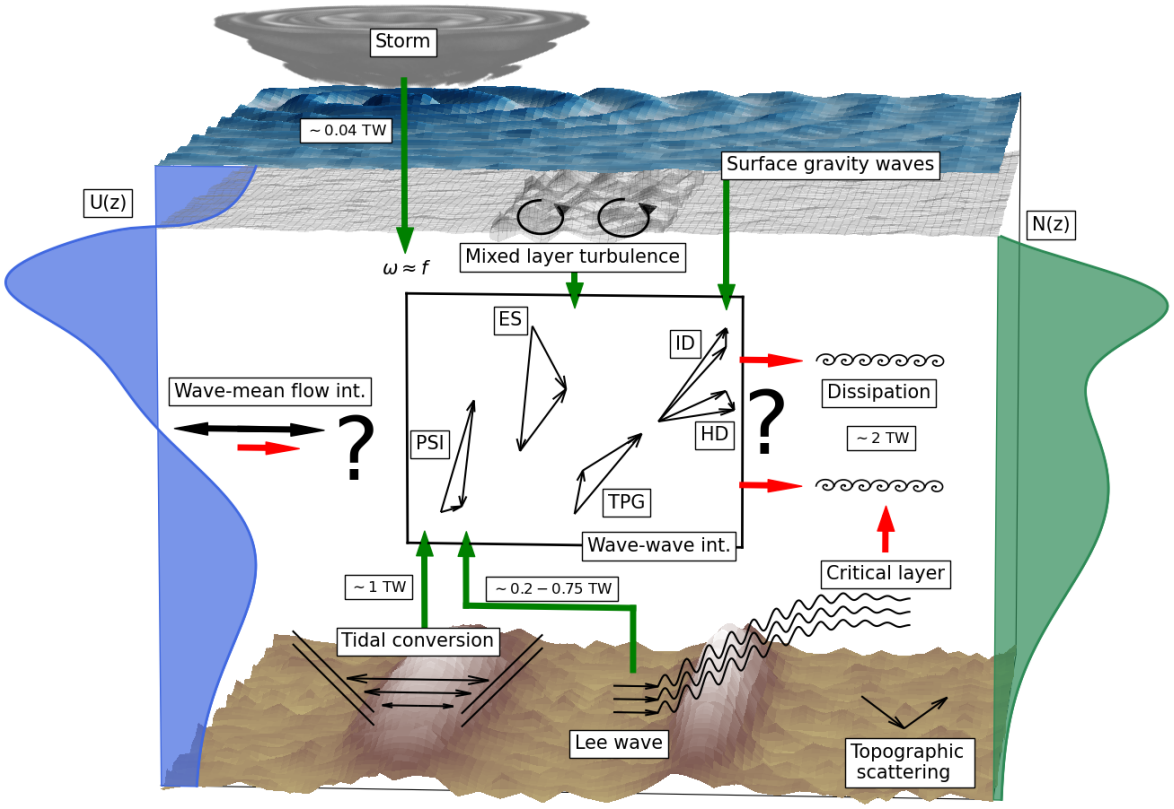

Figure 1.3: Sketch of processes contributing to the energy balance of the IGW field. Wave energy is generated by external forcing mechanisms. The energy input from the surface by inertial pumping (via wind stress fluctuations represented by the storm), surface gravity waves, and mixed layer turbulence; and from the bottom by tidal conversion (barotropic tides interacting with topography generating baroclinic tidal constituents), lee waves (large-scale motions flowing over topography), and topographic scattering to the IGW field as represented by green arrows. This energy is then transferred within the IGW field through interactions with the large-scale mean flow $U(z)$ (represented by the first baroclinic mode, in blue), refraction by stratification $N(z)$ (in green), and through wave-wave interactions (the central box shows the main resonant triad interaction mechanisms – ID, HD, ES, PSI, and TPG). Eventually, the energy reaches scales where it becomes unstable and is dissipated by various processes, like wave breaking at critical layers through wave-mean flow interactions or by the downscale scattering by wave-wave interactions (red arrows). To each process, an estimated rate of energy transfer is indicated, quantifying its contribution to the overall energy budget. While the processes shown reflect current knowledge, some well quantified and others still uncertain, additional pathways may exist, such as secondary wave generation following wave breaking or other multistage cascade processes. This sketch is updated from Olbers (1983).

predominantly two large-scale processes: i. Wind stress fluctuations (represented by the storm in Fig. 1.3) induce near-inertial pumping at the base of the ocean's mixed layer (D'Asaro, 1985; Olbers et al., 2020a). Wind stress fluctuations over the ocean surface contribute a total wind work estimated between 0.3 – 1.5 TW, depending on the methodology and data used (Alford, 2001; Watanabe and Hibiya, 2002; Rimac et al., 2013). Of this, approximately 15 – 25 % is believed to radiate away from the mixed layer into the ocean interior as near-inertial internal waves (Crawford and Large, 1996; Furuichi et al., 2008; Olbers et al., 2020a). ii. Tidal conversion: Barotropic tides interacting with topography or large-scale motions flowing over topography generate Lee waves (Bell, 1973; Nikurashin and Ferrari, 2011). Approximately

1 TW of energy is supplied by the barotropic tide (see Egbert and Ray (2000) for estimates from satellite-based observations, Müller (2013) from numerical modeling, and Nycander (2005) from linear theory), with an additional $0.2 - 0.75$ TW attributed to Lee wave generation as geostrophic currents impinge on bottom topography (Nikurashin and Ferrari, 2011; Wright et al., 2014). The energy input from mixed layer turbulence and surface gravity waves have been attempted to be estimated in the past (see Bell, 1978; Olbers and Herterich, 1979, respectively), and were reported to be small compared to the sources by tidal conversion, wind stress and Lee waves. Taken together, these sources may supply the IGW field with the 2 TW of energy required to sustain observed levels of diapycnal mixing (represented by the dissipation in Fig. 1.3). While the processes shown summarize the present state of knowledge, some of them well quantified and others still requiring further investigation, they likely do not constitute a complete description of the IGW energy cycle. Additional pathways may exist that remain unresolved or are only beginning to be recognized, such as secondary wave generation following wave breaking or other multistage cascade processes. These potential mechanisms underline the need for continued theoretical, numerical, and observational work to fully close the IGW energy budget.

Once IGWs are generated, they interact with their background environment, leading to energy transfers across different wavenumbers and frequencies. This interaction causes the energy to spread in spectral space, ultimately resulting in a continuum of IGWs. Remarkably, the energy spectra of this IGW continuum exhibit similar shapes across wide regions of the ocean, a phenomenon first identified by Garrett and Munk (1972) and now commonly referred to as the Garrett–Munk (GM) model. This model was initially based on mooring observations at Site D in the North Atlantic (Fofonoff, 1969; Webster, 1972), and later supported by data from the three-dimensional IWEX array (Briscoe, 1975; Müller et al., 1978). These studies confirmed the general concept of a universal deep ocean IGW spectrum as described by the GM model, see also Cairns and Williams (1976); Munk (1981), with spectral slopes close to -2 in both vertical and horizontal wavenumber and frequency and a near-inertial peak. Such a universal IGW spectrum would be possible in a steady-state regime, where wave dissipation balances the input of energy, producing the characteristic GM spectral shape. However, regional deviations from the universal GM model (Polzin and Lvov, 2011; Pollmann, 2020; Le Boyer and Alford, 2021) are misrepresented by its statistical framework, as it does not capture the substantial regional variability in forcing, interactions, and consequently variability. The interactions that are thought to be predominantly responsible for the generation of the IGW continuum are wave-mean flow and wave-wave interactions (Olbers, 1983; Müller et al., 1986).

Wave-mean flow interactions are represented in Fig. 1.3 as interactions of the IGW field with a depth-varying large-scale flow $U(z)$ including a background stratification $N(z)$. Such interactions can lead to the trapping of waves at critical layers (in the bottom right of Fig. 1.3), where the waves become unstable and break. This is, however, just one example of how waves may interact with the large-scale mean flow. Wave-mean flow interactions actually depend on the relative scales and characteristics of IGWs and mean flows, as discussed in Sec. (1.2.1) and Sec. (1.2.3), which adds complexity to the IGWs life cycle. The respective rates of energy transfers by wave-mean flow interactions are, however, still not well constrained and remain undetermined, leading to uncertainties in the overall energy budget of the IGW field. Furthermore, the IGW field interacts with itself by wave-wave interactions represented with the box at the center of Fig. 1.3 by typical interaction processes like induced diffusion (ID), parametric subharmonic instability (PSI), elastic scattering (ES), and the newly found

horizontal diffusion (HD) and third parametric generation (TPG). Wave-wave interactions act to cascade wave energy towards small scales, eventually feeding the turbulent regime by wave breaking. The intricacies of wave-wave interactions, however, expand beyond this simplified description where, for example, non-resonant interactions are ignored. Furthermore, wave-wave interactions depend on the shape of the IGW spectrum itself, environmental parameters such as the Coriolis frequency or stratification, as well as external forcing such as tidal constituents. The rates of energy transfer by wave-wave interactions are thus also not well constrained, adding further uncertainty to the overall energy budget of the IGW field. Because of these complex interactions, understanding the life cycle of the IGW field is a challenging task. Gaining a deep understanding of the IGW life cycle is fundamental for improving knowledge of the ocean's energy cycle and, consequently, climate predictions (see Eden and Iske, 2019).

In the past, several approaches have been proposed to analyze interactions within the IGW field and its surroundings, see reviews by Olbers (1983); Müller et al. (1986). These include the evaluation of the scattering integral describing weakly and resonantly interacting waves, first investigated by Olbers (1974, 1976); the integration of the eikonal or ray equations describing the propagation of small-scale IGWs in a large-scale background environment (Henyey et al., 1986; Bühler, 2014); and the direct numerical simulation (Chouksey et al., 2018). Building on these early approaches, studies such as McComas and Bretherton (1977) and Henyey et al. (1986) further advanced the understanding of energy transfers within the IGW field, particularly the mechanisms that drive energy toward smaller scales and ultimately into turbulence. Their work laid the foundation for energetic, consistent parameterizations for IGW-induced mixing. Consequently, Müller and Briscoe (2000) and Natarov and Müller (2005) proposed a promising concept based on a prognostic spectral energy balance for IGWs, the Internal Wave Action Model (IWAM). The introduced six-dimensional model with three dimensions in the spatial physical space and three in the wavenumber space (and time) is, however, hindered due to analytical, practical, and computational limitations, and no actual application was published. To overcome these practical limitations, Olbers and Eden (2013) tackled this six-dimensional problem by drastic simplifications. By integrating the spectral energy balance over the wavenumber space, an energetically consistent parameterization for diapycnal diffusivity is provided in the presented model for Internal Wave Dissipation, Energy and Mixing (IDEMIX), see Olbers et al. (2019).

This thesis does not aim to further simplify the six-dimensional problem but to analyze the evolution of the IGW spectrum in its full form. With the technological and computational advances since the 1970s and 1980s, efficient numerical tools are developed to explore the detailed evolution of the IGW spectrum. The focus of this thesis is on understanding the various interaction processes – between IGWs and large-scale mean flows, and within the IGW field itself – that ultimately drive energy transfers into the turbulent regime and induce mixing. To this end, both ray theory and the scattering integral framework are adopted and extended to establish a robust theoretical basis for interpreting results from modern observations and simulations.

1.2. Modeling internal gravity waves

In oceanography, it is common to adopt the Boussinesq approximation to describe the fluid dynamics under the influence of gravity, density stratification, and Earth's rotation. This approximation is well-suited for geophysical flows like those in the ocean, where density variations are small compared to the reference density but still play a crucial role in driving buoyancy forces. The Boussinesq approximation assumes that density variations around a constant reference density ρ_0 are negligible. The density field $\rho(\boldsymbol{x}, t) = \rho_0 + \bar{\rho}(z) + \rho'(\boldsymbol{x}, z, t)$ can be decomposed into a constant part ρ_0, a reference state $\bar{\rho}(z)$ with constant temperature and salinity that varies with the depth z, and a perturbation $\rho'(\boldsymbol{x}, z, t)$ that depends on the horizontal spatial position denoted by the vector $\boldsymbol{x} = (x, y)^T$, depth, and time t. In the ocean $\rho'(\boldsymbol{x}, t)/\bar{\rho}(z) \lesssim 2 \times 10^{-3}$ and the variations of $\bar{\rho}(z)$ are at most $2 - 3\,\%$. Due to the smallness of the deviations from the background reference, we approximate ρ with ρ_0.

To define the background stratification, we consider perturbations with respect to a specified background state that reflects the depth-stratified density $\bar{\rho}(z)$ caused by variations in temperature and salinity. This reference density $\bar{\rho}(z)$ is defined as the horizontal average of the density field considering a pressure field $\bar{p}(z)$ in hydrostatic balance $\partial_z \bar{p}(z) = -g\bar{\rho}(z) \approx -g\rho_0$, where g is the gravity acceleration. We further define the buoyancy or Brunt-Väisälä frequency $N = \sqrt{-\frac{g}{\rho_0}\partial_z \bar{\rho}(z)}$. The Brunt-Väisälä frequency is the frequency with which a displaced fluid parcel oscillates around its equilibrium position by the restoring buoyancy force. We consider stably stratified fluids, where density decreases with height, i.e., $\partial_z \bar{\rho}(z) < 0$.

Earth's rotation is represented under the traditional approximation, where horizontal scales are assumed to dominate, allowing us to retain only the vertical component of the Earth's rotation vector. Under this simplification, Earth's rotation vector is approximated by $\boldsymbol{\Omega} = (0, 0, f/2)^T$, where $f = 2\Omega \sin(\phi)$ is the Coriolis frequency with Earth's rotation rate $\Omega \approx 7 \times 10^{-5}\,\mathrm{s}^{-1}$ and latitude ϕ. We further apply the f-plane approximation where the meridional variations of the Coriolis frequency are suppressed, i.e., $f = \text{const}$.

We can now write the Boussinesq model as

$$\begin{aligned} \partial_t \boldsymbol{u} + f\,\underset{\neg}{\boldsymbol{u}} + \boldsymbol{\nabla} p = -\boldsymbol{u} \cdot \boldsymbol{\nabla}\boldsymbol{u} - w\partial_z \boldsymbol{u} \quad &, \quad \partial_t w - b + \partial_z p = -\boldsymbol{u} \cdot \boldsymbol{\nabla} w - w\partial_z w \\ \partial_t b + N^2 w = -\boldsymbol{u} \cdot \boldsymbol{\nabla} b - w\partial_z b \quad &, \quad \boldsymbol{\nabla} \cdot \boldsymbol{u} + \partial_z w = 0 \end{aligned} \tag{1.1}$$

where all vectors are two-dimensional, and $\underset{\neg}{\boldsymbol{u}}$ denotes anticlockwise rotation of $\boldsymbol{u}$ by 90°. The first and second equations are the horizontal and vertical momentum equations, respectively, with horizontal $\boldsymbol{u}$ and vertical w velocities. Using the hydrostatic balance in the momentum equations, the kinematic pressure $p = p'/\rho_0$ is introduced, which is the perturbation scaled by the constant background. The third equation represents the continuity condition, where the buoyancy $b(\boldsymbol{x}, t) = -\frac{g}{\rho_0}\rho'(\boldsymbol{x}, t)$ has been readily introduced and N substituted. In the Boussinesq approximation, the continuity condition simplifies to the last equation as density variations are small and neglected except in the buoyancy term. The last equation is the incompressibility condition, stating that the volume of fluid parcels is conserved, i.e., no net expansion or compression.

Note that the system of equations in Eq. (3.1) describes the full nonlinear non-hydrostatic Boussinesq system without distinction between the different dynamical regimes in the ocean, for example, between geostrophically balanced motions and unbalanced IGWs. Unbalanced

and balanced motions are interlinked through the nonlinear terms on the right-hand side of Eq. (3.1). A simple Reynold's decomposition separating a mean slowly varying part that represents balanced motions from a fast-varying perturbation that represents unbalanced motions already reveals the intricacy of their interactions. Balanced motions may interact with other balanced motions, advecting each other; balanced motions may interact with unbalanced motions, advecting them or being advected by the unbalanced motions; and lastly, unbalanced motions may interact with other unbalanced motions, advecting each other. Reynolds averaging, inter alia, is a commonly used method to separate balanced from unbalanced motions by some kind of simple, straightforward spatial and/or temporal averaging. However, the dynamical distinction of both motions is crudely handled and thus inaccurate, which in turn leads to an ambiguous interpretation of the underlying dynamics.

Efforts in the realm of flow decomposition have risen since 1922, when the mathematician, physicist, and meteorologist Lewis Fry Richardson published Weather Forecasting by Numerical Process, developing the idea of Richardson's Fantastic Forecast Factory, see Richardson (2007). It describes an imagined, large-scale, human-powered facility where thousands of workers calculate weather forecasts manually – each one computing a piece of the atmospheric equations by hand, simulating the behavior of the atmosphere step-by-step. Richardson's own early forecast failed due to unresolved IGWs. This directly relates to the importance of separating balanced motions (i.e., geostrophic balanced flows) from unbalanced ones (i.e., IGWs), making flow decomposition methods (see e.g. Chouksey et al., 2018; Eden et al., 2019c; Masur and Oliver, 2020; Chouksey et al., 2023) a useful tool to investigate IGW interactions in direct numerical simulation. Direct numerical simulations, although powerful for studying strongly interacting waves, are limited by finite computer resolutions at high computational costs. Furthermore, this kind of approach does not provide any information on the underlying processes that are actually causing the energy transfers between waves and balanced motions. An additional complication arises when considering a spectrum of motions where one cannot differentiate between, for example, different kinds of wave-wave interactions.

Nevertheless, let us assume that we have been able to separate waves from mean flow motions; we readily identify different regimes of interactions depending on the amplitude and length scales of the mean flow compared to the wave field. Let the wave field $\boldsymbol{u}$ with characteristic velocity u and length scale l be superimposed on a mean flow $\boldsymbol{U}$ with characteristic velocity U and length scale L. Scaling the wave's horizontal momentum equations by the characteristic wave and flow parameters and the Coriolis parameter f, we obtain

$$\partial_t \boldsymbol{u} + f \underline{\boldsymbol{u}} + \boldsymbol{\nabla} p = -Ro(\boldsymbol{u} \cdot \boldsymbol{\nabla}\boldsymbol{U} + w\partial_z \boldsymbol{U}) - Ro\frac{L}{l}(\boldsymbol{U} \cdot \boldsymbol{\nabla}\boldsymbol{u} + W\partial_z \boldsymbol{u}) - Ro\frac{uL}{Ul}\boldsymbol{u} \cdot \boldsymbol{\nabla}\boldsymbol{u}. \tag{1.2}$$

The first two terms on the right-hand side represent the wave-mean flow interactions, while the last represents the wave-wave interactions. These interaction terms scale with variations of the Rossby number $Ro = \frac{U}{fL}$, which quantifies the influence of rotation on the mean flow, controlling so the strength of the wave-mean flow and/or wave-wave interactions. Notably, the second interaction term scales with $Ro\frac{L}{l}$, highlighting the influence of scale separation.

Typically, the Rossby number in the ocean is of the order of $Ro = 0.01$, and often mean flow motions are more energetic than the wave field $U > u$. In this case, wave-mean flow interactions drive the energy changes, while the quadratic nonlinearities of the wave field are

negligible. Consequently, the wave field can be linearized about a slowly evolving background flow field. Further, if the wave field and mean flow are separated by scales, where $l \ll L$, only the Doppler shift survives as it dominates over the strain of the wave field since $Ro\frac{L}{l} > Ro$. This is the so-called WKBJ regime, where the wave's behavior is described by the eikonal or ray equations, see Sec. (1.2.1). In this regime, this thesis investigates wave–eddy interactions by integrating the ray equations, focusing on the propagation and refraction of short, fast IGWs through a comparably large-scale, slow (actually steady) background. However, it's unclear whether these scale-separated interactions with larger-scale motions compete with or are overwhelmed by interactions among similar scales.

In contrast, when considering scale-similar waves and mean flows $l \approx L$, all terms on the right-hand side of Eq. (1.2) become comparable. This defines the scattering regime. If $u \ll U$, the quadratic nonlinearities of the wave field can be neglected, and the wave-mean flow interactions dominate. However, both wave–mean flow interaction terms attain comparable magnitudes, and the dynamics cannot be captured by a simple Doppler shift. Instead, the wave field experiences what can be described as a scattering process by the mean flow. If $u \approx U$, wave–wave interactions must also be retained, and the full nonlinear structure of the system must be considered.

The dynamics in the scattering regime are captured by the kinetic equation, a statistical framework governing weakly nonlinear wave interactions (see Hasselmann, 1966; Nazarenko, 2011). This equation, also known as the transfer or scattering integral, describes the redistribution of wave energy through triad interactions. It has been foundational in characterizing energy transfer by wave–wave interactions (Olbers, 1974, 1976) and developing an inertial-range theory for IGWs (McComas and Bretherton, 1977). However, the range of validity for this approximation is uncertain, especially for high-wavenumber, high-frequency waves. Extensions of this theory include wave–mean flow interactions (also known as wave-vortical scattering), notably in Savva et al. (2021) although for the linearized Boussinesq system, or in Eden et al. (2020) for the full nonlinear nonhydrostatic Boussinesq system. In this work, the kinetic equation for the Boussinesq system is derived to capture both wave–wave and wave–mean flow scattering. Explicit evaluations of the transfer integral for wave–wave interactions are presented, and evaluations of wave-mean flow scattering are proposed for future work.

1.2.1. Linear internal gravity waves and their interactions with the large-scale mean flow

The ocean can be described as a body of water with characteristic stratification. Applying the Reynolds decomposition to Eq. (3.1) the background field $(\boldsymbol{U}, W, B)$ is identified as large-scale and slowly changing in space L and time T compared to the small-scale, rapidly fluctuating wave field $(\boldsymbol{u}, w, b)$. The non-hydrostatic Boussinesq equations can be linearized about the background flow for the wave field:

$$\begin{aligned}
\partial_t \boldsymbol{u} + f\,\underline{\boldsymbol{u}} + \boldsymbol{\nabla} p &= -\boldsymbol{u}\cdot\boldsymbol{\nabla}\boldsymbol{U} - \boldsymbol{U}\cdot\boldsymbol{\nabla}\boldsymbol{u} - w\partial_z\boldsymbol{U} - W\partial_z\boldsymbol{u} \\
\partial_t w - b + \partial_z p &= -\boldsymbol{u}\cdot\boldsymbol{\nabla} W - \boldsymbol{U}\cdot\boldsymbol{\nabla} w - w\partial_z W - W\partial_z w \\
\partial_t b + N^2 w &= -\boldsymbol{u}\cdot\boldsymbol{\nabla} B - \boldsymbol{U}\cdot\boldsymbol{\nabla} b - w\partial_z B - W\partial_z b \\
\boldsymbol{\nabla}\cdot\boldsymbol{u} + \partial_z w &= 0.
\end{aligned} \tag{1.3}$$

Considering a horizontal mean flow $\boldsymbol{U} = (U, V)$ with vertical and horizontal shear and stratification $N(z)$, the combination of the time derivative of the divergence and vorticity of the horizontal velocity equations, and the buoyancy equation in Eq. (1.3) leads to the equation for vertical velocity. The equation for vertical velocity has no general solution and has to be therefore approximated with the WKBJ (Wentzel, Kramers, Brillouin and Jeffreys) method. The WKBJ approximation can be applied as long as wavelengths and periods are short compared to the scales of the mean environmental fields – $\frac{2\pi}{k} \ll L$ where k is the wave's horizontal wavenumber and $\frac{2\pi}{\omega} \ll T$ where ω is the wave's frequency. It can be therefore further stated that $\boldsymbol{u} \cdot \boldsymbol{\nabla U} \ll \boldsymbol{U} \cdot \boldsymbol{\nabla u}$ (and similar for the rest of the field variables), such that advection by the Doppler shift dominates over the strain of the wave field.

Considering freely propagating waves with wave ansatz $e^{i(\boldsymbol{k}\cdot\boldsymbol{x}+mz-\omega_{enc}t)}$ and wave vector $\boldsymbol{K} = (\boldsymbol{k}, m)$, the local dispersion relation or intrinsic frequency ω_{int} follows

$$(\omega_{int}(\boldsymbol{k}, m, \boldsymbol{x}, z, t))^2 = (\omega_{enc} - \boldsymbol{U} \cdot \boldsymbol{k})^2 = \frac{N^2(z)k^2 + f^2m^2}{k^2 + m^2}. \tag{1.4}$$

The intrinsic frequency follows the wave properties of IGWs propagating in a motionless background and is observed by moving along the mean current. The frequency of encounter ω_{enc} is noticed by a stationary observer and is shifted by the Doppler shift $\boldsymbol{k} \cdot \boldsymbol{U}$. Waves are represented as slowly evolving wave trains under the WKBJ approximation. It relies on the separation of spatio-temporal scales of wave and mean-flow motion and not on small Doppler shifts, wave amplitudes, or energies compared to the mean flow.

The ray equations from Eq. (1.4) are derived as follows:

$$\begin{pmatrix}\dot{\boldsymbol{x}}\\ \dot{z}\end{pmatrix} = \begin{pmatrix}\nabla_{\boldsymbol{k}}\omega_{enc}\\ \partial_m\omega_{enc}\end{pmatrix} \quad , \quad \begin{pmatrix}\dot{\boldsymbol{k}}\\ \dot{m}\end{pmatrix} = \begin{pmatrix}\nabla_{\boldsymbol{x}}\omega_{enc}\\ \partial_z\omega_{enc}\end{pmatrix} \tag{1.5}$$

$$\dot{\omega} = \partial_t\omega_{int} + \boldsymbol{U} \cdot \boldsymbol{\nabla}\omega_{int} - \dot{\boldsymbol{x}} \cdot (\boldsymbol{k} \cdot \boldsymbol{\nabla U}) - \dot{z}\boldsymbol{k} \cdot \partial_z\boldsymbol{U} \tag{1.6}$$

Note that all terms in relation to the vertical component of the mean flow are omitted as $W = 0$. The wave group velocities $\dot{\boldsymbol{x}}$ and $\dot{z}$ in Eq. (1.5) are orthogonal to the wavenumber vector with the additional velocity of the mean flow. Thus, waves with negative (positive) vertical wavenumber have an upward (downward) wave group propagation and a downward (upward) phase propagation. Energy propagation follows the wave group propagation and is hence upward for negative vertical wavenumbers and vice versa. The horizontal and vertical wave refraction ($\dot{\boldsymbol{k}}$ and $\dot{m}$ respectively) are expressed in Eq. (1.5). In the case of a horizontally varying mean flow, its horizontal shear contributes to the horizontal wave refraction. The vertical wave refraction is modulated by the vertical shear of the stratification and mean flow. Vertical wave refraction and the changes in stratification with depth have opposite signs. The depths at which the vertical wave refraction changes sign by the influence of the stratification are called turning points. At the thermocline, for example, stratification has a maximum, and thus vertical wave refraction is negative below the thermocline and positive above.

When IGWs encounter a rigid boundary – such as the ocean surface or bottom, idealized as a plane – they behave similarly to waves encountering a turning point. These boundaries act as reflection points, where the wave group is reflected without a change in frequency or horizontal wave vector $\boldsymbol{k}$. However, the vertical component of the wavenumber changes sign, causing the waves to propagate in the opposite vertical direction.

Turning points
In contrast to rigid boundaries, turning points arise from gradual changes in the ocean's background stratification. These are locations where IGWs are refracted due to variations in the buoyancy frequency $N(z)$, altering their direction of propagation. For simplicity, a scenario without mean flow is considered. For vertically varying stratification, the behavior of IGWs can be analyzed through the vertical wavenumber, given by

$$m(z) = \pm \left(\frac{N^2(z) - \omega_{int}^2}{\omega_{int}^2 - f^2} \right)^{1/2} k_h \tag{1.7}$$

As downward (upward) propagating waves approach a turning point, the vertical wavenumber respectively decreases (increases) due to wave refraction. At a specific depth z_{turn}, the wavenumber becomes zero, i.e., $m(z_{\text{turn}}) = 0$. This corresponds to the condition where the local stratification matches the wave's intrinsic frequency: $m(z_{turn}) \sim (N^2(z_{turn}) - \omega_{int}^2)^{1/2} \to 0$. At this point, the group velocity vanishes in all directions, and the WKBJ approximation fails since the assumption of slowly varying background ($\partial/\partial z \ll |m|$) is violated. Here, waves become very long in wavelength and energy-dense, making dissipation unlikely. Because IGWs are constrained to propagate within the range $f < \omega < N(z)$, further propagation beyond this point is inhibited, and reflection at z_{turn} becomes the only viable outcome.

Turning points have implications for IGW dynamics. They can lead to the trapping of wave energy in specific ocean layers, influencing vertical energy fluxes and eventually inducing mixing processes. For example, near-surface stratification maxima create shallow turning points for high-frequency IGWs. Similarly, deep pycnoclines can trap wave energy and generate waveguides.

Absorption in the critical layer
While turning points are associated with changes in stratification, critical layers arise from the presence of a vertically varying mean flow $\boldsymbol{U}(z)$. At certain depths, IGWs can interact with the mean flow in such a way that their vertical wavenumber becomes singular, indicating a breakdown of linear wave theory. For turning points, the numerator in Eq. (1.7) vanishes. However, when considering a mean flow, the vertical wavenumber is affected by the Doppler shift that enters the dispersion relation, see Eq. (1.4), such that the denominator in Eq. (1.7) may tend to zero, causing m^2 to diverge. This happens when the Doppler-shifted frequency equals the Coriolis frequency $\omega_{enc} - \boldsymbol{U} \cdot \boldsymbol{k} = f$. The depth where this condition is satisfied is called the critical layer, z_{crit}. At z_{crit}, the vertical wavenumber becomes infinite ($m \to \infty$), causing the vertical component of the group velocity to approach zero. Unlike turning points, the horizontal group velocity remains finite and matches the background flow $\boldsymbol{c}_{gh} = \boldsymbol{U}(z_{\text{crit}})$. Waves thus become trapped near the critical layer, propagating horizontally at the same speed as the mean flow. This trapping leads to wave breaking and energy transfer to the mean flow – a process known as critical layer absorption.

Critical layer absorption is a central mechanism in this thesis, as it has key implications for IGW energetics and mixing processes in the ocean. In Chapter 2, the novel Internal Wave Energy Model based on ray tracing theory is introduced to explore how critical layer absorption leads to significant IGW energy changes and mixing. Although wave breaking by vertical shear-induced refraction is not explicitly modeled, the increase in vertical wavenumber m serves as a proxy for enhanced shear and potential wave breaking. In ray tracing models,

where wavenumber space has strict boundaries, an unbounded increase in m may cause waves to leave the defined phase space, effectively representing an energy sink. This lost energy may be transferred to turbulence, leading to vertical mixing, or dissipated as heat.

1.2.2. The wave field as statistical ensemble - The Radiative Transfer Equation

Previous sections have examined IGWs as discrete wave trains characterized by ray-based properties. However, in the ocean, the IGW field is more accurately represented as a superposition of wave packets, each possessing a dominant amplitude, wavevector, and frequency. These properties evolve slowly in accordance with ray theory, as described by Eqs. (1.5, 1.6). As these packets propagate, they may interact with the background stratification or mean flow and, in more general settings, with other wave packets by nonlinear wave-wave interactions or external forcing mechanisms – such as fluctuations in surface wind stress (Alford, 2001) or current–topography interactions (Nikurashin and Ferrari, 2011).

To describe the energetics of the wave field, we introduce the wave energy density $E_{\boldsymbol{k}}(\boldsymbol{x}, t)$ and wave action density $A_{\boldsymbol{k}}(\boldsymbol{x}, t)$, related by the intrinsic frequency as $E_{\boldsymbol{k}}(\boldsymbol{x}, t) = \omega_{\boldsymbol{k}}(t) A_{\boldsymbol{k}}(\boldsymbol{x}, t)$. The wave energy of some wave field $E(\boldsymbol{x}, t)$ satisfies

$$E(\boldsymbol{x}, t) = \int d\boldsymbol{K} \mathcal{E}(\boldsymbol{K}, \boldsymbol{X}, t), \tag{1.8}$$

such that E represents the local wave energy at a fixed spatial location and time. The energy power spectrum $\mathcal{E}(\boldsymbol{K}, \boldsymbol{X}, t)$ is a density in six-dimensional physical and phase space and time. The evolution of the wave action spectrum $\mathcal{A}(\boldsymbol{K}, \boldsymbol{X}, t)$ is governed by the radiative transfer equation (RTE), which can be derived by following, for example, the recipe outlined in Muraschko et al. (2015). Starting from the linearized Boussinesq equations Eq. (1.3), the momentum and buoyancy equations are multiplied by the horizontal velocity, vertical velocity, and buoyancy fields, respectively, and the results are summed. Introducing the polarization relations (derived in Chapter 3 and eigenvector Eq. (3.9)), and subsequently dividing by the intrinsic frequency Eq. (1.4), yields the wave-action conservation law in the presence of a mean flow. In canonical phase space form, and assuming no sources or sinks $\mathcal{S} = 0$, the action conservation equation becomes the RTE:

$$\frac{\partial \mathcal{A}}{\partial t} + \nabla_{\boldsymbol{x}} \cdot (\dot{\boldsymbol{x}} \mathcal{A}) + \frac{\partial}{\partial z}(\dot{z} \mathcal{A}) + \nabla_{\boldsymbol{k}} \cdot (\dot{\boldsymbol{k}} \mathcal{A}) + \frac{\partial}{\partial m}(\dot{m} \mathcal{A}) = \mathcal{S} = 0. \tag{1.9}$$

The left-hand side of Eq. (1.9) accounts for the time tendency, advection in physical space, and propagation and refraction in wavenumber space. Although wave action is conserved under these dynamics, wave energy is not. Reformulating the RTE in terms of the energy spectrum yields an additional term due to the variation of intrinsic frequency:

$$\frac{\partial \mathcal{E}}{\partial t} + \nabla_{\boldsymbol{x}} \cdot (\dot{\boldsymbol{x}} \mathcal{E}) + \frac{\partial}{\partial z}(\dot{z} \mathcal{E}) + \nabla_{\boldsymbol{k}} \cdot (\dot{\boldsymbol{k}} \mathcal{E}) + \frac{\partial}{\partial m}(\dot{m} \mathcal{E}) = \omega \mathcal{S} - \frac{\mathcal{E}}{\omega} \dot{\omega}. \tag{1.10}$$

The term $\frac{\mathcal{E}}{\omega} \dot{\omega}$ represents the exchange of mechanical energy between the wave field and the mean flow. This energy transfer may occur in either direction, depending on the sign of $\dot{\omega}$. The sign convention adopted here is such that an energy gain appears as a reduction in the effective sink on the right-hand side. The rate of change of intrinsic frequency $\dot{\omega}$ is determined by the characteristics of the background fields $\boldsymbol{U}$ and N, as shown in Eq. (1.6).

The source term $\mathcal{S}$ encapsulates processes that may lead to changes in the action spectrum, like generation of waves by external processes and nonlinear interactions with, for example, other waves or dissipative terms that eliminate wave energy. In this thesis, no generation mechanisms are considered, but focus rather lies on the interactions of the already generated IGW spectrum with a prescribed mean flow and the interactions with the IGW spectrum itself.

In the framework of linear IGWs, the advection and refraction of the IGW field by the background flow and stratification is considered, which conserves wave action unless wave breaking is allowed. If wave breaking is present, the resulting spectral fluxes at the boundaries of wavenumber space – by, for example, critical layer absorption – would correspond to energy transfer to turbulence or conversion to internal energy. Nonlinear interactions like wave-vortical scattering or wave-wave scattering are neglected in this framework but are treated separately within the weak-interaction assumption in the scattering integral.

1.2.3. Nonlinear interactions within the internal gravity wave spectrum

Generally, IGW generation processes inject energy into the IGW field at large scales by tidal conversion and inertial pumping. However, mixing processes in the ocean require energy to be present at much smaller scales, associated with short-wavelength, overturning IGWs. This necessitates a cascade of energy from the large scales to the broader IGW continuum, eventually populating the high-wavenumber portion of the spectrum, and eventually to even smaller scales. The mechanism responsible for this scale transition is thought to involve nonlinear wave–wave interactions, which redistribute energy across the IGW spectrum.

Wave-wave interactions are the resulting product of two wave packets occupying the same volume interacting for a short finite time to build up a third component, thus also known as wave triad interactions. Wave-wave interactions are mathematically described by the kinetic equation or scattering integral (Hasselmann, 1966; Nazarenko, 2011), which predicts energy transfers between spectral components under the assumption of weak interaction, i.e., slowly evolving wave amplitudes. This framework has been applied with notable success to several wave systems and has been actively applied to IGWs in the ocean. Earlier efforts to evaluate the kinetic equation for IGWs span a broad range of approaches, from analytic derivations to numerical simulations (e.g., Olbers, 1974, 1976; McComas and Bretherton, 1977; Pomphrey et al., 1980; Lvov and Tabak, 2001; Polzin and Lvov, 2011; Lvov et al., 2012; Eden et al., 2019b,c, 2020; Bel and Tziperman, 2023; Dematteis et al., 2024; Labarre et al., 2024).

Olbers (1974, 1976) firstly evaluated the kinetic equation derived from the Lagrangian equations of the Boussinesq system to investigate the spectral transfers for variations of the GM spectrum. It was found that wave energy is systematically transferred from intermediate frequencies $f < \omega < 5f$ to near-inertial and high-frequency waves with smaller vertical wavelengths in a timescale of 10 days. McComas and Bretherton (1977); Pomphrey et al. (1980) repeated the calculations but within the hydrostatic approximation and found some sensitivity on the spectrum's slope, where a slope of -2 describes closest a steady-state spectrum for wave triad interactions besides for near-inertial frequencies at lowest vertical modes. Following, Lvov and Tabak (2001); Polzin and Lvov (2011); Lvov et al. (2012); Dematteis et al. (2024); Labarre et al. (2024) calculated the nonlinear energy transfers for the GM76 model also using the hydrostatic approximation (some without rotation) with a massive improvement in resolution but with similar results. More recently, Eden et al. (2019b) derived

the kinetic equation from the Euler form of the non-hydrostatic Boussinesq system with rotation and presented improvements in the numerical methods. These studies generally identify consistent qualitative features but often yield quantitatively conflicting results, raising questions about the robustness of the kinetic approach. In this thesis the derivations of the kinetic equation from the Lagrangian and Eulerian frameworks are unified and so provide consistent and robust results on energy transfers by wave-wave interactions.

Concerns have also been raised about the validity of the weak interaction assumption itself. Notably, Holloway (1978, 1980, 1982) and Müller et al. (1986) questioned whether wave amplitudes evolve slowly enough in realistic oceanic conditions to justify the use of the kinetic equation. Given the difficulty of verifying this assumption through observations, Holloway (1981) proposed the use of idealized numerical models. In this spirit, Hibiya et al. (1998) applied external forcing to a two-dimensional model initialized with a GM spectrum and found that energy transfers by wave-wave interactions are most effective in the frequency band $2 < \omega/f < 3$. However, the applicability of this study is limited by its two-dimensional formulation, as wave-wave interactions are inherently three-dimensional.

Despite these uncertainties, the kinetic equation remains a valuable tool for parameterization development. In particular, Eden et al. (2019c) applied it to validate the fine-scale parameterization (Olbers, 1976; Gregg, 1989), enabling improved estimates of wave dissipation rates from observational data – a capability that underpins the IDEMIX gravity wave closure scheme (Olbers and Eden, 2013). More recently, Eden et al. (2019a) found encouraging agreement between kinetic equation predictions and direct numerical simulations of three-dimensional IGW-wave interactions, at least over a restricted range of frequencies and wavenumbers. Both approaches revealed net energy loss in the frequency band $2 < \omega/f < 3$ and energy gain at near-inertial frequencies and higher vertical wavenumbers, consistent with a downscale energy cascade. Notably, discrepancies emerged at the highest wavenumbers, where model resolution degraded, and the weak nonlinearity assumption likely breaks down.

The structure of triad interactions in the IGW field has also been a focus of theoretical work, much of which focuses on resonant interactions and ignores non-resonant interactions (as all citations so far besides Olbers, 1976; Eden et al., 2019b). A wave triad interaction involves two interacting waves with wavenumbers and frequencies $(\boldsymbol{K}_1, \omega_1)$ and $(\boldsymbol{K}_2, \omega_2)$ that scatter off a third wave with wavenumber and frequency $(\boldsymbol{K}_0, \omega_0)$, such that $\boldsymbol{K}_0 = \boldsymbol{K}_1 \pm \boldsymbol{K}_2$. The strength of their interaction is controlled by the interaction coefficient and the size of the wave amplitudes of the interacting waves. However, the crucial point is the resonance condition. If the triad is non-resonant ($\omega_0 \neq \omega_1 \pm \omega_2$), the forcing is oscillatory, and thus the growth of the generated wave and its energy transfers. If the resonance condition is satisfied ($\omega_0 = \omega_1 \pm \omega_2$), the forcing of the generated wave is non-oscillatory, such that the generated wave may grow considerably, leading to an effective, possibly large energy transfer.

McComas and Bretherton (1977) developed a foundational inertial-range theory for IGWs, identifying three principal classes of nonlocal resonant triad interactions (ID, ES, and PSI). These interactions involve nonlocal triads that are scale-separated, where one component has a significantly different wavelength and frequency from the other two. Such nonlocal triads are critical in explaining energy transfers in GM-like spectra, where low-frequency, large-scale motions dominate the energy content, while vertical shear is concentrated at small scales (McComas and Müller, 1981). However, recently Wu and Pan (2023) or Dematteis et al. (2024) argue that the previously ignored local interactions play an important role in energy transfers.

ES describes the interaction between a high-frequency wave and a low-frequency component, resulting in a back-scattered high-frequency wave with approximately reversed vertical wavenumber. This mechanism resembles Bragg scattering and acts to reduce vertical asymmetries in the wave field. Consider a downward-propagating wave $\mathbf{k}_3$, such as those generated near the sea surface. Through interaction with a near-inertial wave $\mathbf{k}_2$, satisfying $m_2 \approx 2m_3$, energy is transferred to an upward-propagating wave $\mathbf{k}_1$ with $m_1 \approx -m_3$, until the upward and downward energy fluxes balance. Conversely, upward-propagating waves generated near the ocean bottom can similarly scatter into downward-directed waves. Thus, earlier assumptions by McComas and Bretherton (1977) stated that ES is energetically unimportant in vertically symmetric IGW spectra, however, Wu and Pan (2023) show that ES contributes to a forward cascade of energy in frequency.

ID is a process whereby high-frequency, high-wavenumber waves interact with a low-frequency, large-scale component to generate another high-frequency wave. The result is a diffusive-like transfer of wave action in spectral space, reminiscent of diffusion of particles in physical space. Specifically, wavevectors $\mathbf{k}$ and $\mathbf{k}_3$ at high frequencies and wavenumbers interact with a slow, energetic component $\mathbf{k}_2$. When the wave spectrum decreases sharply beyond $|\mathbf{k}_3|$, this triad interaction facilitates a diffusion of action into this region, enhancing the population of high-frequency, small-scale waves at the expense of the low-frequency component.

PSI describes the decay of a low-frequency, low-wavenumber wave into two waves with approximately half the frequency and higher vertical wavenumber. PSI is responsible for the transfer of energy into the near-inertial band at small vertical scales, a key feature in GM-like models. The interaction involves a parent wave $\mathbf{k}_2$ and two daughter waves $\mathbf{k}_1$ and $\mathbf{k}_3$, with nearly opposite wavenumbers and nearly identical frequencies.

Beyond shaping the overall spectrum, wave-wave interactions play a key role in the formation and decay of spectral distortions such as peaks or asymmetries, particularly those associated with coherent features like internal tides. As internal tides propagate through a turbulent IGW background, they are subject to nonlinear triad interactions that lead to damping and energy redistribution. For example, Onuki and Hibiya (2018) showed that this damping process enriches the ambient IGW field. More specifically, Olbers et al. (2020b) investigated the semidiurnal M_2 tidal energy dissipation through PSI interactions with a GM-like background and found that, in the tropical latitude band 28°S-28°N, PSI interactions dominate the energy transfer, converting baroclinic tidal energy into IGWs at half the tidal frequency. Outside this band, more general triad interactions contribute, albeit with lower efficiency. The globally integrated tidal energy transfer was estimated to be between 0.1 and 0.3 TW, aligning well with the 0.5 to 1 TW of energy estimated for the barotropic-to-baroclinic conversion (Falahat et al., 2014), and leaving room for additional dissipation mechanisms such as local wave breaking and tide-eddy interactions.

Understanding the spectrum of wave-wave interactions and their interplay with other energy exchange processes remains essential to quantifying the full IGW energy budget. This, in turn, is key to advancing parameterizations of mixing and energy dissipation in ocean general circulation models.

1.3. Thesis overview

> To borrow some words of Phillips (1968), the contrast is between the "strong, promiscuous interactions" in the critical layer and the "weak, selective interactions" of the triads.
> By Munk (1981) – Internal Waves and Small Scale Processes

The statement by Munk (1981) and Phillips (1968) sets up the spirit of this thesis, where critical layer interactions – equivalent to the wave-mean flow interactions explained within linear wave theory in Sec. (1.2.1) – are compared to the wave-wave interactions. These are the two major topics subject to the dissertation. This thesis comprises five parts: three publications with an overarching research question each, supplemental material, and a concluding chapter. Chapter 2 consists of a published research paper in the *Journal of Physical Oceanography*. Chapters 3 and 4 are two research papers submitted to the *Journal of Physical Oceanography*. Chapter 5 consists of supplemental material that belongs to Chapter 4. The thesis is concluded with Chapter 5, a summary of the key results and conclusions based on the research papers, together with an outlook with respect to open questions.

1. How do interactions between internal gravity waves and a mesoscale eddy shape the internal gravity wave spectrum?

Chapter 2: Evolution of internal gravity waves in a meso-scale eddy simulated using a novel model, see Sebastia Saez et al. (2024)

Chapter 2 examines the evolution of IGWs as they propagate through a coherent mesoscale eddy using the Internal Wave Energy Model (IWEM), a novel framework based on the six-dimensional radiative transfer equation. The interaction of IGWs with an idealized mean flow and stratification motivated by observations of an eddy in the Canary Current System is investigated. Central goals include resolving the full spectral energy balance to quantify wave-eddy interactions, assessing how the eddy's lateral and vertical shear refract wave energy, and determining the relative importance of vertical and horizontal refraction as pathways for wave dissipation. Because refraction-driven wave breaking contributes to density mixing (a key component of large-scale ocean circulation), the results have important implications for understanding the oceanic energy cycle and for improving IGW parameterizations in ocean models.

2. How do nonlinear interactions among internal gravity waves govern energy transfers within the oceanic internal gravity wave field?

Chapter 3: Wave-wave interactions of internal gravity waves. Part A: Comparison of Eulerian and Lagrangian frameworks, see Sebastia Saez et al. (2025a)

Chapter 3 addresses the fundamental role that wave-wave interactions play in energy transfers within the IGW field. Motivated by the lack of systematic comparison between theoretical frameworks to derive the kinetic equation for wave-wave interactions, the work undertakes the first systematic comparison of the Eulerian and Lagrangian kinetic

equations within a rotating, stratified, non-hydrostatic Boussinesq system. It examines how these formalisms differ, most notably in their representations of energy, which is strictly quadratic in Eulerian amplitudes but appears as an infinite series in amplitude powers the Lagrangian framework, and establishes how their interaction coefficients relate. The analysis reveals that the resulting kinetic equations are generally not equivalent across formalisms, although they are equal under resonant conditions. The potential significance of typically neglected non-resonant interactions is highlighted, which may meaningfully influence energy transfers through the imaginary part of the time response function, particularly under anisotropic conditions. By clarifying the connections and discrepancies between the Euler and Lagrange frameworks, the study provides a unified theoretical basis for understanding the spectral evolution and energetics of IGWs in the ocean.

3. How do interactions within the internal gravity wave field affect variations of the universal oceanic internal gravity wave spectrum?

Chapter 4: Wave-wave interactions of internal gravity waves. Part B: Spectral energy transfers in a typical internal gravity wave field, see Sebastia Saez et al. (2025b)

Chapter 4 is driven by the longstanding challenge of reliably quantifying energy transfers by wave-wave interactions within the IGW field. Although the kinetic equation under the weak-interaction assumption provides the primary theoretical framework for describing spectral energy transfers, past applications have produced results that agree qualitatively yet diverge quantitatively, prompting questions about the framework's robustness. To address these issues, new numerical methods are developed to tackle two key theoretical limitations: (i) The validity of the weak-interaction assumption for GM-like spectra is confirmed with consistently low Boltzmann rates. (ii) The scattering integral diverges for the canonical GM76 model unless the spectrum is modified with steeper slopes in vertical wavenumber or smoother transitions representing turbulence onset. The research also dissects the contributions of different resonant interaction mechanisms, showing that non-local interactions dominate energy transfers while local interactions are negligible. Two previously unrecognized non-local resonant interactions are identified: third parametric generation, the main driver of forward cascades, and horizontal diffusion, which produces strong transfers at high frequencies. These findings yield convergent results at unprecedented high resolution, greatly improving the efficiency and reliability of IGW energy transfer estimates.

2

Evolution of internal gravity waves in a meso-scale eddy simulated using a novel model

This chapter is a reprint of the publication Sebastia Saez et al. (2024):
Sebastia Saez, P., Eden, C., Chouksey, M., (2024): "Evolution of internal gravity waves in a meso-scale eddy simulated using a novel model", published in *Journal of Physical Oceanography*

Authors: Pablo Sebastia Saez[a] [1], Carsten Eden[a], and Manita Chouksey[a,b,c]
Affilitations: a: Institut für Meereskunde, Universität Hamburg, Germany, b: Institut für Umweltphysik, Universität Bremen and MARUM, Germany, c: Leibniz-Institut für Ostseeforschung Warnemünde, Germany

Abstract

We investigate the effect of wave-eddy interaction and dissipation of internal gravity waves propagating in a coherent meso-scale eddy simulated using a novel numerical model called the Internal Wave Energy Model based on the six-dimensional radiative transfer equation. We use an idealized mean flow structure and stratification, motivated by observations of a coherent eddy in the Canary Current System. In a spin-down simulation using the Garret-Munk model spectrum as initial conditions, we find that wave energy decreases at the eddy rim. Lateral shear leads to wave energy gain due to a developing horizontal anisotropy outside the eddy and at the rim, while vertical shear leads to wave energy loss which is enhanced at the eddy rim. Wave energy loss by wave dissipation due to vertical shear dominates over horizontal shear. Our results show similar behaviour of the internal gravity wave in a cyclonic as well as an anticyclonic eddy. Wave dissipation by vertical wave refraction occurs predominantly at the eddy rim near the surface, where related vertical diffusivities range from $O(10^{-7})$ to $O(10^{-5})$ $m^2 s^{-1}$.

[1]Corresponding author: Pablo Sebastia Saez - pablo.sebastia.saez@uni-hamburg.de

Statement

Using a novel model and observations from the Canary Current system of a coherent eddy of 100 km diameter, we explore the interaction between a realistic internal gravity wave field and this eddy. We study wave refraction and energy transfers between the waves and the eddy induced by the eddy's lateral and vertical shear. Waves lose energy at the eddy rim by vertical shear and gain outside the eddy rim by horizontal shear. We find large vertical wave refraction by vertical shear at the eddy rim, where waves break and mix density, which can have wide ranging effects on the ocean's circulation. These results are important for understanding the ocean's mixing and energy cycle and to develop eddy and wave parameterizations.

2.1. Introduction

Internal gravity waves (IGW) are ubiquitous in the ocean and their spectra are observed to be quite continuous in wavenumber and frequency space, as described by the Garrett-Munk model spectrum (Garrett and Munk, 1975, 1979). IGWs are generated by a variety of mechanisms, primarily by winds and tides (Wunsch and Ferrari, 2003), and also by meso-scale eddies (e.g. Nikurashin and Ferrari, 2011; Chouksey et al., 2018, 2022) in the ocean. Although IGWs evolve over fast time scales, their propagation and associated energy transfers can occur over large spatial scales, ranging from a few meters to hundreds of kilometers. Interactions between IGWs and meso-scale eddies, which evolve at much slower time scales, are important for the energy transfers in the ocean, however, these interactions make it challenging to separate, diagnose and quantify the associated oceanic processes. This study focuses on the evolution of IGWs propagating in a coherent meso-scale eddy using a novel Internal Wave Energy Model (IWEM) based on the six-dimensional radiative transfer equation which distinguishes a priori between some of the processes as described below.

During their propagation, IGWs are refracted by their changing environment and can interact with the mean flow, topography, small-scale turbulence, other waves such as Rossby waves, or with IGWs themselves. For instance, when IGWs propagate in a vertically sheared mean flow, energy can be transferred from the waves to the mean flow and vice versa. Similarly, due to horizontal shear waves can exchange energy with the mean flow. In a critical layer, IGWs get trapped with growing vertical wavenumber (but constant horizontal wavenumber) due to the vertical shear, which eventually leads to wave breaking and thus wave dissipation, sometimes called critical layer absorption. A similar process is wave capture (Bühler and McIntyre, 2005) where horizontal shear is involved and all three wavenumber components grow without bounds which may also lead to wave breaking and dissipation.

During breaking, the IGW energy is partly converted to small-scale turbulent energy (which is the dissipated wave energy) and is transferred to smaller scales, where it is converted into both internal energy by molecular dissipation and potential energy by turbulent density mixing. This transfer to potential energy by density mixing is known to be an important driver of the large-scale ocean circulation (e.g. Wunsch and Ferrari, 2003; Kunze and Smith, 2004). However, mixing by wave breaking is not only generated by wave dissipation by vertical and horizontal wave refraction due the mean flow. The energy transport towards waves with smaller vertical wavelengths, which are prone to breaking as a result of resonant triad wave-wave interactions within the IGW field itself, is also thought to be an important driver of wave breaking and mixing. The importance of vertical and horizontal wave refraction for

wave dissipation as compared to other processes, however, remains largely unknown, and is thus the focus of the present study.

Estimates of IGW energy dissipation and turbulent mixing from observational studies (e.g. Polzin, 2004, 2009) confirm that the complexity of the vertical and horizontal structure of IGW induced mixing is not captured by a constant vertical diffusivity, as typically used in ocean models. Addressing these issues, Müller and Briscoe (2000) and Natarov and Müller (2005) proposed a promising concept based on a prognostic spectral energy balance for IGWs, called the Internal Wave Action Model (IWAM) with six-dimensions, with three dimensions in the spatial physical space and three in the wavenumber space (in addition to the time dimension). However, no actual application was published from the IWAM model due to analytical, practical, and computational limitations owing to the need to parameterize wave generation, energy transfers, and dissipation. Consequently, Olbers and Eden (2013) drastically simplified this six-dimensional problem, and by integrating the spectral energy balance over the wavenumber space an energetically consistent parameterization for diapycnal diffusivity was given (Olbers et al., 2019).

For the spectral energy balance to hold, it is necessary to assume slowly varying mean flow and stratification compared to wave lengths and periods, i.e. the WKBJ approximation. Recently, Savva et al. (2021) derived a kinetic equation similar to the spectral energy transfer equation using the Wigner transform (Ryzhik et al., 1996) without assumptions of spatial scale separation. However, in contrast to Savva et al. (2021), we use in the present study the spectral energy balance as in Müller and Briscoe (2000) (and also Kafiabad et al. (2019)), for reasons discussed in the concluding section. We resolve the spectral energy balance in its full form with the novel numerical model called the Internal Wave Energy Model (IWEM), to understand the interaction between the geostrophically balanced mean flow in form of a coherent eddy, with IGWs in the ocean.

In Section 2.2, we revisit the propagation and refraction of IGWs in a mean flow with vertical and meridional shear in the Wentzel-Kramer-Brillouin (WKB) approximation. With the novel numerical code IWEM, we describe the evolution of a continuous wave field by the spectral energy balance of IGWs which includes transport, refraction, and wave-mean flow interactions within the limits of the WKB approximation. We use the turbulent kinetic equation to infer vertical mixing related to wave dissipation by vertical and horizontal wave refraction. In Section 2.3, numerical experiments with IWEM based on observations of a coherent meso-scale eddy in the Canary Current System are discussed to understand the role of the horizontal and vertical gradients of the mean flow. We close with a summary and discussion of the results.

2.2. Energetics of IGWs

The ocean can be described as a body of water with characteristic stratification N, where IGWs are superimposed on a mean current $\mathbf{U}$ with (usually) large temporal and spatial scales in contrast to the shorter periods and wavelengths of the waves. Considering a horizontally and vertically sheared horizontal mean flow $\mathbf{U}_h(\mathbf{x}_h, z)$, stratification frequency $N(z)$, and assuming that the temporal and spatial scales of $\mathbf{U}_h$ and N are large compared to the periods and wavelengths of the waves, the WKB approximation can be applied. Freely propagating waves with wave ansatz $\exp i(\mathbf{k}_h \cdot \mathbf{x}_h + k_z z - \omega_{enc} t)$ and wave vector $\mathbf{k} = (\mathbf{k}_h, k_z) = (k_x, k_y, k_z)$

obey the local dispersion relation for the intrinsic frequency $\omega = \omega_{enc} - \mathbf{k}_h \cdot \mathbf{U}_h$ of IGWs

$$(\omega_{enc} - \mathbf{U}_h \cdot \mathbf{k}_h)^2 = \omega(\mathbf{k}_h, k_z, \mathbf{x}_h, z, t)^2 = \frac{N^2 k_h^2 + f^2 k_z^2}{k_h^2 + k_z^2} \tag{2.1}$$

where ω_{enc} is the frequency of encounter (sometimes also called absolute frequency). The intrinsic frequency ω follows from the wave properties of IGWs propagating in a motionless background and is observed by moving along with the mean current. The frequency of encounter ω_{enc} is noticed by a stationary observer and is shifted by $\mathbf{k}_h \cdot \mathbf{U}_h$, the Doppler shift.

2.2.1. Spectral energy balance

The IGW field in the ocean is depicted here by a superposition of wave packets. The wave packets have a dominant amplitude, wave vector, and frequency, that change according to the familiar ray equations (see e.g. Olbers et al., 2012). Propagating wave packets can interact with the background stratification N or mean flow $\mathbf{U}_h$, they can be influenced by wave-wave interactions and other non-linear processes, and there can be forcing or dissipation mechanisms that create new wave packets or destroy the existing ones. For instance, IGWs can be excited by wind-driven vertical velocity fluctuations at the base of the surface mixed layer, or by horizontal (tidal) currents flowing over bottom topography. However, here we exclude forcing, explicit dissipation, and non-linear processes and focus on progpagation, refraction, and mean-flow interaction in spin-down simulations of a given wave field.

To describe the energetics of an ensemble of IGWs with energy density in space and time $E(\mathbf{x}_h, z, t)$ and corresponding wave action density $A = E/\omega$, we define its energy power spectral density $\mathcal{E}$, such that $E = \int \mathcal{E}\, \mathrm{d}\mathbf{k}_h\, \mathrm{d}k_z$, and the corresponding wave action density $\mathcal{A} = \mathcal{E}/\omega$. From wave action conservation of IGWs follows the spectral balance

$$\partial_t \mathcal{A} + \nabla_{\mathbf{x}_h} \cdot (\dot{\mathbf{x}}_h \mathcal{A}) + \partial_z(\dot{z}\mathcal{A}) + \nabla_{\mathbf{k}_h} \cdot (\dot{\mathbf{k}}_h \mathcal{A}) + \partial_{k_z}(\dot{k_z}\mathcal{A}) = \mathcal{S} \tag{2.2}$$

The left-hand side of Eq. (2.2) describes changes of $\mathcal{A}$ due to tendency, horizontal and vertical propagation by group velocity $(\dot{\mathbf{x}}_h, \dot{z}) = (\nabla_{\mathbf{k}_h}\omega_{enc}, \partial_{k_z}\omega_{enc})$, and refraction in horizontal and vertical wave vector components by $(\dot{\mathbf{k}}_h, \dot{k}_z) = -(\nabla_{\mathbf{x}_h}\omega_{enc}, \partial_z\omega_{enc})$. The term $\mathcal{S}$ on the right hand side describes processes violating wave action conservation, such as wave-wave interaction, forcing, or dissipation. Reformulating Eq. (2.2) for energy $\mathcal{E} = \omega\mathcal{A}$, an additional term arises on the right hand side

$$\partial_t \mathcal{E} + \nabla_{\mathbf{x}_h} \cdot (\dot{\mathbf{x}}_h \mathcal{E}) + \partial_z(\dot{z}\mathcal{E}) + \nabla_{\mathbf{k}_h} \cdot (\dot{\mathbf{k}}_h \mathcal{E}) + \partial_{k_z}(\dot{k}_z \mathcal{E}) = \omega\mathcal{S} + (\mathcal{E}/\omega)\, \dot{\omega}, \tag{2.3}$$

where the changes in frequency are defined as:

$$\dot{\omega} = -(\dot{\mathbf{x}}_h - \mathbf{U}_h) \cdot (\mathbf{k}_h \cdot \nabla_{\mathbf{x}_h}\mathbf{U}_h) - \dot{z}(\mathbf{k}_h \cdot \partial_z \mathbf{U}_h) \tag{2.4}$$

with $\dot{\mathbf{x}}_h - \mathbf{U}_h$ being the instrinsic group velocity. The term $(\mathcal{E}/\omega)\dot{\omega}$ in Eq. (2.3) is a source of mechanical energy gathered along the wave path by interaction of the wave field with the background flow. This energy can be transferred in both directions, i.e. from the mean flow to the wave field or the other way around. Note that wave-wave interaction and wave forcing as part of $\mathcal{S}$ are neglected in Eq. (2.3), while dissipation is implicitly present as discussed next.

2.2.2. Wave breaking and dissipation

As noted earlier, in this study we exclude any explicit wave dissipation. On the other hand, dissipation (and thus non-zero $\mathcal{S}$ in Eq. (2.3)) is still implicitly present in our model by a possible wave energy flux F_{crit} across the large vertical wavenumber threshold $k_z^c > 0$

$$F_v = \int \left\{ \begin{array}{ll} \left[\dot{k_z}\mathcal{E}\right]_{k_z=k_z^c} & \text{if } \dot{k_z} > 0 \\ 0 & \text{else} \end{array} \right\} \mathrm{d}\mathbf{k}_h - \int \left\{ \begin{array}{ll} \left[\dot{k_z}\mathcal{E}\right]_{k_z=-k_z^c} & \text{if } \dot{k_z} < 0 \\ 0 & \text{else} \end{array} \right\} \mathrm{d}\mathbf{k}_h \tag{2.5}$$

and the flux $F_h = F_h^x + F_h^y$ across the large horizontal wavenumber threshold $k_h^c > 0$

$$F_h^x = \int \left\{ \begin{array}{ll} \left[\dot{k_x}\mathcal{E}\right]_{k_x=k_h^c} & \text{if } \dot{k_x} > 0 \\ 0 & \text{else} \end{array} \right\} \mathrm{d}k_z \mathrm{d}k_y - \int \left\{ \begin{array}{ll} \left[\dot{k_x}\mathcal{E}\right]_{k_x=-k_h^c} & \text{if } \dot{k_x} < 0 \\ 0 & \text{else} \end{array} \right\} \mathrm{d}k_z \mathrm{d}k_y \tag{2.6}$$

and similar for F_h^y. We set $\pm k_z^c$ and $\pm k_h^c$ to the maximal values of the model domain in wavenumber space. The positive definite energy fluxes F_v and F_h across the wavenumber thresholds are taken to equal the energy transfer from the waves to small-scale turbulence and thus density mixing or further dissipation to internal energy. This happens, for example, for the case of wave breaking at critical layers, where waves are refracted with growing vertical wavenumber but constant horizontal wavenumber due to the vertical shear only. Note, however, that often there is both horizontal and vertical shear, such that it is difficult to relate the flux F_v only to the special case of critical layer absorption. Further, $N(z)$ can also drive a flux F_v even without any vertical shear. In the following, we refer to wave dissipation by vertical wave refraction for wave energy to cross the vertical wavenumber threshold k_z^c generating the flux F_v, see Eq. (2.5), and similar for F_h from Eq. (2.6). We will test below if the vertical wavenumbers (or related Richardson number) of the wave field at the thresholds are already large (or small) enough to warrant this approach.

To treat the fate of the energy transfer $F_v + F_h$ to small-scale turbulence, we consider the turbulent kinetic energy (TKE) equation. Under the assumption of stationarity and horizontal homogeneity and neglection of the transport terms, the TKE equation simplifies to a local balance of production terms and dissipation ϵ, i.e. the Osborn-Cox relation (see Osborn and Cox, 1972) given by

$$-\overline{\mathbf{u}_h' w'} \cdot \partial_z \overline{\mathbf{u}}_h + \overline{b' w'} - \epsilon = 0 \tag{2.7}$$

The primed terms in Eq. (2.7) stand for small-scale turbulent fluctuations, $\overline{\mathbf{u}}_h$ denotes wave velocity, and ϵ dissipation of TKE. The vertical turbulent buoyancy flux is given by $\overline{b' w'}$, with buoyancy $b = -g\rho/\rho_0$ and density ρ. The shear production term $\overline{\mathbf{u}_h' w'} \cdot \partial_z \overline{\mathbf{u}}_h$ represents the wave-mean flow energy exchange, i.e. the flux $F_v + F_h$. With the diffusive parameterization $\overline{b' w'} = \kappa N^2$, it follows that

$$\kappa = \frac{\gamma}{1+\gamma} \frac{F_v + F_h}{N^2} \tag{2.8}$$

where κ is the turbulent diffusivity and γ the relative mixing efficiency (see Osborn, 1980). The energy transfer by wave breaking $F_v + F_h$, assumed to be equal to the shear production term $\overline{\mathbf{u}_h' w'} \cdot \partial_z \overline{\mathbf{u}}_h$, can either be dissipated into heat or leads to an increase of potential energy by density mixing. The fraction of the energy dissipated into heat or converted into potential energy by density mixing is represented by the relative mixing efficiency γ. Based on fine

scale measurements by Osborn and Cox (1972) and, e.g., Garanaik and Venayagamoorthy (2019), the relative mixing efficiency is $\gamma \approx 0.2$ for stratified flows such as the ocean. Typical values of local turbulent diffusivity in the interior of the ocean are $\kappa \approx 10^{-5}$ m^{2}s^{-1}, inferred from typical observational estimates of dissipation in the range of $\epsilon \approx 10^{-10}$ to 10^{-9} m^{2}s^{-3}.

2.2.3. The Garrett-Munk model spectrum

The GM model spectrum (Garrett and Munk, 1975, 1979) is a representation of the energy density spectrum $\mathcal{E}$ of IGWs derived from observations, and is used here as the initial condition for our simulations described below. The GM model spectrum describes a horizontally isotropic and vertically symmetric spectrum with a spectral power law of -2 in frequency and vertical wavenumber. There are several different versions of the GM model spectrum, here we use the following form

$$\mathcal{E}(k_z, \omega, \phi, z) = \frac{E(z)}{2\pi} A'(k_z, \omega) B'(\omega) \ , \ \mathcal{E}(\mathbf{k}, z) = \mathcal{E}(k_z, \omega, \phi, z)\, J^{-1} \tag{2.9}$$

with wavenumber angle ϕ and

$$A'(k_z, \omega) = \frac{\tilde{A}(k_z/k_z^*(\omega))}{k_z^*(\omega)} \ , \ \tilde{A}'(\zeta) = \frac{n_a}{1+\zeta^2} \ , \ B'(\omega) = \frac{n_b f}{\omega\sqrt{\omega^2 - f^2}} \tag{2.10}$$

$$J = \frac{\partial(\mathbf{k})}{\partial(k_z, \omega, \phi)} \ , \ k_z^*(\omega) = \frac{\sqrt{N^2 - \omega^2}}{c^*} \ , \ c^* = \int_{-h}^{0} \frac{N(z)}{j^*\pi}\, dz \tag{2.11}$$

where J denotes the Jacobi determinant for the coordinate transformation $(k_z, \omega, \phi) \rightarrow (\mathbf{k})$, k_z^* the bandwidth of the vertical wavenumber spectrum equivalent to the vertical mode number $j^* = 10$ and $\zeta = k_z/k_z^*(\omega)$. The energy density spectrum $\mathcal{E}$ is factorized with the wavenumber shape function A' and the frequency shape function B'. Both shape functions integrate to one by choice of the parameter n_a and n_b. The energy density spectrum is then normalized to the total mechanical energy of the wave field in physical space, such that

$$E(z) = E_0 N(z)/N(z_0) = \int_f^N \int_{-\infty}^{\infty} \int_0^{2\pi} \mathcal{E}\, \mathrm{d}\omega \mathrm{d}k_z \mathrm{d}\phi \tag{2.12}$$

where E_0 denotes the total energy content E_0 at z_0, and the factor $N(z)/N(z_0)$, the so-called WKB-scaling. We use $E_0 = 3 \times 10^{-3}$ m^2/s^2 and $z_0 = 0$ m as classical parameter, but note that this is probably an underestimation of the typical wave energy (Pollmann et al., 2017). While the original GM spectrum uses analytical expressions for the parameters n_a and n_b, we choose them such that $E(z) = \int_{-\boldsymbol{k}_h^c}^{\boldsymbol{k}_h^c} \int_{-k_z^c}^{k_z^c} \mathcal{E}\, \mathrm{d}\mathbf{k}_h \mathrm{d}k_z$ at all depths.

2.2.4. Instability at wavenumber thresholds

For the assessment of the stability of the wave field, the shear generated by the total wave ensemble given by $\mathcal{E}$ can be analysed and a critical value for the vertical wavenumber threshold k_z^c calculated. Wave instabilities can be assessed by the bulk Richardson number $\mathrm{Ri}_{\mathrm{Bulk}} = N^2/(\partial_z \boldsymbol{u})^2$, where $\mathrm{Ri}_{\mathrm{Bulk}} < 1/4$ characterises an unstable situation and $\mathrm{Ri}_{\mathrm{Bulk}} > 1/4$ a stable one. Following Munk (1981), k_z^c can be inferred in terms of a critical Richardson

number sustained by the wave field, so that waves with $|k_z| > k_z^c$ are particularly prone to break,

$$\mathrm{Ri}_{\mathrm{Bulk}}^{-1} = \int_{-k_z^c}^{k_z^c} \mathrm{d}k_z \int_f^N \mathrm{d}\omega \, \mathrm{Ri}^{-1}(k_z, \omega) = \int_{-k_z^c}^{k_z^c} dk_z \int_f^N \mathrm{d}\omega \, \frac{\omega^2 + f^2}{\omega^2 N^2} k_z^2 \mathcal{E}(k_z, \omega) \tag{2.13}$$

where $\mathrm{Ri}(k_z, \omega)$ is the spectrum of the Richardson number, for which $\partial_z \boldsymbol{u}$ is expressed by the shear spectrum in the second step.

For k_z^c, different authors use corresponding wavelengths from $\lambda = 10$ m down to $\lambda = 1$ m. According to Gargett et al. (1981) and in agreement with Gregg (1987), the IGW spectral shape obtained from measurements in the Northwest Atlantic Ocean comprises primarily of IGWs with vertical wavelengths 10 m $\leq \lambda <$ 100 m, fine-structure and decaying internal waves between 1 m $\leq \lambda <$ 10 m, and small scale turbulence at centimeter scales. Gargett et al. (1981) find that the observed spectrum results in $\mathrm{Ri}_{\mathrm{Bulk}} = 1$ and suggests a cut-off vertical wavelength $\lambda_z^c = 10m$. Munk (1981) predicted $\mathrm{Ri}_{\mathrm{Bulk}}^{-1}(k_z^c) = 0.5$ with a roll-off at $k_z^c = 0.6$ m^{-1} (wavelength of about 10 m), showing more agreement with observations by Sherman and Pinkel (1991), where $\mathrm{Ri}_{\mathrm{Bulk}}^{-1} \approx 0.3$ (Sherman, 1989) for spectra close to the model spectrum by (Cairns and Williams, 1976). Moreover, Duda and Cox (1989) found $\mathrm{Ri}_{\mathrm{Bulk}}$ between one and three from observations in the upper ocean, where $\mathrm{Ri}_{\mathrm{Bulk}} = 1$ indicates high non-linearity of the IGW field and the upper bound of $\mathrm{Ri}_{\mathrm{Bulk}} = 3$ indicated saturated situations with maximum allowable shear.

Here, $k_z^c = 1\,\mathrm{m}^{-1}$ (or wavelength 6.28 m) is used and a zonal and meridional wavenumber threshold of $k_h^c = 0.5\,\mathrm{m}^{-1}$. This choice results in a $\mathrm{Ri}_{\mathrm{Bulk}}^{-1} = 0.9$ under consideration of a depth-invariant stratification of $N = 5 \times 10^{-3} s^{-1}$ and the GM model spectrum for $\mathcal{E}$ from above. For the case of a depth-dependent exponential stratification $N = N_1(z)$ given by Eq. (2.14), we find $\mathrm{Ri}_{\mathrm{Bulk}}^{-1} \approx 1.4$ at the surface, and $\mathrm{Ri}_{\mathrm{Bulk}}^{-1} \approx 0.2$ in the deep ocean. These predictions of IGW instability are in partial agreement with Gargett et al. (1981). However, $\mathrm{Ri}_{\mathrm{Bulk}}^{-1}$ depends on the total wave energy, i.e. on the parameter E_0 of the GM model spectrum. With larger E_0, $\mathrm{Ri}_{\mathrm{Bulk}}^{-1}$ will increase and k_z^c will decrease. Note that three times larger values than used here for E_0 are found by Pollmann et al. (2017) from ARGO float observations, i.e., the value for E_0 used here is most likely a low bias.

2.3. Numerical simulations

The numerical simulations in this study are performed with the IWEM, which integrates Eq. (2.3) in time. A detailed description of the model is provided in Appendix A. All numerical experiments are spin-down simulations initialized with the IGW field given by the GM model spectrum from Section 2.2.3, embedded in a stationary horizontally and vertically varying mean flow and a stationary, vertically varying, but horizontally constant stratification. The integration time is 6 days, for which we assume the mean flow and stratification to be stationary. There is no wave forcing, and dissipation only by the energy transports across the vertical and horizontal wavenumber thresholds as described in Section 2.2.2. The initial wave field is horizontally homogeneous, isotropic in $\mathbf{k}_h$ and symmetric in k_z, but the total wave energy is vertically increasing towards the surface since the GM-spectrum is proportional to the local stratification N (see Section 2.2.3).

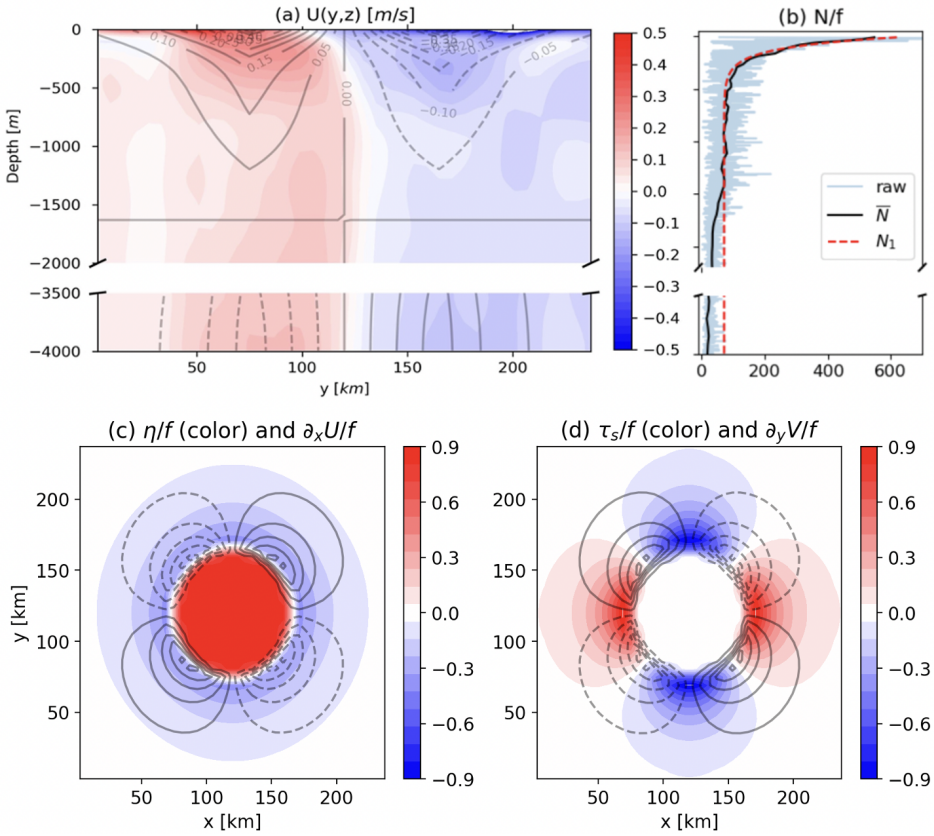

Figure 2.1: (a) Zonal velocity in the coherent eddy in colors calculated from the observed zonal velocity as detailed in Appendix B. Grey contours show the zonal velocity of the idealized eddy as detailed in Appendix B. (b) Observations of N (light-blue) at (14.5°N, 24.9°W), smoothed profile $\overline{N}$ (black) and the respective idealized exponential fit N_1 (red) given by Eq. (2.14) scaled with the Coriolis frequency f. (c) shows the scaled vorticity $\eta = \partial_x V - \partial_y U$ in color and zonal shear as contour lines, and (d) shows the shear strain $\tau_s = \partial_x V + \partial_y U$ in color and the meridional shear as contour lines of the idealized eddy close to the surface.

The domain for the simulation has a horizontal extent of 240 km × 240 km and its vertical extent is $L_z = 4$ km deep. In physical space, we use $40 \times 40 \times 60$ grid points in the zonal, meridional, and vertical directions respectively. The resolution in the horizontal direction is $\Delta x = \Delta y = 6$ km. The vertical resolution decreases exponentially from the surface layer with $\Delta z = 15$ m to the bottom layer with $\Delta z = 74$ m. In wavenumber space we use $60 \times 60 \times 60$ grid points, with horizontal wavenumber $\Delta k_{x,y} = 4 \times 10^{-3}$ m^{-1} at $k_{x,y} = 0$ m^{-1} increasing to $\Delta k_{x,y} = 18 \times 10^{-3}$ m^{-1} at $\pm k^c_{x,y}$, and vertical wavenumber $\Delta k_z = 8 \times 10^{-3}$ m^{-1} at $k_z = 0$ m^{-1} increasing to $\Delta k_z = 36 \times 10^{-3}$ m^{-1} at $\pm k^c_z$. The model time step is $2s$. The total number of grid points is about 20×10^9, which corresponds roughly to a global ocean model with horizontal resolution of $1-2$ km. Using even finer grids, the model quickly becomes computationally very expensive such that the simulations presented here are already at the upper end of available resources to us.

The background flow in our model simulations is inspired by measurements of a coherent meso-scale eddy in the tropical northeastern Atlantic Ocean provided by the REEBUS[2] project

[2]REEBUS: Role of eddies in the carbon pump of the eastern boundary upwelling systems (2019) - Process

and shown in Fig. 2.1 (see also Appendix B), which we think is representative for a typical coherent eddy at midlatitudes. The eddy measurements were made in the Eastern Boundary Upwelling System at the Mauritanian coast west of Africa in the Canary Current System in December 2019, between 14°- 15°N and 24°- 26°W, and was named CE_2019_14N_25W by REEBUS. The observed coherent eddy is of cyclonic type with positive zonal velocity south of the eddy center and negative north of it (Fig. 2.1). At the eddy rim, at a distance of around 45 km from the eddy center on either side, the velocities are the largest and reach 0.4 ms^{-1} and -0.6 ms^{-1} at the surface. Between the eddy rim, the horizontal change of the velocity is approximately linear. Outside the eddy, velocity decays exponentially in the horizontal. As suggested by Browning et al. (2021) this motivates the idealized eddy structure as detailed in Appendix C, which is also shown in Fig. 2.1 (grey contour lines). Since the velocity observations reach only to 1000 m depth, we use the first baroclinic vertical mode to extrapolate the observations down to the bottom at 4000 m. We also have a further simulation with an anticyclonic background flow which is simply a mirror of the cyclonic one. However, if not otherwise noted we always refer to the cyclonic eddy in our discussion of the results.

The background stratification is computed from in-situ measurements at the eddy center. A mean background stratification $\overline{N}$ is computed by smoothing the observations with a moving mean of 150 m with a minimum of ten data points, shown in Fig. 2.1. $\overline{N}$ is then fitted with an exponential function $N_1(z)$ given by

$$N_1(z) \;=\; 2.5\times10^{-3}\ \mathrm{s}^{-1} + 12.5\times10^{-3}\ \mathrm{s}^{-1}\ \exp\frac{z+50\ \mathrm{m}}{100\ \mathrm{m}} \tag{2.14}$$

Before we proceed to a discussion of the results of the model simulations, we check the validity of the WKB approximation, inherent to the model approach here. For the approximation to hold, it is necessary that the background flow $\boldsymbol{U}(\boldsymbol{x}, z)$ and stratification $N(z)$ are only slowly changing compared to vertical and horizontal wave length, i.e. $|\partial_z N|/|k_z N| \ll 1$, $|\partial_z \boldsymbol{U}_h|/|k_z \boldsymbol{U}_h| \ll 1$, and $|\partial_{\boldsymbol{x}} \boldsymbol{U}_h|/|\boldsymbol{k}_h \boldsymbol{U}_h| \ll 1$. Fig. 2.2 shows the maximal corresponding ratios. For both $\partial_z N$ and $\partial_z \boldsymbol{U}$ the ratios are indeed very low, except for very small k_z and the zero crossing of $\boldsymbol{U}$ at middepth. The ratios for lateral shear stay well below one everywhere. We do not regard the large ratios at the smallest k_z as a problem, since here turning points are expected which do not show any singular behaviour for the wave energy, and which are also limited by the finite depth. Therefore, the WKB approximation appears to be valid for our model configuration.

2.3.1. Waves in a coherent eddy

We first discuss a simulation with stratification $N_1(z)$ and the idealized cyclonic coherent eddy. The speed of the cyclone is shown in a horizontal plane close to the surface in Fig. 2.3 (a) and a meridional cross-section of zonal velocities of the eddy center in Fig. 2.3 (d). We choose to show in Fig. 2.3 the WKB-scaled wave energy $\mathcal{E}$, i.e. $N_0\mathcal{E}/N(z)$, so that the depth-dependency of $\mathcal{E}$ vanishes at time $t = t_0$. We also use the so-called stretched vertical coordinates $z^*(z)$ instead of z with $\mathrm{d}z^* = N(z)/N_0\,\mathrm{d}z$, where $N_0 = \int_{-h}^{0}(N(z)/h)dz$ and $h = 4000$ m, to better show the dominant processes close to the surface.

After 6 days of simulation, we see already a notable change in wave energy in Fig. 2.3 (b,e). Wave energy has remained relatively stable at the eddy center over the whole water

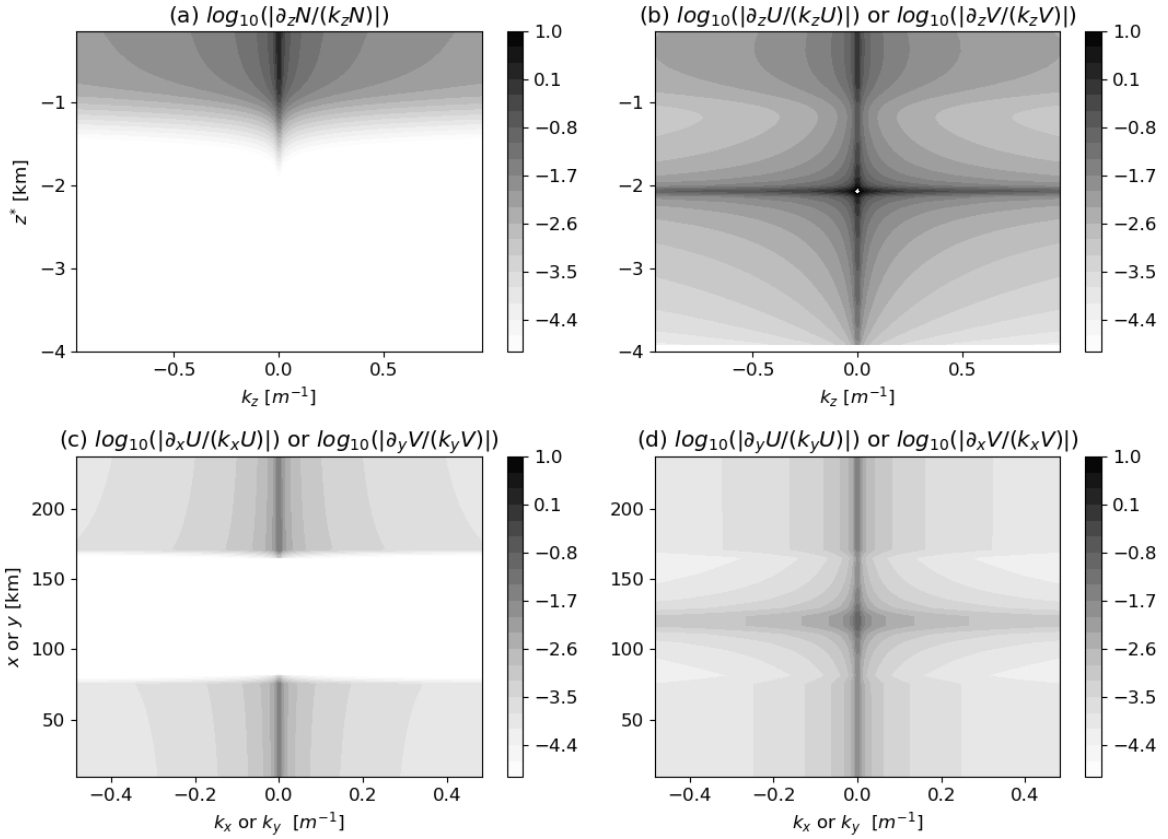

Figure 2.2: The parameters $\epsilon = |\partial_z N|/|k_z N|$, $|\partial_z U|/|k_z U|$, $|\partial_z V|/|k_z V|$, $|\partial_x U|/|k_x U|$, etc., which need to be small for the WKB approximation to hold. Values for the vertical shear in (a) and (b) are taken at the position of their maximal values in x and y, and the same holds for (c) and (d) for lateral shear in z. In (b) and (c), the maximum of the two alternatives are shown.

column, while wave energy decreases the most at the eddy rims close to the surface (Fig. 2.3 b,e). Wave energy changes over time (Fig. 2.3 c,f) show an overall decrease in wave energy towards the surface, with maxima at the vicinity of the eddy rim and a minimum at the eddy center. The waves at the eddy center have gained a small amount of energy while IGWs at the eddy rim have lost energy throughout the water column. It will be shown below that a similar inhomogeneous distribution of wave energy within the coherent eddy can also be seen in the available observations. This energy change is the main result of this paper which we aim to understand in the following.

In a simulation with an anticyclonic eddy using the same stratification $N_1(z)$ but simply the negative of the eddy velocities of the cyclone, the energy changes are almost identical. In both spin-down simulations, there is a total wave energy loss of 14.7% relative to the initial energy integrated over the whole domain. At the eddy rim there is a relative energy loss of 28.8% integrated over the water column, while the eddy center gains 2.8%. Note, that the asymmetries in Fig. 2.3 are due to the finite size effect of simulating the propagation of IGWs in a radial symmetric eddy in Cartesian coordinates. The results are symmetric in the eddy core, but the discontinuity in the eddy velocities at the circular eddy rim lead to slight asymmetries from the eddy rim outwards.

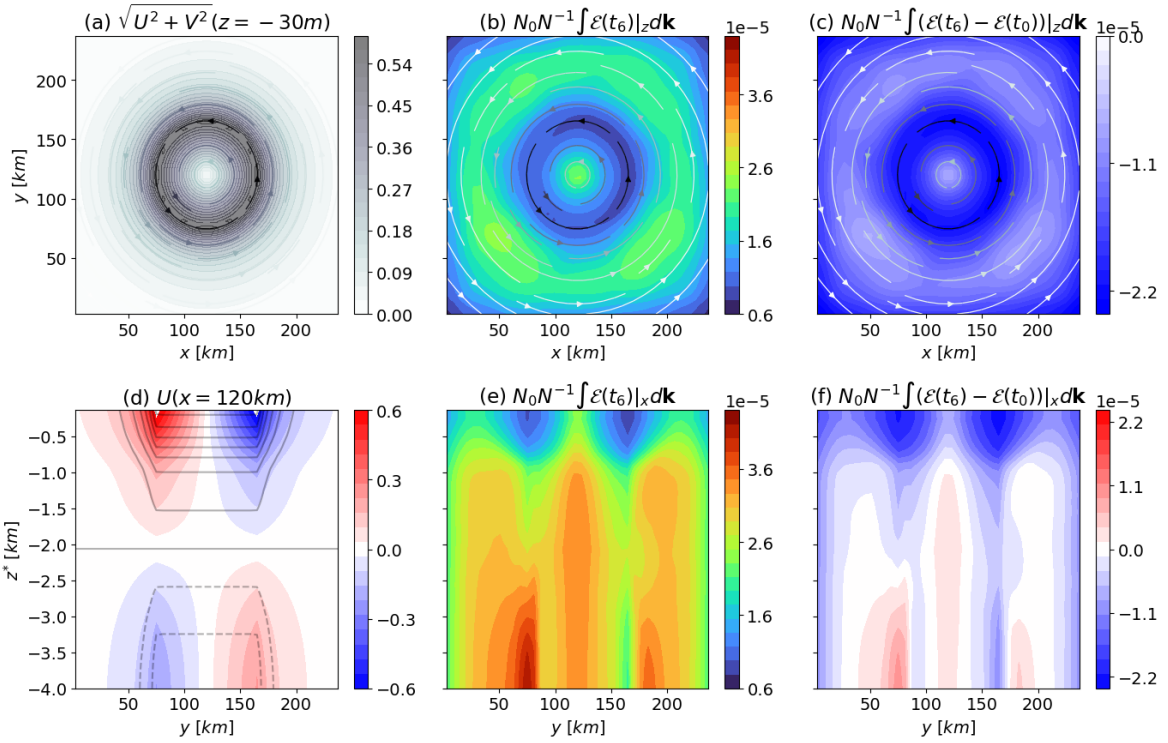

Figure 2.3: (a) Surface speed of cyclonic eddy in (ms^{-1}). (b) Wave energy density $\int \mathcal{E}(t_6)d\mathbf{k}$ in m^2s^{-2} at $z = -30$ m ($z^* = -266$ m) and $t_6 = 6$ days. (c) Wave energy change over 6 days in (m^2s^{-2}). The speed of the backgroud flow is shown in contour lines in panels (a)-(c) with the same colorscale as in (a). (d) Meridional cross-section of zonal background velocity U in (ms^{-1}) through the eddy center at $x = 120$ km with meridional velocities in grey contours. (e) Wave energy density and wave energy change (f) over 6 days. Wave energy is WKB-scaled by the factor $N_0N(z)^{-1}$. In (d)-(f) we use stretched vertical coordinate z^* with $dz^* = N/N_0\,dz$, where $N_0 = \int_{-h}^{0}(N/h)dz$ with $h = 4000$ m.

2.3.2. Wave-mean flow interaction

We first consider the wave energy change due to wave-mean flow interaction. The wave-mean flow interaction is given by the term $\mathcal{E}\dot{\omega}\omega^{-1}$ in Eq. (2.3) and depends thus directly on the changes in frequency, see Eq. (3.2). We split the discussion into effect of lateral and vertical shear, i.e.,

$$\mathcal{E}\dot{\omega}\omega^{-1} = \mathcal{E}\dot{\omega}_h\omega^{-1} + \mathcal{E}\dot{\omega}_z\omega^{-1} \tag{2.15}$$

with $\dot{\omega}_h = -(\dot{\mathbf{x}}_h - \mathbf{U}_h)\cdot(\mathbf{k}_h\cdot\nabla_{\mathbf{x}_h}\mathbf{U})$ and $\dot{\omega}_z = -\dot{z}(\mathbf{k}_h\cdot\partial_z\mathbf{U})$. All terms are shown in Fig. 2.4.

Consider the effect of lateral shear first. The horizontal intrinsic group velocity can be written as $\dot{\mathbf{x}}_h - \mathbf{U}_h = v(k,|k_z|)(\cos\phi,\sin\phi)$, with $\mathbf{k}_h = k(\cos\phi,\sin\phi)$ and appropriate function v. Then $\dot{\omega}_h$ becomes

$$\dot{\omega}_h = -vk\left(\cos^2\phi\partial_x U + \cos\phi\sin\phi(\partial_y U + \partial_x V) + \sin^2\phi\partial_y V\right) \tag{2.16}$$

Since τ_s=$\partial_y U + \partial_x V = 0$, and $\partial_x U = \partial_y V = 0$ within the idealized eddy (Fig. 2.1 c,d), it holds that $\dot{\omega}_h = 0$ there, and the wave-mean flow interaction by $\mathcal{E}\dot{\omega}_h\omega^{-1}$ vanishes from the eddy rim towards the center, as seen in Fig. 2.4 (a) and (d). Outside the eddy rim, the waves gain

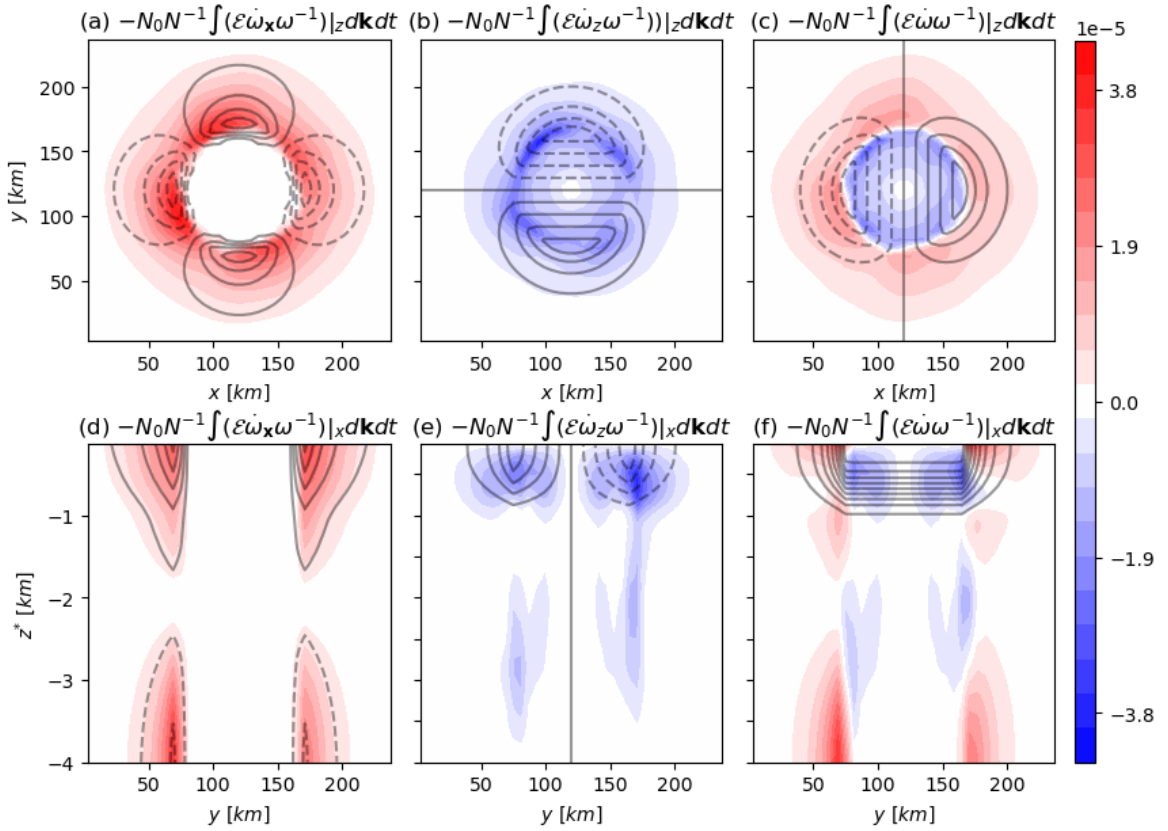

Figure 2.4: Wave energy change by (a) horizontal, (b) vertical and (c) total wave-mean flow interaction (m^2s^{-2}) after 6 days of simulation at $z = -30$ m ($z^* = -266$ m). The grey contours show $\partial_y U + \partial_x V$ in (a), $\partial_z U$ in (b), and $\partial_z V$ in (c). (d)-(f) The same respective components of wave-mean flow interaction and mean flow's shear along the meridional cross-section at $x = 120$ km. Positive values in the figure denote a total energy gain.

energy due to $\mathcal{E}\dot{\omega}_h\omega^{-1}$, which amounts to 6.7% of the initial wave energy when integrated over the whole model domain, with a maximum close to the eddy rim near the surface of 48.8% relative to the initial water column's energy.

Outside the eddy rim, the waves gain energy due to $\mathcal{E}\dot{\omega}_h\omega^{-1}$ because of a developing anisotropic spectrum, which can be understood as follows: For an initially isotropic spectrum $\mathcal{E}/\omega = \mathcal{A}(\phi, k, |k_z|)$ with $\partial_\phi \mathcal{A} = 0$, we have

$$\int \mathcal{A}\dot{\omega}_h dk d\phi dk_z = -\pi \left(\partial_x U + \partial_y V\right) \int \mathcal{A} v k dk dk_z = 0 \tag{2.17}$$

since $\partial_x U + \partial_y V = 0$ for the idealized eddy, $\int_0^{2\pi} \cos^2\phi d\phi = \int_0^{2\pi} \sin^2\phi d\phi = \pi$, and $\int_0^{2\pi} \cos\phi \sin\phi d\phi = 0$. For an isotropic spectrum without ϕ dependency, as specified in the initial conditions, the wave-mean flow interaction by lateral shear is thus vanishing everywhere in the idealized eddy. Only with anisotropy in $\mathcal{E}$, non-vanishing wave-mean flow interaction by lateral shear develops outside the eddy rim, as seen in Fig. 2.4 (a,d).

The horizontal anisotropy in $\mathcal{E}$ at the eddy rim is generated in the first place by the effect of vertical refraction, energy transfer to mean flow by vertical shear, and energy dissipation

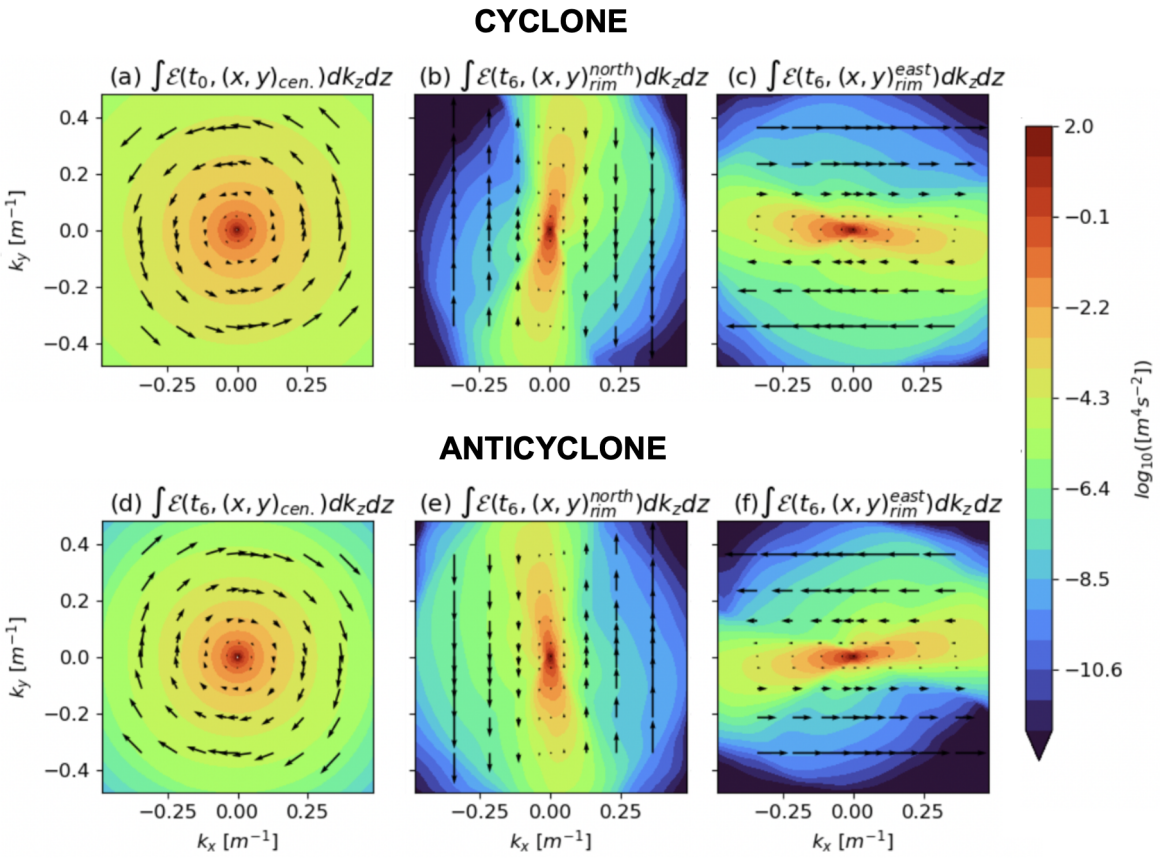

Figure 2.5: Wave energy density integrated over vertical wavenumber k_z and over depth z for the cyclone (top) and anticyclone (bottom): (a) at the eddy center at t_0, and after 6 days of simulation (d) at the eddy center , (b,e) at the northern eddy rim, (c,f) and at the eastern eddy rim . The vector field shows the respective $\dot{\mathbf{k}}_h = (k_y, -k_x)\partial_y U$ in (a, d), $(0, -k_x)\partial_y U$ in (b,e), and $(-k_y, 0)\partial_x V$ in (c,f).

by vertical shear, which is largest at the eddy rim, and discussed in detail below. Using single column simulations (excluding dimensions x and y but not k_x and k_y, not shown) with $\boldsymbol{U}(z)$ from the eddy rim and the same $N(z)$ as before, i.e. excluding all horizontal processes, we see a similar horizontal anisotropy developing in $\mathcal{E}$. The effect of vertical refraction, energy transfer to mean flow by vertical shear, and energy dissipation by vertical shear deforms the initially isotropic isolines (circles) of $\mathcal{E}$ (or $\mathcal{A}$) in the $k_x - k_y$ plane towards ellipses with a major axis roughly oriented towards the eddy center with maximal energies inside the ellipse. This is shown in Fig. 2.5 for the northern and eastern position at the rim.

At the eddy center, however, vertical shear and thus the effects of vertical refraction, energy transfer to mean flow, and energy dissipation are vanishing, and no anisotropy is generated by them. Also the horizontal refraction $\dot{\mathbf{k}}_h$ does not generate any anisotropy in $\mathcal{E}$ at the center, since here $\partial_x U = \partial_y V = 0$ and $\partial_y U = -\partial_x V$ (Fig. 2.1 c,d), and so

$$\dot{\mathbf{k}}_h = -\nabla_{\mathbf{x}_h}\omega_{enc} = -\nabla_{\mathbf{x}_h}(\mathbf{k}_h \cdot \mathbf{U}_h) = (k_y, -k_x)\partial_y U \sim \mathbf{z} \times \mathbf{k}_h \tag{2.18}$$

such that transports by $\dot{\mathbf{k}}_h$ are perpendicular to $\mathbf{k}_h$ with no effect on the isotropic isolines (circles) of $\mathcal{E}$ (see also Fig. 2.5 a). Since the horizontal intrinsic group velocity $\dot{\boldsymbol{x}}_h - \boldsymbol{U}$ does not

depend on wave angle ϕ and thus also does not generate any anisotropy from an initially isotropic spectrum, and since for the Doppler shift $\boldsymbol{U}$ in the group velocity the same holds, $\mathcal{E}$ stays perfectly isotropic (Fig. 2.5 d). Only an isotropic loss of energy due to horizontal wave propagation $\dot{\boldsymbol{x}}_h\mathcal{E}$ is visible at higher wavenumbers in Fig. 2.5 (d). This isotropic loss adds to the other effects also at the rim.

An exactly north-south oriented ellipse at the eddy rim is still not effective in generating mean-flow interaction by $\dot{\omega}_h$ since it generates an anomaly $\mathcal{A}' \sim -\cos 2\phi$ with

$$\int \mathcal{A}'\dot{\omega}_h d\phi \sim -\int vk(-\cos 2\phi)\cos\phi\sin\phi(\partial_y U + \partial_x V)d\phi = 0 \tag{2.19}$$

The same is true for a general orientation of the ellipse towards the eddy center. However, an anomaly with $\sim \sin 2\phi$ becomes effective at the northern position at the rim. In fact, if the ellipse is slightly tilted from north-south direction as seen in Fig. 2.5 (b), it has a component $\sim \sin 2\phi$. With $\partial_x V > 0$ but $\partial_x V \ll \partial_y U$ the transports have indeed a tilt in positive ϕ direction and an additional anomaly $\mathcal{A} \sim -\sin 2\phi$ develops with

$$\int \mathcal{A}'\dot{\omega}_h d\phi \sim \int vk\sin 2\phi\cos\phi\sin\phi(\partial_y U + \partial_x V)d\phi = vk(\partial_y U + \partial_x V)\pi/2 > 0 \tag{2.20}$$

which generates gain of wave energy related to $\dot{\omega}_h$, as seen in Fig. 2.5 (b). The same is true for a general orientation of the ellipse towards the eddy center, see e.g. Fig. 2.5 (c). The slight tilt in positive ϕ direction of the orientation of the anisotropic ellipses in $\mathcal{E}$ thus explains the energy gain outside the eddy rim by the effect of lateral shear.

The small tilt is generated by horizontal refraction $\dot{\mathbf{k}}_h$. North or south of the eddy rim is $\partial_x U = \partial_y V = 0$ and $\partial_y U \gg \partial_x V > 0$ (Fig. 2.1 c,d). The wave refraction is here roughly given by

$$\dot{\mathbf{k}}_h = -\nabla_{\mathbf{x}_h}\omega_{enc} = -\mathbf{k}_h \cdot \nabla_{\mathbf{x}_h}\mathbf{U}_h = -(k_y\partial_x V, k_x\partial_y U) \approx -(0, k_x)\partial_y U \tag{2.21}$$

which is also indicated in Fig. 2.5 b). This flow in the k_x-k_y-plane tilts the ellipse slightly to generate the wave energy gain.

In case of the anticyclone, (Fig. 2.5 e and f), lateral wave-mean flow interaction can be explained analogously, keeping in mind that the horizontal velocities rotate in opposite direction. The development of anisotropy as well the orientation of the ellipses towards the eddy center is identical to the cyclone, now however with $\dot{\mathbf{k}}_h$ pointing in opposite direction, which thus generates the slight tilt opposite to the one of the cyclonic case.

Fig. 2.4 (b,e) shows that the effect of the vertical shear in $\mathcal{E}\dot{\omega}/\omega$ is negative, i.e. the waves lose energy. This is because of the following reason: The sign of the vertical group velocity $\dot{z}$ in $\dot{\omega}_z = -\dot{z}(\mathbf{k}_h \cdot \partial_z \mathbf{U}_h)$ depends on the sign of k_z. Since that sign changes when the wave is reflected at the top or bottom boundary while all other wave properties are conserved, the effect due to $\dot{\omega}_z$ is completely reversed after reflection, without any net effect after a full cycle of reflection at surface and bottom. Only dissipation during the wave propagation can break this cycle, and in our model this dissipation is the energy flux F_v across the vertical wavenumber boundaries. When the waves propagate toward a critical layer, they always lose energy to the mean flow, thus we see only wave energy loss by the wave-mean flow interaction related to $\dot{\omega}_z$. To understand this, consider a wave ray propagating in a vertically sheared mean flow and assume also constant N for simplicity. The wave ray has wave action $A = E/\omega$ starting at time t_0 with initially zero mean flow and approaches a critical layer

at time t. Because of wave action conservation $\dot{A} = 0$, and $\omega(t) = |f| = \omega(t_0) - |U_h k_h| \rightarrow E(t)/|f| = E(t_0)/\omega(t_0)$. Since $|f|/\omega(t_0) = |f|/(|f| + |k_h U_h|) < 1$, wave energy is lost to the mean flow during the approach of the ray into the critical layer. In the critical layer, the wave breaks and the remainder of the energy is transferred to small-scale turbulence (or generates secondary waves). In our model, the remainder of the energy propagates beyond the positive or negative vertical wavenumber boundary which we diagnose as energy flux F_v, and which is available for mixing. Note that only near-inertial waves transport a significant fraction of energy into the critical layer and to turbulence.

We do not have the rather special case of a pure critical layer due to the additional horizontal shear. We, however, observe a "critical layer like" wave dissipation by vertical wave refraction, such that the above explanation transfers to our case. To justify that, Fig. 2.6 shows the outward flux $\dot{k_z}\mathcal{E}$ at the k_z^c-threshold at the eddy rim where critical layer absorption is strongest (see below). The outward dissipative flux $\dot{k_z}\mathcal{E}$ is largest at $k \rightarrow 0$ m^{-1}, i.e. most energy leaves at $\omega \rightarrow f$, indicative of a critical layer. In Fig. 2.6 (b) we show the vertical group velocity $\dot{z}$ (color), which is highest for $k_z \rightarrow 0$ m^{-1} and tends to zero for large k_z. The figure also shows that the intrinsic horizontal group velocity $\partial_k \omega(k, k_z)$ (or $\dot{\mathbf{x}}_h - \mathbf{U}_h$) also tends to zero for large k_z (contours). We can interpret all these features as critical-layer-like wave dissipation behaviour.

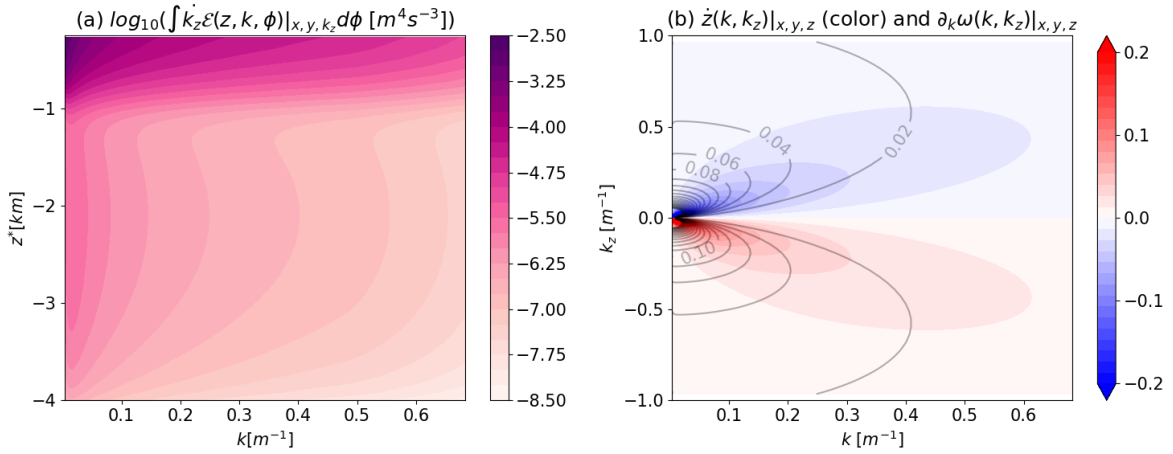

Figure 2.6: (a) Flux $\dot{k_z}\mathcal{E}$ at $k_z = +k_z^c$ and for $k_x > 0$ m^{-1} integrated over waveangle ϕ and evaluated at the northern eddy rim. (b) Vertical group velocity $\dot{z}$ (ms^{-1}; color) and intrinsic horizontal group velocity $\partial_k \omega(k, k_z)$ (ms^{-1}; contours), both for $k_x > 0$ m^{-1} and evaluated at the surface at the northern eddy rim.

Toward the eddy rims, the vertical shear in the mean flow increases, thus $\dot{\omega}_z$ strengthens, with the result that the waves lose more energy to the mean flow there. Towards the eddy center $\partial_z \mathbf{U}_h \rightarrow 0$ and the vertical wave-mean flow interaction vanishes. The magnitude of the vertical wave-mean flow interaction is increasing towards the surface because of the stronger vertical shear of the mean flow. The total relative energy loss by vertical wave-mean flow interaction over the whole domain amounts to 5% of the initial wave energy, with 27.3% relative to the initial energy at the northern position at the rim.

For the case of the anticyclone, the vertical wave-mean flow interaction is again analogous to the case of the cyclone, keeping in mind, that now the vertical shear in velocities has the opposite sign to the one for the cyclone. Nevertheless, the magnitude of the vertical

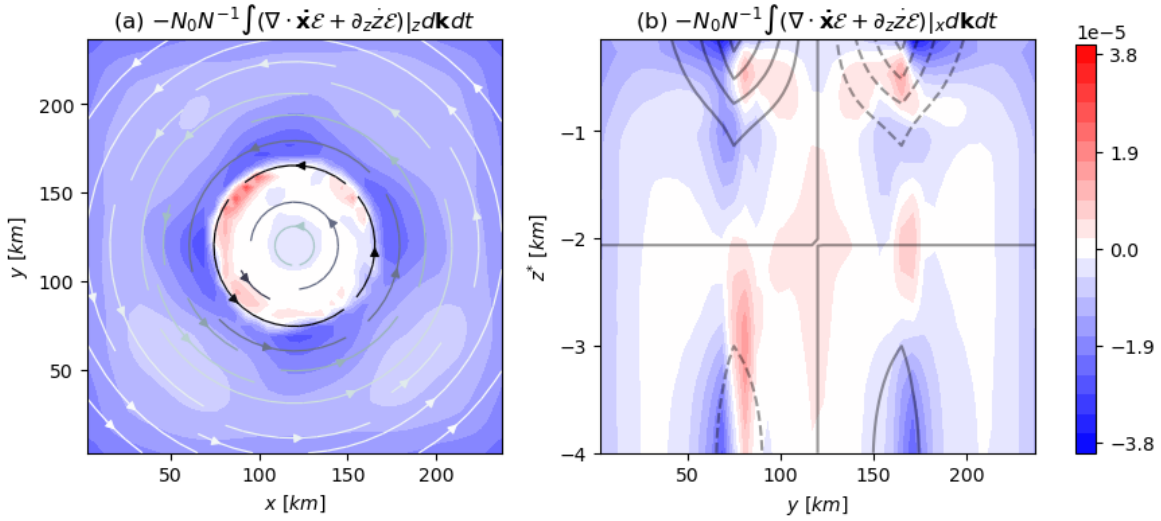

Figure 2.7: Wave energy change due to wave propagation (in $\mathrm{m^2 s^{-2}}$) after 6 days of simulation (a) at $z = -30$ m ($z^* = -266$ m) and (b) over the meridional cross-section at $x = 120$ km. Contour lines show the speed of the eddy in (a) and zonal velocities in (b). The quantities are WKB-scaled by the factor $N_0 N(z)^{-1}$. In (b) we use stretched vertical coordinate z^* with $\mathrm{d}z^* = N/N_0\,\mathrm{d}z$, where $N_0 = \int_{-h}^{0}(N/h)dz$ with $h = 4000$ m.

wave-mean flow interaction increases as well towards the surface due to the stronger vertical shear of the mean flow and leads to a loss of energy, again enhanced at the vicinity of the eddy rim.

The net effect of the wave-mean flow interaction is loss of wave energy from eddy rim to the center and gain outside of similar magnitude (i.e. the eddy would be accelerated inside and decelerated outside) such that both effects appear to cancel each other. We calculate the integrated net effect of wave-mean flow interaction as

$$WM = \frac{\int\int \mathcal{E}\dot{\omega}/\omega\,\mathrm{d}(\boldsymbol{x},z)\mathrm{d}(\boldsymbol{k},m)dt}{\int\int |\mathcal{E}\dot{\omega}/\omega|\,\mathrm{d}(\boldsymbol{x},z)\mathrm{d}(\boldsymbol{k},m)dt} \tag{2.22}$$

which is $WM = 0.14$ for both cyclone and anticyclone. There is thus a small net gain of energy by the waves. Wave-mean flow interaction contributes to a total energy gain of 1.7% relative to the initial energy and integrated over the whole cyclone or anticyclone after the 6 days of simulation.

2.3.3. Wave propagation

The total energy change by wave propagation integrated over wavenumber space and the 6 days of simulation is shown in Fig. 2.7 for the horizontal plane close to the surface and the meridional cross-section through the eddy. The effect of wave propagation is as large as the mean-flow interaction and partly counterbalances it, but is more inhomogeneous in its spatial pattern and hence more difficult to understand. Horizontal and vertical propagation (not shown) contribute with similar magnitudes to the total wave propagation effect in Fig. 2.7. The vertically integrated relative maximal energy loss by wave propagation is 40.6% relative to the initial energy. Wave propagation contributes to a total energy loss of 14.1% relative to

the initial energy and integrated over the whole cyclone or anticyclone after the 6 days of simulation.

The intrinsic horizontal group velocity $\dot{\mathbf{x}}_h - \mathbf{U}_h$ depends on the wavenumber magnitudes, but is identical for different wavenumber angles ϕ. For the initially isotropic wave field we thus expect no net effect of the horizontal transport $\dot{\mathbf{x}}_h\mathcal{E}$, except for a radiation out of the model domain, thus a general decrease of the wave energy. In principle, this can be seen in $\nabla \cdot \dot{\mathbf{x}}\mathcal{E}$, but at the eddy rim, however, there is predominantly wave energy gain by $\nabla \cdot \dot{\mathbf{x}}\mathcal{E}$ (not shown) which is related to the developing anisotropy at the eddy rim. Outside the eddy and towards the center there is loss of wave energy by the term, with largest magnitudes at the surface and bottom. Towards the eddy center, the effect of $\nabla \cdot \dot{\mathbf{x}}\mathcal{E}$ vanishes, since there the wave field stays isotropic.

The effect of the vertical propagation $\partial_z \dot{z}\mathcal{E}$ (not shown) is close to the surface and bottom predominantly negative at the rim, and positive towards the center, while outside the eddy no coherent pattern can be seen. The net effect by the wave propagation is a wave energy loss outside the eddy rim related to wave dissipation by wave refraction (see below), and small gain or vanishing effect towards the eddy center, see Fig. 2.7. If it is not a loss, the effect of vertical wave propagation tends to be a redistribution of the wave energy over the eddy. In the vertical propagation effect $\partial_z \dot{z}\mathcal{E}$, however, we see artifacts of the chosen snapshot sampling in time (half daily in our case) which decrease using higher snapshot frequencies (which do not show up in other terms), but which makes it difficult to understand the role of the term. For the case of the anticyclone, the wave propagation is again analogous to the case of the cyclone.

We use horizontal open boundaries such that waves propagating out of the domain across the horizontal boundaries lead to the largest relative energy loss. We assess the role of open boundaries by comparing to an equivalent simulation with horizontally cyclic boundaries. The relative energy loss in time and due to the effect of wave propagation relative to the initial energy integrated over the whole domain is now reduced to approximately 1%. However, the effects of wave-mean flow interaction as well as wave dissipation are almost identical for both simulations. Therefore, the waves that propagate out of the domain in the simulations with horizontal open boundaries do not affect our results owith respect to the wave-mean flow interaction and dissipation.

2.3.4. Vertical wave refraction and wave dissipation

In this section, we discuss the role of wave dissipation by vertical refraction in more detail and its role for mixing. The vertical wave refraction is given by

$$\dot{k_z} = -\partial_z \omega_{enc} = -\mathbf{k}_h \cdot \partial_z \mathbf{U}_h - \frac{k_h^2}{(k_h^2 + k_z^2)^2} \frac{N}{\omega} \partial_z N \tag{2.23}$$

Strong vertical shear $\partial_z \mathbf{U}_h$ and large $\partial_z N$ can refract waves such that waves eventually leave the wavenumber domain across the vertical wavenumber threshold k_z^c contributing so to the energy flux F_v , which we interpret as wave dissipation by vertical refraction. F_v contributes to a total of 2.3% of energy loss relative to the initial energy and integrated over the whole cyclone or anticyclone after the 6 days of simulation.

The effect of the vertical shear $\partial_z \mathbf{U}_h$ dominates the effect of $\partial_z N$ in the flux F_v. Using single column simulations (excluding dimensions x and y but not k_x and k_y, not shown) with

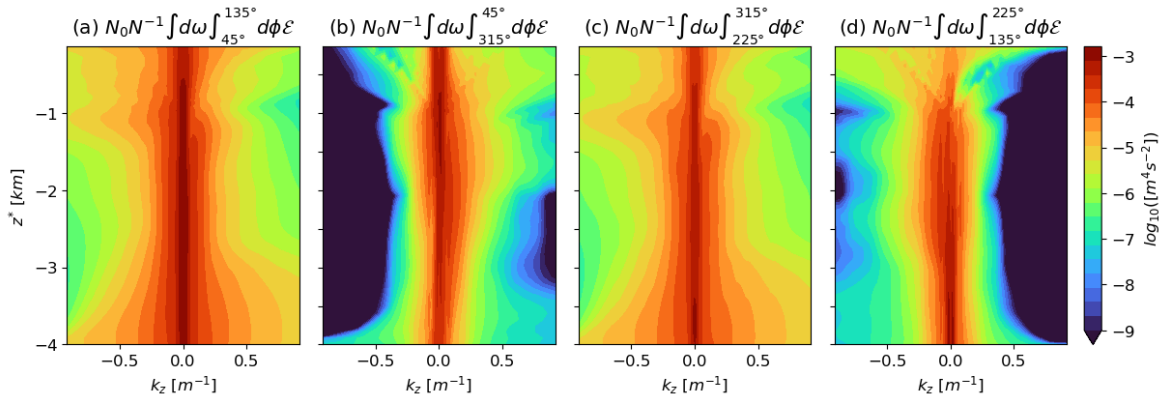

Figure 2.8: Wave energy density at time $t = t_6$ [$\log_{10}(\mathrm{m}^4/\mathrm{s}^2)$] at the northern eddy rim (x, y) = (120 km, 165 km) for the wave compartments: (a) north with $45° < \phi < 135°$, (b) east with $315° < \phi < 45°$, (c) south with $225° < \phi < 315°$ and (d) west with $135° < \phi < 225°$, where ϕ is the angle with respect to the zonal wavenumber (k_x) axis. The x axis in the figure indicates the vertical wavenumber and y axis the depth.

$\boldsymbol{U} = 0$ but the same $\partial_z N$, we see much less wave dissipation by vertical refraction (in this case critical layer absorption) and much smaller flux F_v than including $\partial_z \boldsymbol{U}_h$. However, the effect of $\partial_z N$ only also drives a small flux F_v, reducing the total energy by 0.6 % over the 6-day simulation.

Since the dominant effect by $\partial_z \mathbf{U}_h$ in Eq. (2.23) depends on the horizontal wavenumber vector $\mathbf{k}_h$, it is useful to divide the diagnostics into different wave compartments: north/-southward and west/eastward propagating waves. That means we perform a coordinate transformation $\mathcal{E}(\mathbf{k}_h, k_z, z) \rightarrow \mathcal{E}(k_z, \omega, \phi, z)$ and integrate over frequency ω and the four major cardinal direction, where north is $45° < \phi < 135°$, east is $315° < \phi < 45°$, south is $225° < \phi < 315°$ and west is $135° < \phi < 225°$, where ϕ is the angle with respect to the zonal wavenumber (k_x) axis. We show the compartment-wise integrated energies at the northern eddy rim as function of depth and k_z in Fig. 2.8 (where $k_z < 0$ denotes upward and $k_z > 0$ downward propagating waves) after 6 days of simulation. At the northern eddy rim is $\partial_z U < 0$ and $\partial_z V \rightarrow 0$, i.e. $\dot{k}_z > 0$ for eastward propagating waves and $\dot{k}_z < 0$ for westward propagating waves (ignoring the minor effect of $\partial_z N$). Accordingly, Fig. 2.8 (b) shows that for the compartment of the eastward propagating waves the upward propagating branch with $k_z < 0$ is emptied, and wave energy is transported towards the downward propagating branch with $k_z > 0$, where the flux by $\dot{k}_z$ across the wavenumber threshold $+k_z^c$ contributes to F_v. That means that east- and downward propagating waves dissipate by vertical refraction at the northern rim. The opposite is true for the westward propagating waves (Fig. 2.8 d), where west- and upward propagating waves dissipate by vertical refraction. The net effect is a drainage of energy in east and westward propagating waves, and no such effect in north and southward propagating waves, generating the horizontal anisotropy and the ellipse with major axis oriented toward the eddy center seen in Fig. 2.5. The same holds for the other positions at the rim, and for the anticylonic eddy accordingly. The effect of $\partial_z N$ on $\dot{k}_z$ is minor but can also contribute to F_v which can be seen in Fig. 2.8 (a) and (c) where the effect of $\partial_z \boldsymbol{U}_h$ vanishes for the north and southward compartments. Around 1000 m depth, the maximal $\partial_z N >$ generates the largest magnitude of $\dot{k}_z < 0$, which give rise to a small flux F_v for upward propagating waves.

Horizontal shear can also lead to wave breaking and dissipation by horizontal refraction. Due to the lateral shear, waves refract according to $\dot{\boldsymbol{k}}_h = -\boldsymbol{k}_h \cdot \nabla_{\boldsymbol{x}_h} \boldsymbol{U}_h$ and can eventually leave the wavenumber domain across the lateral wavenumber threshold k_h^c and contribute to the energy flux F_h, which we interpret as wave dissipation by horizontal refraction. This effect is, however, two orders of magnitude smaller than F_v in all our simulations, therefore we do not discuss it in more detail.

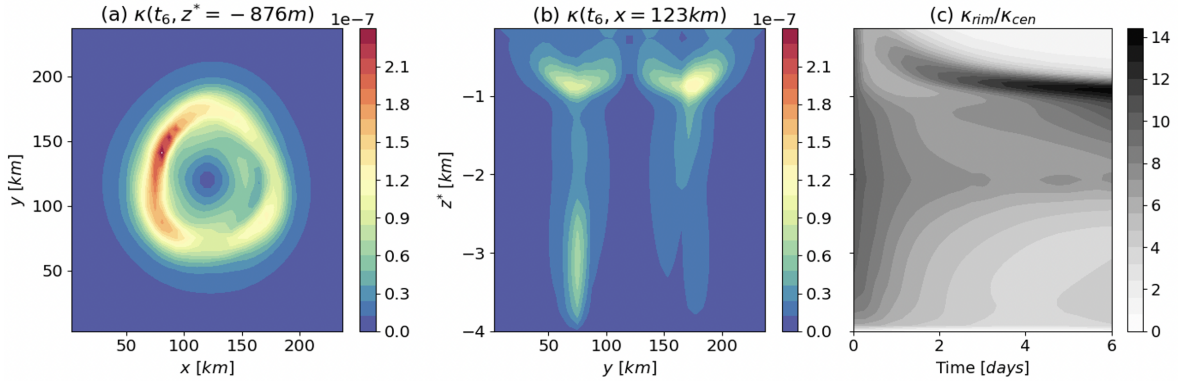

Figure 2.9: Vertical diffusivity κ in (m^2s^{-1}) from wave energy fluxes due to wave dissipation by vertical refraction F_v (and F_h) (a) at $z = 268$ m ($z^* = -876$ m), and (b) over the meridional cross-section at $x = 120$ km at time $t = t_6$. (c) Ratio of vertical diffusivity between the northern eddy rim and center in time.

The vertical diffusivity κ is computed from the flux by wave dissipation F_v from Eq. (2.8), and is shown in Fig. 2.9 (a,b) after 6 days simulation. Vertical diffusivities for the case of the cyclonic and anticyclonic eddy are identical. κ is large near the surface with (decreasing) values of $\kappa \approx 10^{-5}$ to 10^{-7} m^2s^{-1} during the simulation period. The diffusivity is maximal at the eddy rim close to the surface where most of the wave breaking takes place as waves get trapped by the mean shear and dissipate. κ is mainly related to F_v with a minor contribution of F_h. κ is maximal at the eddy rim and decays towards the eddy center and outside the eddy as the vertical shear of the mean flow decreases.

The simulations show much larger diffusivities of the order of $\kappa \approx 10^{-5}$ m^2s^{-1} towards the surface at the eddy rims during the first two days of simulation (not shown). In Fig. 2.9 (c) we show the evolution of the fraction between the diffusivities at the northern eddy rim against the center. While at the beginning the diffusivities at the rim are overall larger than at the center, where the shallower maxima in κ are predominant (not shown), the lower ones strengthen with time at the rims by more than an order of magnitude. Eventually, as there is no energy fed to the system, no waves are left to break and no more energy is transported outside of the wavenumber domain, and thus diffusivities vanish.

2.3.5. Comparison to observations

Available observations appear to show the key feature predicted by our model. A mooring with a downward looking ADCP with 75 kHz and a sampling period of 8 min was deployed for 22 days at the core of our eddy within the REEBUS project. We divide the measured horizontal velocity time series in two series of 6 days since then the first time series corresponds roughly to measurements at the eddy core and the second at the eddy rim. We compute the

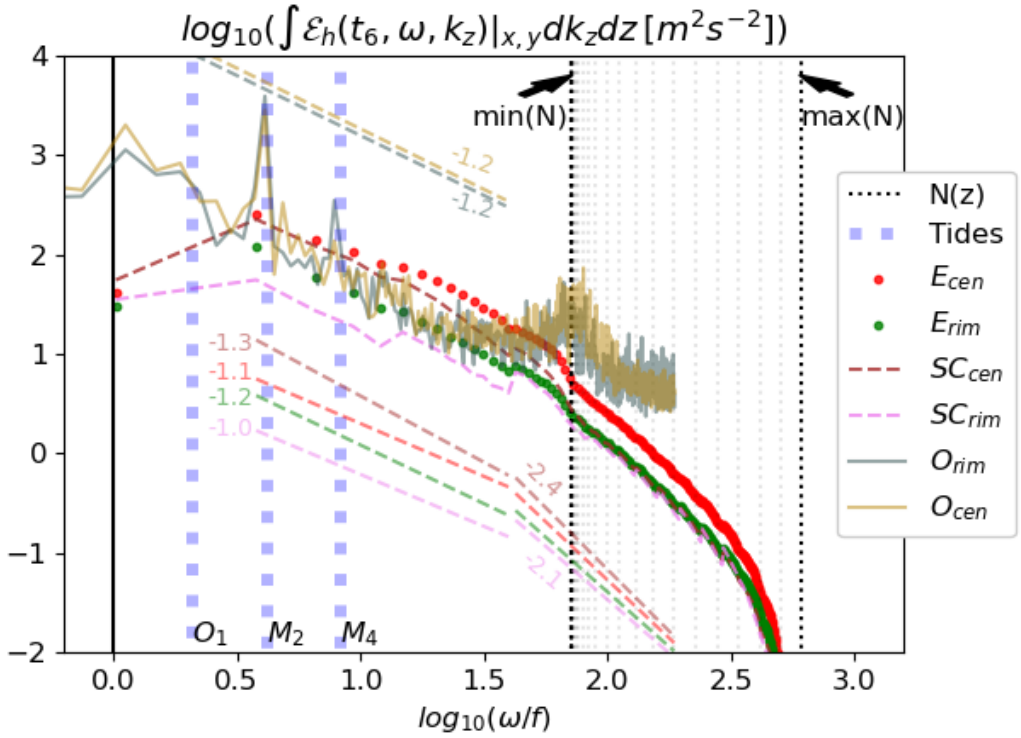

Figure 2.10: Spectra of horizontal kinetic energy densities in frequency space at the eddy center and eddy rim in the upper 1 km from observations (O_{cen} and O_{rim}) and after 6 days of model simulation [$E_{cen}(t_{end})$ and $E_{rim}(t_{end})$] and of single column simulations (SC_{cen} and SC_{rim}). To each spectrum we show the fitted linear regression vertically displaced (dashed lines), where the numbers denote the slopes. Dashed blue vertical lines represent tidal frequencies and harmonics (O_1, M_2...) and dotted grey lines indicate the depth-dependent N where waves may encounter turning points. Black lines define the frequency domain in which waves live $f \leq \omega \leq max(N)$. Note that the x axis is scaled with the Coriolis frequency f.

horizontal kinetic energy spectral estimate $\mathcal{E}_h(\omega, k_z)$ for a moving window of 4 days for five depth-ranges of 206 m, to finally integrate in vertical wavenumber.

Fig. 2.10 shows the observed frequency spectra of horizontal kinetic energy densities $\mathcal{E}_h$ at the eddy center and the rim. They contain both elevated energy levels at tidal frequencies (O_1, M_2 and harmonics), but also all other (wave) frequencies between the local f and N are populated with energy, akin to the GM model spectrum. At all such frequencies except for the tidal frequencies, the energy seems indeed to be higher for the eddy center than at the rim. Without more observations from other eddies, it is difficult to say if the difference of the energy level in the observations is statistically significant or just by chance. We made an attempt to proof that the spectral estimate at the eddy center is indeed statistically significantly larger compared to the eddy rim by performing a χ^2-goodness of fit[3] of the fraction of the

[3]The χ^2-goodness of fit is a statistical method to test two hypotheses: the null and alternative hypothesis. The null hypothesis in this case is: The IGW energy at the eddy center are significantly larger compared to the IGW energy at the rim. The alternative hypothesis is: The IGW energy at the eddy center are not significantly larger compared to the IGW energy at the rim. This statistical test is computed with the Pearson's χ^2 as $\chi^2 = \sum_f \frac{(O-E)^2}{E}$, where O is the observed variable (in this case the fraction of IGW energy at center against rim for each frequency), E is the expected fraction (in this case, it is $E = 1.2$), and $\sum_f$ denotes a sum over all frequencies.

kinetic energy at the center and rim. With a simple minimum-finding algorithm we compute an expected fraction of 1.2 that significantly fits ($p > 0.05$) our hypothesis.

However, the difference in the observations clearly has a smaller magnitude than in the model. The corresponding spectra from the model – after a coordinate transformation of $\mathcal{E}_h(\mathbf{k})$ to frequency space $\mathcal{E}_h(\omega, k_z) = \frac{1}{2}\frac{N^2-\omega^2}{N^2-f^2}\frac{\omega^2+f^2}{\omega^2}\mathcal{E}(\omega, k_z)$ – at $t = 0$ and $t = 5$ days for the eddy center and rim are also shown in Fig. 2.10. Since there is no forcing in the model, and since we initialized with the generic GM model spectrum, it is possible that the larger difference in energy levels at eddy rim and center in the model would decrease over time similar to the observations, including appropriate forcing and other components neglected so far in Eq. (2.3). We also compare the spectra for single column and eddy simulations, where the additional horizontal shear in the eddy simulations leads to elevated energies for the center and rim.

We also observe prominent elevated IGW energies at the frequency $\omega = 2.5 \times 10^{-3}$ s^{-1} (or $log_{10}\omega f^{-1} \approx 1.9$) in the observations both at rim and center. This frequency is in fact the smallest value to which the Brunt-Väisälä frequency converges and therefore suggest that it is a distinct prevalent turning point. Although observations show a peak in energy at this frequency, our simulations do not model this peak, and so we conclude, that it may be caused by other wave processes.

Lastly, we compare the slopes of the observations (where the tidal signal has been filtered out) and model results fitted with a linear regression. The slopes fitted up to the frequency $\omega = 2.5 \times 10^{-3}$ s^{-1} show a very good agreement with a mean slope of $s = -1.2$ ($R^2 = 0.9$), where the single column simulations show the biggest difference due to the missing horizontal wave processes. Recently, Dong et al. (2023) also approximate a stationary energy spectrum that satisfies a power law with slope $s = -1$ from simulations based on the ray-tracing equations. The fits show steeper slopes for higher frequencies that range from $s = -2.1$ to -2.4.

2.4. Summary and discussion

A novel numerical approach based on the radiative transfer equation is presented to study the propagation and refraction of IGWs in a meso-scale eddy in the ocean. In its full complexity the model includes six dimensions, three in physical and three in wavenumber space, in addition to the time dimension. The simulations presented here are the first ones, to our knowledge, to comprehensively describe the evolution of the full IGW spectrum inside a meso-scale coherent eddy, within the WKBJ-approximation, and detail the effects of wave propagation, reflection, refraction, interaction with the mean flow, and breaking related to wave dissipation by vertical and horizontal refraction.

Stratification and mean flow for the simulation are motivated from the observations of the coherent cyclonic eddy structure CE_2019_14N_25W in the Canary Current System, which we think is representative for a typical coherent eddy at mid-latitudes. Mean flow and stratification are assumed to be stationary during a 6-day simulation in which the wave field evolves and interacts with the background field, but no additional wave forcing is applied. We use the GM model spectrum as the initial condition. A reflection boundary condition at the bottom and surface is used and open boundaries are implemented in the lateral direction, where energy freely flows out of the model domain, but no energy flows in.

In wavenumber space, we use also open boundaries at the wavenumber thresholds $k_z^c = \pm 1$ m^{-1} vertically and $k_h^c = \pm 0.5$ m^{-1} horizontally, and interpret the fluxes across k_z^c and k_h^c towards smaller wavelength as wave breaking and dissipation by vertical and horizontal refraction, respectively. For given $\mathcal{E}$ from the GM model spectrum, k_z^c is large enough for waves to be considered as unstable with $\mathrm{Ri}_{\mathrm{Bulk}}^{-1} \geq 1$ and thus are prone to breaking at k_z^c. The vertical wavenumber threshold k_z^c is not uniquely given in literature, although a slightly larger vertical wavelength of $\lambda_c = 10$ m (i.e. $k_z^c = 0.63$ m^{-1}) has been reported previously (cf. Gargett et al. (1981); Gregg (1987)). We test the impact of the choice $k_z^c = 0.63$ m^{-1} on our results using single column simulations initialized with identical horizontal wavenumber space, wave energy (the GM model), mean flow corresponding to the northern eddy rim and stratification, but different k_z^c. Reducing the vertical wavenumber cutoff from $k_z^c = 1$ m^{-1} to $k_z^c = 0.63$ m^{-1} leads to a 1.4 times larger wave energy loss after 6 days, by wave-mean flow interaction and dissipation. Furthermore, the resulting diffusivities are enhanced by an averaged value of 1.5 times. Note that only constructively superimposing waves are considered here, thus a condition $\mathrm{Ri}_{\mathrm{Bulk}}^{-1} > 4$ may overestimate the breaking. However, $\mathrm{Ri}_{\mathrm{Bulk}}^{-1}$ depends on the total wave energy that we use as the initial condition, i.e. on the parameter E_0 of the GM model spectrum. $\mathrm{Ri}_{\mathrm{Bulk}}^{-1}$ increases and k_z^c decreases for larger E_0. The value for E_0 used here is most likely a low bias, as for example Pollmann et al. (2017) found three times larger values for E_0.

There is no known analogous treatise for k_h^c as far as we know. Although we find that fluxes across k_h^c are of two orders of magnitude smaller than fluxes across k_z^c, this may differ for cases with strong horizontally sheared mean flows. Thus, a proper assessment of horizontal wavenumber thresholds may thus be required in such cases, but here we found the effects to be minor.

The key results from this study are as follows:

- Wave energy significantly decreases at the eddy rim, while the eddy center shows an increase in the wave energy. We made an attempt to find such a difference in wave energy in the available observations, which tend to show also larger wave energy in the eddy center, although with a much weaker difference in the amplitudes.
- Waves gain energy from the mean flow outside the eddy rim by lateral shear, while from eddy rim towards the center the effect vanishes. By vertical shear, the waves always lose energy to the mean flow, and this effect is largest at the eddy rim and towards the surface. The net effect is to accelerate the eddy inside and to decelerate it outside its rim, with net deceleration overall.
- Lateral shear generates wave energy gain only due to a developing horizontal anisotropy outside the eddy rim. This anisotropy is given by an ellipse with maximal energy towards its center and its major axis oriented towards the eddy center, but slightly tilted clockwise. The ellipse is generated in the first place by the effect of vertical refraction by vertical shear. The tilt is important for the effective wave energy gain and generated by horizontal refraction.
- Vertical shear extracts wave energy by propagation into critical layers, without such dissipation wave-mean flow interaction by vertical shear has no net effect because of vertical reflection.
- The effect of lateral wave propagation is as large as the mean-flow interaction and partly counterbalancing it, but is more inhomogeneous in its pattern and more difficult to

understand.

- The effect of vertical propagation tends to be a redistribution of energy, but at the eddy rim a loss of wave energy because of transports towards critical layers.
- Wave breaking related to dissipation by vertical refraction due to vertical shear is two orders of magnitude larger than the effect of horizontal shear (dissipation by horizontal refraction).
- Wave breaking and dissipation by vertical refraction occurs predominantly at the eddy rims close to the surface where vertical shear and changes in N are largest, and yields overall 2.3 % energy loss over the integration period. The effect of $\partial_z \boldsymbol{U}_h$ dominates but $\partial_z N$ can also drive a minor energy loss by dissipation by vertical refraction.
- Related vertical diffusivities are also largest at the eddy rims close to the surface and smallest at the eddy center and decay with depth, with maximal values ranging from $\kappa = 10^{-5}$ m^{2}s^{-1} at the start to $\kappa = 10^{-7}$ m^{2}s^{-1} at the end of the simulation. These mixing rates appear low but note that they depend on our choice of E_0 of the GM model spectrum we use as initial condition, which is likely to have a low bias.
- The anticyclonic eddy behaves similar to the cyclonic one with respect to the results mentioned above, except for the slight tilt of the horizontal anisotropy which is anticlockwise, opposite to the cyclonic eddy.

Dissipation measurements within the coherent eddy in the Canary Current system taken during the observational campaign will be used in the future to compare with the predicted enhanced mixing at the eddy rim, but are not yet available to us. At the rim of a coherent meso-scale eddy in the Lofoten Basin, Fer et al. (2018) indeed find enhanced dissipation rates by turbulent mixing and relate that to internal wave breaking. However, they also find enhanced dissipation at the eddy center, in contradiction to our model simulation. This difference might be related to different energy sources such as the instability of the background shear which Fer et al. (2018) also find, or to the many limitations of our model approach.

The following limitations are inherent to our approach. Wave propagation and refraction lead to numerical grid dispersion errors which are getting smaller using finer grid resolution, but fine grids quickly become computationallvery expensive for our model. The simulations presented here are already at the upper end of available resources to us such that using finer grids are not possible at the moment. However, since the spectra and spatial distributions we simulate here remain continuous without large gradients on the small scales where the numerical errors are largest, we regard the effect of numerical grid dispersion errors as minor. The issue could be tested using some kind of self-refining or unstructured grids (triangular domain decomposition may have better properties than the rectangular grid used here).

Because of the assumed stationarity of the mean flow and stratification, the wave field might continuously build up energy at locations where the wave-mean flow interaction is strong despite the large energy sinks by wave-mean flow interaction or wave breaking. The missing implementation of the mean flow's reaction related to the wave energy changes by wave-mean flow interaction as well as changes in stratification caused by induced mixing due to wave breaking, can lead to an unrealistic representation of the evolution of the wave field. However, without implementation of an interactive mean flow and stratification these effects are difficult to assess and left for future studies. Further, the mean flow is not in balance with the background density field in our simulations, but we regard this effect as minor since the

refraction by changing density should be dominated by the background vertical gradient $N^2(z)$. Both issues could be assessed by comparing with a numerical simulation in physical space of waves interacting with a balanced eddy flow. There, however, other processes as wave-wave interaction and wave scattering at the mean flow and stratification are also present, but which have been neglected in the present model simulations.

Recently, Savva et al. (2021) derived (for N = const) a kinetic equation using the Wigner transform (Ryzhik et al., 1996) similar to Eq. (2.3), which avoids the WKBJ assumption of slowly varying background conditions. In contrast, this assumption is necessary in our approach using the spectral energy balance Eq. (2.3), but note that we tested the WKBJ assumption in Fig. 2.2 without finding significant violations. The kinetic equation by Savva et al. (2021) could in principle also be used instead of the spectral energy balance Eq. (2.3) (although a realistic $N(z)$ from observations as used here could not be used). In the kinetic equation by Savva et al. (2021) the transport terms in wavenumber space and the energy transfer to or from the mean flow in Eq. (2.3) are replaced by a scattering term involving all other wavenumbers. Practically, this scattering integral over all wavenumbers would drastically slow down a parallel integration since for each time step a sum over the (parallelized) wavenumber space needs to be performed. Conceptually, it is not obvious how to implement dissipation in the kinetic equation by Savva et al. (2021) since the fluxes across wavenumber boundaries are missing there and are replaced by the scattering integral. In contrast, Eq. (2.3) is easily parallelized and dissipation is naturally implemented as described above. A possible modification of IWEM to the kinetic equation by Savva et al. (2021) is therefore postponed for now to a later study.

Wave forcing by tidal flow at the bottom or oscillatory Ekman pumping at the surface appears simple to implement to our model. Here, we ignore these source terms and consider idealized spin-down simulations only, because of the other limitations which we also currently not resolve. Another possible forcing which is more difficult to include is the secondary wave generation during the wave breaking process. Currently, we assume that all the wave energy propagating to smaller wavelength across the thresholds k_z^c and k_h^c is converted entirely to small-scale turbulence. However, a certain amount of the energy will certainly generate other waves at other wavelengths during the breaking process, but this process is largely unknown and needs further attention.

Another limitation of our study is that as initial condition we use the generic GM model spectrum, but inside the eddy the spectrum is changing such that it is likely that in a stationary state the wave field will differ from GM inside the eddy. We found that even in single column simulations (not shown) with vanishing mean flow but depth-dependent stratification, the initial GM model spectrum is not stationary but evolves in time due to vertical wave propagation and refraction. This effect is related to the scaling of the GM model spectrum by N, i.e. by the term $E(z) = E_0 N(z)/N(0)$ in Eq. (13). The GM model spectrum only remains stationary for $N = const$ in our model. Similar to Gregg (1989), different power laws of N for the formulation (larger and smaller than 1) have been tested for stationarity of the GM model spectrum, and it was found that other descriptions even increase the non-stationarity. Thus, the description of the GM model spectrum by the scaling $\mathcal{E} \sim N(z)/N_0$ appears to be a reasonable zero order approximation, but may not be the best representation (Garrett and Munk, 1975). In fact, the observed GM model spectrum might be far from stationary such that relatively large wave sources, transports and sinks are needed to explain the observations. It is likely that for the GM model spectrum with its power law of -2 the downscale energy

transfers by non-linear wave-wave interactions also play an important role. Such transports are also not considered here and including a full evaluation of the scattering integral as in Eden et al. (2019c) appears in principle possible but computationally expensive. Some kind of approximation as in Hasselmann et al. (1985) might help in this respect and is a subject of future work.

Acknowledgments

We thank Oliver Bühler and another anonymous reviewer for their comments and suggestions on this manuscript. This paper is a contribution to subprojects W6 and W2 of the Collaborative Research Centre TRR 181 "Energy Transfers in Atmosphere and Ocean" funded by the Deutsche Forschungsgemeinschaft (DFG, German Research Foundation) under project number 274762653. This paper is also associated with the research project REEBUS (Role of Eddies in the Carbon Pump of Eastern Boundary Upwelling Systems) funded by the Bundesministerium für Bildung und Forschung (BMBF, German Federal Ministry of Education and Research). We thank M. Dengler and J. Karstensen from GEOMAR, Kiel for providing the observational data and collaboration in REEBUS.

Datastatement

The novel numerical spectral Internal Wave Energy Model (IWEM) can be accessed via `https://github.com/ceden/IWEM.git`. The observational data used is taken from the data portal of the Helmholtz Centre for Ocean Research Kiel - GEOMAR, with restricted access.

A. The Internal Wave Energy Model (IWEM)

The Internal Wave Energy Model (IWEM) integrates the six-dimensional Radiative Transfer Equation Eq. (2.3) in time, and simulates the interaction of the IGW field with the background medium. The model describes the propagation and refraction of IGWs in a variable background stratification and mean flow and the energy exchange of the wave field with the mean flow.

Using a staggered C-grid discretisation, wave energy E, stratification N and mean flow velocities U, V, W take values at the center of the grid boxes, while zonal, meridional and vertical group velocities are located at the eastern, northern and upper side of the grid boxes. For the wave refraction in k_x, k_y, k_z-direction the discretisation is analogous. We use an equidistant grid in the meridional direction, a surface refined non-equidistant grid in vertical direction, and also a non-equidistant grid in wavenumber space, with finer resolution for small wavenumber components. For parallelisation, each processor unit solves Eq. (2.3) on a subdomain of the model.

At the surface and bottom, waves are reflected back, so that upward propagating waves with $k_z < 0$ propagate downward with $k_z > 0$ after reflection and vice versa. All other boundaries are open, so that energy can freely flow out of the domain, but no energy can propagate into the domain. For the computation of fluxes a necessary amount of numerical diffusion is introduced, so that energies remain positive definite. All fluxes are therefore computed with

a second order advection scheme with superbee flux limiter and forward time-stepping. The numerical model code can be accessed at `https://github.com/ceden/IWEM.git`.

B. Observed velocities

The observed zonal velocities in the meridional eddy cross section reach down to 1000 m depth. This is insufficient for a complete representation of the evolution of the IGW field, for which we need the mean flow over the whole depth. Moreover, the observed velocities may include IGW signals which we need to remove. To approximate the mean flow to the whole depth and to smooth the observations, a projection on the vertical modes is used. The orthogonal vertical eigenfunctions Φ_n result from the vertical eigenvalue problem

$$\frac{\mathrm{d}}{\mathrm{d}z} f^2 N^{-2} \frac{\mathrm{d}\Phi_n}{\mathrm{d}z} + f^2 c_n^{-2} \Phi_n = 0 \;\text{ with }\; \frac{\mathrm{d}\Phi_n}{\mathrm{d}z} = 0 \;\; at \;\; z = 0, -h \tag{24}$$

with approximate solution

$$\Phi_n \approx \sqrt{\frac{2N}{h\widetilde{N}}} cos\left(\int_{-h}^{z} N/c_n \mathrm{d}z'\right), \;\; c_n \approx h\widetilde{N}/(n\pi), \;\; \widetilde{N} = \frac{1}{h}\int_{-h}^{0} N \mathrm{d}z \tag{25}$$

Velocity U is then given by $U = \sum_{n=0}^{\infty} u_n \Phi_n(z)$ with $u_n = \int_{-h}^{0} U \Phi_n \mathrm{d}z$. Since U is not available for the whole depth down to 4000 m, the amplitudes u_n for each mode are fitted for the available observations in the upper 1000 m of the ocean. The eigenfunctions are calculated for $\overline{N}$ and the fitted profiles $N_1(z)$ and $N_2(z)$. We carry out the fit with the Python function $scipy.optimize.curve_fit$ first for the barotropic mode, subtract then the resulting velocities from the observed ones and follow this procedure iteratively up to the 10^{th} baroclinic mode, to obtain the mean flow. This is done for each meridional position along the eddy cross section. The barotropic and the first three baroclinic modes are the most powerful ones. The fit of these four modes results in a Pearson coefficient of $\rho = 0.8$, hence the fit and the observed velocities correlate very well. The velocities resulting from the sum of the first 4 modes represent hence most of the mean flow and are used for the eddy simulations.

C. Idealized velocities

Following, for example Castelão and Johns (2011) and Browning et al. (2021), eddies captured in the tropical Atlantic can be well described by the following idealized structure: exponential decay outside the eddy and a linear transition in-between eddy rims. The eddy rim is located at a radius $r = \sqrt{x_{rim}^2 + y_{rim}^2} = 45$ km from the eddy center at $(x, y)_{center} = (120, 120)$ km. For the vertical direction, the first baroclinic mode $\Phi_1(z)$ from Appendix B is used.

$$U(x, y, z) = -0.2\sqrt{L_x^2 + L_y^2}\Phi_1(z) R(x, y) \sin(\tan^{-1} y/x) \tag{26}$$

$$V(x, y, z) = 0.2\sqrt{L_x^2 + L_y^2}\Phi_1(z) R(x, y) \cos(\tan^{-1} y/x) \tag{27}$$

$$R(x, y) = \begin{cases} \sqrt{x^2 + y^2} & \text{for } \sqrt{x^2 + y^2} < r \\ r \exp\left(-\left(\sqrt{x^2 + y^2} - r\right)/2r\right) & \text{for } \sqrt{x^2 + y^2} > r \end{cases} \tag{28}$$

where L_x and L_y denote the horizontal extent of the domain.

3

Wave-wave interactions of internal gravity waves. Part A: Comparison of Eulerian and Lagrangian frameworks

Sebastia Saez, P., Eden, C., Olbers, D., Chouksey, M., (2025): "Wave-wave interactions of internal gravity waves. Part A: Comparison of Eulerian and Lagrangian frameworks", submitted to *Journal of Physical Oceanography*

Authors: Pablo Sebastia Saez[a] [1], Manita Chouksey[a,b], Carsten Eden[a] and Dirk Olbers[c]
Affilitations: a: Institut für Meereskunde, Universität Hamburg, Germany, b: Leibniz-Institut für Ostseeforschung Warnemünde, Germany c: Alfred Wegener Institute for Polar and Marine Research, and MARUM-Center for Marine Environmental Sciences, Germany

Abstract

The energy transfers by wave–wave interactions among internal gravity waves and their interactions with the vortical mode can be described by the kinetic equation using the weak-interaction assumption. In Part A of this study, we compare two different kinetic equations based on Eulerian and Lagrangian frameworks for a rotating, stratified, non-hydrostatic Boussinesq system. In the Eulerian case, we explicitly account for inertial and buoyancy oscillations as eigensolutions of the system and include the vortical mode, which forms the basis of the numerical evaluations at unprecedented high resolution in Part B of this study. The detailed derivation of the Lagrange and Euler interaction coefficients, evolution equations of the normal mode amplitudes, and the corresponding kinetic equations show the following: Eulerian energy is exactly quadratic in the amplitudes, whereas Lagrangian energy appears as an infinite series in amplitude powers. Under resonant conditions, the Lagrangian kinetic equation reduces to lowest order, i.e., quadratic form only, and equals the resonant Eulerian kinetic equation. Eulerian and Lagrangian interaction coefficients are equal for resonant interactions, which are also the only contributions that remain under horizontally isotropic spectra. Non-resonant interactions persist under anisotropic conditions through the usually

[1]Corresponding author: Pablo Sebastia Saez - pablo.sebastia.saez@uni-hamburg.de

unconsidered imaginary part of the time response function, and may therefore contribute more to energy transfers than previously thought. By revealing how these frameworks relate, our work provides a unified theoretical foundation for understanding the spectral evolution and energetics of internal waves in the ocean.

Statement

Internal gravity waves redistribute energy throughout the ocean and ultimately drive mixing that influences the large-scale circulation. To understand how waves interact and transfer energy between one another, we use the kinetic equation, but its predictions depend on the theoretical framework used. We show that Eulerian and Lagrangian formulations, which differ in how they define wave energy, give identical results for resonant interactions in isotropic wave fields. Importantly, additional non-resonant interactions vanish under isotropy but may become significant when the wave field is anisotropic. By linking the two formulations, we provide a coherent theoretical framework that supports more consistent predictions of internal wave spectra and energetics.

3.1. Introduction

Internal gravity waves (IGWs) occur naturally in stratified rotating fluids under the restoring forces of buoyancy, and are a crucial component of the ocean's energy cycle. IGWs are high-frequency oscillations, bounded by the Coriolis frequency (f) at the lower end and the Brunt-Väisälä frequency (N) at the upper end. This spectrum of IGWs exhibits wave-wave interactions that can transfer energy within the IGW spectrum and with other oceanic processes, such as geostrophically balanced eddies (or vortical mode), with key implications for the ocean energetics (see Olbers, 1983; Müller et al., 1986). These wave-wave interactions are primarily nonlinear, and challenging to diagnose and quantify, that impedes our understanding of their role in the ocean's energy cycle.

Wave–wave interactions are central to the redistribution of energy within the IGW spectrum and are governed by a kinetic equation that describes the evolution of wave spectra under weakly nonlinear conditions, which was originally developed in a Hamiltonian/Lagrangian formalism by Hasselmann (1966) in the general context of a Lagrangian theory of ocean waves. Consequently, Olbers (1974, 1976) used the Lagrangian formalism to derive a kinetic equation from the Lagrangian coordinate system for the rotating, non-hydrostatic Boussinesq system. The studies marked as Lagrangian in Tab. 3.1 used the same procedure as Olbers (1974, 1976) and the same interaction coefficients. Since then, a variety of approaches have been pursued to re-derive the kinetic equation and interaction coefficients. Tab. 3.1 shows a representative list of publications evaluating the scattering integral that use the Eulerian, Lagrangian, or Hamiltonian formalism, however, often – including some recent studies – invoking the hydrostatic approximation or neglecting rotation, thus excluding important features of the oceanic wave field.

While both Eulerian and Lagrangian formulations have been used to study IGWs, systematic comparisons between the two approaches are missing. In principle, one would assume that under the same approximations, the resulting kinetic equations for wave-wave interactions should be independent of the formalism used to derive it. In this work, however,

Source	Formalism	Rotation	Non-Hydrostatic	Vortical mode included
Olbers (1974, 1976)	Lagrangian	Yes	Yes	No
Müller and Olbers (1975)	Lagrangian	Yes	Yes	No
McComas and Bretherton (1977)	Lagrangian	Yes	No	No
Pomphrey et al. (1980)	Lagrangian	Yes	No	No
Müller et al. (1986)	Lagrangian	Yes	No	No
Caillol and Zeitlin (2000)	Eulerian	No	Yes	No
Lvov et al. (2012)	Hamiltonian	Yes	No	No
Eden et al. (2019b,c)	Eulerian	Yes	Yes	Yes
Bel and Tziperman (2023)	Eulerian	Yes	Yes	No
Wu and Pan (2023)	Hamiltonian	Yes	No	No
Dematteis et al. (2024)	Hamiltonian	Yes	No	No
Part A and B of this study	Eulerian + Lagrangian	Yes + Yes	Yes + Yes	Yes + No

Table 3.1: A list of studies using different formalisms to derive the kinetic equation for wave-wave interaction with or without rotation in the non-hydrostatic Boussinesq system or under hydrostatic approximation.

we find the opposite and give reasons for it. We derive and compare interaction coefficients in both Eulerian (along the lines of Eden et al., 2019b) and Lagrangian (see Olbers, 1976) frameworks under constant rotation and stratification. Our derivations are fully self-contained, and include inertial and buoyancy oscillations as distinct eigensolutions only for the Eulerian case. Note that the Eulerian framework naturally also accounts for interactions with and within the vortical (geostrophically balanced) mode, while the Lagrangian excludes it when making an expansion about an equilibrium state; see Müller et al. (1986). Although it is possible to include an arbitrary reference flow in the Lagrangian framework as in Salmon (2013), we ignore here for now the potentially important interaction of waves and vortical mode.

The kinetic equation has typically been formulated only for resonant interactions (where the sum or difference of the frequencies of the interacting waves equal the frequency of the generated one), while non-resonant interactions (where there is a mismatch in the sum or difference of frequencies of the interacting waves compared to the generated one) have been ignored and their role remains underexplored. Exceptions include Lvov et al. (2012) who consider near-resonant interactions although within the hydrostatic approximation; and Eden et al. (2019b) who derive the kinetic equation for the rotating non-hydrostatic Boussinesq system within the Eulerian framework and subsequently Eden et al. (2019c) who evaluate all kinds of triad interactions numerically, though without distinction between resonant and non-resonant contributions.

This is the first part of a two-part study, and here we derive kinetic equations for both resonant and non-resonant wave-wave interactions, with their respective interaction coefficients. Based on that derivation, in Part B of this study (Sebastia Saez et al., 2025b) we numerically evaluate the kinetic equation for realistic internal wave spectra at an unprecedented high resolution. In Part A, we also show that Eulerian and Lagrangian coefficients are identical for resonant interactions, but differ for non-resonant interactions. Importantly, resonant interactions contribute through the real part of the time response function, while non-resonant interactions emerge through its imaginary part. The transfer of energy by non-resonant interactions vanishes for horizontally isotropic spectra but are potentially relevant under anisotropy.

Section 2 presents the Eulerian formulation of the rotating non-hydrostatic Boussinesq system and the derivation of interaction coefficients, including the vortical mode. Section 3 develops the corresponding Lagrangian formulation in a self-contained manner. In Section 4, we establish the relationship between the two frameworks by examining energy conservation and the fundamental coupling coefficients. Section 5 introduces the kinetic equation and analyzes both resonant and non-resonant triad interactions, with emphasis on the role of the time response function. Section 6 summarizes the paper with a discussion and key conclusions.

3.2. The Eulerian framework

We start with the non-hydrostatic Boussinesq system of equations in the familiar Eulerian framework (e.g. Olbers et al., 2012)

$$\begin{aligned} \partial_t \boldsymbol{u} + f \underset{\neg}{\boldsymbol{u}} + \boldsymbol{\nabla} p = -\boldsymbol{u} \cdot \boldsymbol{\nabla} \boldsymbol{u} - w \partial_z \boldsymbol{u} \quad &, \quad \partial_t w - b + \partial_z p = -\boldsymbol{u} \cdot \boldsymbol{\nabla} w - w \partial_z w \\ \partial_t b + N^2 w = -\boldsymbol{u} \cdot \boldsymbol{\nabla} b - w \partial_z b \quad &, \quad \boldsymbol{\nabla} \cdot \boldsymbol{u} + \partial_z w = 0 \end{aligned} \tag{3.1}$$

for a rotating stratified fluid with constant Coriolis frequency f and constant Brunt-Väisälä frequency N, with the continuity equation in last place. All vectors are two-dimensional in Eq. (3.1), and $\underset{\neg}{\boldsymbol{u}}$ denotes anticlockwise rotation of $\boldsymbol{u}$ by 90^o. The system given by Eq. (3.1) has five variables: $\boldsymbol{u}$ are horizontal and w vertical velocities, b is the buoyancy, and p the pressure (scaled by a constant reference density). We aim to rewrite Eq. (3.1) in the compact form

$$\partial_t \boldsymbol{\Theta} + \boldsymbol{A} \cdot \boldsymbol{\Theta} = \boldsymbol{S} \tag{3.2}$$

with the state vector $\boldsymbol{\Theta}$ formed by the state variables of the system e.g. $\boldsymbol{\Theta}$=$(\boldsymbol{u}, w, b)$, the system matrix $\boldsymbol{A}$ representing the linear terms, and the vector function $\boldsymbol{S} = (S_1, \ldots S_4)$ containing the nonlinear source terms given by the right-hand side of Eq. (3.1), i.e. $S_1 = -\boldsymbol{u} \cdot \boldsymbol{\nabla} u - w \partial_z u$, and correspondingly for the other components.

There are various ways to rewrite Eq. (3.1) to Eq. (3.2), differing in the choice of the state variables. Often horizontal divergency and/or vorticity are used instead of $\boldsymbol{u}$ and w (e.g. Hasselmann, 1970; Olbers, 1986; Olbers et al., 2012). Since we aim to identify the limits of pure horizontal (inertial) and vertical (buoyancy) oscillations in Eq. (3.2) and their effects, there is, however, the danger of eliminating certain possible solutions in these limits by taking derivatives of the state variables as in horizontal divergency or vorticity. Therefore, we choose $\boldsymbol{u}, w, b$ as state variables. To eliminate the pressure, we first take the divergence of the three-dimensional momentum equation and use the continuity equation to derive the diagnostic pressure equation

$$(\boldsymbol{\nabla}^2 + \partial_z{}^2) p = f \underset{\neg}{\boldsymbol{\nabla}} \cdot \boldsymbol{u} + \partial_z b + \partial_x S_1 + \partial_y S_2 + \partial_z S_3 \tag{3.3}$$

We express the pressure as $p(\boldsymbol{X}, t) = \int d^3K \hat{p}(\boldsymbol{K}, t) \exp(i\boldsymbol{K} \cdot \boldsymbol{X})$ with wave amplitudes $\hat{p}$, the three-dimensional position $\boldsymbol{X}$, and the three-dimensional wavenumber vector $\boldsymbol{K} = (\boldsymbol{k}, m) = (k_x, k_y, m)$, and similar for $\boldsymbol{u}$, S_1, etc. Multiplying with $\exp(-i\boldsymbol{K}' \cdot \boldsymbol{X})$, integrating over space, and using the orthogonality conditions of the Fourier integrals, Eq. (3.3) becomes

$$\hat{p} = \frac{1}{K^2}(if \underset{\neg}{\boldsymbol{k}} \cdot \hat{\boldsymbol{u}} + im\hat{b} + \hat{S}_5) \ , \ \hat{S}_5 = i\boldsymbol{K} \cdot (\hat{S}_1, \hat{S}_2, \hat{S}_3) \tag{3.4}$$

where $K = |\boldsymbol{K}|$. As Eq. (3.3), we also spectrally transform Eq. (3.1) and use Eq. (3.4) to replace $\hat{p}$, which yields the spectrally transformed version of Eq. (3.2)

$$\partial_t \hat{\boldsymbol{\Theta}} - i\hat{\boldsymbol{A}} \cdot \hat{\boldsymbol{\Theta}} = \hat{\boldsymbol{S}} \tag{3.5}$$

with $\hat{\boldsymbol{\Theta}} = (\hat{\boldsymbol{u}}, \hat{w}, \hat{b})$, and the matrix $\hat{\boldsymbol{A}}$ and the vector $\hat{\boldsymbol{S}}$ given by

$$\hat{\boldsymbol{A}} = \frac{i}{K^2} \begin{pmatrix} -fk_xk_y & -f(k_y^2 + m^2) & 0 & k_x m \\ f(k_x^2 + m^2) & fk_xk_y & 0 & k_y m \\ -fk_y m & fk_x m & 0 & -k^2 \\ 0 & 0 & N^2K^2 & 0 \end{pmatrix} \ , \ \hat{\boldsymbol{S}} = \begin{pmatrix} \hat{S}_1 \\ \hat{S}_2 \\ \hat{S}_3 \\ \hat{S}_4 \end{pmatrix} + \frac{i}{K^2} \begin{pmatrix} \boldsymbol{K} \\ 0 \end{pmatrix} \hat{S}_5 \tag{3.6}$$

The matrix $\hat{\boldsymbol{A}}$ has three different eigenvalues $\lambda^0 = 0$ and $\lambda^\pm = \pm\omega$ and the corresponding right eigenvector $\boldsymbol{Q}^s = (\boldsymbol{U}^s, W^s, B^s)$ with $\boldsymbol{U}^s = (U^s, V^s)$ and the left eigenvector $\boldsymbol{P}^s$, for $s = 0, \pm$, and $\hat{\boldsymbol{A}} \cdot \boldsymbol{Q}^s = \lambda^s \hat{\boldsymbol{A}}$ and $\boldsymbol{P}^s \cdot \hat{\boldsymbol{A}} = \lambda^s \hat{\boldsymbol{A}}$. There is another vanishing eigenvalue of $\boldsymbol{A}$ with zero eigenvector which is not relevant here. The eigenvalues $\lambda^\pm$ are related to the dispersion

relation of IGWs for the wave frequency $\omega = \sqrt{(N^2k^2 + f^2m^2)/K^2}$, with $f^2 < \omega^2 < N^2$, and with special cases for the pure inertial ($\omega^2 = f^2$) and buoyancy oscillations ($\omega^2 = N^2$), while λ^0 corresponds to the slowly evolving vortical mode. We normalize the eigenvectors with the factor n^s such that orthonormality $\boldsymbol{P}^s \cdot \boldsymbol{Q}^{s'} = \delta_{s,s'}$ holds and $\boldsymbol{P}^s = n^s(\boldsymbol{U}^s, W^s, B^s N^{-2})^*$.

Similar to Bartello (1995) and making use of his nomenclature, we differentiate between the barotropic mode with $m = 0$, vertical variability with $k = 0$, mixed barotropic-vertical variability with $k = 0$ and $m = 0$, and the baroclinic mode with $k \neq 0$ and $m \neq 0$, and list the eigenvectors separately for these cases:

- The barotropic mode with $m = 0$ includes geostrophic flow without buoyancy variations for the eigenvalue $\lambda^0 = 0$ and vertically constant buoyancy oscillations without horizontal flow for the eigenvalue $\lambda^\pm = \pm N$

$$\boldsymbol{Q}^s = \begin{pmatrix} \underset{\neg}{\boldsymbol{k}}(1 - s^2) \\ \frac{-is}{N} \\ s^2 \end{pmatrix}, \; n^0 = k^{-2}, \; n^\pm = \frac{N^2}{2} \tag{3.7}$$

- The vertical variability mode with $k = 0$ includes constant buoyancy without flow for the eigenvalue $\lambda^0 = 0$ and horizontally constant inertial oscillations without buoyancy variations for the eigenvalues $\lambda^\pm = \pm f$

$$\boldsymbol{Q}^s = \begin{pmatrix} -is \\ s^2 \\ 0 \\ 1 - s^2 \end{pmatrix}, \; n^0 = N^2, \; n^\pm = \frac{1}{2} \tag{3.8}$$

- The baroclinic mode with $k \neq 0$ and $m \neq 0$ includes baroclinic geostrophic flow for $s = 0$ and the internal gravity waves for $s = \pm$ and allows for rich interactions in both cases

$$\boldsymbol{Q}^s = \begin{pmatrix} \frac{if\underset{\neg}{\boldsymbol{k}} + \boldsymbol{k}\omega s}{f^2 - s^2\omega^2} \\ \frac{ms\omega}{N^2 - s^2\omega^2} \\ \frac{imN^2}{N^2 - s^2\omega^2} \end{pmatrix}, \; n^s = \frac{|(N^2 - s^2\omega^2)(s^2\omega^2 - f^2)|}{K^2(1 + s^2)\omega^2} \tag{3.9}$$

- The mixed barotropic-vertical variability mode with $k = 0$ and $m = 0$ includes two pairs of fast oscillations with eigenvalues $\pm N$ and $\pm f$ and the corresponding eigenvectors as in the barotropic mode and vertical variability mode for $s = \pm$, but there are no vortical mode solutions for $s = 0$. Note, that this mode does not interact with the others, as the related interaction coefficients vanish (see below), and is therefore not further discussed.

The eigenvector for the baroclinic mode is identical to the one given in Eden et al. (2019c), but here we add the special solutions for inertial and buoyancy oscillations as in Bartello (1995). In Borchert et al. (2014) another pair of eigenvectors with vanishing eigenvalue related to sound wave activity and enabling volume conservation is introduced, which result from a different set of state variables, and which we do not need here. Note that using $\boldsymbol{\Theta} = (\delta, \eta, b)$ as state variables with horizontal divergence $\delta = \boldsymbol{\nabla} \cdot \boldsymbol{u}$ and vorticity $\eta = \partial_x v - \partial_y u$, care has to be taken to include to correct limits for inertial and buoyancy oscillations. Only with a certain,

energy related normalization, it can be shown that the eigenvectors converge correctly in that case in the limits $m \to 0$ or $k \to 0$.

We simplify Eq. (3.5) by expressing the state vector $\hat{\mathbf{\Theta}}$ in terms of the eigenvectors $\boldsymbol{Q}^s$ and projecting Eq. (3.5) on $\boldsymbol{P}^s$, which yields

$$\hat{\mathbf{\Theta}} = \sum_s g^s \boldsymbol{Q}^s \ , \ \ g^s = \boldsymbol{P}^s \cdot \hat{\mathbf{\Theta}} \ , \ \ \partial_t g^s - i\lambda^s g^s = \boldsymbol{P}^s \cdot \hat{\boldsymbol{S}} \tag{3.10}$$

using the orthonormality $\boldsymbol{P}^s \cdot \boldsymbol{Q}^{s'} = \delta_{s,s'}$. The wave oscillation generated by the term $-i\lambda^s g^s$ can be removed by setting

$$g^s = p^s e^s(t) \exp(i\lambda^s t) \ \ \rightarrow \ \ \partial_t e^s = \exp(-i\lambda^s t) \boldsymbol{P}^s \cdot \hat{\boldsymbol{S}}/p^s \tag{3.11}$$

with $p^{\pm} = \sqrt{n^{\pm}}$ and $p^0 = \sqrt{2n^0}$, in order to focus only on the (scaled) wave amplitude e^s. The term on the right-hand side of Eq. (3.11) involves the vector $\hat{\boldsymbol{S}}$ and thus the Fourier transform of the nonlinear terms of Eq. (3.1), which are responsible for the interaction between the modes. Since $(U^s, V^s, W^s) \cdot \boldsymbol{K} = 0$ and $\boldsymbol{P}^s = n^s (U^s, V^s, W^s, B^s N^{-2})^*$, the second part of the expression for $\hat{\boldsymbol{S}}$ in Eq. (3.6) vanishes. The remaining vector, given by the (Fourier transform of the) right-hand side of Eq. (3.1), can be written as

$$(\hat{S}_1, \ldots, \hat{S}_4)^T(\boldsymbol{K}_0) = -i \iint d\boldsymbol{K}_1 d\boldsymbol{K}_2 \, \hat{\mathbf{\Theta}}_{\mathbf{2}}(\hat{\boldsymbol{u}}_{\mathbf{1}}, \hat{w}_1) \cdot \boldsymbol{K}_2 \delta(\boldsymbol{K}_1 + \boldsymbol{K}_2 - \boldsymbol{K}_0) \tag{3.12}$$

with $\hat{\boldsymbol{u}}_{\mathbf{1}} = \hat{\boldsymbol{u}}(\boldsymbol{K}_1)$, $\hat{\mathbf{\Theta}}_{\mathbf{2}} = \hat{\mathbf{\Theta}}(\boldsymbol{K}_2)$ etc., and where the δ function results from the orthogonality of the Fourier integrals. Expressing again $\hat{\mathbf{\Theta}}$, $\hat{\boldsymbol{u}}$, etc. in Eq. (3.12) as in Eqs. (3.10, 3.11), and projecting on $\boldsymbol{P}^s$, finally yields

$$\partial_t e_0^{s_0} = -i \sum_{s_1=0,\pm} \sum_{s_2=0,\pm} \iint d\boldsymbol{K}_1 d\boldsymbol{K}_2 e_1^{s_1} e_2^{s_2} \mathcal{S}^{-s_0 \ s_1 \ s_2}_{-\boldsymbol{K}_0 \boldsymbol{K}_1 \boldsymbol{K}_2} \delta(\boldsymbol{K}_0 - \boldsymbol{K}_1 - \boldsymbol{K}_2) \exp(i(\omega_0^{s_0} - \omega_1^{s_1} - \omega_2^{s_2})t) \tag{3.13}$$

with $e_0^{s_0} = e^{s_0}(\boldsymbol{K}_0)$ and the coupling coefficients

$$\begin{aligned} \mathcal{S}^{-s_0 \ s_1 \ s_2}_{-\boldsymbol{K}_0 \boldsymbol{K}_1 \boldsymbol{K}_2} &= \frac{p_1^{s_1} p_2^{s_2}}{p_0^{s_0}} \boldsymbol{K}_2 \cdot \begin{pmatrix} \boldsymbol{U}_1^{s_1} \\ W_1^{s_1} \end{pmatrix} \boldsymbol{P}_{-0}^{-s_0} \cdot \boldsymbol{Q}_2^{s_2} \\ &= \frac{p_0^{s_0} p_1^{s_1} p_2^{s_2}}{2} (-\boldsymbol{K}_0) \cdot \begin{pmatrix} \boldsymbol{U}_1^{s_1} \\ W_1^{s_1} \end{pmatrix} \left((\boldsymbol{U}_0^{s_0})^* \cdot \boldsymbol{U}_2^{s_2} + (W_0^{s_0})^* W_2^{s_2} + \frac{1}{N^2} (B_0^{s_0})^* B_2^{s_2} \right) \end{aligned} \tag{3.14}$$

with $\boldsymbol{P}_0^{s_0} = \boldsymbol{P}^{s_0}(\boldsymbol{K}_0)$, etc.

It becomes obvious that the mixed barotropic-vertical variability is uncoupled from the system as the interaction coefficients vanish for $\boldsymbol{K}_0 = 0$.

Finally, the interactions coefficients $\mathcal{S}^{-s_0 \ s_1 \ s_2}_{-\boldsymbol{K}_0 \boldsymbol{K}_1 \boldsymbol{K}_2}$ are made symmetric in the last two indices, simply by switching sums and integrals and renaming integration variables

$$C^{-s_0 \ s_1 \ s_2}_{-\boldsymbol{K}_0 \boldsymbol{K}_1 \boldsymbol{K}_2} = C^{-s_0 \ s_2 \ s_1}_{-\boldsymbol{K}_0 \boldsymbol{K}_2 \boldsymbol{K}_1} = \frac{1}{2} (\mathcal{S}^{-s_0 \ s_1 \ s_2}_{-\boldsymbol{K}_0 \boldsymbol{K}_1 \boldsymbol{K}_2} + \mathcal{S}^{-s_0 \ s_2 \ s_1}_{-\boldsymbol{K}_0 \boldsymbol{K}_2 \boldsymbol{K}_1}). \tag{3.15}$$

It should be noted that for all state variables chosen in the beginning, we obtain the same evolution equation Eq. (3.13) with identical coupling coefficients $\mathcal{S}$. However, for the limits

of the barotropic and vertical variability modes, see respective eigenvectors Eq. (3.7) and Eq. (3.8), $\mathcal{S}$ may differ for reasons explained above. Considering the equations of motion in Lagrangian coordinates — discussed in the following section — will lead to similar evolution equation as Eq. (3.13), but with different coefficients. It is one aim of the present study, to investigate the differences between both, since Eq. (3.13) or its Lagrangian alternative Eq. (3.26) forms the basis for the derivation of the kinetic equation discussed below in Sec. (3.5).

3.3. The Lagrangian framework

The Euler form of the momentum equations in Eq. (3.1) can be cast in a Lagrangian form, (see Serrin, 1959; Olbers, 1976; Salmon, 1998). Here, one follows the position $\boldsymbol{X}(\boldsymbol{a}, t)$ of individual fluid parcels, each labeled with their position $\boldsymbol{a} = \boldsymbol{X}(\boldsymbol{a}, t_0)$ at initial time t_0. For adiabatic conditions, the parcels conserve their density and buoyancy. The label $\boldsymbol{a}$ serves as a new coordinate system in which we express the equations of motion, given that the mapping $\boldsymbol{a} = \boldsymbol{a}(\boldsymbol{x}, t)$ for the coordinate transformation exists for all times. Lagrangian coordinates are sometimes of advantage to understand wave kinematics, wave-mean flow and wave-wave interactions (see e.g. Olbers, 1976; Lvov and Tabak, 2001; Bühler, 2014; Dematteis et al., 2024; Labarre et al., 2024). One can make use of the Lagrangian variational principle of least action to formulate the governing dynamics in the Lagrangian coordinates, which in principle can simplify the derivation of conservation equations. We will see that Lagrangian interaction coefficients show a higher degree of symmetry than the Eulerian ones. While the algebraic expression for the Lagrangian and Eulerian interaction coefficient differ, we show that they are equal up to numerical precision if resonant condition is applied; they differ, however, for the case of non-resonance.

3.3.1. The Lagrangian equations of motion

The Lagrangian form of the non-hydrostatic Boussinesq equations as in Eq. (3.1) is given by

$$\partial_t{}^2\xi_1 - f\,\partial_t\xi_2 = -\frac{\partial J}{\partial(\partial\xi_1/\partial a_j)}\frac{\partial\hat{\pi}}{\partial a_j} \quad \text{(3.16a)} \qquad \partial_t{}^2\xi_2 + f\,\partial_t\xi_1 = -\frac{\partial J}{\partial(\partial\xi_2/\partial a_j)}\frac{\partial\hat{\pi}}{\partial a_j} \quad \text{(3.16b)}$$

$$\partial_t{}^2\xi_3 - \tilde{b}(a_3+\xi_3) = -\frac{\partial J}{\partial(\partial\xi_3/\partial a_j)}\frac{\partial\hat{\pi}}{\partial a_j} \quad \text{(3.16c)} \qquad J = 1 \quad \text{(3.16d)}$$

formulated for the displacement $\boldsymbol{\xi} = (\xi_1, \xi_2, \xi_3) = \boldsymbol{X} - \boldsymbol{a}$ of the actual parcel position $\boldsymbol{X} = (X_1, X_2, X_3)$ from its initial position $\boldsymbol{a} = (a_1, a_2, a_3)$, and the Lagrangian perturbation pressure $\hat{\pi}(\boldsymbol{a}, t)$. Here and in Section 3.3.2, 3.3.3 the sum convention for repeated indices is used. The partial time derivative is defined for fixed particle label $\boldsymbol{a}$, it is therefore material. The form of the gradient of the Lagrangian pressure $\hat{\pi}$ results from a complicated but straightforward transformation of the Eulerian pressure gradient $\boldsymbol{\nabla} p$, see e.g. Salmon (1998). Eqs. (3.16a, 3.16b) include the Coriolis force on the left-hand side. The buoyancy term in the Eq. (3.16c) is handled as follows. The full buoyancy b is conserved per particle, i.e. $b(\boldsymbol{X}(\boldsymbol{a}, t), t) = b(\boldsymbol{a})$. We define a background buoyancy $b_m(z)$, which is hydrostatically balanced with a mean pressure $p_m(z)$. A particle starting at the initial position $z = a_3$ then has the buoyancy $b_m(a_3)$, which is conserved. At later times, the particle is at the position $X_3 = a_3 + \xi_3$ where the environment has the buoyancy $b_m(a_3 + \xi_3)$. The buoyancy perturbation

is thus $\tilde{b}(a_3+\xi_3) = b_m(a_3) - b_m(a_3+\xi_3)$, and for small excursions $\tilde{b} = -N^2\xi_3$ with the (constant) Brunt-Väisälä frequency $N^2 = \partial_z b_m$.

Eq. (3.16d) is the statement of conservation of volume, $d^3X = d^3a$, using the Jacobian J for the transformation from the parcel's initial position $\boldsymbol{a}$ to its actual position $\boldsymbol{X}$. The Jacobian is given by

$$\begin{aligned} J(\boldsymbol{a},t) &= \frac{\partial(X_1,X_2,X_3)}{\partial(a_1,a_2,a_3)} \equiv \begin{vmatrix} \partial X_1/\partial a_1 & \partial X_1/\partial a_2 & \partial X_1/\partial a_3 \\ \partial X_2/\partial a_1 & \partial X_2/\partial a_2 & \partial X_2/\partial a_3 \\ \partial X_3/\partial a_1 & \partial X_3/\partial a_2 & \partial X_3/\partial a_3 \end{vmatrix} \\ &= \begin{vmatrix} \partial\xi_1/\partial a_1+1 & \partial\xi_1/\partial a_2 & \partial\xi_1/\partial a_3 \\ \partial\xi_2/\partial a_1 & \partial\xi_2/\partial a_2+1 & \partial\xi_2/\partial a_3 \\ \partial\xi_3/\partial a_1 & \partial\xi_3/\partial a_2 & \partial\xi_3/\partial a_3+1 \end{vmatrix} = 1 + \frac{\partial\xi_i}{\partial a_i} + \Delta_{ii} + \Delta \end{aligned} \tag{3.17}$$

and rewritten in terms of the displacement ξ_i using the Jacobian $\Delta = \partial(\xi_1,\xi_2,\xi_3)/\partial(a_1,a_2,a_3)$. Further, Δ_{ij} is the co-factor of $\partial\xi_i/\partial a_j$, i.e. the subdeterminant of Δ obtained by canceling row i and column j and multiplying with $(-1)^{i+j}$.

Note that the Lagrangian momentum equation in Eq. (3.16) has linear acceleration terms, while these are non-linear in the Euler form Eq. (3.1). The non-linearity in the Lagrangian form shows up in the pressure gradient, which is linear in the Euler form. Furthermore, the non-linearity in the Euler form is quadratic, while in the Lagrangian form non-linearities up to third order are found. The Lagrangian and Eulerian equations are completely equivalent, they can be transformed into the respective other form. In contrast to various Hamiltonian treatments with isopycnal coordinates (e.g. Lvov and Tabak, 2001; Dematteis et al., 2024; Labarre et al., 2024), the Lagrangian equations Eq. (3.16) used here are non-hydrostatic and include rotation.

3.3.2. The Lagrangian density functional

According to the Lagrangian theory for continuous systems (see e.g. Goldstein, 1972), the Lagrangian equations of motion Eq. (3.16) can be derived from the Lagrangian density L using the Euler-Lagrange equations. The theory is based on Hamilton's principle: A parcel with label $\boldsymbol{a}$ will travel in the time interval t_0 to t_1 such that its action functional $\int_{t_0}^{t_1}\int L\, d^3a\, dt$ becomes stationary under all variations of the arguments of the functional L within that time interval and spatial domain. The Lagrangian density L is a functional of the field variables and the coordinates. Olbers (1974, 1976) found L to be

$$L\left(\xi_j, \partial_t\xi_j, \frac{\partial\xi_j}{\partial a_i}, \hat{\pi}\right) = \frac{1}{2}\left(\partial_t\xi_j\partial_t\xi_j + f(\xi_1\partial_t\xi_2 - \xi_2\partial_t\xi_1) - N^2\xi_3^2\right) + \hat{\pi}(J-1) \tag{3.18}$$

The continuity condition $J = 1$ is implemented via a side constraint with pressure as Lagrangian multiplier. Further we note the terms of kinetic and potential energies and also the Coriolis term. For arbitrary variations of the arguments of L, the Euler-Lagrange equations follow as

$$\partial_t\frac{\partial L}{\partial(\partial_t\xi_i)} + \frac{\partial}{\partial a_j}\frac{\partial L}{\partial(\partial\xi_i/\partial a_j)} - \frac{\partial L}{\partial\xi_i} = 0 \quad i = 1,\cdots,3 \tag{3.19}$$

from which the Lagrangian equations of motion Eq. (3.16) can be derived. Variation with respect to ξ_j yields the equations of motion, while variation with respect to the pressure variable $\hat{\pi}$ recovers $J = 1$. The buoyancy equation does not need derivation, since buoyancy is conserved, as explained above.

3.3.3. Lagrangian interaction coefficients

To derive interaction coefficients for the Eulerian case it is sufficient to use the representation of the variables by the linear eigenvector form, as in Sec. (3.2). This procedure is owed to the linearity of the continuity equation in Eq. (3.1). The Lagrangian condition of incompressibility $J = 1$, however, is non-linear and linear eigenvectors are not sufficient to satisfy this constraint.

We satisfy $J = 1$ a priori by expanding the displacement into a power series of Lagrangian amplitudes $\ell_0^{s_0} = \ell^{s_0}(\boldsymbol{K}_0)$ according to

$$\begin{aligned}\boldsymbol{\xi}(\boldsymbol{a},t) = &\sum_{s_0}\int d\boldsymbol{K}_0 \ell_0^{s_0}\boldsymbol{Z}_0^{s_0}\exp\left(i(\boldsymbol{K}_0\cdot\boldsymbol{a}-\omega_0^{s_0}t)\right)\\ &+\sum_{s_1,s_2}\iint d\boldsymbol{K}_1 d\boldsymbol{K}_2 \ell_1^{s_1}\ell_2^{s_2}\boldsymbol{Z}_{1\ 2}^{s_1\,s_2}\exp\left(i(\boldsymbol{K}_1+\boldsymbol{K}_2)\cdot\boldsymbol{a}-i(\omega_1^{s_1}+\omega_2^{s_2})t\right)+O(\ell^3)\end{aligned} \tag{3.20}$$

where the polarization vector for the linear system is $\boldsymbol{Z}_0^{s_0} = \boldsymbol{Z}^{s_0}(\boldsymbol{K}_0)$, see Appendix A for a detailed derivation. Note that the sums over s_n run only over the internal wave indices $s_n = \pm$. To derive the expansion coefficients $\boldsymbol{Z}_{1\ 2}^{s_1\,s_2} = \boldsymbol{Z}^{s_1 s_2}(\boldsymbol{K}_1,\boldsymbol{K}_2)$ in Eq. (3.20), we insert the expansion Eq. (3.20) into the constraint $J-1 = \partial\xi_i/\partial a_i + \Delta_{ii} + \Delta = 0$ (see last equation in Eq. (3.17)), group the terms with respect to the orders of amplitudes and satisfy the constraint at each order. The first order terms, where only $\partial\xi_i/\partial a_i$ contributes, yield $\boldsymbol{K}\cdot\boldsymbol{Z}^s(\boldsymbol{K}) = 0$ which is satisfied by the linear polarization vector Eq. (54). The second order terms, where $\partial\xi_i/\partial a_i + \Delta_{ii}$ contribute, yield

$$\boldsymbol{Z}_{1\ 2}^{s_1\,s_2} \;=\; \frac{i}{2}\frac{(\boldsymbol{K}_1+\boldsymbol{K}_2)}{(\boldsymbol{K}_1+\boldsymbol{K}_2)^2}(\boldsymbol{K}_1\cdot\boldsymbol{Z}_2^{s_2})(\boldsymbol{K}_2\cdot\boldsymbol{Z}_1^{s_1}) \tag{3.21}$$

Third or higher order terms, where all terms in the constraint contribute, are not needed as we restrict ourselves to triad interactions.

We now substitute the expansion Eq. (3.20) with Eq. (3.21) into the Lagrangian Eq. (3.18), and integrate over the $\boldsymbol{a}$-space, indicated by an overbar, to find

$$\bar{L} = \bar{L}_2 + \bar{L}_{int} \tag{3.22}$$

with the quadratic part

$$\bar{L}_2 = \frac{1}{2}\sum_{s_0=\pm}\int d\boldsymbol{K}_0 \frac{1}{(\omega_0^{s_0})^2}\left(\left(1+\frac{f^2}{(\omega_0^{s_0})^2}\frac{m_0^2}{K_0^2}\right)\partial_t\ell_0^{s_0}\partial_t\ell_0^{s_0*} - i\omega_0^{s_0}\left(\ell_0^{s_0}\partial_t\ell_0^{s_0*}-\ell_0^{s_0*}\partial_t\ell_0^{s_0}\right)\right) \tag{3.23}$$

and the interaction part

$$\begin{aligned}\bar{L}_{int} = \sum_{s_0,s_1,s_2}\iiint d\boldsymbol{K}_0 d\boldsymbol{K}_1 d\boldsymbol{K}_2 \Big(&\ell_0^{s_0}\ell_1^{s_1}\ell_2^{s_2}\mathcal{A}_{\boldsymbol{K}_0\boldsymbol{K}_1\boldsymbol{K}_2}^{s_0\ s_1\ s_2} + (\partial_t\ell_0^{s_0})\ell_1^{s_1}\ell_2^{s_2}\mathcal{B}_{\boldsymbol{K}_0\boldsymbol{K}_1\boldsymbol{K}_2}^{s_0\ s_1\ s_2}\\ &+(\partial_t\ell_0^{s_0})(\partial_t\ell_1^{s_1})\ell_2^{s_2}\mathcal{M}_{\boldsymbol{K}_0\boldsymbol{K}_1\boldsymbol{K}_2}^{s_0\ s_1\ s_2}\Big)\delta(\boldsymbol{K}_0+\boldsymbol{K}_1+\boldsymbol{K}_2)\exp\left(-i(\omega_0^{s_0}+\omega_1^{s_1}+\omega_2^{s_2})t\right)+O(\ell^4)\end{aligned} \tag{3.24}$$

In the Lagrangian coupling coefficients $\mathcal{A}^{s_0\ s_1\ s_2}_{\boldsymbol{K}_0\boldsymbol{K}_1\boldsymbol{K}_2}$, $\mathcal{B}^{s_0\ s_1\ s_2}_{\boldsymbol{K}_0\boldsymbol{K}_1\boldsymbol{K}_2}$ and $\mathcal{M}^{s_0\ s_1\ s_2}_{\boldsymbol{K}_0\boldsymbol{K}_1\boldsymbol{K}_2}$ we have collected all contributions from respective products of the fields ξ_i. Note that the constraint $\hat{\pi}(J-1)$ now has no contribution. The specific algebraic form of the coefficients is derived in Appendix B. The sum in $\bar{L}_{int}$ is only over wavevectors which satisfy $\boldsymbol{K}_0+\boldsymbol{K}_1+\boldsymbol{K}_2=0$ since all other terms vanish in the spatial integration. The equations of motion for the amplitudes follow from the Lagrange equations

$$\frac{d}{dt}\frac{\partial\bar{L}}{\partial(\partial_t\ell_0^*)}-\frac{\partial\bar{L}}{\partial\ell_0^*}=0. \tag{3.25}$$

So far no approximations have been made, except that some higher order terms of the amplitude expansion have not been written out. However, the system simplifies[2] significantly, if we assume that the amplitudes $\ell(t)$ vary only slowly in time compared to the rapid oscillation of the phase factor $e^{-i\omega t}$. Formally, we demand $|\partial_t\ell/(\omega\ell)|=\epsilon\ll 1$ but, to be consistent, the effect of the interactions on the amplitude evolution, implied by $\bar{L}_{int}$, must be small, and hence the requirement of slowly varying amplitudes demand essentially small amplitudes, $\ell=O(\epsilon)$. This is in agreement with the weak-interaction theory of wave-turbulence, which can also be though of a two timescale approximation (as described in Davidson, 1967). We thus neglect terms in the equations of motion accordingly so that Eq. (3.25) leads to

$$\partial_t\ell_0^{s_0}=-3i\omega_0^{s_0}\sum_{s_1,s_2}\iint d\boldsymbol{K}_1d\boldsymbol{K}_2\ell_1^{s_1}\ell_2^{s_2}\mathcal{L}^{-s_0\ s_1\ s_2}_{-\boldsymbol{K}_0\boldsymbol{K}_1\boldsymbol{K}_2}\delta(\boldsymbol{K}_0-\boldsymbol{K}_1-\boldsymbol{K}_2)\exp\left(i(\omega_0^{s_0}-\omega_1^{s_1}-\omega_2^{s_2})t\right)+O(\ell^3) \tag{3.26}$$

with

$$\mathcal{L}^{-s_0\ s_1\ s_2}_{-\boldsymbol{K}_0\boldsymbol{K}_1\boldsymbol{K}_2}=-\frac{1}{2}\mathcal{A}^{-s_0\ s_1\ s_2}_{-\boldsymbol{K}_0\boldsymbol{K}_1\boldsymbol{K}_2}+\frac{i}{6}\left(\omega_0^{s_0}-\omega_1^{s_1}-\omega_2^{s_2}\right)\mathcal{B}^{-s_0\ s_1\ s_2}_{-\boldsymbol{K}_0\boldsymbol{K}_1\boldsymbol{K}_2}. \tag{3.27}$$

The $\mathcal{M}^{-s_0\ s_1\ s_2}_{-\boldsymbol{K}_0\boldsymbol{K}_1\boldsymbol{K}_2}$ coefficient are of higher order in $|\partial_t\ell/\omega\ell|$ and drop out in the perturbation expansion. Note that resonant triad coupling involves $\mathcal{A}^{-s_0\ s_1\ s_2}_{-\boldsymbol{K}_0\boldsymbol{K}_1\boldsymbol{K}_2}$ alone. This coefficient is symmetric in *all* three index pairs. This is a major advantage of the derivation from a Lagrangian, where terms other than symmetric ones drop out of the sum. The coefficient $\mathcal{B}^{-s_0\ s_1\ s_2}_{-\boldsymbol{K}_0\boldsymbol{K}_1\boldsymbol{K}_2}$ shares this symmetry property only for the last two index pairs, and hence this applies also to $\mathcal{L}^{-s_0\ s_1\ s_2}_{-\boldsymbol{K}_0\boldsymbol{K}_1\boldsymbol{K}_2}$. We show, however, in Appendix B, where the algebraic form of $\mathcal{L}^{-s_0\ s_1\ s_2}_{-\boldsymbol{K}_0\boldsymbol{K}_1\boldsymbol{K}_2}$ is derived, that $\mathcal{L}^{-s_0\ s_1\ s_2}_{-\boldsymbol{K}_0\boldsymbol{K}_1\boldsymbol{K}_2}$ is symmetric in all three indices because the term $\mathcal{B}^{-s_0\ s_1\ s_2}_{-\boldsymbol{K}_0\boldsymbol{K}_1\boldsymbol{K}_2}$ cancels out. A further property is

$$\mathcal{L}^{-s_0\ -s_1\ -s_2}_{-\boldsymbol{K}_0-\boldsymbol{K}_1-\boldsymbol{K}_2}=\left(\mathcal{L}^{s_0\ s_1\ s_2}_{\boldsymbol{K}_0\boldsymbol{K}_1\boldsymbol{K}_2}\right)^* \tag{3.28}$$

which is the reality condition for the Lagrangian $\bar{L}_{int}$. Eq. (3.26) is in the canonical form of the amplitude evolution equation and looks identical to the Eulerian amplitude balance Eq. (3.13). Note, however, that the nonlinearities in Eulerian and Lagrangian systems take different forms, and thus the respective amplitudes have different physical interpretations. In

[2]The Lagrangian equations for the amplitude evolution are second order in time. The assumption of slow temporal evolution leads to first order equations.

the next section we show that only under resonant conditions the Eulerian and Lagrangian interaction coefficients and thus of the corresponding kinetic equations are equal, whereas non-resonant Euler and Lagrangian interaction coefficients and kinetic equations differ.

3.4. Energy conservation and the fundamental relation

We use the notation e^s for the wave amplitudes in the Eulerian system Eq. (3.13) and ℓ^s in the Lagrangian system Eq. (3.26), both defined for $s = \pm$. The form of the equations of motion for these systems, either Eq. (3.13) or Eq. (3.26), is identical, but the Eulerian and Lagrangian amplitudes and interaction coefficients generally differ. The aim of this section is to discuss the relation between Eulerian and Lagrangian amplitudes, energies, and interaction coefficients.

3.4.1. The fundamental relation

From the equation of motion for the Eulerian amplitude Eq. (3.13), we calculate the rate of change for the wave energy spectrum $e_0 e_0^*$ as

$$\partial_t (e_0^{s_0} e_0^{s_0 *}) = -i \sum_{s_1,s_2} \iint d\boldsymbol{K}_1 d\boldsymbol{K}_2 e_1^{s_1} e_2^{s_2} e_0^{s_0 *} C^{-s_0\ s_1\ s_2}_{-\boldsymbol{K}_0 \boldsymbol{K}_1 \boldsymbol{K}_2} \delta(\boldsymbol{K}_0 - \boldsymbol{K}_1 - \boldsymbol{K}_2) \exp\left(i(\omega_0^{s_0} - \omega_1^{s_1} - \omega_2^{s_2})t\right) \tag{3.29}$$

excluding the cases with $s_{1,2} = 0$. Summation of the spectrum over all wavenumbers leads to the conservation of total energy $\partial_t \sum_{s_0} \int d\boldsymbol{K}_0 e_0^{s_0} e_0^{s_0 *} = 0$. Note that this is not a property of amplitudes but is owed to the structure of the interaction coefficient and the underlying Boussinesq equations, as we show in the following.

A deeper insight into the structure of the Eulerian interaction coefficient $C^{s_0\ s_1\ s_2}_{\boldsymbol{K}_0 \boldsymbol{K}_1 \boldsymbol{K}_2}$ is gained by considering an interacting triad at $(s_0, \boldsymbol{K}_0)$, $(s_1, \boldsymbol{K}_1)$, and $(s_2, \boldsymbol{K}_2)$ in isolation. From Eq. (3.29), we then obtain

$$\begin{aligned}
\partial_t (e_0^{s_0} e_0^{s_0 *}) &= -i e_0^{s_0 *} e_1^{s_1} e_2^{s_2} C^{-s_0\ s_1\ s_2}_{-\boldsymbol{K}_0 \boldsymbol{K}_1 \boldsymbol{K}_2} \delta(\boldsymbol{K}_0 - \boldsymbol{K}_1 - \boldsymbol{K}_2) \exp\left(i(\omega_0^{s_0} - \omega_1^{s_1} - \omega_2^{s_2})t\right) + c.c. \\
\partial_t (e_1^{s_1} e_1^{s_1 *}) &= -i e_1^{s_1 *} e_0^{s_0} e_2^{s_2 *} C^{-s_1\ s_0\ -s_2}_{-\boldsymbol{K}_1 \boldsymbol{K}_0 -\boldsymbol{K}_2} \delta(\boldsymbol{K}_1 - \boldsymbol{K}_0 + \boldsymbol{K}_2) \exp\left(i(\omega_1^{s_1} - \omega_0^{s_0} + \omega_2^{s_2})t\right) + c.c. \\
\partial_t (e_2^{s_2} e_2^{s_2 *}) &= -i e_2^{s_2 *} e_0^{s_0} e_1^{s_1 *} C^{-s_2\ s_0\ -s_1}_{-\boldsymbol{K}_2 \boldsymbol{K}_0 -\boldsymbol{K}_1} \delta(\boldsymbol{K}_2 - \boldsymbol{K}_0 + \boldsymbol{K}_1) \exp\left(i(\omega_2^{s_2} - \omega_0^{s_0} + \omega_1^{s_1})t\right) + c.c.
\end{aligned} \tag{3.30}$$

Using the property Eq. (3.28) of the interaction coefficient and summing Eq. (3.30) yields the energy balance of the triad

$$\begin{aligned}
&\partial_t \left(e_0^{s_0} e_0^{s_0 *} + e_1^{s_1} e_1^{s_1 *} + e_2^{s_2} e_2^{s_2 *}\right) = \\
&- i e_0^{s_0 *} e_1^{s_1} e_2^{s_2} \left(C^{-s_0\ s_1\ s_2}_{-\boldsymbol{K}_0 \boldsymbol{K}_1 \boldsymbol{K}_2} + C^{-s_1\ s_0\ -s_2\ *}_{-\boldsymbol{K}_1 \boldsymbol{K}_0 -\boldsymbol{K}_2} + C^{-s_2\ s_0\ -s_1\ *}_{-\boldsymbol{K}_2 \boldsymbol{K}_0 -\boldsymbol{K}_1}\right) \delta(\boldsymbol{K}_0 - \boldsymbol{K}_1 - \boldsymbol{K}_2) \exp\left(i(\omega_0^{s_0} - \omega_1^{s_1} - \omega_2^{s_2})t\right) \\
&+ c.c.
\end{aligned} \tag{3.31}$$

Since the triad amplitudes are arbitrary the conservation of energy for the triad requires

$$\begin{aligned}
&C^{-s_0\ s_1\ s_2}_{-\boldsymbol{K}_0 \boldsymbol{K}_1 \boldsymbol{K}_2} + C^{-s_1\ s_0\ -s_2\ *}_{-\boldsymbol{K}_1 \boldsymbol{K}_0 -\boldsymbol{K}_2} + C^{-s_2\ s_0\ -s_1\ *}_{-\boldsymbol{K}_2 \boldsymbol{K}_0 -\boldsymbol{K}_1} = 0 \\
\text{or} \qquad &C^{s_0\ s_1\ s_2}_{\boldsymbol{K}_0 \boldsymbol{K}_1 \boldsymbol{K}_2} + C^{s_1\ s_0\ s_2}_{\boldsymbol{K}_1 \boldsymbol{K}_0 \boldsymbol{K}_2} + C^{s_2\ s_0\ s_1}_{\boldsymbol{K}_2 \boldsymbol{K}_0 \boldsymbol{K}_1} = 0.
\end{aligned} \tag{3.32}$$

The interaction coefficients must satisfy this fundamental relation for any triad combination of waves. It is a fairly complex relation that could not be anticipated from the lengthy algebraic expressions of the interactions coefficient given in Sec. (3.2). There is extensive literature supporting the validity of the fundamental relation within a closed triad, inter alia Hasselmann (1962, 1963a,b); Kraichnan (1973); Remmel and Smith (2009).

The relation Eq. (3.32) is easily verified by numerical means for the Eulerian case, both for resonant and non-resonant triad interactions. Since all members of the triad are waves we put $C^{s_0\ s_1\ s_2}_{\boldsymbol{K}_0\boldsymbol{K}_1\boldsymbol{K}_2} = 3\omega_0\mathcal{D}^{s_0\ s_1\ s_2}_{\boldsymbol{K}_0\boldsymbol{K}_1\boldsymbol{K}_2}$ (this allows comparison with the Lagrangian coefficient). In a resonant system one finds the equality $\mathcal{D}^{s_0\ s_1\ s_2}_{\boldsymbol{K}_0\boldsymbol{K}_1\boldsymbol{K}_2} = \mathcal{D}^{s_1\ s_0\ s_2}_{\boldsymbol{K}_1\boldsymbol{K}_0\boldsymbol{K}_2} = \mathcal{D}^{s_2\ s_0\ s_1}_{\boldsymbol{K}_2\boldsymbol{K}_0\boldsymbol{K}_1}$ in the numerical checks. In the Lagrangian framework and in case of resonance the validity of $\omega_0\mathcal{L}^{s_0\ s_1\ s_2}_{\boldsymbol{K}_0\boldsymbol{K}_1\boldsymbol{K}_2} + \omega_1\mathcal{L}^{s_1\ s_0\ s_2}_{\boldsymbol{K}_1\boldsymbol{K}_0\boldsymbol{K}_2} + \omega_2\mathcal{L}^{s_2\ s_0\ s_1}_{\boldsymbol{K}_2\boldsymbol{K}_0\boldsymbol{K}_1} = 0$ is trivial because all three $\mathcal{L}$ coefficients are equal. Moreover, it is found that $\mathcal{L}^{s_0\ s_1\ s_2}_{\boldsymbol{K}_0\boldsymbol{K}_1\boldsymbol{K}_2} = \mathcal{D}^{s_0\ s_1\ s_2}_{\boldsymbol{K}_0\boldsymbol{K}_1\boldsymbol{K}_2}$. An analytical proof of these properties follows in the next section. However, while the Lagrangian non-resonant interaction coefficients are all equal, the sum of the frequencies is not zero, and thus the fundamental relation is not satisfied for Lagrangian non-resonant interactions.

3.4.2. Relations between the coupling coefficients

The relation between the Eulerian and Lagrangian amplitudes is nonlinear and arises from the equality of Eulerian and Lagrangian velocity variables ($\boldsymbol{u}^E$ and $\boldsymbol{u}^L$ respectively) at the same position $\boldsymbol{X}$ and time t, such that $\boldsymbol{u}^E(\boldsymbol{X},t) = \boldsymbol{u}^L(\boldsymbol{a},t) = \partial_t\boldsymbol{\xi}(\boldsymbol{a},t)$. A power series of the form

$$e_0^{s_0} = \ell_0^{s_0} + \sum_{s_1,s_2}\iint d\boldsymbol{K}_1 d\boldsymbol{K}_2 \ell_1^{s_1}\ell_2^{s_2}\mathcal{T}^{-s_0\ s_1\ s_2}_{-\boldsymbol{K}_0\boldsymbol{K}_1\boldsymbol{K}_2}\delta(\boldsymbol{K}_0-\boldsymbol{K}_1-\boldsymbol{K}_2)\exp\left(i(\omega_0^{s_0}-\omega_1^{s_1}-\omega_2^{s_2})t\right) + O(\ell^3) \tag{3.33}$$

is a reasonable assumption and will be confirmed later. We assume that the coefficient $\mathcal{T}^{-s_0\ s_1\ s_2}_{-\boldsymbol{K}_0\boldsymbol{K}_1\boldsymbol{K}_2}$ has been symmetrized in the last two indices on account of the summation with symmetric amplitude factor. A quadratic expansion as Eq. (3.33) is sufficient for our purpose and the following equations neglect terms of third order and higher in the amplitudes. The coefficient $\mathcal{T}^{-s_0\ s_1\ s_2}_{-\boldsymbol{K}_0\boldsymbol{K}_1\boldsymbol{K}_2}$ will be determined.

Eq. (3.33) implies that the Eulerian and Lagrangian interaction coefficients for triad interactions are related. To show this we use the equations for the evolution of the amplitudes, given for the Eulerian amplitude by Eq. (3.13) but with the symmetric interaction coefficient $C^{-s_0\ s_1\ s_2}_{-\boldsymbol{K}_0\boldsymbol{K}_1\boldsymbol{K}_2}$ and for the Lagrangian amplitude by Eq. (3.26).

We take the difference of the two equations Eqs. (3.13, 3.26) and use Eq. (3.33) to find

$$
\begin{aligned}
&\partial_t \ell_0^{s_0} - \partial_t e_0^{s_0} \\
&= -i \sum_{s_1,s_2} \iint d\boldsymbol{K}_1 d\boldsymbol{K}_2 \left(3\omega_0^{s_0} \ell_1^{s_1} \ell_2^{s_2} \mathcal{L}^{-s_0\ s_1\ s_2}_{-\boldsymbol{K}_0 \boldsymbol{K}_1 \boldsymbol{K}_2} - e_1^{s_1} e_2^{s_2} C^{-s_0\ s_1\ s_2}_{-\boldsymbol{K}_0 \boldsymbol{K}_1 \boldsymbol{K}_2} \right) \delta(\boldsymbol{K}_0 - \boldsymbol{K}_1 - \boldsymbol{K}_2) \exp\left(i(\omega_0^{s_0} - \omega_1^{s_1} - \omega_2^{s_2})t\right) \\
&= \sum_{s_1,s_2} \iint d\boldsymbol{K}_1 d\boldsymbol{K}_2 \left(\partial_t \ell_1^{s_1} \ell_2^{s_2} + \ell_1^{s_1} \partial_t \ell_2^{s_2} \right) \mathcal{T}^{-s_0\ s_1\ s_2}_{-\boldsymbol{K}_0 \boldsymbol{K}_1 \boldsymbol{K}_2} \delta(\boldsymbol{K}_0 - \boldsymbol{K}_1 - \boldsymbol{K}_2) \exp\left(i(\omega_0^{s_0} - \omega_1^{s_1} - \omega_2^{s_2})t\right) \\
&\quad - \sum_{s_1,s_2} \iint d\boldsymbol{K}_1 d\boldsymbol{K}_2 \left(i(\omega_0^{s_0} - \omega_1^{s_1} - \omega_2^{s_2}) \ell_1^{s_1} \ell_2^{s_2} \right) \mathcal{T}^{-s_0\ s_1\ s_2}_{-\boldsymbol{K}_0 \boldsymbol{K}_1 \boldsymbol{K}_2} \delta(\boldsymbol{K}_0 - \boldsymbol{K}_1 - \boldsymbol{K}_2) \exp\left(i(\omega_0^{s_0} - \omega_1^{s_1} - \omega_2^{s_2})t\right) \\
&= -i \sum_{s_1,s_2} \iint d\boldsymbol{K}_1 d\boldsymbol{K}_2 \left((\omega_0^{s_0} - \omega_1^{s_1} - \omega_2^{s_2}) \ell_1^{s_1} \ell_2^{s_2} \right) \mathcal{T}^{-s_0\ s_1\ s_2}_{-\boldsymbol{K}_0 \boldsymbol{K}_1 \boldsymbol{K}_2} \delta(\boldsymbol{K}_0 - \boldsymbol{K}_1 - \boldsymbol{K}_2) \exp\left(i(\omega_0^{s_0} - \omega_1^{s_1} - \omega_2^{s_2})t\right) \\
&\quad + O(\ell^3).
\end{aligned}
$$

Now replace the first term on left-hand side by use of Eq. (3.33),

$$
\begin{aligned}
&-i \sum_{s_1,s_2} \iint d\boldsymbol{K}_1 d\boldsymbol{K}_2 \left(3\omega_0^{s_0} \ell_1^{s_1} \ell_2^{s_2} \mathcal{L}^{-s_0\ s_1\ s_2}_{-\boldsymbol{K}_0 \boldsymbol{K}_1 \boldsymbol{K}_2} - e_1^{s_1} e_2^{s_2} C^{-s_0\ s_1\ s_2}_{-\boldsymbol{K}_0 \boldsymbol{K}_1 \boldsymbol{K}_2} \right) \delta(\boldsymbol{K}_0 - \boldsymbol{K}_1 - \boldsymbol{K}_2) \exp\left(i(\omega_0^{s_0} - \omega_1^{s_1} - \omega_2^{s_2})t\right) \\
&= -i \sum_{s_1,s_2} \iint d\boldsymbol{K}_1 d\boldsymbol{K}_2 \left((\omega_0^{s_0} - \omega_1^{s_1} - \omega_2^{s_2}) \ell_1^{s_1} \ell_2^{s_2} \right) \mathcal{T}^{-s_0\ s_1\ s_2}_{-\boldsymbol{K}_0 \boldsymbol{K}_1 \boldsymbol{K}_2} \delta(\boldsymbol{K}_0 - \boldsymbol{K}_1 - \boldsymbol{K}_2) \exp\left(i(\omega_0^{s_0} - \omega_1^{s_1} - \omega_2^{s_2})t\right)
\end{aligned}
\tag{3.34}
$$

and replace e according to Eq. (3.33) by ℓ and higher order ℓ-terms which are then neglected. This yields

$$
C^{-s_0\ s_1\ s_2}_{-\boldsymbol{K}_0 \boldsymbol{K}_1 \boldsymbol{K}_2} = 3\omega_0^{s_0} \mathcal{D}^{-s_0\ s_1\ s_2}_{-\boldsymbol{K}_0 \boldsymbol{K}_1 \boldsymbol{K}_2} = 3\omega_0^{s_0} \mathcal{L}^{-s_0\ s_1\ s_2}_{-\boldsymbol{K}_0 \boldsymbol{K}_1 \boldsymbol{K}_2} - (\omega_0^{s_0} - \omega_1^{s_1} - \omega_2^{s_2}) \mathcal{T}^{-s_0\ s_1\ s_2}_{-\boldsymbol{K}_0 \boldsymbol{K}_1 \boldsymbol{K}_2}. \tag{3.35}
$$

We obtain the important result that Eulerian and Lagrangian coefficients for triad interactions are identical for *resonant* conditions where $\omega_1^{s_1} + \omega_2^{s_2} - \omega_0^{s_0} = 0$, and symmetric in all three indices, such that

$$
\mathcal{D}^{-s_0\ s_1\ s_2}_{-\boldsymbol{K}_0 \boldsymbol{K}_1 \boldsymbol{K}_2} = \mathcal{L}^{-s_0\ s_1\ s_2}_{-\boldsymbol{K}_0 \boldsymbol{K}_1 \boldsymbol{K}_2}. \tag{3.36}
$$

On the other hand, we may utilize Eq. (3.35) for the general non-resonant case to compute the coefficient

$$
\mathcal{T}^{-s_0\ s_1\ s_2}_{-\boldsymbol{K}_0 \boldsymbol{K}_1 \boldsymbol{K}_2} = \frac{3\omega_0^{s_0}}{\omega_1^{s_1} + \omega_2^{s_2} - \omega_0^{s_0}} \left(\mathcal{D}^{-s_0\ s_1\ s_2}_{-\boldsymbol{K}_0 \boldsymbol{K}_1 \boldsymbol{K}_2} - \mathcal{L}^{-s_0\ s_1\ s_2}_{-\boldsymbol{K}_0 \boldsymbol{K}_1 \boldsymbol{K}_2} \right) \tag{3.37}
$$

because $\mathcal{D}^{-s_0\ s_1\ s_2}_{-\boldsymbol{K}_0 \boldsymbol{K}_1 \boldsymbol{K}_2}$ and $\mathcal{L}^{-s_0\ s_1\ s_2}_{-\boldsymbol{K}_0 \boldsymbol{K}_1 \boldsymbol{K}_2}$ are known algebraic expressions.

There is a further relationship between the $\mathcal{L}^{-s_0\ s_1\ s_2}_{-\boldsymbol{K}_0 \boldsymbol{K}_1 \boldsymbol{K}_2}$ and $\mathcal{T}^{-s_0\ s_1\ s_2}_{-\boldsymbol{K}_0 \boldsymbol{K}_1 \boldsymbol{K}_2}$ coefficients. Use of the fundamental relation Eq. (3.32) leads to

$$
\begin{aligned}
&3 \left(\omega_0^{s_0} \mathcal{L}^{s_0\ s_1\ s_2}_{\boldsymbol{K}_0 \boldsymbol{K}_1 \boldsymbol{K}_2} + \omega_1^{s_1} \mathcal{L}^{s_1\ s_0\ s_2}_{\boldsymbol{K}_1 \boldsymbol{K}_0 \boldsymbol{K}_2} + \omega_2^{s_2} \mathcal{L}^{s_2\ s_0\ s_1}_{\boldsymbol{K}_2 \boldsymbol{K}_0 \boldsymbol{K}_1} \right) \\
&= (\omega_1^{s_1} + \omega_2^{s_2} + \omega_0^{s_0}) \left(\mathcal{T}^{s_0\ s_1\ s_2}_{\boldsymbol{K}_0 \boldsymbol{K}_1 \boldsymbol{K}_2} + \mathcal{T}^{s_1\ s_0\ s_2}_{\boldsymbol{K}_1 \boldsymbol{K}_0 \boldsymbol{K}_2} + \mathcal{T}^{s_2\ s_0\ s_1}_{\boldsymbol{K}_2 \boldsymbol{K}_0 \boldsymbol{K}_1} \right).
\end{aligned}
\tag{3.38}
$$

Because the Lagrangian coefficients are totally symmetric and all $\mathcal{L}$ coefficients are identical this implies

$$3\mathcal{L}^{s_0\ s_1\ s_2}_{\boldsymbol{K}_0\boldsymbol{K}_1\boldsymbol{K}_2} = \mathcal{T}^{s_0\ s_1\ s_2}_{\boldsymbol{K}_0\boldsymbol{K}_1\boldsymbol{K}_2} + \mathcal{T}^{s_1\ s_0\ s_2}_{\boldsymbol{K}_1\boldsymbol{K}_0\boldsymbol{K}_2} + \mathcal{T}^{s_2\ s_0\ s_1}_{\boldsymbol{K}_2\boldsymbol{K}_0\boldsymbol{K}_1}. \tag{3.39}$$

Hence $\mathcal{L}^{s_0\ s_1\ s_2}_{\boldsymbol{K}_0\boldsymbol{K}_1\boldsymbol{K}_2}$ equals the totally symmetric part of $\mathcal{T}^{s_0\ s_1\ s_2}_{\boldsymbol{K}_0\boldsymbol{K}_1\boldsymbol{K}_2}$.

3.4.3. Eulerian and Lagrangian energies

The Eulerian energy is strictly quadratic in the Boussinesq variables $\boldsymbol{u}, w$ and b and also in the wave amplitudes e^s. The total Eulerian energy E^E is

$$E^E = \int d^3X \frac{1}{2}\left(|\boldsymbol{u}|^2 + w^2 + b^2/N^2\right) = \sum_{s_0=\pm}\int d\boldsymbol{K}_0 e_0^{s_0} e_0^{s_0*} \tag{3.40}$$

where $e^s e^{s*}$ is the Eulerian energy spectrum. The reason for the quadratic appearance of the variables in energy in both physical space and Fourier space is found in the linear representation of the Boussinesq fields by eigenvectors of the linear system, given in Sec. (3.2).

The total Lagrangian energy E^L is a sum of quadratic terms of the displacements,

$$E^L = \int d^3a \frac{1}{2}\left((\partial_t \xi_j)\partial_t \xi_j + N^2\xi_3^2\right). \tag{3.41}$$

Since they refer to the same position in physical space, Eulerian and Lagrangian variables are identical. Thus, the energies must also be the same, $E^E = E^L = E$. But the Lagrangian displacement is not represented by a linear eigenvector, but instead by a power series of the Lagrangian wave amplitudes, see Eq. (3.20).

Using Eq. (3.33) it becomes evident that the Eulerian energy $e^s e^{s*}$ is not equal to the Lagrangian expression $\ell^s \ell^{s*}$, but contains higher order terms in the ℓ-amplitudes,

$$\begin{aligned} e_0^{s_0} e_0^{s_0*} &= \ell_0^{s_0}\ell_0^{s_0*} \\ &\quad + 2\Re\sum_{s_1,s_2}\iint d\boldsymbol{K}_1 d\boldsymbol{K}_2 \ell_0^{s_0}\ell_1^{s_1}\ell_2^{s_2}\mathcal{T}^{-s_0\ s_1\ s_2}_{-\boldsymbol{K}_0\boldsymbol{K}_1\boldsymbol{K}_2}\delta(\boldsymbol{K}_0-\boldsymbol{K}_1-\boldsymbol{K}_2)\exp\left(i(\omega_0^{s_0}-\omega_1^{s_1}-\omega_2^{s_2})t\right) \\ &\quad + O(\ell^4). \end{aligned} \tag{3.42}$$

Integrating over all wavenumbers and making use of the symmetrization of $\mathcal{T}^{-s_0\ s_1\ s_2}_{-\boldsymbol{K}_0\boldsymbol{K}_1\boldsymbol{K}_2}$ in all three indices in Eq. (3.39), we obtain the equality between Eulerian and Lagrangian total energy

$$\begin{aligned} E^E &= E^L \\ &= \sum_{s_0=\pm}\int d\boldsymbol{K}_0 \ell_0^{s_0}\ell_0^{s_0*} \\ &\quad + 2\Re\sum_{s_0,s_1,s_2}\iiint d\boldsymbol{K}_0 d\boldsymbol{K}_1 d\boldsymbol{K}_2 \ell_0^{s_0}\ell_1^{s_1}\ell_2^{s_2}\mathcal{L}^{-s_0\ s_1\ s_2}_{-\boldsymbol{K}_0\boldsymbol{K}_1\boldsymbol{K}_2}\delta(\boldsymbol{K}_0-\boldsymbol{K}_1-\boldsymbol{K}_2)\exp\left(i(\omega_0^{s_0}-\omega_1^{s_1}-\omega_2^{s_2})t\right) \\ &\quad + O(\ell^4). \end{aligned} \tag{3.43}$$

The total energy of the Eulerian system is conserved, hence $\frac{D}{Dt}E^E = 0$ and thus also $\frac{D}{Dt}E^L = 0$. Evaluating for E^L yields

$$\frac{D}{Dt}E^L = \frac{D}{Dt}\left(\sum_{s_0=\pm}\int d\boldsymbol{K}_0 \ell_0^{s_0}\ell_0^{s_0*}\right) \tag{3.44}$$
$$+ 2\Re\sum_{s_0,s_1,s_2}\iiint d\boldsymbol{K}_0 d\boldsymbol{K}_1 d\boldsymbol{K}_2 i(\omega_0^{s_0} - \omega_1^{s_1} - \omega_2^{s_2})\ell_0^{s_0}\ell_1^{s_1}\ell_2^{s_2}\mathcal{L}^{-s_0\ s_1\ s_2}_{-\boldsymbol{K}_0\boldsymbol{K}_1\boldsymbol{K}_2}\delta(\boldsymbol{K}_0 - \boldsymbol{K}_1 - \boldsymbol{K}_2)\exp\left(i(\omega_0^{s_0} - \omega_1^{s_1} - \omega_2^{s_2})t\right)$$
$$+ O(\ell^4) = 0.$$

Note that only for the resonant case where $\omega_0^{s_0} - \omega_1^{s_1} - \omega_2^{s_2} = 0$, Eq. (3.44) reduces to the conservation of a quadratic term of the Lagrangian wave amplitudes, which is then correct to fourth order.

In summary, in the Eulerian framework the squares of the amplitude in both physical and Fourier space are exactly the energy (locally or integrated over the domain), while in the Lagrangian framework the Lagrangian energy is quadratic only in physical space but represented by an infinite series in terms of powers of the normal mode amplitudes. Eulerian and Lagrangian energy spectra differ thus by third and higher order terms of the amplitudes. Note that the fundamental relation is not valid for Lagrangian coefficients unless resonant conditions are considered such that the energy conservation reduces to the conservation of quadratic terms of Lagrangian amplitudes. We thus find the coefficients for triadic wave-wave interactions in the Eulerian and the Lagrangian framework to be equal under resonant conditions, but not under non-resonant conditions.

3.5. Kinetic equation

It is sufficient to derive the wave kinetic equation for the Eulerian case. The kinetic equation represents the evolution of energy for a weakly interacting random ensemble of waves. The essential point of the kinetic equation is that it is closed on the level of the energy spectrum, being the quadratic expression $E_0^{s_0} = \langle e_0^{s_0} e_0^{s_0*}\rangle$, where $e_0^{s_0} = e^{s_0}(\boldsymbol{K}_0)$ and the brackets denote the ensemble mean. More precisely, the rate of change of $E_0^{s_0}$ should be a functional of $E_0^{s_0}$ with no higher wave correlations involved. A number of approaches is known, among them the weak-interaction theory of (e.g. Hasselmann, 1966) or the more elaborate wave-turbulence framework (e.g. Nazarenko, 2011). We like to mention here also the cumulant scaling in the multiple timescale approach of Davidson (1967). All methods rely on a perturbation expansion of the amplitude such that $e = e^{(0)} + \epsilon e^{(1)}(t) + \epsilon^2 e^{(2)}(t) + (...)$ where $\epsilon << 1$ is a small parameter. Changes of the amplitudes by the nonlinear terms in the evolution equation are captured by the first and higher order terms, they should be small. Other assumptions concern the statistical properties of the wave ensemble. Following the Hasselmann route, the basic wave state, represented by the lowest order $e^{(0)}$, is assumed to have Gaussian statistics where all moments can be expressed by second order correlations, i.e. by the spectrum $E_0^{s_0}$. The Gaussian property is not demanded for the whole history of evolution of the wave field but only for a set of initial conditions which then, however, march through the evolution of the wave field.

Using the amplitude equation Eq. (3.13) we frame these interactions as one of the source terms in the radiative transfer equation as the evolution equation of the wave correlation,

i.e. in terms of the rate of change of the spectral energy by wave-wave, wave-vortex, and or vortex-vortex interactions like

$$\begin{aligned}\partial_t E_0^{s_0} =&\partial_t \langle e_0^{s_0} e_0^{s_0 *}\rangle = \langle \partial_t e_0^{s_0}\rangle e_0^{s_0 *} + e_0^{s_0}\langle \partial_t e_0^{s_0 *}\rangle \\ =& -i \sum_{s_1,s_2} \iint d\boldsymbol{K}_1 d\boldsymbol{K}_2 (\langle e_1^{s_1} e_2^{s_2} e_0^{s_0 *}\rangle C^{-s_0\ s_1\ s_2}_{-\boldsymbol{K}_0 \boldsymbol{K}_1 \boldsymbol{K}_2} \delta(\boldsymbol{K}_0 - \boldsymbol{K}_1 - \boldsymbol{K}_2) \exp(i(\omega_0^{s_0} - \omega_1^{s_1} - \omega_2^{s_2})t) \\ &+ \langle e_1^{s_1 *} e_2^{s_2 *} e_0^{s_0}\rangle (C^{-s_0\ s_1\ s_2}_{-\boldsymbol{K}_0 \boldsymbol{K}_1 \boldsymbol{K}_2})^* \delta(\boldsymbol{K}_0 - \boldsymbol{K}_1 - \boldsymbol{K}_2) \exp(-i(\omega_0^{s_0} - \omega_1^{s_1} - \omega_2^{s_2})t)). \end{aligned} \tag{3.45}$$

To lowest order the involved triple covariance $\langle e_1^{s_1} e_2^{s_2} e_0^{s_0 *}\rangle$ vanishes and higher orders of the amplitudes are demanded, such that triple covariances evolve with a first-order amplitude

$$\begin{aligned} &e_0^{s_0,(1)}(t) = \\ &-i \sum_{s_1,s_2} \iint d\boldsymbol{K}_1 d\boldsymbol{K}_2 e_1^{s_1,(0)} e_2^{s_2,(0)} C^{-s_0\ s_1\ s_2}_{-\boldsymbol{K}_0 \boldsymbol{K}_1 \boldsymbol{K}_2} \delta(\boldsymbol{K}_0 - \boldsymbol{K}_1 - \boldsymbol{K}_2) \int_0^t dt' \exp(i(\omega_0^{s_0} - \omega_1^{s_1} - \omega_2^{s_2})t'). \end{aligned} \tag{3.46}$$

By inserting Eq. (3.46) in Eq. (3.45) after the perturbation of amplitudes we express the first-order triple covariances in zero-order quadruple-covariances and break them by the Gaussian assumption in three products of zero-order covariances. The indices in the kinetic equation Eq. (3.47) apply to waves but also to vortical modes. It is assumed that they are initially uncorrelated and thus $\langle e^{\pm} e^{\pm} ... e^0 e^0 ...\rangle = \langle e^{\pm} e^{\pm} ...\rangle \langle e^0 e^0 ...\rangle$ with $\langle e^s\rangle = 0$. The kinetic equation results in the form

$$\begin{aligned}\partial_t E_0^{s_0} =& -4 \sum_{s_1,s_2} \iint d\boldsymbol{K}_1 d\boldsymbol{K}_2 C^{-s_0\ s_1\ s_2}_{-\boldsymbol{K}_0 \boldsymbol{K}_1 \boldsymbol{K}_2} (E_1 E_0 C^{-s_2\ -s_1\ s_0}_{-\boldsymbol{K}_2 - \boldsymbol{K}_1 \boldsymbol{K}_0} + E_0 E_2 C^{-s_1\ s_0\ -s_2}_{-\boldsymbol{K}_1 \boldsymbol{K}_0 - \boldsymbol{K}_2} \\ &- E_1 E_2 (C^{-s_0\ s_1\ s_2}_{-\boldsymbol{K}_0 \boldsymbol{K}_1 \boldsymbol{K}_2})^*) \delta(\boldsymbol{K}_0 - \boldsymbol{K}_1 - \boldsymbol{K}_2) \Delta(\omega_0^{s_0} - \omega_1^{s_1} - \omega_2^{s_2}, t) \\ &- 2 \sum_{s_2} \int d\boldsymbol{K}_2 E_2 E_0 C^{-s_0\ s_0\ s_1}_{-\boldsymbol{K}_0 \boldsymbol{K}_0 \boldsymbol{K}_1 = 0} C^{-s_1\ s_2\ -s_2}_{-\boldsymbol{K}_1 = 0 \boldsymbol{K}_2 - \boldsymbol{K}_2} \int \exp(i\omega_1^{s_1} t) dt \\ &- 2 \sum_{s_1} \int d\boldsymbol{K}_1 E_1 E_0 C^{-s_0\ s_0\ s_2}_{-\boldsymbol{K}_0 \boldsymbol{K}_0 \boldsymbol{K}_2 = 0} C^{-s_2\ s_1\ -s_1}_{-\boldsymbol{K}_2 = 0 \boldsymbol{K}_1 - \boldsymbol{K}_1} \int \exp(i\omega_2^{s_2} t) dt \\ &+ 2 \sum_{s_1,s_2} \iint d\boldsymbol{K}_1 d\boldsymbol{K}_2 E_1 E_2 C^{-s_0\ s_1\ s_1}_{-\boldsymbol{K}_0 \boldsymbol{K}_1 \boldsymbol{K}_1 = 0} (C^{-s_0\ s_2\ -s_2}_{-\boldsymbol{K}_0 = 0 \boldsymbol{K}_2 - \boldsymbol{K}_2})^* \int_0^t dt' \exp(-i\omega_0^{s_0} t') + c.c. \end{aligned} \tag{3.47}$$

with the time response function

$$\Delta(\Omega, t) = \exp(i\Omega t) \int_0^t \exp(-i\Omega t') dt' = \frac{1 - \exp(-i\Omega t)}{i\Omega}. \tag{3.48}$$

Note that the last three terms in Eq. (3.47) vanish as mixed barotropic-vertical variability is uncoupled from the system, see Sec. (3.2).

3.5.1. Resonance and non-resonance

The kinetic equation Eq. (3.47) conserves energy (but not action $A = E/\omega$) for resonant as well as for non-resonant interactions individually. More detailed, it can be shown that energy is conserved individually for wave-wave interactions, mixed wave-vortex interactions, and vortex-vortex interactions. For proving these statements, the fundamental relation is useful. In our computations, resonant ($\omega_0 = \omega_1 \pm \omega_2$) and non-resonant ($\omega_0 \neq \omega_1 \pm \omega_2$) interaction coefficients, derived from the Eulerian framework, satisfy the fundamental relation in Eq. (3.32) within numerical precision $O(10^{-16})$.

Note that the time response function in Eq. (3.48) has a regular behavior in the limit $(\omega_0^{s_0} - \omega_1^{s_1} - \omega_2^{s_2}) \to 0$, but still weights the integral on the right-hand side of Eq. (3.47). We thus consider its limiting behavior for increasing time t.

$$\Re \frac{1 - \exp(-i\Omega t)}{i\Omega} = \frac{\sin(\Omega t)}{\Omega} \xrightarrow{t\to\infty} \pi\delta(\Omega) \tag{3.49}$$

$$\Im \frac{1 - \exp(-i\Omega t)}{i\Omega} = -\frac{1 - \cos(\Omega t)}{\Omega} \xrightarrow{t\to\infty} -\frac{\mathcal{P}}{\Omega} \tag{3.50}$$

The real part delivers the δ-function, see Eq. (3.49), such that the zero triad component grows linearly with the slow timescale. The imaginary contains the Cauchy principle value $\mathcal{P}$, where the singular point at $\Omega = 0$ is cut out from the integral by small interval $(\Omega - \eta, \Omega + \eta)$ and the limit $\eta \to 0$ is taken. For long times, resonant interactions contribute notably to the spectral evolution and thus energy transfers such that the kinetic equation Eq. (3.47) becomes

$$\begin{aligned}
&\partial_t E_0|_{res}(\boldsymbol{K}_0) = \\
&-8\pi \iint d\boldsymbol{K}_1 d\boldsymbol{K}_2 \left\{ |C^{-}_{-\boldsymbol{K}_0 \overset{+}{\boldsymbol{K}_1} \overset{+}{\boldsymbol{K}_2}}|^2 \left(\frac{\omega_2}{\omega_0} E_1 E_0 + \frac{\omega_1}{\omega_0} E_0 E_2 - E_1 E_2 \right) \delta(\boldsymbol{K}_0 - \boldsymbol{K}_1 - \boldsymbol{K}_2) \delta(\omega_0 - \omega_1 - \omega_2) \right. \\
&\left. +2|C^{-}_{-\boldsymbol{K}_0 \overset{+}{\boldsymbol{K}_1} \overset{-}{\boldsymbol{K}_2}}|^2 \left(\frac{\omega_2}{\omega_0} E_1 E_0 - \frac{\omega_1}{\omega_0} E_0 E_2 - E_1 E_2 \right) \delta(\boldsymbol{K}_0 - \boldsymbol{K}_1 + \boldsymbol{K}_2) \delta(\omega_0 - \omega_1 + \omega_2) \right\}
\end{aligned} \tag{3.51}$$

where the δ-function for wavenumbers can be eliminated by integration over $\boldsymbol{K}_2$.Note, that ω_0, ω_1 and ω_2 in Eq. (3.51) and Eq. (3.52) are positive, such that $\omega_0 = \omega_0^+$ and so on.

However, non-resonant interactions may also contribute to energy transfers through the imaginary part of the time response function. The kinetic equation Eq. (3.47) simplifies to two non-resonant interactions and becomes

$$\begin{aligned}
&\partial_t E_0|_{nres}(\boldsymbol{K}_0) = 8 \iint d\boldsymbol{K}_1 d\boldsymbol{K}_2 E_0 \left\{ \left(\Im(C^{-}_{-\boldsymbol{K}_0 \overset{+}{\boldsymbol{K}_1} \overset{+}{\boldsymbol{K}_2}} C^{-}_{-\boldsymbol{K}_2 \overset{-}{-\boldsymbol{K}_1} \overset{+}{\boldsymbol{K}_0}}) E_1 \right.\right. \\
&\left. + \Im(C^{-}_{-\boldsymbol{K}_0 \overset{+}{\boldsymbol{K}_1} \overset{+}{\boldsymbol{K}_2}} C^{-}_{-\boldsymbol{K}_1 \overset{+}{\boldsymbol{K}_0} \overset{-}{-\boldsymbol{K}_2}}) E_2 \right) \delta(\boldsymbol{K}_0 - \boldsymbol{K}_1 - \boldsymbol{K}_2) \frac{\mathcal{P}}{\omega_0 - \omega_1 - \omega_2} \\
&\left. +2 \left(\Im(C^{-}_{-\boldsymbol{K}_0 \overset{+}{\boldsymbol{K}_1} \overset{-}{-\boldsymbol{K}_2}} C^{+}_{\boldsymbol{K}_2 \overset{-}{-\boldsymbol{K}_1} \overset{+}{\boldsymbol{K}_0}}) E_1 - \Im(C^{-}_{-\boldsymbol{K}_0 \overset{+}{\boldsymbol{K}_1} \overset{-}{-\boldsymbol{K}_2}} C^{-}_{-\boldsymbol{K}_1 \overset{+}{\boldsymbol{K}_0} \overset{+}{\boldsymbol{K}_2}}) E_2 \right) \delta(\boldsymbol{K}_0 - \boldsymbol{K}_1 + \boldsymbol{K}_2) \frac{\mathcal{P}}{\omega_0 - \omega_1 + \omega_2} \right\}.
\end{aligned} \tag{3.52}$$

Remarkably, non-resonant interactions only become relevant if the energy spectra of the components in the interacting triad are anisotropic in wave angle $\phi = \arctan(\frac{k_x}{k_y})$. The reason

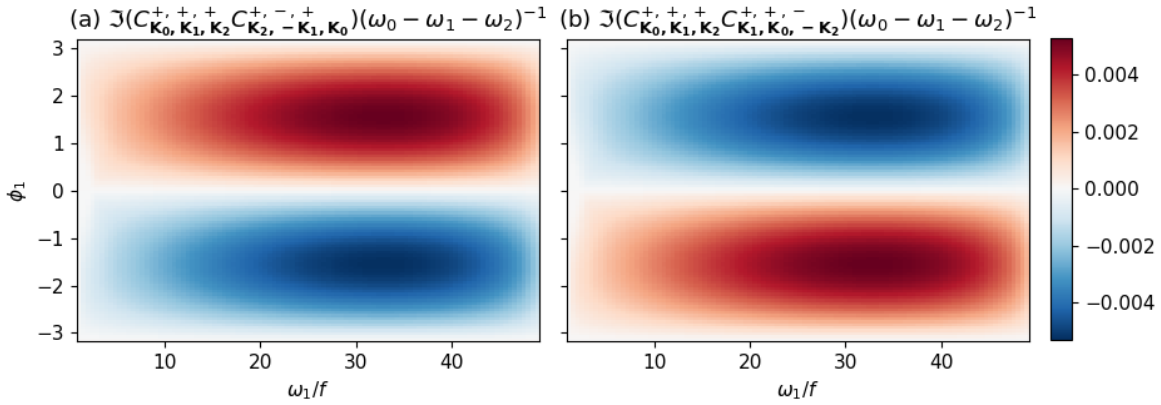

Figure 3.1: Transfer function for non-resonant interactions as a function of horizontal wavenumber k_1 and a specific vertical wavenumber m_1 projected onto the (ω_1, ϕ_1)-space for exemplary triads with waves characterized with $\boldsymbol{K}_0$ and $\boldsymbol{K}_2 = \boldsymbol{K}_0 - \boldsymbol{K}_1$.

is that non-resonant transfer functions (the imaginary parts of the interaction coefficients in Eq. (3.52)) are periodic and odd (asymmetric) with respect to ϕ_1 and their contribution to the integral vanishes if the spectrum is isotropic, see Fig. 3.1. In Fig. 3.1 we show the non-resonant transfer functions of interacting waves in (k_{x1}, k_{y_1})-space and a specific vertical wavenumber m_1 with waves with $\boldsymbol{K}_2 = \boldsymbol{K}_0 - \boldsymbol{K}_1$ that create a wave with $\boldsymbol{K}_0$ (we project onto the (ω_1, ϕ_1)-space). It can be shown that the anisotropy and asymmetry of the transfer functions also holds for the case of wave-vortex triads. An analysis of non-resonant interactions for anisotropic spectra has not been done so far and is beyond the scope of this paper.

3.6. Conclusions

We revisit the kinetic equation for wave-wave interactions in a non-hydrostatic Boussinesq system with constant rotation and stability frequency. Energy transfers by triad interactions are derived under the weak-interaction assumption. We compare the kinetic equations from the Eulerian (as in Eden et al., 2019b) and from the Lagrangian (as in Olbers, 1974, 1976) framework derived in self-contained forms, including their respective interaction coefficients. The comparison appears necessary since a large body of literature on the topic is based on the Lagrangian framework (see Tab. 3.1), while some recent numerical evaluations are based on the simpler Eulerian framework. Using the theoretical framework developed in this study, we evaluate the kinetic equation for wave–wave interactions within realistic IGW spectra in the ocean in Part B of this study (Sebastia Saez et al., 2025b) at unprecedented high resolution.

Although the Euler and Lagrange equations of motion can be transformed into each other, the forms of their corresponding nonlinearities differ from each other. As a consequence, the kinetic equations, including the wave amplitudes and interactions coefficients, differ in general due to a different truncation of the nonlinearities. The differences between the Eulerian and Lagrangian approaches can be summarized and understood as follows:

- In the Eulerian framework, the momentum balance contains only strictly quadratic nonlinearities by the advection terms. By applying the Fourier ansatz to the normal form of the linear system, one can readily identify a linear wave solution and the

corresponding evolution equation for the normal-mode amplitudes Eq. (3.13). This includes an integral of nonlinear terms over wavenumbers. From that the kinetic equation is derived, using the weak-interaction assumption.

- In contrast, the Lagrangian momentum balance is linear, but cubic nonlinearities enter through the pressure gradient. The Lagrangian continuity equation is also nonlinear, and linear eigenvectors cannot satisfy it such that a normal mode formulation is of no use. Instead, the continuity equation is enforced order by order in a power series expansion of the displacement variables in terms of wave amplitudes, yielding a polarization vector for the linear solution and expansion coefficients for higher-order terms. The resulting amplitude evolution equation Eq. (3.26) is formally identical to the Eulerian normal mode amplitude equation Eq. (3.13), when in fact its meaning is different.
- Due to the different forms of the nonlinearities in the Eulerian and Lagrangian systems, and despite the similarity between the Lagrangian and Eulerian amplitude evolution equations, the respective wave amplitudes, interaction coefficients and energies have a different physical meaning.
- In the Eulerian framework, energy is strictly quadratic in normal mode amplitudes, whereas in the Lagrangian framework energy is represented by an infinite series in terms of powers of amplitudes.
- Despite these fundamental differences, the Eulerian and Lagrangian kinetic equations become identical under resonant conditions as the Lagrangian kinetic equation reduces to the lowest order, i.e. to a quadratic form in amplitudes. The higher order terms in the Lagrangian kinetic equation vanish as they are related to non-resonant interactions.
- Total energy within a closed triad is conserved, which leads to the fundamental relation of the interaction coefficients Eq. (3.32) (Hasselmann, 1962, 1963a,b; Kraichnan, 1973; Remmel and Smith, 2009). Eulerian resonant and non-resonant interaction coefficients satisfy the fundamental relation, while the Lagrangian interaction coefficients only follow the fundamental relation under resonant conditions, but not under non-resonant.
- We find that for isotropic wave spectra, as the GM76 model, see Garrett and Munk (1975, 1979), the non-resonant interactions vanish and the kinetic equations for Euler and Lagrange frameworks become identical.

In the limit of infinite timescale separation of amplitude variations and wave oscillation, triad interactions split into resonant ones ($\omega_0 - (\omega_1 \pm \omega_2) = 0$), and non-resonant interactions ($\omega_0 - (\omega_1 \pm \omega_2) \neq 0$). While the resonant ones can lead to significant wave growth, non-resonant interactions are expected to remain small and unimportant for $t > (\omega_0 - (\omega_1 \pm \omega_2))^{-1}$. However, we pointed out that non-resonant interactions may still contribute significantly through the imaginary part of the time response function Eq. (3.50), which has not received much attention so far.

Acknowledgments

This paper is a contribution to the subprojects W6 and L2 of the Collaborative Research Centre TRR 181 "Energy Transfers in Atmosphere and Ocean" funded by the Deutsche Forschungsgemeinschaft (DFG, German Research Foundation) under project number 274762653. During the preparation of this manuscript, AI has been used for language polishing. We also acknowledge discussions with to Jacques Vanneste at Bornö Oceanographic Station.

A. The Lagrangian polarization vector

In this appendix, we analyze the linearized Lagrangian system, as we did for the Eulerian case, see Sec. (3.2). We assume that there is a linear wave solution of the form

$$\begin{pmatrix} \xi_j(\boldsymbol{a},t) \\ \hat{\pi}(\boldsymbol{a},t) \end{pmatrix} = \ell \begin{pmatrix} Z_j \\ \Pi \end{pmatrix} \exp\left(i(\boldsymbol{K}\cdot\boldsymbol{a} - \omega t)\right) + c.c. \tag{53}$$

where ℓ is the Lagrangian wave amplitude and Z_j and Π represent the polarization vector. There is no eigenvector framework as in Eulerian case because the Lagrangian equations are second order in the time derivative. The analysis, however, is straightforward: inserting Eq. (53) into the linearized momentum equations Eq. (3.16) and the linearized incompressibility equation $\partial\xi_j/\partial a_j = 0$, a set of four linear equations for Z_j and Π results, the determinant of which yields a polynomial of degree six in ω. Four solutions are zero and the remaining two constitute the dispersion relation of internal waves, $\omega = \pm\left(N^2k^2 + f^2m^2\right)^{1/2}/K$. The solutions for $\omega = 0$ yields the polarizations $\Pi = 0$, $Z_3 = 0$ and $k_xZ_1 + k_yZ_2 = 0$, i.e. a steady horizontal displacement with vanishing divergence. However, this does not correspond to the vortical mode of the Eulerian system: there is no steady vortical (geostrophic) mode in the linearized Lagrangian system. The polarization of the internal waves is found as

$$\begin{pmatrix} Z_1 \\ Z_2 \\ Z_3 \\ \Pi \end{pmatrix} = C \begin{pmatrix} \left(-k_x - i\frac{f}{\omega}k_y\right) m/k^2 \\ \left(-k_y + i\frac{f}{\omega}k_x\right) m/k^2 \\ 1 \\ i\left(\omega^2 - f^2\right) m/k^2 \end{pmatrix} \tag{54}$$

where C is an arbitrary normalization factor. Similarly to the Eulerian case, we use an energy-related normalization, then $|C| = k/(|\omega|K)$.

B. The Lagrangian interaction coefficient

The coefficients $\mathcal{A}^{s_0\ s_1\ s_2}_{\boldsymbol{K}_0\boldsymbol{K}_1\boldsymbol{K}_2}$ and $\mathcal{B}^{s_0\ s_1\ s_2}_{\boldsymbol{K}_0\boldsymbol{K}_1\boldsymbol{K}_2}$ are obtained by substituting the expression Eq. (3.20) for the displacement vector into the Lagrangian Eq. (3.18). In the first (quite lengthy) step, all terms are expressed by the vector $\boldsymbol{Z}_0^{s_0} = \boldsymbol{Z}_0$ given by Eq. (54) and $\boldsymbol{F}_{1\ 2}^{s_1 s_2} = \boldsymbol{F}_{12}$ given by Eq. (3.21) . Then, the second order Lagrangian becomes Eq. (3.23). The coefficients of $\bar{L}_{int}$

become

$$\mathcal{A}^{s_0\ s_1\ s_2}_{\boldsymbol{K}_0\boldsymbol{K}_1\boldsymbol{K}_2} = -\left(\omega_0^{s_0}(\omega_1^{s_1}+\omega_2^{s_2})Z_{j|0}F_{j|12}+N^2Z_{3|0}F_{3|12}\right)-\frac{1}{2}if(\omega_1^{s_1}+\omega_2^{s_2}-\omega_0^{s_0})(Z_{1|0}F_{2|12}-Z_{2|0}F_{1|12})$$

$$\begin{aligned}\mathcal{B}^{s_0\ s_1\ s_2}_{\boldsymbol{K}_0\boldsymbol{K}_1\boldsymbol{K}_2} =& -i\omega_2^{s_2}Z_{j|2}F_{j|10}-i\omega_1^{s_1}Z_{j|1}F_{j|20}+\frac{1}{2}\left(-i(\omega_1^{s_1}+\omega_2^{s_2})Z_{j|0}F_{j|12}\right)\\ &+\frac{1}{2}f\left(Z_{2|0}F_{1|12}-Z_{1|0}F_{2|12}+Z_{1|2}F_{2|10}-Z_{2|2}F_{1|10}+Z_{2|1}F_{1|02}-Z_{1|1}F_{2|02}\right)\end{aligned}$$

In $Z_{j|0}$ and $F_{j|12}$ the index in front of the vertical line | refers to the vector component and the indices behind it to the respective wavenumbers $\overset{s}{\boldsymbol{K}}$.

The coefficient $\mathcal{A}^{s_0\ s_1\ s_2}_{\boldsymbol{K}_0\boldsymbol{K}_1\boldsymbol{K}_2}$ may be symmetrized also with respect to all indices and then becomes (Olbers, 1974)

$$\mathcal{A}^{s_0\ s_1\ s_2}_{\boldsymbol{K}_0\boldsymbol{K}_1\boldsymbol{K}_2} = \frac{i}{6}\frac{m_0C_0}{K_0^2}\left(N^2-f^2+f^2\frac{\omega_0^{s_0}+\omega_1^{s_1}+\omega_2^{s_2}}{2\omega_0^{s_0}}\right)(\boldsymbol{K}_1\cdot\boldsymbol{Z}_2)(\boldsymbol{K}_2\cdot\boldsymbol{Z}_1)+(0\leftrightarrow1)+(0\leftrightarrow2) \tag{55}$$

with $C_0 = k_0/(\omega_0^{s_0}K_0)$. Here, we apply the replacement rule where $(0\leftrightarrow1)$ requires to switch the index 0 with index 1 and similarly with $(0\leftrightarrow2)$, such that $\mathcal{A}^{s_0\ s_1\ s_2}_{\boldsymbol{K}_0\boldsymbol{K}_1\boldsymbol{K}_2}$ is symmetric in all indices.

Because of $\boldsymbol{K}_0+\boldsymbol{K}_1+\boldsymbol{K}_2=0$ some of the terms in $\mathcal{B}^{s_0\ s_1\ s_2}_{\boldsymbol{K}_0\boldsymbol{K}_1\boldsymbol{K}_2}$ vanish and only terms proportional to f remain,

$$\mathcal{B}^{s_0\ s_1\ s_2}_{\boldsymbol{K}_0\boldsymbol{K}_1\boldsymbol{K}_2} = \frac{f^2}{4\omega_0^{s_0}K_0^2}m_0C_0(\boldsymbol{K}_1\cdot\boldsymbol{Z}_2)(\boldsymbol{K}_2\cdot\boldsymbol{Z}_1)+(0\leftrightarrow1)+(0\leftrightarrow2) \tag{56}$$

which is symmetric in all three indices. Surprisingly, the coefficient $\mathcal{B}^{s_0\ s_1\ s_2}_{\boldsymbol{K}_0\boldsymbol{K}_1\boldsymbol{K}_2}$, now reduced to Eq. (56), exactly cancels the third term in the brackets of the coefficient $\mathcal{A}^{s_0\ s_1\ s_2}_{\boldsymbol{K}_0\boldsymbol{K}_1\boldsymbol{K}_2}$ in Eq. (55). Hence we find as Olbers (1976)

$$\begin{aligned}\mathcal{L}^{s_0\ s_1\ s_2}_{\boldsymbol{K}_0\boldsymbol{K}_1\boldsymbol{K}_2} &= -\frac{1}{2}\mathcal{A}^{s_0\ s_1\ s_2}_{\boldsymbol{K}_0\boldsymbol{K}_1\boldsymbol{K}_2}+\frac{i}{6}\left(\omega_0^{s_0}+\omega_1^{s_1}+\omega_2^{s_2}\right)\mathcal{B}^{s_0\ s_1\ s_2}_{\boldsymbol{K}_0\boldsymbol{K}_1\boldsymbol{K}_2}\\ &= -\frac{i}{12}\frac{m_0C_0}{K_0^2}(N^2-f^2)(\boldsymbol{K}_1\cdot\boldsymbol{Z}_2)(\boldsymbol{K}_2\cdot\boldsymbol{Z}_1)+(0\leftrightarrow1)+(0\leftrightarrow2)\end{aligned} \tag{57}$$

for the net interaction coefficient Eq. (57). This reduced form of the Lagrangian coupling coefficient is symmetric in all indices. Note that it is valid for both resonant and non-resonant interactions.

4

Wave-wave interactions of internal gravity waves. Part B: Spectral energy transfers in a typical internal gravity wave field

Sebastia Saez, P., Chouksey, M., Eden, C., Olbers, D., (2025): "Wave-wave interactions of internal gravity waves. Part B: Spectral energy transfers in a typical internal gravity wave field", submitted to *Journal of Physical Oceanography*

Authors: Pablo Sebastia Saez[a] [1], Manita Chouksey[a,b], Carsten Eden[a] and Dirk Olbers[c]
Affilitations: a: Institut für Meereskunde, Universität Hamburg, Germany, b: Leibniz-Institut für Ostseeforschung Warnemünde, Germany c: Alfred Wegener Institute for Polar and Marine Research, and MARUM-Center for Marine Environmental Sciences, Germany

Abstract

We investigate wave-wave interactions in the internal gravity wave field by developing numerical methods to evaluate the kinetic equation, as formulated in Part A of this study. We introduce five methods to evaluate resonant interactions, some methods include non-resonant interactions. We also include inertial and buoyancy oscillations and find that their transfers are negligible. Our most advanced method at unprecedented high resolution shows consistently low Boltzmann rates, supporting the weak-interaction assumption. Applied to the GM76 model, the scattering integral diverges, requiring spectral modifications for convergence like steeper slopes or smooth transitions representing turbulence onset. The contribution of local and non-local interactions to the scattering integral are investigated. We find non-local interactions to govern the energy transfers and local interactions to be negligible. Parametric subharmonic instability is the main driver of inverse frequency cascades; induced diffusion drives bidirectional frequency transfers; elastic scattering contributes weak forward transfers. We also identify two new mechanisms: third parametric generation is the principal driver of

[1]Corresponding author: Pablo Sebastia Saez - pablo.sebastia.saez@uni-hamburg.de

forward energy cascades, and horizontal diffusion generates strong energy transfers at high frequencies. These findings provide convergent results at an unprecedented high resolution, improving the efficiency and reliability of energy transfer evaluations in oceanic internal gravity wave spectra.

Satement

Internal gravity waves connect large-scale ocean forcing with small-scale mixing, yet energy transfers along this route remain difficult to quantify. The energy transfers are principally described within the theoretical framework of the kinetic equation under the weak-interaction assumption. Previous studies often report qualitatively consistent but quantitative divergent results, raising questions about the robustness of the framework and motivating further methodological developments. We develop five numerical methods that efficiently evaluate resonant and non-resonant wave–wave interactions, resolving long-standing issues of weak-interaction consistency and convergence. We discuss the roles of interaction mechanisms for Garrett-Munk-like spectra and show that non-local interactions dominate and local interactions are negligible. These advances establish a robust framework for quantifying nonlinear energy transfers in internal gravity wave fields.

4.1. Introduction

Internal gravity waves (IGWs) are a key link between large-scale energy sources and small-scale mixing in the ocean. Their energy originates primarily from tidal motions (see Bell, 1973; Nikurashin and Ferrari, 2011) and from wind forcing at near-inertial frequency (see D'Asaro, 1985; Olbers et al., 2020a), which inject energy at relatively large spatial and temporal scales. However, mixing and dissipation occur at much smaller scales, where internal waves overturn and break. This mismatch requires a downscale transfer of energy through the IGW spectrum, progressively populating its high-wavenumber range. Nonlinear wave–wave interactions are widely regarded as the main pathway for this downscale transfer, redistributing energy across scales. Here, in the second part of the two-part study, we evaluate wave-wave interactions and the resulting energy transfers within an already established IGW continuum, rather than on its initial generation.

The kinetic equation, or scattering integral, provides the principal theoretical framework to describe wave-wave interactions (Hasselmann, 1966; Nazarenko, 2011). It predicts statistical energy redistribution in frequency–wavenumber space under the assumption of weak nonlinearity, i.e., wave amplitudes evolve slowly compared to their oscillation periods. Early work using Lagrangian formulations (Olbers, 1974, 1976) and hydrostatic approximations (McComas and Bretherton, 1977; Pomphrey et al., 1980) identified systematic energy transfers from intermediate to near-inertial and high-frequency waves. Subsequent work refined these approaches with higher-resolution calculations and varying simplifications (e.g., Lvov and Tabak, 2001; Polzin and Lvov, 2011; Lvov et al., 2012; Dematteis et al., 2024; Labarre et al., 2024), while more recent efforts have derived the equation directly from the Eulerian non-hydrostatic Boussinesq system with rotation (Eden et al., 2020). Despite consistent qualitative findings, these studies often yield diverging quantitative results, raising questions about the robustness of the framework (see Bel and Tziperman, 2023) and motivating further

methodological developments. In Part A of this study, see Sebastia Saez et al. (2025a), we unify the derivations of the kinetic equation from the Lagrangian and Eulerian frameworks and discuss their differences. Here we present a comprehensive set of numerical methods to evaluate wave-wave interactions and provide convergent results at unprecedented resolution and reduced computational costs, improving the efficiency and reliability of energy transfer evaluations in oceanic IGW spectra.

Wave–wave interactions arise when two internal wave packets overlap in space and time to generate a third wave. These triad interactions are governed by the resonance condition embedded in the time-response function of the kinetic equation, which determine whether energy transfers accumulate significantly. If the resonance condition is met – meaning the frequency of the generated wave equals the sum or difference of the frequencies of the interacting waves (also known as the sum and difference interactions respectively) – the forcing is non-oscillatory and can lead to substantial persistent energy transfer. In contrast, when resonance is not satisfied, transfers remain weak and oscillatory. Most previous studies have therefore emphasized resonant interactions, while the role of non-resonant processes has received much less attention. Exceptions include Lvov et al. (2012), who considered them in an approximate form, and Eden et al. (2020, 2019b), who treated resonant and non-resonant contributions without distinction. Building on this, we formulate three kinetic equations in Part A Sebastia Saez et al. (2025a): one to be evaluated at finite times which includes both resonant and non-resonant interactions without distinction (their Eq. 50); and two to be evaluated at infinite times which treat resonant and non-resonant interactions separately (their Eqs. 54 and 55 respectively). In the present work, we focus on finite-time evaluations and on the resonant formulation, since for typical oceanic IGW spectra such as the GM76 model (Garrett and Munk, 1975, 1979) which is horizontally isotropic and vertically symmetric, non-resonant contributions vanish (see Sebastia Saez et al., 2025a). We consider the full IGW spectrum in a triply periodic domain (including inertial and buoyancy oscillations) with constant stratification and no background flow.

With these advances, we are able to revisit longstanding issues that have historically limited confidence in the theory of interacting IGWs, notably the validity of the weak-interaction assumption and the convergence of the scattering integral. The weak-interaction assumption, questioned by Holloway (1978, 1980, 1982); Müller et al. (1986); and recently by Bel and Tziperman (2023), is shown here to be largely satisfied for GM-like spectra. Deviations occur only at very high (near-buoyancy) frequencies when adopting the classical GM76 model with a -2-slope. The same slope has also been reported to prevent convergence of the scattering integral for the case of ultra-violet divergence (as the vertical wavenumber goes to infinity) and the infra-red divergence (as the vertical wavenumber goes to zero) but for a non-rotating system in hydrostatic balance (see Lvov et al., 2010). Olbers et al. (2020b) consider the rotating non-hydrostatic system to study the decay of a tidal line specifically by PSI (parametric subharmonic instability) interactions and find a divergent solution for the GM76 model with a -2-slope in vertical wavenumber, which raises doubts about the dynamical consistency of the model. Observations, however, indicate regional variations in spectral slope (Polzin and Lvov, 2011; Pollmann et al., 2017; Pollmann, 2020), motivating the consideration of alternative spectra. We test explicitly the convergence of the scattering integral for variations of the IGW spectrum and find convergence when considering a cutoff that mimics the turbulence onset which, in turn invalidates the weak-interaction assumption. As consequence, we consider steeper slopes, which ensure convergence and satisfy the weak-interaction assumption. These

results resolve two of the principal theoretical limitations of the kinetic theory of IGWs.

The structure of triad interactions in the IGW field has been extensively studied, with seminal work by McComas and Bretherton (1977) identifying three principal classes of non-local resonant interactions: parametric subharmonic instability (PSI), induced diffusion (ID), and elastic scattering (ES). PSI efficiently transfers energy from low-mode internal tides to higher modes and smaller scales, while ID and ES contribute to the scattering of energy throughout the spectrum. Foundational studies (Bretherton, 1964; McComas and Bretherton, 1977) provided the resonance conditions underpinning these interactions, and Müller et al. (1986) further extended this understanding in the context of IGW spectra. More recent work has suggested that local interactions, previously overlooked, may also contribute to spectral energy redistribution (Wu and Pan, 2023; Dematteis et al., 2024). Our analysis indicates that these local interactions remain relatively weak, but it also identifies two additional non-local mechanisms: horizontal diffusion (HD), which becomes relevant at elevated frequencies, and third parametric generation (TPG), which facilitates forward energy transfers. Together, these new mechanisms extend the classical picture of PSI, ID, and ES, providing a more complete characterization of the triad interactions that shape the IGW continuum.

This paper is structured as follows: Section 2 details the five numerical methods to evaluate the kinetic equation. The evaluations of the resonant and non-resonant interactions using the different numerical methods are presented in Section 3. Section 4 discusses the convergence of the kinetic equation with respect to variations in the IGW spectrum. In Section 5 we compare the contributions of local and non-local interaction mechanisms and assess their relative importance within the energy transfers. Section 7 wraps up the paper with a discussion and key conclusions.

4.2. Methods to evaluate the scattering integral

We revisit the kinetic equation derived in a non-hydrostatic Boussinesq system for energy transfers by internal gravity wave-wave interactions within the weak-interaction assumption as detailed in Part A of this study (Sebastia Saez et al., 2025a). Here we expand upon previous numerical methods to integrate the kinetic equation, see Olbers (1976); Eden et al. (2019c). Specifically, we extend the three evaluation methods in Eden et al. (2019c) by including inertial and buoyancy oscillations to assess their role in energy transfers. For that we evaluate the scattering integral on regular grids in the three-dimensional wavenumber space $\boldsymbol{K} = (k_x, k_y, m)$ (see methods M1, M2 and M3 in Tab. 4.1). We further develop efficient numerical algorithms that resolve multi-scale interactions at an unprecedented resolution. For that we formulate the scattering integral in the (k, m, ϕ)- coordinate system where the horizontal wavenumber is $k = \sqrt{k_x^2 + k_y^2}$ such that $\boldsymbol{k} = (k_x, k_y) = k(\cos\phi, \sin\phi)$ with angle ϕ, and evaluate it on a loglog-grid (see method M4 in Tab. 4.1). Finally, we formulate the scattering integral in the (ω, m, ϕ)- coordinate system where ω is the frequency, and evaluate it on a more complex finer non-equidistant grid, see method M5 in Tab. 4.1.

M1 & M2 - Integration for finite times

First, we follow Eden et al. (2019c) to evaluate the scattering integral as in Eq. 50 in Sebastia Saez et al. (2025a) on a regular grid in $\boldsymbol{K}$-space, using positive and negative wavenumbers including

	$(\boldsymbol{K}_0, \omega_0)$-Domain	# grids	$(\boldsymbol{K}_1, \omega_1)$-Domain	# grids
M1 Regular grid $\Delta t = 10$ d	$\begin{pmatrix} -0.03\,\mathrm{m}^{-1} \le \boldsymbol{k}_0 \le 0.03\,\mathrm{m}^{-1} \\ -0.39\,\mathrm{m}^{-1} \le \mathrm{m}_0 \le 0.39\,\mathrm{m}^{-1} \end{pmatrix}$	$\begin{pmatrix} 251^2 \\ 251 \end{pmatrix}$	$\begin{pmatrix} -0.03\,\mathrm{m}^{-1} \le \boldsymbol{k}_1 \le 0.03\,\mathrm{m}^{-1} \\ -0.39\,\mathrm{m}^{-1} \le \mathrm{m}_1 \le 0.39\,\mathrm{m}^{-1} \end{pmatrix}$	$\begin{pmatrix} 251^2 \\ 251 \end{pmatrix}$
M2 Regular grid $\Delta t = 10$ d	$\begin{pmatrix} -0.03\,\mathrm{m}^{-1} \le \mathrm{k}_{x,0} \le 0.03\,\mathrm{m}^{-1} \\ k_{y,0} = 0\,\mathrm{m}^{-1} \\ -0.39 m^{-1} \le m_0 \le 0.39\,\mathrm{m}^{-1} \end{pmatrix}$	$\begin{pmatrix} 251 \\ 1 \\ 251 \end{pmatrix}$	$\begin{pmatrix} -0.03\,\mathrm{m}^{-1} \le \boldsymbol{k}_1 \le 0.03\,\mathrm{m}^{-1} \\ -0.39\,\mathrm{m}^{-1} \le \mathrm{m}_1 \le 0.39\,\mathrm{m}^{-1} \end{pmatrix}$	$\begin{pmatrix} 251^2 \\ 251 \end{pmatrix}$
M3 Regular grid $\Delta t \to \infty$	$\begin{pmatrix} 0\,\mathrm{m}^{-1} \le \mathrm{k}_{x,0} \le 0.025\,\mathrm{m}^{-1} \\ k_{y,0} = 0\,\mathrm{m}^{-1} \\ 0\,\mathrm{m}^{-1} \le \mathrm{m}_0 \le 0.47\,\mathrm{m}^{-1} \end{pmatrix}$	$\begin{pmatrix} 401 \\ 1 \\ 551 \end{pmatrix}$	$\begin{pmatrix} -0.025\,\mathrm{m}^{-1} \le \mathrm{k}_{x,1} \le 0.025\,\mathrm{m}^{-1} \\ 0\,\mathrm{m}^{-1} \le \mathrm{k}_{y,1} \le 0.025\,\mathrm{m}^{-1} \\ 0\,\mathrm{m}^{-1} \le \lvert \pm \mathrm{m}_1 \rvert \le 0.47\,\mathrm{m}^{-1} \end{pmatrix}$	$\begin{pmatrix} 801 \\ 401 \\ 2 \end{pmatrix}$
M4 Eq. (4.1) Loglog grid $\Delta t \to \infty$	$\begin{pmatrix} 10^{-4}\,\mathrm{m}^{-1} \le \mathrm{k}_0 \le 0.1\,\mathrm{m}^{-1} \\ 10^{-3}\,\mathrm{m}^{-1} \le \mathrm{m}_0 \le 1\,\mathrm{m}^{-1} \\ \phi_0 = 0^\circ \end{pmatrix}$	$\begin{pmatrix} 1060 \\ 1040 \\ 1 \end{pmatrix}$	$\begin{pmatrix} 10^{-4}\,\mathrm{m}^{-1} \le \mathrm{k}_1 \le 0.1\,\mathrm{m}^{-1}) \\ 10^{-3}\,\mathrm{m}^{-1} \le \lvert \pm \mathrm{m}_1 \rvert \le 1\,\mathrm{m}^{-1} \\ 0^\circ \le \phi_1 \le \pi \end{pmatrix}$	$\begin{pmatrix} 1060 \\ 2 \\ 1020 \end{pmatrix}$
M5 Eq. (4.3) Non-eq. grid $\Delta t \to \infty$	$\begin{pmatrix} f < \omega_0 < N \\ 10^{-3} m^{-1} \le m_0 \le 1 m^{-1} \\ \phi_0 = 0^\circ \end{pmatrix}$	$\begin{pmatrix} 1862 \\ 1860 \\ 1 \end{pmatrix}$	Sum interaction: $\begin{pmatrix} f < \omega_1 < \omega_0\vert_{\omega_0 > 2f} - f \\ m^{\pm}_{1,\mathrm{min}} < \lvert m_1 \rvert < m^{\pm}_{1,\mathrm{max}} \end{pmatrix}$ Difference interaction: $\begin{pmatrix} \omega_0\vert_{\omega_0 < N-f} + f < \omega_1 < N \\ m^{\pm}_{1,\mathrm{min}} < \lvert m_1 \rvert < m^{\pm}_{1,\mathrm{max}} \end{pmatrix}$	$\begin{pmatrix} 1862 \\ 1860 \end{pmatrix}$ $\begin{pmatrix} 1862 \\ 1860 \end{pmatrix}$

Table 4.1: Computational methods (M1–M5) and their corresponding grids in $(\mathbf{K}_0, \omega_0)$ and $(\mathbf{K}_1, \omega_1)$. Methods M1 and M2 involve the evaluation of the scattering integral for finite time intervals ($\Delta t = 10$ days) within a horizontal domain of $L_{x,y} = 25$ km and a vertical domain $L_z = 2$ km. Methods M3 (with $L_{x,y} = 75$ km and $L_z = 6$ km) to M5 focus on resonant interactions by taking the limit of infinite time ($\Delta t \to \infty$) in the time response function.

zeros, see M1 and M2 in Tab. 4.1. While in M1 we evaluate the kinetic equation in the full $\boldsymbol{K}$-space, in M2 we make use of the isotropic property of the GM76 model to simplify the computation, by evaluating on the plane with $k_y = 0$ in $\boldsymbol{K}$-space only. This computation results in an evaluation of around 10^{15} triad interactions. The equidistant grid in M1 and M2 allows for exactly matching triads, where all three wavenumber vectors in a specific triad can be interchanged. We therefore achieve energy conservation up to numerical precision of $\int \partial_t E d\boldsymbol{K} \approx O(10^{-12})\,\mathrm{m^2 s^{-3}}$ or $\int \partial_t E d\boldsymbol{K} / \int |\partial_t E| d\boldsymbol{K} \approx O(10^{-7})$ with M1 and a few permill of 0.4% with M2.

The computational domain spans 25 km × 25 km horizontally and 2 km vertically, with 251^3 grid points, and a resolution of about 100 m horizontally and 8 m vertically. We evaluate the kinetic equation for a finite time interval of $\Delta t = 10$ days in the time response function and thus include all possible interactions (resonant and non-resonant) within the prescribed wave spectrum. We further extend both M1 and M2 by including triads with inertial ($\boldsymbol{k} = 0$) and buoyancy ($m = 0$) oscillations, where singularities in the GM76 model are avoided as detailed in Appendix A. M1 integrations compute about 10^{15} triad interactions which we divide in 80 subdomains each parallelized across 40 nodes with 128 CPUs running for 6 hours each and takes about a day in total. M2 integrations compute about 10^{11} triad interactions and run on 10 nodes with 128 CPUs over 2 hours for each sum and difference interactions.

M3 - Integration for infinite times

We make use of the resonant condition and use the limiting behavior of the time response function for infinite times $\Delta t \to \infty$ to derive a kinetic equation for resonant interactions, see Eq. 54 in Sebastia Saez et al. (2025a). In other words, we evaluate resonant triads between waves $(\boldsymbol{K}_1, \omega_1)$ and $(\boldsymbol{K}_2, \omega_2)$ that generate a wave $(\boldsymbol{K}_0, \omega_0)$ with $((k_x|_{k_x\geq 0}, 0, m|_{m\geq 0})_0^T = \boldsymbol{K}_1 \pm \boldsymbol{K}_2, \omega_0 = \omega_1 \pm \omega_2)$. When fixing $\boldsymbol{K}_0$ and $\boldsymbol{k}_1$, we calculate $\boldsymbol{k}_2$ and use a minimum finding algorithm to extract the corresponding m_1 (with a positive and a negative solution), such that the frequency mismatch in the triad is minimized to numerical precision. The computation is done on a regular equidistant grid (M3 in Tab. 4.1), which is equivalent to Method 3 in Eden et al. (2019b). In addition, here we also include inertial and buoyancy oscillations. Note, that as in M2 we take advantage of the horizontal isotropy and vertical symmetry in the wave spectrum and consider only for a plane $(k_x, 0, m)$ in $\boldsymbol{K}$-space. In M3 the computational costs are reduced to 6 hours with 15 nodes (128 processors per node) for around twice the resolution compared to M1 and M2, see Tab. 4.1, and 1% relative error in energy conservation.

M4 - Resonant interactions in (k, m, ϕ)-space

The isotropic assumption of wave energy density spectra calls for a coordinate transformation. We transform the energy density spectrum from $\boldsymbol{K}$-space to cylindrical wavenumber space $E(k, m, \phi)$ and the integration accordingly, in which the dependence on the wave angle vanishes for isotropic spectra. After the coordinate transformation we have

$$\begin{aligned}
&\partial_t E_0|_{res} = \\
&-8\pi \iiint dk_1 dm_1 d\phi_1 \left(\frac{1}{k_2} |C^{-}_{-\boldsymbol{K}_0 \overset{+}{\boldsymbol{K}_1} \overset{+}{\boldsymbol{K}_2}}|^2 \left(\frac{k_1\omega_1}{\omega_0} E_0 E_2 + \frac{k_2\omega_2}{\omega_0} E_1 E_0 - k_0 E_1 E_2 \right) \delta(\omega_0 - \omega_1 - \omega_2) \right. \\
&\left. + \frac{2}{k_2} |C^{-}_{-\boldsymbol{K}_0 \overset{+}{\boldsymbol{K}_1} \overset{-}{\boldsymbol{K}_2}}|^2 \left(\frac{k_1\omega_1}{\omega_0} E_0 E_2 - \frac{k_2\omega_2}{\omega_0} E_1 E_0 - k_0 E_1 E_2 \right) \delta(\omega_0 - \omega_1 + \omega_2) \right). \qquad (4.1)
\end{aligned}$$

We then evaluate the transformed kinetic equation on resonant surfaces with a minimum finding algorithm for m_1 as in M3. Now the roots for m_1 depend on k, m, k_1 and ϕ_1 via

$$k_2^2 = k^2 + k_1^2 - 2kk_1 \cos(\gamma) \;\text{ with }\; \gamma = \phi_1 - \phi. \qquad (4.2)$$

It remains an integral over k_1 and ϕ_1 which we solve numerically for the grid detailed under method M4 in Tab. 4.1. For the evaluation in (k, m, ϕ)-space, we take advantage of the GM76 model's horizontal isotropy and vertical symmetry to reduce the integration to positive m_0 and $0 < \phi_1 \leq \pi$. With method M4 we improve the numerical cost notably. We evaluate the scattering integral in a loglog-grid with around twice as much grid points, and resolve twice the resolution in vertical wavenumber and four times in horizontal wavenumber compared to M3. We compute around 10^{12} triad interactions in about 6 hours using 5 nodes with 128 CPUs with a relative error of 6%.

M5 - Resonant interactions in (ω, m, ϕ)-space

In this section we transform the kinetic equation to (ω, m, ϕ)-space and avoid the implementation of a minimum finding algorithm, such that the computational costs can be further

reduced. We express now energy density spectra in (ω, m, ϕ)-space and reformulate their transfer rate as

$$\partial_t E_0|_{res}(\omega_0, m_0) =$$
$$-8\pi \sum_{\mathrm{sign}(\gamma)} \left(\int_f^{\omega - f} d\omega_1 \sum_{\mathrm{sign}(m_1)} \int_{m_{1,min}^+}^{m_{1,max}^+} d|m_1| \hat{C}^+ \left(\frac{J_1\omega_1}{\omega_0} E_0E_2 + \frac{J_2\omega_2}{\omega_0} E_1E_0 - J_0E_1E_2 \right) \right.$$
$$\left. +2 \int_{\omega+f}^{N} d\omega_1 \sum_{\mathrm{sign}(m_1)} \int_{m_{1,min}^-}^{m_{1,max}^-} d|m_1| \hat{C}^- \left(\frac{J_1\omega_1}{\omega_0} E_0E_2 - \frac{J_2\omega_2}{\omega_0} E_1E_0 - J_0E_1E_2 \right) \right) \quad (4.3)$$

where γ is given in Eq. (4.2). We transform the coordinate system from $\boldsymbol{K}$-space to (ω, m, ϕ)-space through the Jacobian $J_i = \frac{\partial(\boldsymbol{k}_i, m_i)}{\partial(m_i, \omega_i, \phi_i)} = m_i^2 \frac{\omega_i(N^2 - f^2)}{(N^2 - \omega_i^2)^2}$ where $i = 0, 1, 2$ represents a triad component. The modified scattering coefficients become

$$\hat{C}^{\pm} = |C^-_{-\boldsymbol{K}_0 \boldsymbol{K}_1 \pm \boldsymbol{K}_2}|^2 \left(J_2 |\frac{d\omega_2}{d\phi_1}| \right)^{-1} = |C^-_{-\boldsymbol{K}_0 \boldsymbol{K}_1 \pm \boldsymbol{K}_2}|^2 \frac{1}{k k_1 |\ \sin(\gamma)|} \quad (4.4)$$

where the resonance condition is fulfilled through the function $|\frac{d\omega_2}{d\phi_1}|$ and integration over ϕ_1, where

$$|\frac{d\omega_2}{d\phi_1}| = \frac{k k_1 |\sin(\gamma)|}{k_2^2} \frac{(\omega_2^2 - f^2)(N^2 - \omega_2^2)}{\omega_2 (N^2 - f^2)}. \quad (4.5)$$

The integration limits differ between sum and difference interactions, and we use a non-equidistant grid as detailed under method M5 in Tab. 4.1. Sum interactions ($\omega_0 = \omega_1 + \omega_2$) are only active in $\omega_0 > 2f$ and so $f < \omega_1 < \omega_0 - f$. Difference interactions ($\omega_0 = \omega_1 - \omega_2$) are only active in $\omega_0 < N - f$ and so $\omega_0 + f < \omega_1 < N$. If $N < 2f$, triads are not allowed.

We take advantage of the clearly defined ω-ranges to construct our numerical grid. We span a loglog-grid in (ω_0, m_0)-space. For each of the spectral regions where sum or difference interactions are allowed, we span individual log-grids in ω_1. The limits in the m_1-integration can be derived analytically, which is the major advantage of the method M5. For that, we solve for the roots of k_1 within the boundaries of resonant surfaces defined by $\cos(\gamma) = \pm 1$, as explained in detail in Appendix B. For each ω_0, m_0 and ω_1, we span the resonant surfaces with an equidistant grid between the m_1/m-limits (see Appendix B). We integrate numerically over the resonant surfaces and analytically at the boundaries. The number of grid points for the respective ω_0 and ω_1 grids is the same, as well as for the respective m_0 and m_1 grids. With the highest resolution from all methods, we improve the numerical cost even further and are able to carry out the computation in about 2 hours with 10 nodes and 128 CPUs and conserve energy up to a numerical error ranging from 1% to 7%, see Tab. 4.3. Furthermore, now the integration can even be done on a private computer with 8 processors in about 20 minutes with method M5 and lowest resolution which has the largest relative error of 17%.

4.3. Evaluations of resonant and non-resonant interactions

In this section, we revisit and expand upon previous results on wave-wave interactions (see Olbers, 1976; Pomphrey et al., 1980; Eden et al., 2019c) by evaluating the scattering integral

with the five methods presented in Sec. 4.2. We discuss the relative importance of inertial and buoyancy oscillations for energy transfers within the IGW spectrum. We discuss the convergence of the scattering integral when considering a wavenumber cutoff and different slopes in the IGW energy spectrum. We further filter out non-local resonant triads - induced diffusion (ID), elastic scattering (ES), parametric subharmonic instability (PSI)- and the local triads to assess their role for energy transfers. We introduce two further non-local resonant interaction mechanism – horizontal diffusion (HD) and third parametric generation (TPG). In all methods, we evaluate the scattering integral for the GM76 and GM-like models – a typical isotropic and vertically symmetric oceanic IGW spectrum as detailed in Appendix A.

4.3.1. Evaluations including all interactions

Fig. 4.1 shows the content spectra of energy transfers for all possible interactions using M2. The integration is separated into near-resonant interactions where $\omega_0 - (\omega_1 \mp \omega_2) < 10^{-4}$ s^{-1} (upper panels), and the residual representing non-resonant interactions (lower panels). Due to the vertical symmetry and azimuthal isotropy of the energy spectrum E, we transform the spectral representation from $E(\boldsymbol{K})$ to $E(k, m, \phi)$, integrate over the azimuthal angle ϕ, and restrict the analysis to positive vertical wavenumbers m. Results are shown on a log-log scale using a symmetric logarithmic color scale. Symmetric means that we apply the logarithmic scale in both positive (energy sources shown in green) and negative (energy sinks shown in brown) energy transfers from the origin.

In Fig. 4.1 (a) we exclude triads involving inertial or buoyancy oscillations. The near-resonant energy transfers reveal a clear sink within the frequency band $2f < \omega < 3f$ (although not strictly as there are negative energy transfers also at neighboring frequencies), indicating a loss of energy from this region and redistribution to frequencies $\omega < 2f$ and $\omega \geq 3f$, where positive transfers dominate. Fig. 4.1 (b) shows only triads with at least one inertial oscillation. The resulting near-resonant transfer spectrum resembles that of panel (a), albeit with increased noise, and again shows a dominant energy sink in the $2f < \omega < 3f$ band. Fig. 4.1 (c) incorporates triads involving at least one buoyancy oscillation. Energy transfers associated with near-resonant interactions involving inertial and buoyancy oscillations are significantly weaker – at least an order of magnitude smaller – than those within the IGW spectrum, and can therefore be neglected.

Non-resonant interactions, shown in the lower panels in Fig. 4.1, exhibit no coherent patterns and primarily contribute to background noise in the transfer spectra. Notably, the combined effect of near- and non-resonant interactions in panel (a) and (d) closely resembles the results shown in Fig. 1(a,b) of Eden et al. (2019c), and becomes identical when using the same initial GM76 model (not shown).

The results in Fig. 4.1 are sensitive to the choice of Δt in the time response function. Here we use $\Delta t = 10$ d, and the results are rather noisy. Eden et al. (2019c) show that the scattering integral becomes even noisier, the larger Δt becomes, while evaluations considering only resonant interactions for $\Delta t \to \infty$ are generally much smoother. The equidistant grids in M1 and M2 allow for matching triads but not necessarily for resonant interactions which become more relevant for larger Δt. Higher grid resolution improves the representation of near-resonant interactions as $\omega_0 - (\omega_1 \mp \omega_2) \to 0$ and generally leads to smoother energy transfer spectra. This behavior has been confirmed by comparing results at different resolutions, where lower resolutions resulted in notably noisier outcomes (not shown). However, increasing

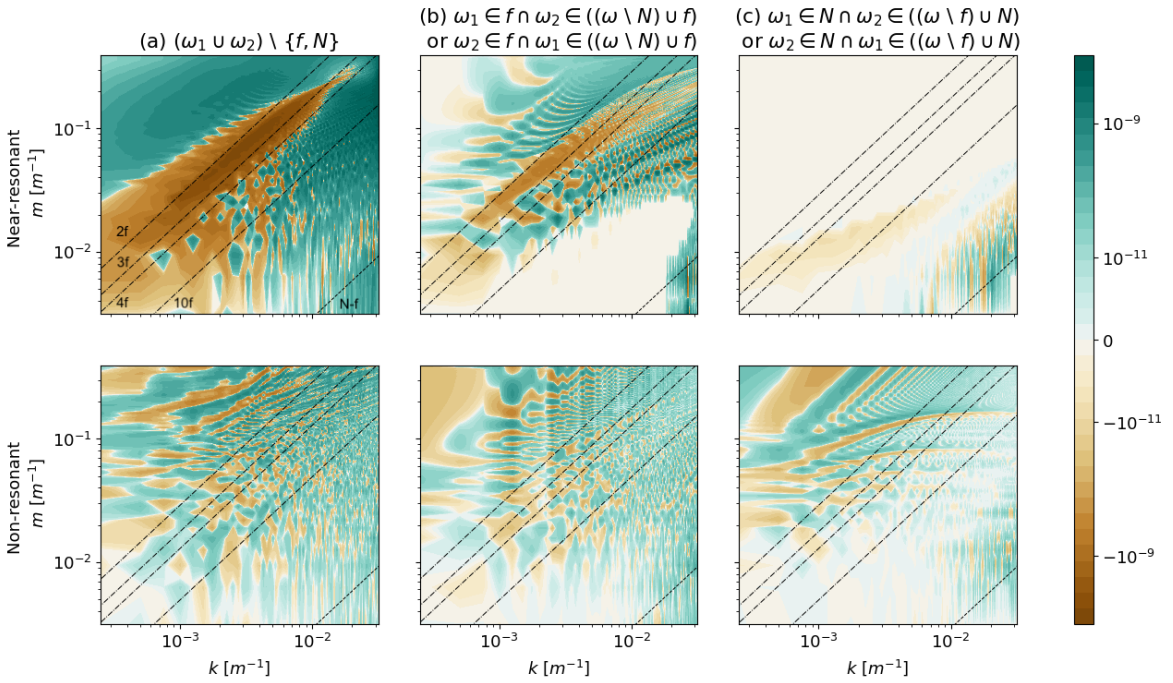

Figure 4.1: Content spectra of energy transfers using the method M2 in Tab.4.1 for a finite time of $\Delta t = 10$ d within the modified GM76 model, see Appendix A. In (a) we exclude inertial and buoyancy oscillations. In (b) either the first or the second component of the interacting triad is an inertial oscillation. In (c) either the first or the second component of the interacting triad is a buoyancy oscillation. In the upper row, we integrate over near-resonant interactions, where $\omega_0 - (\omega_1 \mp \omega_2) < 10^{-4} s^{-1}$; whereas in the lower row, we integrate over the remaining non-resonant interactions. The dashed-dotted lines show $\omega = 2f, 3f, 4f, 10f$ from top to bottom, and the dashed shows $\omega = N - 2f$ for $f = 10^{-4}\,\mathrm{s}^{-1}$ and $N = 50f$.

resolution rapidly increases computational costs. As a result, we follow the approach in Eden et al. (2019c) and focus on strictly resonant interactions using Method M3, which is computationally more efficient.

4.3.2. Evaluations including only resonant interactions

Fig. 4.2 (a,b and c) show the content spectra of energy transfers for resonant interactions using M3. The results are similar to those of M1 and M2, but the energy transfers become smoother by applying the resonant condition. In Fig. 4.2 (a) we exclude inertial and buoyancy oscillations. The prominent energy loss between $2f < \omega < 3f$ in Fig. 4.2 (a) is similar to that in Fig. 4.1 (a) for near-resonant interactions and has also been extensively reported in the literature (Olbers, 1976; McComas and Bretherton, 1977; Pomphrey et al., 1980; Hibiya et al., 1998; Lvov et al., 2012; Eden et al., 2019b,c, 2020). The remainder due to non-resonant interactions in Fig. 4.1 vanishes when a horizontally isotropic energy density spectrum is assumed. This removal of non-resonant contributions effectively reduces the background noise, making the spectra obtained via M3 equivalent to those from M1 or M2 for horizontally isotropic energy density spectra.

Fig. 4.2 (b) shows energy changes from triad interactions involving at least one inertial oscillation. IGW interactions with inertial oscillations are significantly smaller by at least two

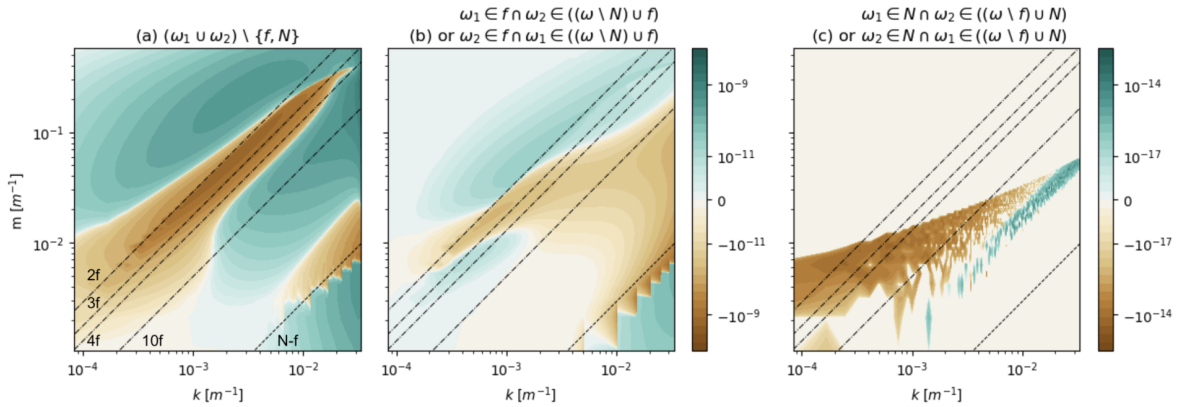

Figure 4.2: Same as Fig. 4.1 but for M3 in Tab. 4.1. In (a) we exclude inertial and buoyancy oscillations. In (b) either the first or the second component of the interacting triad is an inertial oscillation. In (c) either the first or the second component of the interacting triad is a buoyancy oscillation. The dashed-dotted and dashed indicate the same as in Fig. 4.1. Note, that the ranges of the colorbar in (a,b) are five orders of magnitude larger than in (c).

orders of magnitude than interactions between IGWs. Note that the inertial peak in our initial IGW spectrum – a modified version of the GM76 model – is based on observational estimates (see Appendix A). Although we assume a depth-invariant energy spectrum, observed inertial energy decays with depth, likely leading to an overestimation of our energy transfers involving inertial oscillations.

Fig. 4.2 (c) shows energy changes from triad interactions involving at least one buoyancy oscillation. In sum interactions, triads with buoyancy oscillations are only active if $\omega_0 = N$ and lead to a weak energy gain (not shown). In difference interactions, triads with buoyancy oscillations balance the sum interaction and lead to a very weak energy loss on the order of $O(10^{-15})\,\mathrm{ms}^{-3}$. Such behavior is similar to ID as a high-frequency wave $\omega_0 = N$ with high wavenumber $|\boldsymbol{K}_0|$ is fed with the energy transferred from the interaction between a high-frequency wave ω_1 with high wavenumber $|\boldsymbol{K}_1|$ and a lower-frequency wave $\omega_2 < \omega_1$ with lower wavenumber $|\boldsymbol{K}_2| < |\boldsymbol{K}_1|$.

Compared to the results in Fig. 4.1, the results in Fig. 4.2 (a), where we use twice the resolution, reveal an additional energy loss at higher frequencies near $\omega_0 \to N - f$. The validity of this energy sink is questionable as rapid wave amplitude changes may invalidate the weak-interaction assumption, see Holloway (1978, 1980, 1981, 1982). The timescale for energy transfers, shown in Fig. 4.3, is described by the Boltzmann rate which is normalized by the intrinsic oscillation rate of the wave itself ω as we assume that the nonlinear evolution has to be slow compared to the phase oscillation $e^{-i\omega t}$. Formally, we write the Boltzmann rates normalized by the wave frequency as $\lambda_\omega = \partial_t E/(E\omega)$ and show them in Fig. 4.3 (a). For comparison, following Lvov et al. (2012), we also consider the more conservative approach by normalizing the Boltzmann rates by the inverse wave period as $\lambda_n = 2\pi\partial_t E/(E\omega)$, see Fig. 4.3 (b). For the rest of the analysis, we adopt the conservative approach, possibly overestimating the breakdown of the weak-interaction assumption. If $|\lambda_n| < 1$, the weak-interaction assumption holds; if $|\lambda_n| \geq 1$, it breaks down. Fig. 4.3 shows large spectral regions with $m_0 > 0.1\,\mathrm{m}^{-1}$, $2f < \omega_0 < 4f$ or $\omega_0 > N - f$ where the weak-interaction assumption fails, as also reported in Wu and Pan (2023). Such criterion may be, however, insufficient as triads may integrate to large time scales while individually having short time scales that break the

weak-interaction assumption, see Müller et al. (1986).

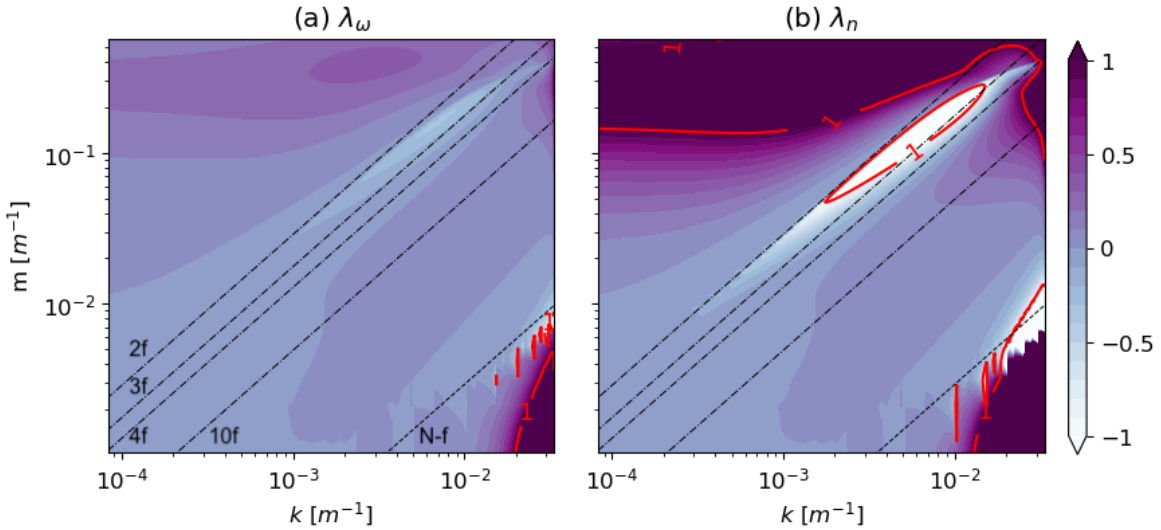

Figure 4.3: Boltzmann rates normalized by the wave frequency $\lambda_\omega = \partial_t E/(E\omega)$ in (a) and normalized by the inverse wave period $\lambda_n = 2\pi\partial_t E/(E\omega)$ in (b) for the energy transfers for the sum of the results in Fig. 4.2. The dashed-dotted and dashed indicate the same as in Fig. 4.1.

Note that Boltzmann rates are sensitive to the energy at the inertial frequency. The validity of the weak-interaction assumption depends on the relative amplitude of the inertial peak: if it is unrealistically large compared to the rest of the IGW continuum, as in Fig. 14(b) for $\epsilon = 0.1$, the resulting Boltzmann rates increase and the weak-interaction assumption breaks down. Greater inertial energy leads to stronger transfers, and thus a higher Boltzmann rate over broader spectral regions. We therefore test the validity of the weak-interaction assumption under a cuspless IGW energy spectrum where the inertial peak is suppressed. For that we redefine the frequency shape function of the GM-spectrum as $B(\omega) = n_b \frac{f}{\omega^2}$ with $n_b = (1 - \frac{f}{N})^{-1}$. The cuspless spectrum does not reduce the Boltzmann rates, in fact the energy transfers are almost identical to Fig. 4.2 (a) and the Boltzmann rates to Fig. 4.3. However, in the next sections we show that the Boltzmann rates are effectively reduced in our more advanced integration methods M4, where we increase resolution considerably, and in particular M5, where additionally to a higher resolution, we calculate the resonant condition analytically and integrate analytically over the boundaries of the resonant surfaces.

4.3.3. Resonant interactions in (m, k, ϕ)- and (m, ω, ϕ)-space

To improve the evaluation of the resonant scattering integral, we explore alternative grids that offer higher resolution at lower computational cost. Specifically, we use a loglog-grid in (m, k, ϕ)-space, see method M4, and a non-equidistant grid in (m, ω, ϕ)-space, see M5. In contrast to methods M1 and M2, methods M3, M4 and M5 cannot guarantee energy conservation to numerical precision as the triad components are not interchangeable on resonant surfaces for a given grid. The resulting small relative error in total energy conservation stems from the fact that the extracted vertical wavenumbers m_1 (and hence m_2), obtained via a minimum-finding algorithm, typically do not lie on the same discrete grid as

m_0. Consequently, the three waves forming a resonant triad are not interchangeable when computing the kinetic equation in fixed $\boldsymbol{K}_0$-space. We overcome this issue with methods M4 and M5 which are numerically notably more efficient without a proportional increase in cost. Methods M4 and M5 enable so finer resolution, see Tab. 4.1, that reduces the relative error in energy conservation, see Tab. 4.3.

Fig. 4.4 (a) shows the evaluation of the scattering integral in (m, k)-space integrated over wave angle ϕ, where inertial and buoyancy oscillations are excluded. The results are thus equivalent to Fig. 4.2 (a) but with almost twice the resolution (see method M4 compared to M3 in Tab. 4.1). Spectral regions where the weak-interaction assumption fails are masked in purple. The energy sink at high frequencies becomes more prominent also at spectral regions where the weak-interaction assumption still holds. Boltzmann rates become higher at larger frequencies $\omega < N - f$ where there is an energy gain.

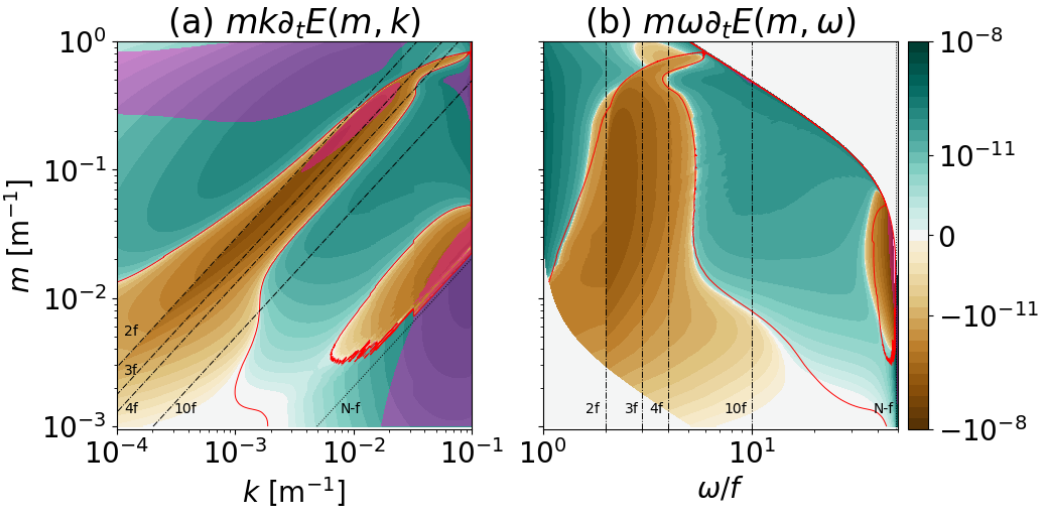

Figure 4.4: As in Fig. 4.2 (a), but with method M4 in (a) evaluated in (k, m)-space in a loglog-grid, and with method M5 in (b) evaluated in (ω, m)-space in a non-equidistant grid. The spectral regions with $|\lambda_n| > 1$ are masked in purple in (a,b). The red contour line is the zero-crossing in (a), which is projected on to (b) in (ω, m)-space.

Fig. 4.4 (b) shows the content spectra of nonlinear energy transfers for resonant interactions using method M5, see Tab. 4.1. The spectrum is bounded between the same horizontal and vertical cutoff wavenumbers as in Fig. 4.4 (a), see method M4. We thus have empty spectral regions for low as well as high vertical wavenumbers and frequencies which correspond to larger and smaller horizontal scales compared to the cutoffs. Similar to Fig. 4.4 (a), the dominant energy loss is in the frequency range $2f < \omega < 3f$ with a second weaker energy loss at higher frequencies $\omega_0 \to N - f$.

Small differences arise between Fig. 4.4 (a) and (b) due to the design of our constructed grid and increased resolution in (b). The differences become obvious with the red contour line on top of the colormaps which shows the change in sign of the energy transfers in Fig. 4.4 (a). Higher resolution (see method M5 compared to M4 in Tab. 4.1) and more accurate integration due to the constructed grid leads to a higher degree of energy conservation, where Fig. 4.4 (a) has a relative error of 6% and (b) of 4%. Furthermore, in method M5 the Boltzmann rates are significantly reduced. Only over small spectral regions at the boundaries at large horizontal

wavenumbers and high frequencies $\omega > N - f$, Boltzmann rates remain high.

In conclusion, the finite-time integrations of the kinetic equation, separating near-resonant from non-resonant interactions, confirm that non-resonant contributions vanish for horizontally isotropic IGW energy spectra and therefore do not affect the net energy transfer. Extending the analysis to the infinite-time limit using three different integration methods we show that, with increasing resolution and more accurate integration over the full resonant surfaces, Boltzmann rates decrease such that the weak-interaction assumption holds.

4.4. Convergence of the scattering integral

Determining whether the scattering integral converges for a given IGW energy spectrum is nontrivial, see Lvov et al. (2010). The finiteness of the scattering integral is not obvious and must be explicitly tested. Here, we assess convergence behavior by varying the domain of integration, omitting the inertial peak, introducing spectral cutoffs, and prescribing steeper spectral slopes.

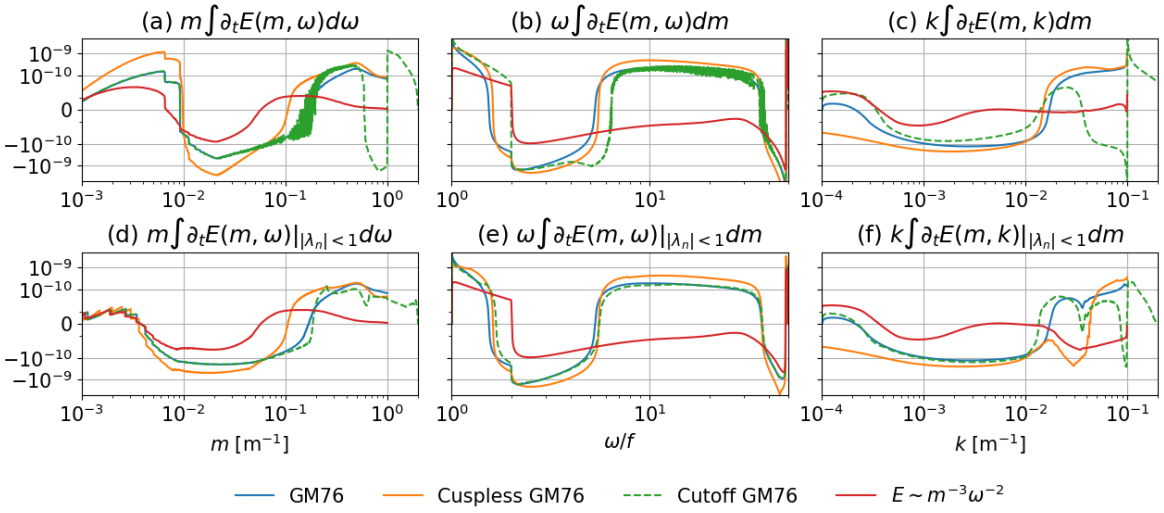

Figure 4.5: Method M5: Content spectra of energy transfers integrated over frequency in (a), over vertical wavenumber in (b), and over vertical wavenumber after a coordinate transformation to (m, k, ϕ)-space. In (d,e,f) Boltzmann rates larger than unity are masked out of the integration. In blue we show the integrations considering the IGW energy spectrum prescribed by the GM76 model and in orange for the cuspless version of the GM76 model. In dashed-green we consider cutoff wavenumbers at $m_c = 1\,\mathrm{m}^{-1}$ and $k_c = 0.1\,\mathrm{m}^{-1}$ in the GM76 model and prescribe vanishing spectral energy level for higher wavenumbers, but evaluate the scattering integral up to a maximal wavenumbers $m = 2m_c$ and $k = 2k_c$. In red we consider an IGW energy spectrum with a steeper slope in vertical wavenumber such that $E \sim m^{-3}\omega^{-2}$.

Fig. 4.5 shows content spectra of energy transfers integrated over frequency in (a,d), vertical wavenumber in (b,e), and horizontal wavenumber in (c,f), for a set of prescribed energy spectra. For the GM76 model (blue curves), the energy transfers do not decay to zero at high wavenumbers or frequencies, indicating that the scattering integral does not converge. This behavior persists when the integration limits are extended, see Fig. 4.6 (a) where we consider larger cutoff wavenumbers at $m_c = (1, 2, 4)\,\mathrm{m}^{-1}$ – while using the same amount of grid points, see method M5 in Tab. 4.1 – and show the content spectrum of energy transfers

integrated over frequency (green, orange and blue respectively). Our results are consistent with findings from Eden et al. (2019b), who demonstrated that the separation scale (marking the wavenumber at which the sign from negative energy transfers changes to positive) shifts to smaller scales in larger domains—another indication of non-convergence.

A further complication arises from high Boltzmann rates. Spectral regions with high Boltzmann rates violate the weak-interaction assumption and are omitted from the integrations shown in panels Fig. 4.5 (d–f) and Fig. 4.6 (d-f). Masking out high Boltzmann rates improves the convergence of the integral, see Fig. 4.6 (d), so we aim to reduce these spectral regions. Specifically we aim to reduce the inertial peak as the energy levels are much higher compared to the rest of the spectrum which may lead to strong interactions breaking the weak-interaction assumption. The cuspless variant of the GM76 model, see orange curves in all panels in Fig. 4.5, however, also fails to achieve convergence. In fact, the inertial peak does not influence the spectral shape of energy transfers and the results are very similar to the GM76 model.

The root cause of the non-convergence of the scattering integral rather lies in the spectral shape prescribed by the GM76 model. It can be shown, that the transfer function $|C^{-}_{-\boldsymbol{K}_0\overset{+}{\boldsymbol{K}}_1\overset{+}{\boldsymbol{K}}_2}|^2$ tends to a constant behavior at high horizontal wavenumbers k_1. Considering $k_1 \to \infty$, or equivalently $\omega \to N$, the eigenvector describing the waves behavior tends to become the one for buoyancy oscillation, see Sebastia Saez et al. (2025a). In this case neither the eigenvector nor the coupling coefficients depend on k_1, and thus $|C^{-}_{-\boldsymbol{K}_0\overset{+}{\boldsymbol{K}}_1\overset{+}{\boldsymbol{K}}_2}|^2 \xrightarrow{k_1\to\infty}$ const. The rest of the integrand in Eq. (4.1) scales with $\sim k_1^{t+1}$ where t is the slope of the prescribed energy density spectrum in horizontal wavenumber. We therefore find, that the integrand scales with $\sim k_1^{-1}$ for the GM76 model (that is $t = -2$) such that the integral $\int_\kappa^\infty k_1^{-1} dk_1 = \infty$ with $\kappa << 1$ does not converge, and similarly for shallower slopes. To address this, we impose a spectral cutoff that mimics the transition from IGWs to turbulence. We prescribe the GM76 model with vanishing spectral energy above the considered cutoff wavenumber at $m_c = 1\,\mathrm{m}^{-1}$ and resolve to a maximal vertical wavenumber $\max(m) = 2\,\mathrm{m}^{-1}$, see green dashed curves in all panels in Fig. 4.5. This approach successfully enforces convergence. However, it produces artificially high energy transfers near the cutoff – where mainly induced diffusion is acting to smooth the discontinuity in energy levels – which in turn results in large Boltzmann rates. As such, this solution, while formally convergent, may not represent a physically realistic scenario.

To improve both convergence and dynamical consistency, we examine alternative spectra with steeper slopes, representing a transition from IGW to turbulent regimes. For the case of a steeper slope like $t = -3$, the integrand in Eq. (4.1) scales with $\sim k_1^{-2}$ such that the integral $\int_\kappa^\infty k_1^{-2} dk_1 = \kappa^{-1}$ leads to finite values. A spectrum with −3-slope in vertical wavenumber (red curves in Fig. 4.5 and Fig. 4.6 (b,e)) leads to vanishing energy transfers at high frequencies and small scales, ensuring convergence of the scattering integral. Importantly, the corresponding Boltzmann rates remain largely below unity, maintaining consistency with the weak-interaction assumption, with exception of the fastest waves oscillating at near Brunt–Väisälä frequency, see negative transfer rates at high horizontal wavenumbers in Fig. 4.5 (f) compared to (c).

The convergence behavior persists for slopes shallower than $t = -3$, provided they remain steeper than $t = -2$. If we consider, however, a −2-slope in vertical wavenumber, we need a change in slope with increasing vertical wavenumber to steeper slopes representing the energetic decay of the IGW field and the transition to turbulence. For that, we consider a

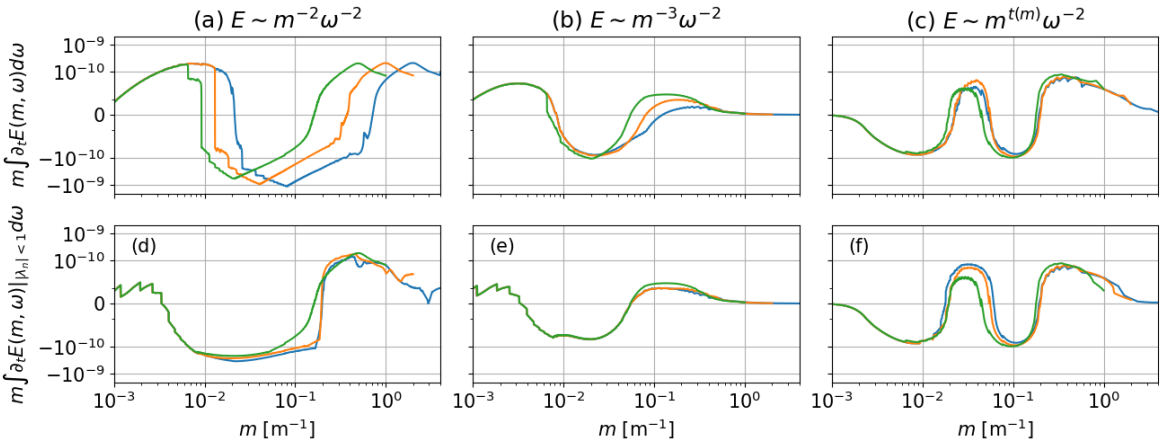

Figure 4.6: Method M5: Content spectra of energy transfers integrated over vertical wavenumber. In (d,e,f) Boltzmann rates larger than unity are masked out of the integration. In (a,d) we show the integrations considering the IGW energy spectrum prescribed by $E \sim m^{-2}\omega^{-2}$ (i.e. the GM76 model), in (d,e) for a steeper slope with $E \sim m^{-3}\omega^{-2}$ and in (c,f) with a changing slope $t(m) = \begin{cases} -2 \text{ for } m < 0.1\,\mathrm{m}^{-1} \\ -3 \text{ for } m > 0.1\,\mathrm{m}^{-1} \end{cases}$. We consider three different cutoff wavenumbers at $m_c = (1, 2, 4)\,\mathrm{m}^{-1}$ with $k_c = 0.1 m_c$ in green, orange and blue, respectively.

slope change from a slope $t_1 = -2$ to a steeper slope $t_2 = -3$ in vertical wavenumber. We modify the spectral shape function $A(m, \omega)$ given in Appendix A by introducing two roll-off wavenumbers $m^*_{r1} = 0.01\,\mathrm{m}^{-1}$ and $m^*_{r2} = 0.1\,\mathrm{m}^{-1}$, and the respective vertical wavenumber scales m^*_1 and m^*_2 that depend on $c^*_1 = N/m^*_{r1}$ and $c^*_2 = N/m^*_{r2}$. The shape function for a changing slope depending on the vertical wavenumber becomes

$$A(m,\omega) = n_a \frac{\tilde{A}(m/m^*_1(\omega, c^*_1), t_1, s)}{m^*_1(\omega, c^*_1)} \frac{\tilde{A}(m/m^*_2(\omega, c^*_2), t_2 - t_1, s)}{m^*_2(\omega, c^*_2)} \tag{4.6}$$

where the parameter $s = 2$ and n_a is the normalization such that the shape function integrates to unity. The frequency shape function $B(\omega)$ remains as in Appendix A. In Fig. 4.7 we show the energy density spectrum and highlight the vertical wavenumber roll-offs $m^*_1(\omega, c^*_1)$ and $m^*_2(\omega, c^*_2)$ that mark the transitions between the different slopes along the vertical wavenumber.

Fig. 4.6 (c,f) shows the integrated energy transfers for the case of a varying slope $t(m)$ in vertical wavenumber. The resulting energy transfers converge for increasing domain boundaries. Furthermore, Boltzmann rates are further reduced such that the integrated energy transfers with or without filtering high Boltzmann rates are very similar, see Fig. 4.6 (c) compared to (f). These findings underscore the critical role of spectral slope in regulating the validity of wave–wave interaction theory for oceanic internal waves.

Note, that an additional roll-off and a change in slope are further parameters that the scattering integral depends on. In supplemental materials we explore the dependence of the energy transfers by gradually varying the second roll-off wavenumber $m^*_{r2} = (1\,\mathrm{m}^{-1}, 0.08\,\mathrm{m}^{-1}, 0.06\,\mathrm{m}^{-1}, 0.05\,\mathrm{m}^{-1}, 0.02\,\mathrm{m}^{-1}, \mathrm{m}^*_{r1})$ for the transition of a -2-slope to a -3-slope in vertical wavenumber. For the case of a higher second roll-off, energy transfers resemble more the ones for a -2-slope. With the gradual nearing of the second roll-off to the first, we observe a gradual resemblance to the energy transfers with a single -3-slope in

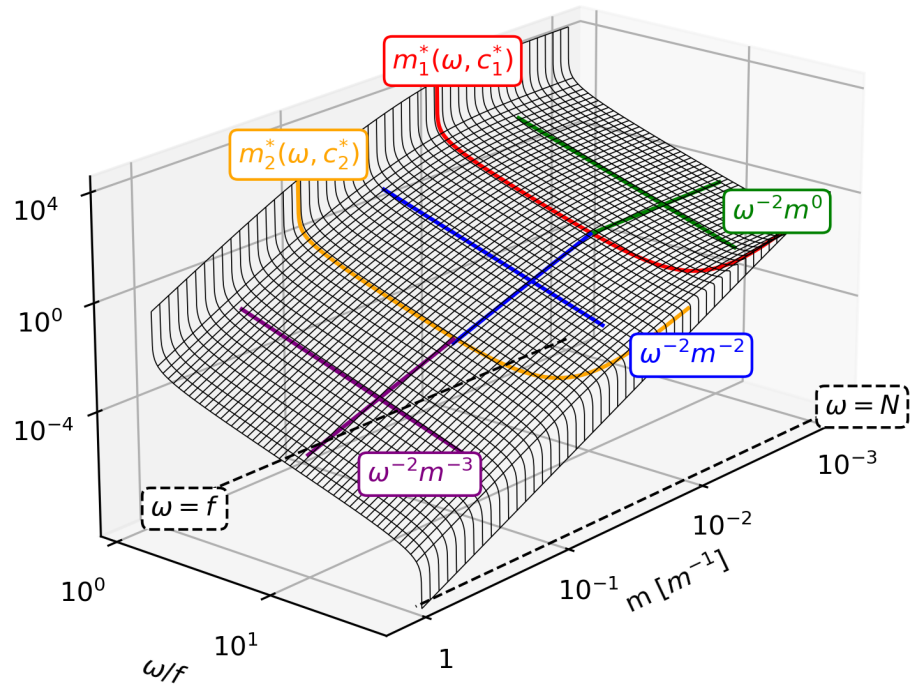

Figure 4.7: Energy density spectrum $E(m, \omega)$ of a GM-like spectrum with modified shape function $A(m, \omega)$ with a change in slope in vertical wavenumber as in Eq. (4.6).

vertical wavenumber.

4.5. Local and Non-local interactions

McComas and Bretherton (1977) identified three key non-local resonant triad interactions: ID, ES and PSI. Non-local means that the triads are scale-separated in wavenumber space where one wave has a significantly different wavelength and frequency compared to the other two waves. Local interactions are those that act between neighboring waves in wavenumber space. In the context of local interactions it is possible to make a connection to the Kolmogorov's view point of energy cascades (Zakharov et al., 1992) to evaluate the Kolmogorov constant that represents the relationship of the energy flux and the spectral energy density for IGWs, see Lvov et al. (2010); Dematteis et al. (2022)

Non-local triads are critical for explaining energy transfers in GM-like spectra, where energy resides in large-scale, low-frequency motions, and vertical shear occurs at small scales (McComas and Müller, 1981). However, recent studies (Wu and Pan, 2023; Dematteis et al., 2024) that evaluate the scattering integral within the hydrostatic approximation suggest that previously neglected local interactions also play a significant role in energy transfer. The assessment of local interactions is sensitive to the filtering criteria used to distinguish them from non-local ones.

We classify interactions using the criteria in Tab. 4.2. We define local interactions between waves whose absolute wavenumbers differ by no more than a factor of 1.5. Our classification for local interactions is rather strict compared to previous literature such as Dematteis et al.

	Sum interaction ($\omega_0 = \omega_1 + \omega_2$)	Difference interaction ($\omega_0 = \omega_1 - \omega_2$)
Local	$\frac{2}{3} < \frac{K_1}{K_2} < \frac{3}{2} \cap \frac{2}{3} < \frac{K_2}{K_0} < \frac{3}{2} \cap \frac{2}{3} < \frac{K_0}{K_1} < \frac{3}{2}$	
ID1 ID2	$\left\lvert\frac{m_1}{m_2}\right\rvert > \eta \cap \frac{\omega_1}{\omega_2} > \eta$ $\left\lvert\frac{m_2}{m_1}\right\rvert > \eta \cap \frac{\omega_2}{\omega_1} > \eta$	$\left\lvert\frac{m_1}{m_2}\right\rvert > \eta \cap \frac{\omega_1}{\omega_2} > \eta$ $\left\lvert\frac{m_1}{m_0}\right\rvert > \eta \cap \frac{\omega_1}{\omega_0} > \eta$
HD1 HD2	$\left\lvert\frac{k_1}{k_2}\right\rvert > \eta \cap \frac{\omega_1}{\omega_2} > \eta \neg$ID1 $\left\lvert\frac{k_2}{k_1}\right\rvert > \eta \cap \frac{\omega_2}{\omega_1} > \eta \neg$ID2	$\left\lvert\frac{k_1}{k_2}\right\rvert > \eta \cap \frac{\omega_1}{\omega_2} > \eta \neg$ID1 $\left\lvert\frac{k_1}{k_0}\right\rvert > \eta \cap \frac{\omega_1}{\omega_0} > \eta \neg$ID2
ES1 ES2	$0 < \left\lvert\frac{m_0}{m_2}\right\rvert - 0.5 < \gamma \cap \frac{\omega_0}{\omega_2} > \eta$ $0 < \left\lvert\frac{m_0}{m_1}\right\rvert - 0.5 < \gamma \cap \frac{\omega_0}{\omega_1} > \eta$	$0 < \left\lvert\frac{m_1}{m_2}\right\rvert - 0.5 < \gamma \cap \frac{\omega_1}{\omega_2} > \eta$ $0 < \left\lvert\frac{m_1}{m_0}\right\rvert - 0.5 < \gamma \cap \frac{\omega_1}{\omega_0} > \eta$
PSI	$\lvert\omega_1 - \omega_2\rvert < \gamma\frac{\omega_0}{2}$	$\lvert\omega_0 - \omega_2\rvert < \gamma\frac{\omega_1}{2}$
TPG1 TPG2	$\lvert\frac{\omega_2}{\omega_0} - \frac{1}{3}\rvert < \gamma$ $\lvert\frac{\omega_1}{\omega_0} - \frac{1}{3}\rvert < \gamma$	$\lvert\frac{\omega_2}{\omega_1} - \frac{1}{3}\rvert < \gamma$ $\lvert\frac{\omega_0}{\omega_1} - \frac{1}{3}\rvert < \gamma$

Table 4.2: Criteria for local and non-local IGW triad interactions. Non-local interactions are induced diffusion ID = ID1 + ID2, horizontal diffusion HD = HD1 + HD2 (where ¬ is the negation symbol) , elastic scattering ES = ES1 + ES2 , parametric subharmonic instability PSI, and third parametric generation TPG = TPG1 + TPG2. We define the constraint parameters $\eta = 2$ and $\gamma = 0.1$ to allow for more or less permissive filtering.

(2024) where they consider a factor 4 in either vertical wavenumber or frequency. We consider a factor 4 as too permissive since it may lead the horizontal wavenumbers to be further apart than a factor of an order of magnitude (even up to a factor of three orders of magnitude within the boundaries that we consider) making the interactions rather non-local. The consequence of a too permissive filter for local interactions is shown in the supplemental materials.

All interaction mechanisms are filtered independently from each other, so we expect some overlapping between the different types depending on how strict we define the constraint parameters η and γ. Apart from ID, ES and PSI, which have been studied in previous literature, we find two new non-local mechanisms – HD and TPG. The non-local interaction mechanisms work as follows:

- ID occurs when high-frequency high-vertical wavenumber waves (m_1, ω_1) interact with a slow near-inertial vertically large-scale wave $(m_2, \omega_2 \sim f)$, producing another high-frequency wave (m_0, ω_0).
- In HD we consider the scale separation in horizontal wavenumber rather than in the vertical wavenumber as in ID.
- ES involves a high-frequency wave interacting with a slow near-inertial wave, producing a back-scattered wave with reversed vertical wavenumber.
- PSI describes a high-frequency, large-scale parent wave $(\boldsymbol{K}_0, \omega_0)$ decaying into two smaller-scale, near-inertial waves $(|\boldsymbol{K}_1| \sim |\boldsymbol{K}_2|, \omega_1 \sim \omega_2 \sim f)$ with nearly opposite wavenumbers and similar frequencies.
- TPG, similarly to PSI, is a type of parametric generation. While in PSI, the second harmonic (parent wave) decays into two first harmonics (near-inertial daughter waves); in TPG, the third harmonic (parent wave) decays into a first and a second harmonic

($\omega_0 \sim 3\omega_{1\cup 2} \sim \frac{3}{2}\omega_{2\cup 1}$ for sum interactions and $\omega_1 \sim 3\omega_{0\cup 2} \sim \frac{3}{2}\omega_{2\cup 1}$ for difference interactions).

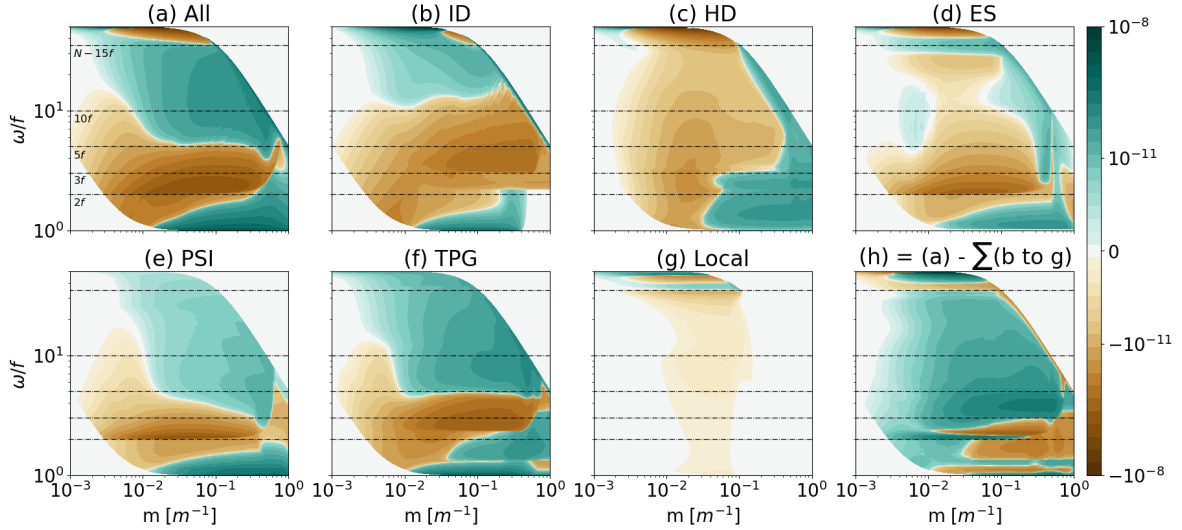

Figure 4.8: Method M5 - Content spectrum of energy transfers within the GM76 model in (a), filtered energy transfers for ID in (b), for HD in (c), for ES in (d), for PSI in (e), for TPG in (f), for local interactions in (g), and the remainder in (h) as the difference of the overall integral in (a) and the sum of the filtered local and non-local interactions in (b to g).

Fig. 4.8 (a) shows overall energy transfers for the whole integral where the sum and difference interactions are added. The energy transfers resulting from the non-local interactions are shown for ID in (b), HD in (c), ES in (d), PSI in (e), and TPG in (f). Fig. 4.8 (g) presents the energy transfers by local interactions. Despite growing attention in recent literature within the hydrostatic approximation (e.g. Wu and Pan, 2023; Dematteis et al., 2024) suggesting a potential role for these triads, our results prove otherwise for the non-hydrostatic system. The energy transfers by local interactions are very weak across the entire spectrum and show only slight activity at very high frequencies. Their spatial extent and magnitudes are minimal, confirming the early predictions of the pioneering work in McComas and Bretherton (1977) that local interactions are energetically insignificant. The remainder in Fig. 4.8 (h) is defined by the difference between Fig. 4.8 (a) and Fig. 4.8 (b to g). The remainder arises by the fact, that the filters are not strictly exclusive between each other. The remainder thus represents the compromise between both the overlap between filters and triads that may not fall into the categories in Tab. 4.2.

Note that in Tab. 4.2, we list two conditions for sum and difference interactions for ID, HD, ES and TPG respectively. For sum interactions ID1, HD1, ES1 and TPG1 are interchangeable with ID2, HD2, ES2 and PSI2 respectively as only the interacting components $(\boldsymbol{K}_1, \omega_1)$ and $(\boldsymbol{K}_2, \omega_2)$ are switched – one of them being a near-inertial wave. For difference interactions the first and second filters differ from each other in each mechanism. In ID1, HD1, ES1 and TPG1 in difference interactions, the near-inertial wave is the second interacting wave $(\boldsymbol{K}_2, \omega_2 \sim f)$. However, in ID2, HD2, ES2 and TPG2 in difference interactions, the role of near-inertial wave changes as it becomes the generated wave $(\boldsymbol{K}_0, \omega_0 \sim f)$. This makes low frequencies susceptible to all interaction mechanisms, including PSI which also generates

subharmonics in difference interactions. To understand the positive and negative energy transfers, we investigate the sum and difference interactions for each one of the non-local interactions mechanisms in the following sections.

4.5.1. Induced diffusion and horizontal diffusion

ID is thought to cause a spectral diffusion of wave action predominantly to high frequencies, see (McComas and Bretherton, 1977). However, Fig. 4.8 (b) reveals a loss of energy at intermediate frequencies $2f \lesssim \omega \lesssim 10f$ predominantly to higher frequencies $\omega > 10f$, but also weakly to lower frequencies $\omega < 2f$. Energy transfers to higher frequencies are due to the sum interaction, see Fig. 4.9 (a), while the smaller energy transfers toward small frequencies are due to the difference interactions classified as ID2, see Fig. 4.9 (c).

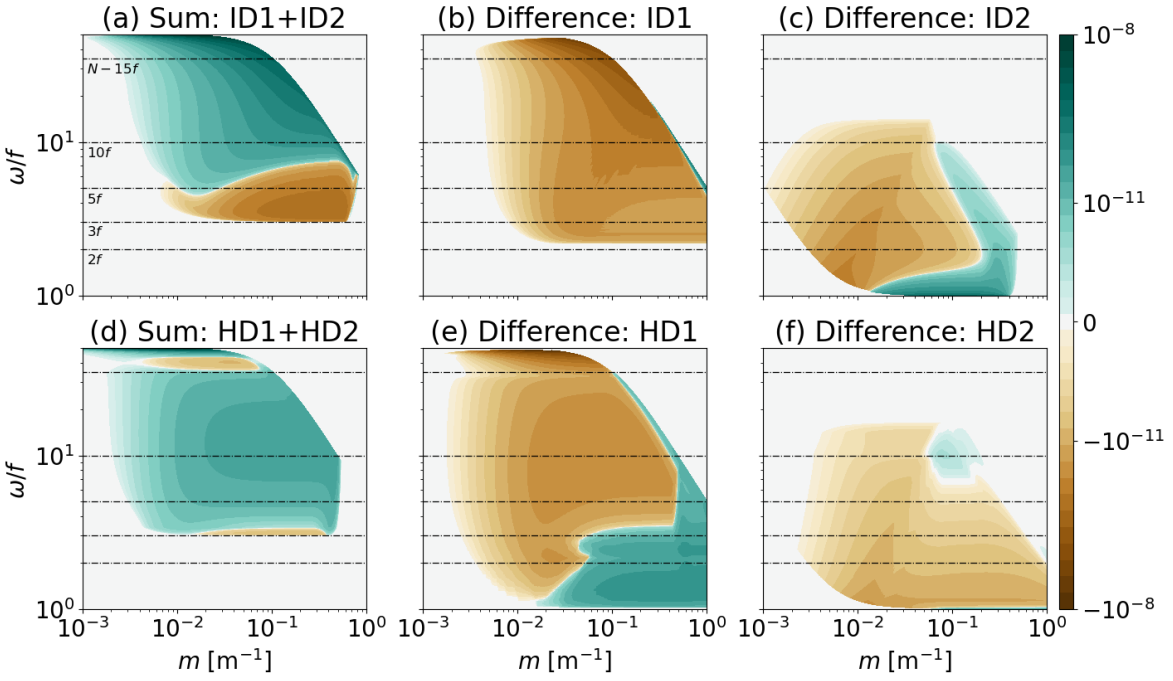

Figure 4.9: Method M5 - (a) shows the energy transfers for the sum interactions for ID1 and ID2, (b) for the difference interaction for ID1, and (c) for the difference interaction for ID2. (d) shows the energy transfers for the sum interactions for HD1 and HD2, (e) for the difference interaction for HD1, and (f) for the difference interaction for HD2.

To understand the positive or negative energy transfers in the sum and difference interactions in ID, we can make the following simplified scaling argument. In ID1 and ID2 the rate of energy change for the primary wave ω_0 due to sum interactions, see Fig. 4.9 (a), may be approximated by simplified energy and frequency scalings. We approximate the integrand of the sum interaction in the resonant kinetic equation as follows:

$$|C^{-}_{-\boldsymbol{K}_0\boldsymbol{K}_1\boldsymbol{K}_2}|^2 \left(E_1E_2 - \frac{\omega_1}{\omega_0}E_0E_2 - \frac{\omega_2}{\omega_0}E_1E_0\right) \sim |C^{-}_{-\boldsymbol{K}_0\boldsymbol{K}_1\boldsymbol{K}_2}|^2\omega_1\omega_2\left(A_1A_2 - A_0A_2 - A_1A_0\right)$$
$$\sim |C^{-}_{-\boldsymbol{K}_0\boldsymbol{K}_1\boldsymbol{K}_2}|^2\omega_1\omega_2A_2(A_1 - A_0) \tag{4.7}$$

where we introduce wave action $A = \frac{E}{\omega}$. In the last approximation in Eq. (4.7), we assume a strongly separated frequency scale $\omega_0 > \omega_1 \gg \omega_2 \sim f$, and thus the scaling of wave action $A_0 < A_1 \ll A_2$. The energy transfer is then positive as long as the vertical wavenumbers hold the relation $m_1 < m_0$ and thus the wave action $A_1 > A_0$. Thus, energy is transferred into the wave ω_0, implying a forward energy cascade towards high-frequencies. The lower the frequency of the generated wave is, the less separated are the frequencies ω_1 and ω_0 within the triad. When a low frequency wave ω_0 is generated through ID, then $\omega_1 \approx \omega_0$ but with vertical wavenumbers $m_1 > m_0$ and thus wave action $A_0 > A_1$. Such interactions are dominant in the lower frequency range where ID is active $3f < \omega < 10f$ and leads to an energy loss.

In ID1, the energy transfer to ω_0 via a difference interaction, see Fig. 4.9 (b), is approximated by:

$$|C^{-}_{-\boldsymbol{K}_0\overset{+}{\boldsymbol{K}}_1\overset{-}{-\boldsymbol{K}_2}}|^2 \left(E_1E_2 + \frac{\omega_2}{\omega_0}E_1E_0 - \frac{\omega_1}{\omega_0}E_0E_2\right) \sim |C^{-}_{-\boldsymbol{K}_0\overset{+}{\boldsymbol{K}}_1\overset{-}{-\boldsymbol{K}_2}}|^2\omega_1\omega_2(A_1A_2 + A_1A_0 - A_0A_2)$$
$$\sim |C^{-}_{-\boldsymbol{K}_0\overset{+}{\boldsymbol{K}}_1\overset{-}{-\boldsymbol{K}_2}}|^2\omega_1\omega_2A_2(A_1 - A_0) < 0, \qquad (4.8)$$

where we assume $\omega_2 \sim f \ll \omega_0 < \omega_1$, and thus the amplitude hierarchy $A_2 \gg A_0 > A_1$. The energy transfers then indicate a net energy loss for ω_0.

In ID2, see Fig. 4.9 (c), we again consider:

$$|C^{-}_{-\boldsymbol{K}_0\overset{+}{\boldsymbol{K}}_1\overset{-}{-\boldsymbol{K}_2}}|^2\omega_1\omega_2(A_1A_2 + A_1A_0 - A_0A_2) \sim |C^{-}_{-\boldsymbol{K}_0\overset{+}{\boldsymbol{K}}_1\overset{-}{-\boldsymbol{K}_2}}|^2\omega_1\omega_2A_0(A_1 - A_2), \qquad (4.9)$$

with near-inertial wave $\omega_0 \sim f$ such that $\omega_0 \ll \omega_2 < \omega_1$ and thus the wave actions $A_0 \gg A_2 > A_1$. Provided $A_2 > A_1$, the transfer into ω_0 is negative. However, when approaching the boundaries of our evaluation domain in (ω_0, m_0), difference interactions are not allowed anymore as $m_1 > m_0$ has to hold. Difference interactions are nevertheless possible between waves with opposing vertical wavenumbers relative to the generated wave. In this case $m_2 > m_1 \gg -m_0$, and thus $A_2 < A_1 \ll A_0$, leading therefore to an energy gain at higher vertical wavenumbers m_0.

In contrast to ID, HD is specially strong at extracting energy at the highest frequencies, see Fig. 4.8 (c). The scaling arguments used in ID can be adopted for the HD filters, now arguing with hierarchies in horizontal wavenumber rather than in vertical wavenumber. For sum interactions, see Fig. 4.9 (d), we can argue with Eq. (4.7) where we consider the near-inertial wave $\omega_2 \sim f$ such that the wave actions have the relation $A_2 \gg A_{0,1}$. The sign of the energy transfers depends on wave actions A_0 and A_1, which are now determined by the difference in horizontal wavenumbers k_0 and k_1 instead of by vertical wavenumbers m_0 and m_1 as in ID.

Similarly, we can adopt the scaling arguments from the difference interactions in ID1 and ID2 to understand HD1 and HD2 in Fig. 4.9 (e,f) respectively. Because HD is not constrained by a fixed relation between vertical wavenumbers, the near-inertial wave in HD does not necessarily have a small vertical wavenumber. In this way, HD1 can also transfer energy between low or high frequency waves with opposite vertical wavenumbers leading to the large positive or negative energy transfers at the respective low or high frequencies, see Fig. 4.9 (e). HD2 leads to an energy loss at low frequency waves with small horizontal but large vertical wavenumber through the interaction between two high frequency waves with high horizontal but small vertical wavenumbers ($\omega_0 \ll \omega_2 < \omega_1$, $k_0 \ll k_2 < k_1$, but $m_0 \gg m_1 > m_2$) such that $A_0 \gg A_2 > A_1$, see Fig. 4.9 (f). Surprisingly, HD shares similarities with ES as we see in Section 4.5.2.

4.5.2. Elastic scattering

ES is postulated to reduce vertical asymmetries, see McComas and Bretherton (1977). For example, a downward wave $(\boldsymbol{K}_1, \omega_1)$ interacting with a near-inertial wave $(\boldsymbol{K}_2, \omega_2 \sim f)$ (where the vertical wavenumber is $m_2 \approx 2m_1$) generates an upward wave $(\boldsymbol{K}_0, \omega_1)$ with opposite vertical wavenumber $m_1 \approx -m_0$, balancing energy fluxes. Though once considered energetically insignificant in symmetric spectra (McComas and Bretherton, 1977), Wu and Pan (2023) show ES contributes to a forward energy cascade in frequency. Our results in Fig. 4.8 (d) show a similar behavior with predominantly a forward energy cascade in frequency and vertical wavenumber.

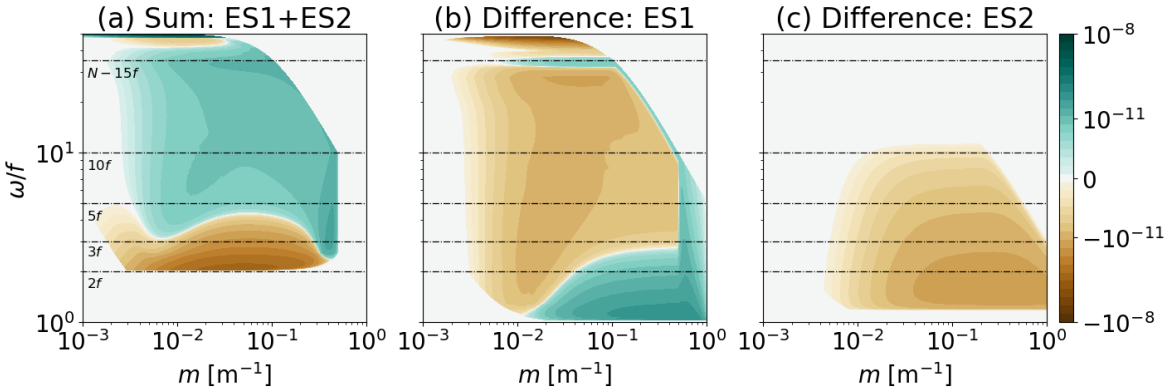

Figure 4.10: Method M5 - (a) shows the energy transfers for the sum interactions for ES1 and ES2, (b) for the difference interaction for ES1, and (c) for the difference interaction for ES2.

To understand the positive and negative energy transfers, we separate sum interactions, see Fig. 4.10 (a) and difference interactions, see Fig. 4.10 (b,c) for ES1 and ES2 respectively. The behavior of sum interactions ES1+ES2 are similar to the sum interactions of ID1+ID2 (and HD1+HD2), and the same scaling argument can be adopted. In this way, sum interactions at low frequencies mainly between $2f < \omega < 4f$, lose energy to high frequencies mainly $\omega > 4f$. The difference to ID is, however, that the vertical wavenumber separation between the near-inertial and the high frequency waves is inverted, such that the near-inertial wave has a relatively high vertical wavenumber, while the high frequency waves have a vertical wavenumber with half the amplitude of the near-inertial one. This leads ES to be active at lower frequencies but still larger than $2f$, and over all vertical scales.

The difference interactions ES1, see Fig. 4.10 (c), reveal an overall loss of energy in phase space, where the scaling arguments of ID1 can be adopted. Similarly to HD1's difference interactions, at low frequencies and high vertical wavenumbers, ES1 leads to an energy gain. In these spectral regions, where the vertical wavenumbers $m_0 \sim m_1$ are relatively high, such that the near-inertial wave has a very large vertical wavenumber $m_2 \sim 2m_0$ and its wave action A_2 is no longer necessarily greater than $A_0 \sim A_1$, the positive terms in the integrand in the first line in Eq. (4.8) may dominate, leading to a positive energy transfer to low frequencies and high vertical wavenumbers.

The difference interactions ES2, see Fig. 4.10 (d), reveal an overall loss of energy in phase space. Here and as in HD2, the energy of the low frequency wave ω_0 is extracted by the interaction of the two vertically opposing waves with the frequency hierarchy $\omega_1 > \omega_2$ and

therefore $A_1 < A_2$. Adopting the simplified scaling of the integrand in Eq. (4.9), ES2 leads to negative energy transfers.

4.5.3. Parametric subharmonic instability

PSI actively transfers energy to small vertical scales and near-inertial frequencies. Our results are in agreement with previous literature, see Eden et al. (2019b) and Wu and Pan (2023), where the strongest energy loss due to PSI is located between frequencies $2f < \omega < 4f$. PSI serves as the strongest mechanism to transfer energy to near-inertial frequencies, see Fig. 4.8 (e).

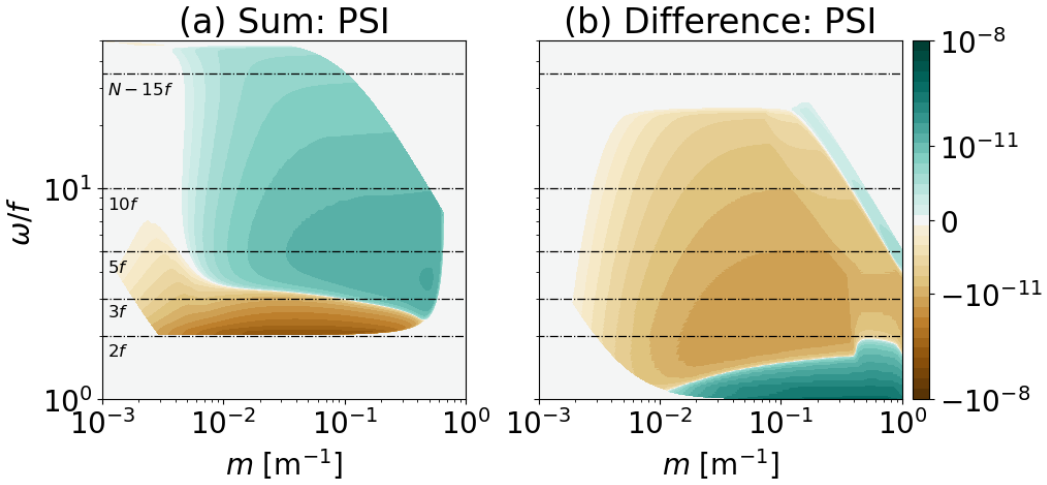

Figure 4.11: Method M5 - (a) shows the energy transfers for the sum interactions for PSI, (b) for the difference interaction for PSI.

Fig. 4.11 (a) shows the energy transfers in sum interactions classified as PSI. These act primarily as forward energy transfers from spectral regions with low frequencies and low wavenumbers to high frequencies and high wavenumbers. Considering the sum interaction of two waves with similar low frequencies $\omega_1 \sim \omega_2$ and high (opposite) vertical wavenumbers $m_1 \sim -m_2$ that generate a wave with twice the frequency but much smaller vertical wavenumber, such that the respective wave actions scale as $A_0 \gg A_1 \sim A_2$, we can adopt the simplified scaling arguments and approximate the integrand in resonant kinetic equation as follows

$$|C^{-}_{-\boldsymbol{K}_0\boldsymbol{K}_1\boldsymbol{K}_2}|^2\omega_1\omega_2\,(A_1A_2 - A_0A_2 - A_1A_0) \sim -|C^{-}_{-\boldsymbol{K}_0\boldsymbol{K}_1\boldsymbol{K}_2}|^2\omega_1\omega_2A_0(A_1 + A_2) < 0 \qquad (4.10)$$

leading to an energy loss. However, since PSI sum interactions do not impose strict constraints on the vertical wavenumbers of the daughter waves, as long as the frequencies match the condition $\frac{\omega_0}{2} \sim \omega_1 \sim \omega_2$, cases can arise where positive energy transfers dominate. That is the case, when the generated high frequency wave has a large vertical wavenumber while the vertical wavenumbers of the interacting waves are much smaller, and thus the wave actions scale as $A_1 \sim A_2 \gg A_0$. PSI sum interactions primarily act as forward energy transfers originating from regions of low frequency and or small vertical wavenumber to spectral regions with high frequency and large vertical wavenumber.

In PSI difference interactions, see Fig. 4.11 (b), the only viable configuration involves the generation of a low-frequency wave ω_0 by the interaction of a high-frequency wave ω_1 with a second lower-frequency wave ω_2. Due to the ordering of frequencies, the second interacting wave must always have lower frequency than ω_1. Hence, it is not possible for two low-frequency waves to generate a high-frequency wave via PSI-type difference interactions, see upper bound in Fig. 4.11 (b). Instead a high frequency wave ω_1 interacts with its half-harmonic to generate another half-harmonic wave, such that low frequency waves are excited. If the high frequency wave has a smaller vertical wavenumber compared to the interacting half-harmonic, and thus the generated half-harmonic, we can simplify the scaling argument with the wave action hierarchy $A_1 \gg A_0 \sim A_2$ to

$$|C^{-}_{-\boldsymbol{K}_0\boldsymbol{K}_1-\boldsymbol{K}_2}|^2\omega_1\omega_2\,(A_1A_2 + A_0A_1 - A_0A_2) \sim |C^{-}_{-\boldsymbol{K}_0\boldsymbol{K}_1-\boldsymbol{K}_2}|^2\omega_1\omega_2A_1(A_0 + A_2) > 0. \tag{4.11}$$

If the high frequency wave has a larger vertical wavenumber compared to the half harmonics, we can use the wave action hierarchy $A_1 \ll A_0 \sim A_2$ and thus the scaling argument

$$|C^{-}_{-\boldsymbol{K}_0\boldsymbol{K}_1-\boldsymbol{K}_2}|^2\omega_1\omega_2\,(A_1A_2 + A_0A_1 - A_0A_2) \sim -|C^{-}_{-\boldsymbol{K}_0\boldsymbol{K}_1-\boldsymbol{K}_2}|^2\omega_1\omega_2A_0A_2 < 0. \tag{4.12}$$

PSI's difference interactions lead then to energy transfers from high frequency waves to subharmonics, exciting so near-inertial waves.

4.5.4. Third parametric generation TPG

Fig. 4.8 (f) shows a strong localized energy loss due to TPG around $\omega \sim 3f$. By involving the third harmonic, TPG turn out to be more active in transferring energy towards high-frequencies compared to PSI. On the other hand, the inverse cascade is weaker in TPG compared to PSI.

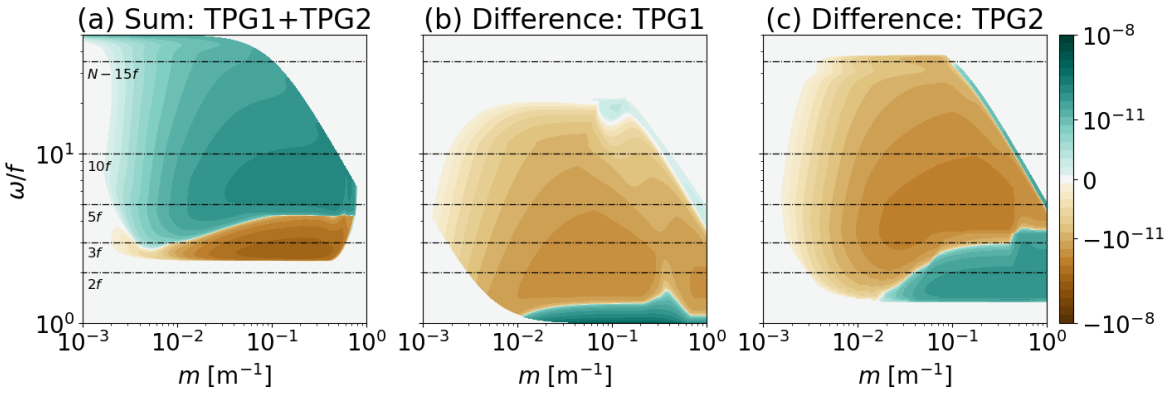

Figure 4.12: Method M5 - (a) shows the energy transfers for the sum interactions for TPG1 and TPG2, (b) for the difference interaction for TPG1, and (c) for the difference interaction for TPG2.

Fig. 4.12 (a) shows the energy transfers in sum interactions classified as TPG. TPG sum interactions are effective in generating the third harmonic out of the interaction of the first and second harmonic. If we consider the second interacting wave to be near-inertial, then the frequencies in the interacting triad are related as $\omega_2 \sim f \sim \frac{\omega_0}{3} \sim \frac{2}{3}\omega_1$. TPG acts similarly to PSI, and thus we can adopt the scaling arguments to explain the resulting forward energy transfers

from low frequencies to high frequencies over all vertical scales. Now however, the largest energy loss is around the third harmonic $\omega_0 \sim 3f$. If the frequency of the generated wave approaches $\omega_0 \rightarrow 3f$, then the interacting waves tend to have large vertical wavenumbers with opposite sign compared to generated wave. In this case, the wave action hierarchy is $A_0 \gg A_1$ or A_2, such that TPG, similarly to PSI, leads to negative energy transfers at low frequencies $\omega_0 \rightarrow 3f$. TPG transfers energy to high frequencies as the interacting waves have smaller frequencies and vertical wavenumbers compared to the generated waves, such that we consider the wave action hierarchy $A_0 \ll A_{1,2}$ leading to positive energy transfers.

The difference interactions of TPG are similar to the ones of PSI. The difference is that TPG can either generate a near inertial wave with TPG1 or its second harmonic through TPG2. However, the scaling arguments can be readily adopted from PSI where the generated low frequency high vertical wavenumber wave gains energy from the high frequency but lower vertical wavenumber waves, see Fig. 4.12 (b,c). TPG leads to negative energy transfers at higher frequencies, where $\omega_0 \sim \frac{\omega_1}{3} \sim \frac{2}{3}\omega_2$ still holds, as the wave action hierarchy $A_1 \ll A_0$ or A_2 holds and thus $A_0(A_1 - A_2) < 0$ or $A_2(A_1 - A_0) < 0$.

4.5.5. Relative importance between local and non-local interactions

The relative importance of local versus non-local interactions has remained controversial despite decades of research. Different studies often reach contradictory conclusions, leaving the role of specific interaction mechanisms under debate. Since the pioneering work of McComas and Bretherton (1977), it has generally been assumed that non-local triads account for most of the transfer rate. More recently, however, Wu and Pan (2023) and Dematteis et al. (2024) have argued that local interactions may also produce substantial energy changes. Within the non-local interactions, McComas and Bretherton (1977) initially dismissed ES as irrelevant due to the symmetry of the GM76 model, but has been shown – including in agreement with our results – to contribute to a forward cascade to small scales. Following these authors, ID was originally considered to make a major part of the total down-scale energy cascade in GM-like models. However, Eden et al. (2019b) recently challenged the importance of ID, while arguing PSI to be the most relevant process. To address this long-standing dispute, we evaluate the relative contributions of the established mechanisms (ID, PSI, ES), as well as the newly identified HD and TPG.

We quantify the importance of each mechanism by integrating positive and negative energy transfers separately within specific frequency bands and comparing them with the total transfer, see Fig. 4.13. The results are displayed on a symmetric logarithmic scale for the total integral (blue) and the contributions of ID (orange), HD (green), ES (red), PSI (purple), TPG (brown), and local interactions (pink). The frequency bands span from near-inertial frequencies ($f < \omega < 2f$) to high frequencies approaching the buoyancy frequency ($N - 15f < \omega < N$). In most cases, the total transfer reflects the competition between positive (energy gain) and negative (energy loss) contributions, and the relative importance of each mechanism varies strongly with frequency.

At near-inertial frequencies ($f < \omega < 2f$), the total transfer is positive, reflecting an inverse cascade from mid-frequencies ($2f < \omega < 5f$) mainly driven by PSI and TPG. In the $2f < \omega < 3f$ band, negative transfers dominate, largely due to the strong signature of TPG. For the inverse energy cascade, ID, HD, and ES play only a minor role.

In the $3f < \omega < 5f$ range, both TPG and ID become more important, with each

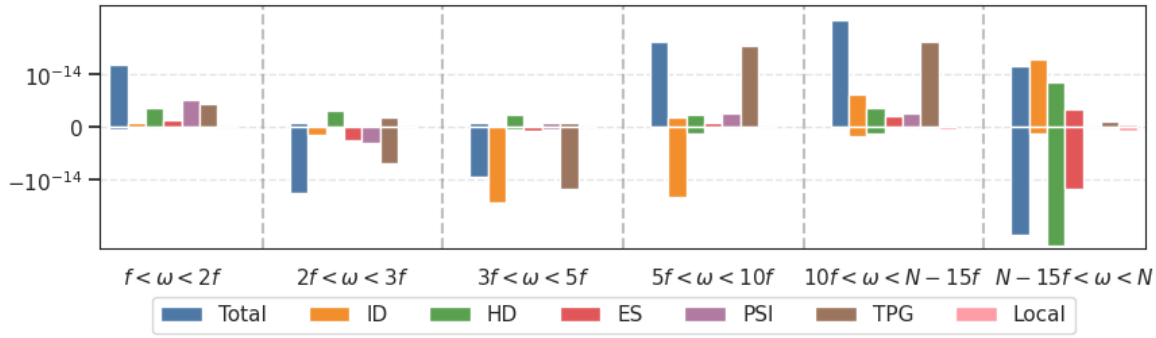

Figure 4.13: Method M5 – Integrated positive and negative energy transfers within specific frequency bands for the total integral and the filtered local and non-local interaction mechanisms within the GM76 model.

contributing to energy loss mainly transferred to small scales. TPG emerges as the dominant forward-driving mechanism from intermediate ($2f < \omega < 5f$) to high frequencies ($5f < \omega < N - 15f$), acting nearly across the entire spectrum. At $5f < \omega < 10f$, ID again contributes negatively, opposing the positive total transfer, while HD, ES, and PSI remain weak.

At the highest frequencies ($N - 15f < \omega < N$), the total transfer nearly balances between positive and negative contributions. In this range, ID becomes more prominent, consistent with its tendency to redistribute energy toward higher frequencies. HD and ES also grow in strength, acting in line with the total transfer and nearly balancing the positive and negative components.

In summary, our results show that local interactions (pink) remain weak at all frequencies, confirming the long-standing view that they are largely irrelevant for energy redistribution in internal wave spectra. Diffusion mechanisms – ID and the newly found HD - are active at high frequencies and remain a substantial contributor to energy transfers. PSI is powerful in driving the inverse cascade, but it also contributes to forward transfers and cannot be considered the sole controlling mechanism. The newly identified TPG is active throughout the spectrum and explains a large portion of the net energy transfers. Finally, sensitivity tests indicate that the relative balance among ID, HD, ES, PSI and TPG depends on the slope of the internal wave spectrum, see supplemental materials for details.

4.6. Conclusions

We review the methods to evaluate wave-wave interactions presented in Eden et al. (2019c) and extend them by including inertial and buoyancy oscillations. As in Eden et al. (2019c), we consider all interactions, i.e. resonant and non-resonant, for the complete IGW spectrum for a fixed choice of time interval $\Delta t = 10$ days. Our evaluations conserve energy and satisfy the fundamental relation up to numerical precision. We reduce the computation cost from a couple of days (with method M1) to 4 hours by exploiting horizontal isotropy and vertical symmetry in the wave spectrum (with method M2), see Tab. 4.3 for cost-efficiency of the different methods. We make use of the simplification in method M2 to increase resolution, such that we conserve energy up to a permil in the relative error. We evaluate all interactions and also only resonant interactions for a single slice in positive phase space ($k_x, k_y = 0, m$). All evaluations show the characteristic energy loss between $2f < \omega < 3f$ that is redistributed

to lower and higher frequencies. Higher resolution reveals another energy sink at higher frequencies near $\omega_0 \rightarrow N - f$. This pattern of energy transfers constitutes the principal character of IG wave-wave interactions and has been reported extensively in literature, see Olbers (1974, 1976); Pomphrey et al. (1980); Hibiya et al. (1998); Polzin and Lvov (2011); Lvov et al. (2012); Eden et al. (2019b,c, 2020). Since the pattern does not change across evaluations for all interactions compared to only resonant interactions, we confirm the finding in Sebastia Saez et al. (2025a) that non-resonant interactions vanish under the consideration of horizontally isotropic wave spectra. However, non-resonant interactions may become important when considering anisotropic wave spectra. The inclusion of inertial and buoyancy oscillations leads to only weak energy transfers which are at least two orders of magnitude smaller than within the IGW spectrum, and are thus negligible. This is because inertial and buoyancy oscillations can engage in only a limited range of interactions constrained by the resonance conditions for sum and difference interactions.

Method	IGW spectrum	Rel. error	CPUs	Comp. time	# triads
M1	GM76	$O(10^{-7})$	$80 \times (40 \times 128)$	80×6 h	$O(10^{15})$
M2		0.4%	$2 \times (10 \times 128)$	2×2 h	$O(10^{11})$
M3		1%	15×128	6 h	$O(10^{11})$
M4		6%	5×128		$O(10^{12})$
M5		17%	7 (local)	1 h	$O(10^{11})$
		4%	10×128	2 h	$O(10^{13})$
	Cuspless GM76	7%			
	Cutoff GM76	4%		4 h	
	$E \sim m^{-3}\omega^{-2}$	2%			
	$E \sim \begin{cases} m^{-2}\omega^{-2} \text{ for } m < 0.1\,\mathrm{m}^{-1} \\ m^{-3}\omega^{-2} \text{ for } m > 0.1\,\mathrm{m}^{-1} \end{cases}$	1%			

Table 4.3: Cost-performance per method and considered initial IGW spectrum. The relative error is measured by $\Delta = \frac{\int \partial_t E d\boldsymbol{K}}{\int |\partial_t E| d\boldsymbol{K}}$. For M1 we use a vectorized Python script, for M2 a sequential Cython script, for M3 a vectorized Julia script and for M5 a sequential Julia script.

We further improve the methods for the evaluation of the kinetic equation by carrying out coordinate transformations to (m, k, ϕ)- and (m, ω, ϕ)-space (methods M4 and M5 respectively) to less than 1 hour for similar resolution which can be evaluated even in a private machine, see Tab. 4.3. Furthermore, the implementation of the analytical derivation for the resonant condition provides considerable improvements in computational cost. These numerical improvements allow for even higher resolution and thus specially for non-uniform grids - a simple loglog-grid for (m, k, ϕ)-transformation and a more complex non-equidistant grid for (m, ω, ϕ)-transformation. With methods M4 and M5 we further increase resolution and achieve energy conservation up to only a small error, see Tab. 4.3. The major advantage of method M5, apart from its computational efficiency, is the handling of the integration over resonant surfaces. For each integration we define a grid tailored for the specific resonant surface. This leads to a higher accuracy in our integrations, which in turn leads to a reduction of the Boltzmann rates. Considering the canonical GM76 model, we find low Boltzmann rates everywhere in the spectral domain except at the highest frequencies. For modifications of the IGW spectrum we find low Boltzmann rates everywhere.

The canonical GM76 model fails to produce a convergent scattering integral due to its

−2-slope in vertical wavenumber, combined with the wavenumber independence of the interaction coefficient for growing wavenumbers. As a result, increasing the integration domain shifts the separation scale toward smaller scales, indicative of divergence. Although filtering regions with high Boltzmann rates helps enforce convergence by removing strongly interacting triads that violate the weak-interaction assumption, this approach does not address the root cause of divergence and may compromise dynamical consistency. Introducing a spectral cutoff at high wavenumbers – intended to mimic the transition from IGWs to turbulence – can formally enforce convergence, but it also introduces sharp discontinuities in the energy transfer spectrum and elevates Boltzmann rates near the cutoff, potentially invalidating the weak-interaction framework. Notably, this pathological behavior persists even when the inertial peak is removed, as in the cuspless variant of the GM76 model. In contrast, prescribing a steeper vertical wavenumber slope, such as −3, or implementing a gradual slope transition from −2 to −3, supports convergence of the scattering integral, and maintains consistency with weak-interaction theory. Such spectral modifications more realistically capture the energetic decay characteristic of the IGW–turbulence transition.

With the aim to understand what mechanism sets the energy transfers by wave-wave interactions in the scattering integral, we adopt the foundational theory for inertial-range IGWs from McComas and Bretherton (1977), and extend it by introducing newly identified mechanisms – horizontal diffusion (HD) and third parametric generation (TPG) – and local interactions. We decompose the energy transfers within the canonical GM76 model for local and non-local (ID, HD, ES, PSI and TPG) interaction mechanisms and arrive at the following conclusions. As correctly predicted by McComas and Bretherton (1977), non-local triad interactions are essential to understanding spectral energy transfers within the IGW field. Contrary to recent findings, e.g. Wu and Pan (2023); Dematteis et al. (2024), which evaluate the scattering integral within the hydrostatic approximation, our results reveal that local interactions are negligible for the non-hydrostatic system. Regarding non-local interactions, ID provides bidirectional energy transfers in frequency (but not in vertical wavenumber), where energy from intermediate frequencies $2f < \omega < 10f$ is transferred to the lower ones, but predominantly to higher frequencies. HD provides forward energy transfers to small scales, and a weak backward cascade in frequency. HD leads to the strongest energy loss at the highest frequencies. ES provides only small energy transfers to higher frequencies and vertical wavenumbers. PSI drives backward energy transfers in frequency and a forward cascade in vertical wavenumber. PSI is particularly effective in transferring energy to subharmonics and is the principal driver of the backward cascade in frequency. TPG provides a forward energy cascade in both frequency and vertical wavenumber. TPG is particularly effective in transferring energy to higher harmonics and is the principal driver of the forward cascade.

The total energy transfers by all the interactions reflect a dynamic competition among the various interaction mechanisms, with some mechanisms even opposing each other. The relative importance of these mechanisms depends on the shape of the IGW spectra. Sensitivity experiments with different vertical wavenumber slopes reveal that a −2-slope particularly enhances PSI, while shallower slopes preserve its role in the backward energy cascade, and steeper slopes diminish its contribution. TPG is also favored by −2 and shallower slopes; however, unlike PSI, it continues to drive strong energy transfers even for steeper slopes. Interestingly, ID produces substantial energy transfers across the entire range of slopes, often mirroring the behavior of the total integral. In contrast, HD results in modest energy gains across all frequencies for slopes steeper than −2, but causes small energy losses on shallower

slopes, with particularly pronounced effects at high frequencies. Among the non-local interactions, ES consistently remains the weakest contributor.

In summary, this study offers a comprehensive re-examination and numerical evaluation of the kinetic equation governing IGW interactions under weak nonlinearity. By incorporating inertial and buoyancy oscillations into the kinetic framework and advancing numerical methods to evaluating energy transfers, we achieve both theoretical clarity and computational efficiency. Our results confirm the dominant role of non-local triads in shaping spectral energy transfers, while also demonstrating the negligible impact of local interactions. Furthermore, we highlight the limitations of scattering integral when considering the canonical GM76 model in modeling energy transfers in a dynamically consistent way and propose spectral modifications that ensure convergence and consistency with weak-interaction theory. These developments not only refine our understanding of wave-wave interactions but also motivate exploring energy transfers within modified IGW spectra, and the role of non-resonant interactions within anisotropic spectra.

Acknowledgments

This paper is a contribution to the subprojects W6 and L2 of the Collaborative Research Centre TRR 181 "Energy Transfers in Atmosphere and Ocean" funded by the Deutsche Forschungsgemeinschaft (DFG, German Research Foundation) under project number 274762653. Our computations have been performed at the Deutsche Klimarechenzentrum (DKRZ) in Hamburg, Germany. During the preparation of this manuscript, AI has been used for language polishing. We also acknowledge discussions with William Young.

Data availability statement

The novel numerical methods developed and used in this study can be accessed via `https://github.com/pablosebastiasaez/ScINET.git`, see Sebastia Saez (2025). The observational data used is taken from Walter et al. (2020).

A. The Garrett-Munk model - GM76

The Garrett-Munk (GM) model spectrum (Garrett and Munk, 1975, 1979) is a representation of the energy density spectrum E of IGWs derived from observations. The GM76 model describes a horizontally isotropic and vertically symmetric spectrum with a spectral power law of -2 in frequency and vertical wavenumber. There are several different versions of the GM model spectrum. For our purpose, we slightly modify the GM76 model (from Müller et al., 1978) by introducing the small wavenumber parameter ϵ to be able to evaluate the original GM76 model at $k = 0$ and $m = 0$. Here we use the following form

$$E(m,\omega,\phi) = \frac{E_0}{4\pi} A(m,\omega) B(\omega) \quad , \quad E(\boldsymbol{K}) = E(m,\omega,\phi)\, J^{-1} = \frac{E(k,\phi,m)}{k} \tag{13}$$

with wavenumber angle ϕ and

$$A(m,\omega) = n_a \frac{\tilde{A}(m/m^*(\omega))}{m^*(\omega)} \quad , \quad \tilde{A}(\zeta,t,s) = (1+\zeta^s)^{t/s} \quad , \quad B(\omega) = \frac{n_b f}{\omega\sqrt{\omega^2 - f^2}} \tag{14}$$

$$J = \frac{\partial(\boldsymbol{K})}{\partial(m,\omega,\phi)} \quad , \quad m^*(\omega(k,m),c^*) = \frac{\sqrt{N^2-\omega^2}}{c^*} \quad , \quad c^* = \frac{1}{j^*\pi}\int_{-h}^{0} N(z)\,dz \tag{15}$$

where J denotes the Jacobi determinant for the coordinate transformation $(\boldsymbol{K}) \rightarrow (m,\omega,\phi)$, m^* the vertical wavenumber scale (often referred as bandwidth) equivalent to the vertical mode number $j^* = 10$, $c^* \approx N/m_r = 0.5\,\mathrm{m\,s^{-1}}$ for $N = 50f$ and the roll-off vertical wavenumber $m_r = 0.01\,\mathrm{m^{-1}}$, and $\zeta = m/m^*(\omega)$. The energy density spectrum E is factorized with the wavenumber shape function A and the frequency shape function B. Both shape functions integrate to one by choice of the parameter $n_a = s\Gamma(t/s)\Gamma(s^{-1})/\Gamma((t-1)s^{-1})$, where Γ is the Gamma function, and $n_b = 2\pi^{-1}$ for $N/f \gg 1$, slope $t = -2$ and parameter $s = 2$. We use $E_0 = 3\times10^{-3}\ \mathrm{m^2/s^2}$ as classical parameter, but note that this is probably an underestimation of the typical wave energy (Pollmann et al., 2017). Fig. 14 (a,b) shows the modified energy density spectrum evaluated at $k_x^\epsilon = k_x + \epsilon\min(|k_x|)$ with $\epsilon = 0.5$ and similar for k_y^ϵ and m^ϵ. Fig. 15 shows the horizontal kinetic energy of the original GM76 model (in solid red), of

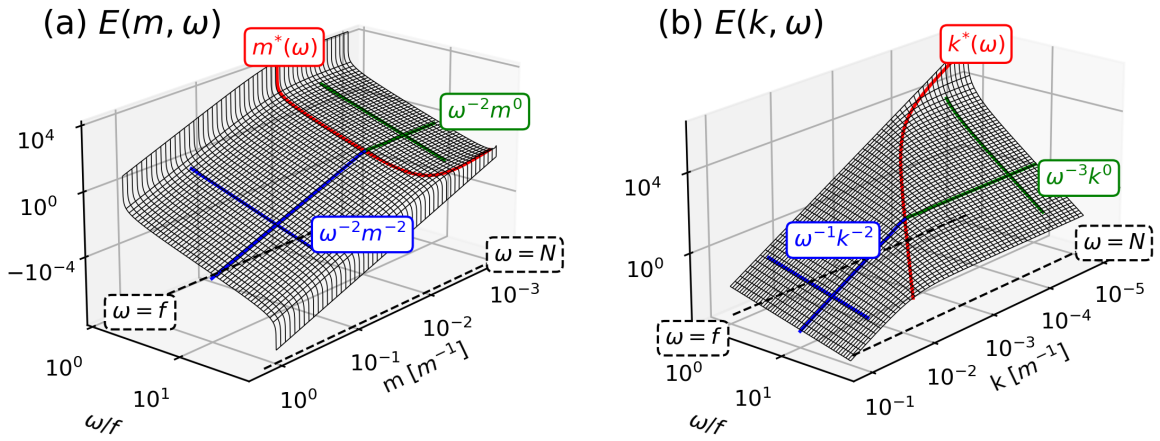

Figure 14: The GM76 model - a typical energy density spectrum of IGWs in the ocean as in Eq. (13) integrated over wave angle ϕ in (m, ω)-space in (a) and in (k, ω)-space in (b).

the GM76 model with $\epsilon = 0.5$ (in dashed-dotted green) and GM76 model with $\epsilon = 0.1$ (in dotted black), and from observations for different depth levels against frequency. We use the observations from a mooring located 30°29.04'N and 30°11.7'W for the period between 8^{th} August 2017 and 10^{th} May 2018, see Walter et al. (2020), and apply the Welch's method for a window of 4 times the inertial period. The peak of maximal horizontal kinetic energy of the GM76 models is shown by crosses of the corresponding colors. Note that the original GM76 model has a singularity at $\omega = f$, thus the spectrum is cropped at $\min(\boldsymbol{K})$. The peak at the inertial frequency of the shallowest observations is an order of magnitude smaller than the GM76 model and the GM76 with $\epsilon = 0.5$ model, and two orders of magnitude smaller than the GM76 with $\epsilon = 0.1$ model. However, the inertial frequency peaks in the observations decrease with depth. For our purposes, we use the GM76 model as an idealized description of the IGW energy density spectrum and assess the importance of the inertial frequency peak by making use of the modified GM76 with $\epsilon = 0.5$ representing the more realistic scenario.

B. Resonant condition in (ω, m, ϕ)-space as in Olbers (1974)

Here we outline how to find a resonant triad for IGWs for the resonant conditions of the sum and difference interactions. We make use of the geometry of the wave triplet in horizontal polar coordinates in phase space and arrive to Eq. (4.2). Furthermore,

$$\cos(\theta) = \frac{k}{K} = \sqrt{\frac{\omega^2 - f^2}{N^2 - f^2}} \quad \text{and} \quad \sin(\theta) = \frac{m}{K} = \text{sign}(m)\sqrt{\frac{N^2 - \omega^2}{N^2 - f^2}}, \tag{16}$$

where θ is the angle between $\boldsymbol{k}$ and $\boldsymbol{K}$ on the horizontal plane, to express $(k_2/k)^2(\omega, \omega_1, \omega_2 = \omega_0 \mp \omega_1, k_1/k)$ as

$$\left(\frac{k_2}{k}\right)^2 = \frac{\cos(\theta_2)^2 m_2^2}{\sin(\theta_2)^2 k^2} = \frac{\cos(\theta_2)^2 (m - m_1)^2}{\sin(\theta_2)^2 k^2} = \frac{\cos(\theta_2)^2}{\sin(\theta_2)^2}\left(\frac{sin(\theta)}{\cos(\theta)} - \frac{k_1}{k}\frac{\sin(\theta_1)}{\cos(\theta_1)}\right)^2. \tag{17}$$

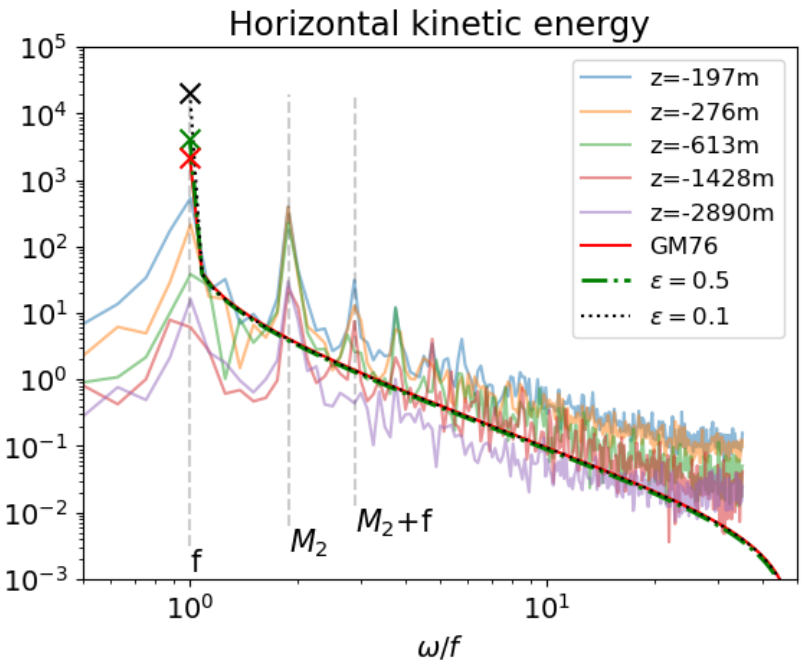

Figure 15: Horizontal kinetic energy $E_h(\omega) = \int \frac{N^2-\omega^2}{N^2-f^2} \frac{\omega^2+f^2}{\omega^2} E(\omega, m) dm$ for the GM76 and GM76 with $\epsilon = \{0.5, 1\}$, and inferred from mooring observations for different depth levels.

Now we reformulate 17, such that we can solve for the roots of k_1/k as

$$(\tan(\theta) - \frac{k_1}{k}\tan(\theta_1))^2 = \tan(\theta_2)^2(1 + \left(\frac{k_1}{k}\right)^2 - 2\frac{k_1}{k}\cos(\gamma)), \tag{18}$$

which we can express in terms of the known frequencies.

The roots of k_1/k, putting $\cos(\gamma) = \pm 1$, determine the limits at which the integration in the (ω_1, k_1)-plane is restricted. We find three ranges in ω_1 with a minimum and maximum limit each for k_1/k: $\omega_1 < \omega/2$, $\omega/2 < \omega_1 < 2\omega$ and $\omega_1 > 2\omega$. The limits are then reformulated to m_1/m-limits using the relation $m = \sin(\theta)K = \frac{\sin(\theta)}{\cos(\theta)}k$.

5

Supplemental Material to Wave-wave interactions of internal gravity waves. Part B: Spectral energy transfers in a typical internal gravity wave field

Sebastia Saez, P., Chouksey, M., Eden, C., Olbers, D., (2025): "Wave-wave interactions of internal gravity waves. Part B: Spectral energy transfers in a typical internal gravity wave field", submitted to *Journal of Physical Oceanography*

Authors: Pablo Sebastia Saez[a] [1], Manita Chouksey[a,b], Carsten Eden[a] and Dirk Olbers[c]
Affilitations: a: Institut für Meereskunde, Universität Hamburg, Germany, b: Leibniz-Institut für Ostseeforschung Warnemünde, Germany c: Alfred Wegener Institute for Polar and Marine Research, and MARUM-Center for Marine Environmental Sciences, Germany

Copyright Statement

© Copyright 2025 American Meteorological Society (AMS). For permission to reuse any portion of this Work, please contact permissions@ametsoc.org. Any use of material in this Work that is determined to be "fair use" under Section 107 of the U.S. Copyright Act (17 U.S. Code § 107) or that satisfies the conditions specified in Section 108 of the U.S. Copyright Act (17 USC § 108) does not require the AMS's permission. Republication, systematic reproduction, posting in electronic form, such as on a website or in a searchable database, or other uses of this material, except as exempted by the above statement, requires written permission or a license from the AMS. All AMS journals and monograph publications are registered with the Copyright Clearance Center (`https://www.copyright.com`). Additional details are provided in the AMS Copyright Policy statement, available on the AMS website (`https://www.ametsoc.org/PUBSCopyrightPolicy`).

[1]Corresponding author: Pablo Sebastia Saez - pablo.sebastia.saez@uni-hamburg.de

5.1. Dependence of the energy transfers by a gradual transition from a −2 to a −3-slope in vertical wavenumber and a changing roll-off wavenumber m_r^*

We explore the dependence of the energy transfers by gradually varying the second roll-off wavenumber $m_{r2}^* = (1\,\mathrm{m}^{-1}, 0.08\,\mathrm{m}^{-1}, 0.06\,\mathrm{m}^{-1}, 0.05\,\mathrm{m}^{-1}, 0.02\,\mathrm{m}^{-1}, \mathrm{m}_{\mathrm{r1}}^*)$ for the transition of a −2-slope to a −3-slope in vertical wavenumber, see Fig. 5.1. For the case of a higher second roll-off, energy transfers resemble more the ones for a −2-slope. With the gradual nearing of the second roll-off to the first, we observe a gradual resemblance to the energy transfers with a single −3-slope in vertical wavenumber.

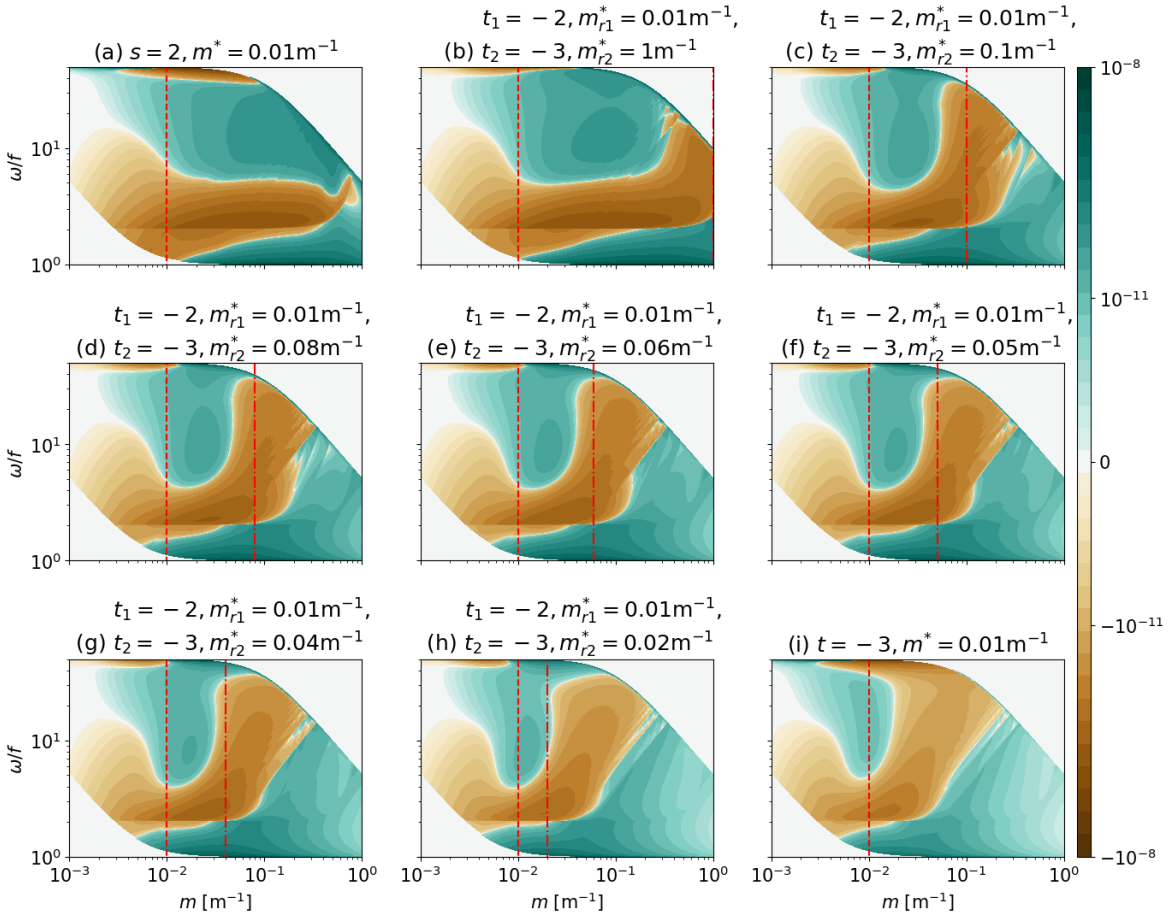

Figure 5.1: Transition of the energy transfers within the GM76 model in (a) to the GM-like model with −3-slope in vertical wavenumber in (i). In (b) to (h) we gradually decrease the bandwidth m_{r2}^* that marks the change in slope $t_1 = -2$ to $t_2 = -3$ in vertical wavenumber. The roll-off wavenumber m_{r1}^* is marked by the vertical dashed red line and m_{r2}^* by the red dash-dotted line.

5.2. Comparison of different filters for triad interaction mechanisms

The assessment of local interactions is sensitive to the filtering criteria used to distinguish them from non-local ones. In our approach, we filter all mechanisms independently from each other. As the filters are not strictly defined, but allow for some tolerance tuned with the parameters η and γ, there is some overlap expected. The more permissive the tolerance is, the more overlap is allowed which is accumulated in the reminder. Similarly, if the filter for local interactions is defined rather permissively, as we find to be a factor 4 in either vertical wavenumber or frequency as used in Dematteis et al. (2024), the overlap of local interactions with non-local ones increases, and so does the reminder, see Fig. 5.2 (h).

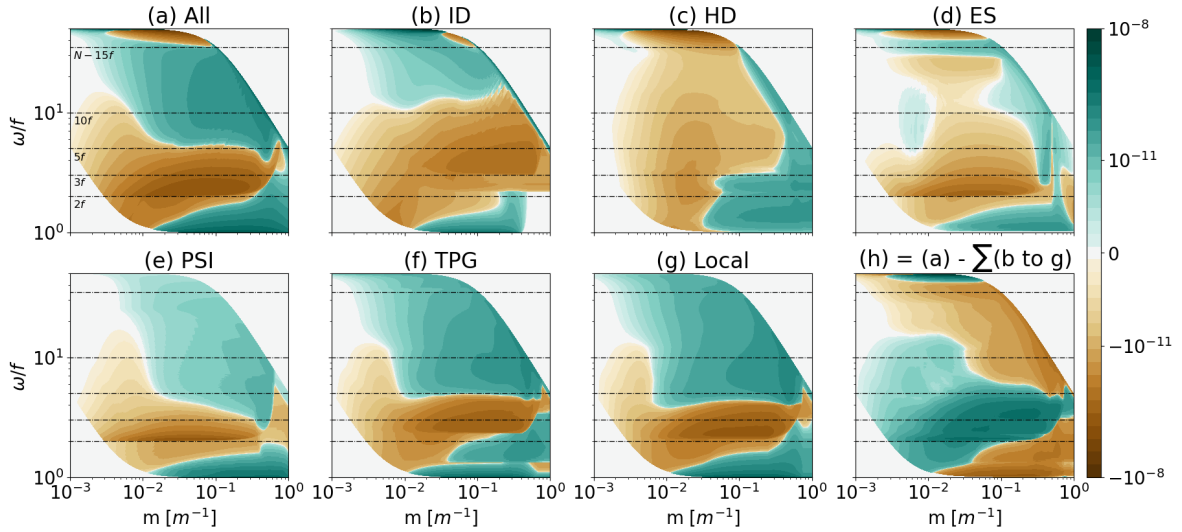

Figure 5.2: Method M5 - Content spectrum of energy transfers within the GM76 model in (a), filtered energy transfers for ID in (b), for HD in (c), for ES in (d), for PSI in (e), for TPG in (f), for local interactions in (g), and the reminder in (h) as the difference of the overall integral in (a) and the sum of the filtered local and non-local interactions in (b to g). The filters for non-local interactions are the same as in Tab. 2. For local interactions, we adopt the filter used in Dematteis et al. 2024, where the interacting waves are allowed to be a factor 4 in either vertical wavenumber or frequency apart.

We assess the relative importance of the interaction mechanisms for a shallower −1.5-slope in vertical wavenumber, see Fig. 5.4 (a), for the case of a changing −2- to −3-slope, see Fig. 5.4 (b), and a steeper −3-slope, see Fig. 5.3 and Fig. 5.4 (c). Shallower slopes lead to overall enhanced energy transfers, while steeper slopes weaken the energy transfers. Shallower slopes enhance the contributions from PSI, whereas steeper slopes weaken PSI becoming even the least important contribution to the overall energy transfers after local interactions, see Fig. 5.4 (c). TPG contributions to energy changes are also enhanced at shallower slopes and weaken with steeper slopes. However, TPG remains one of the dominant mechanisms at low frequencies even for steeper slopes. ID and HD gain relevance for both shallower and steeper slopes, whereas for the canonical GM76 model (−2-slope) ID and HD are comparatively weak. ES becomes more relevant at shallower slopes but remains weak relative to the other non-local interactions. Local interactions are consistently weak across all cases.

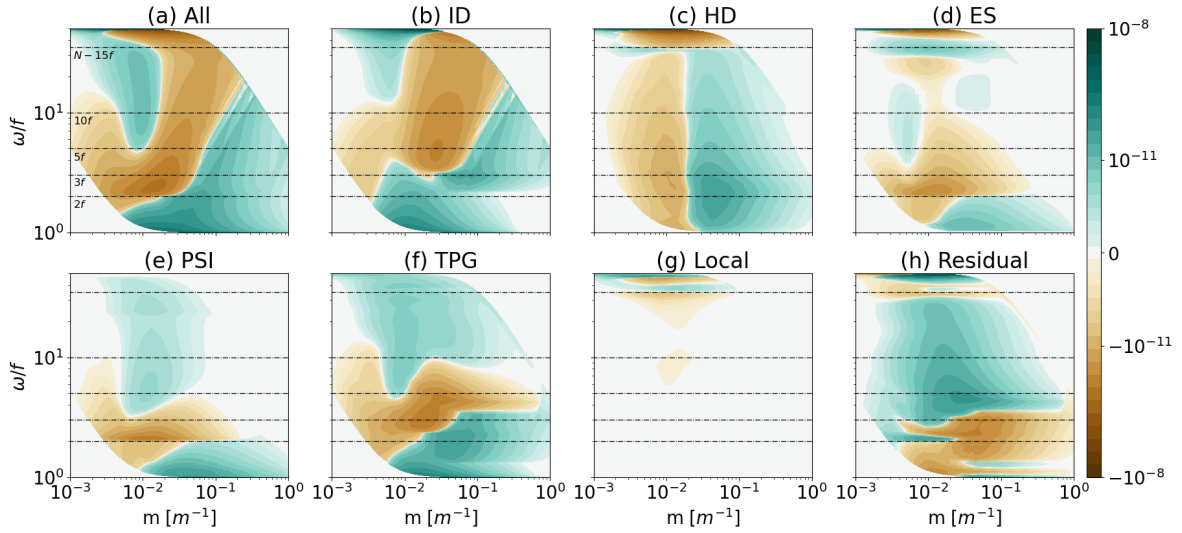

Figure 5.3: Method M5 - Content spectrum of energy transfers within the GM76 like model with −3-slope in vertical wavenumber in (a), filtered energy transfers for ID in (b), for HD in (c), for ES in (d), for PSI in (e), for TPG in (f), for local interactions in (g), and the reminder in (h).

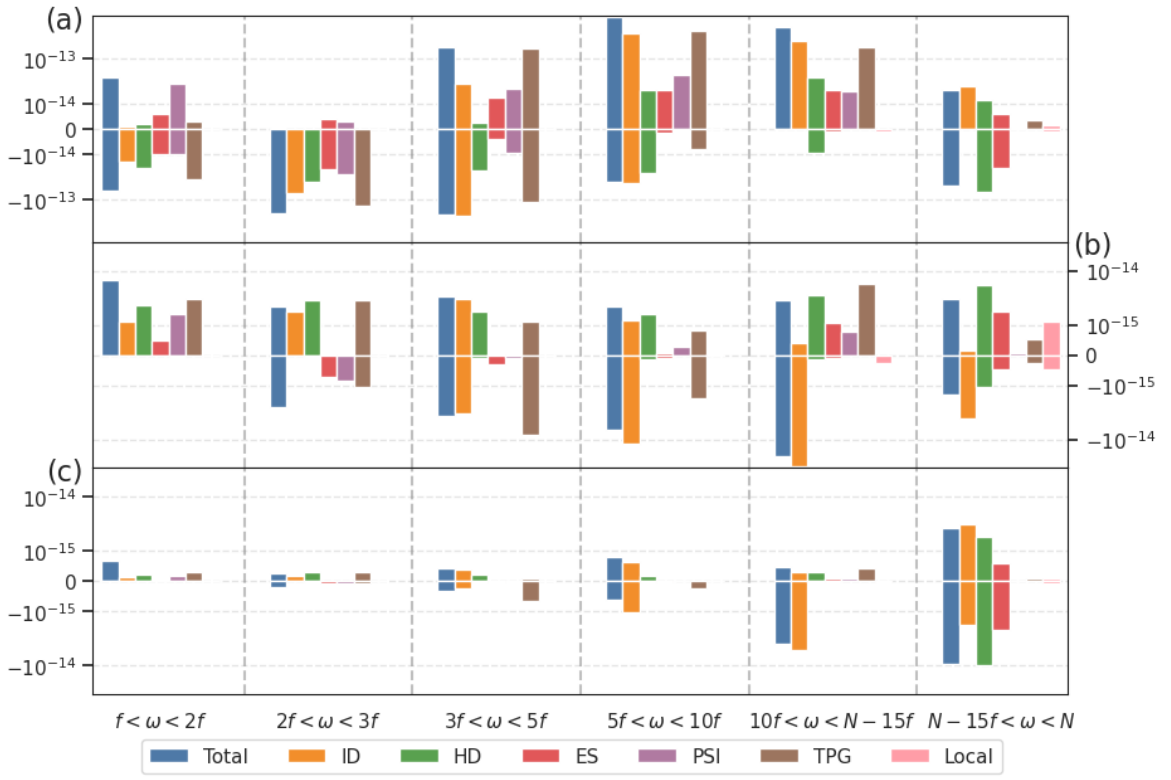

Figure 5.4: Method M5 - Integrations of positive and negative energy transfers within specific frequency bands for the total integral and the filtered local and non-local interaction mechanisms within the GM76 like model with a vertical wavenumber slope of $t = -1.5$ in (a), of $t_1 = -2$ that changes to $t_2 = -3$ at the roll-off wavenumber $m^*_{r2} = 0.1m^{-1}$ in (b), and of $t = -3$ in (c).

6

Conclusions and perspectives

This thesis has examined the dynamics of IGWs in the ocean, focusing on the physical mechanisms governing the evolution of IGW energy. Observations have long indicated that the distribution of IGW energy across wavenumbers exhibits a degree of consistency throughout the global ocean, see Garrett and Munk (1972). This universal spectral shape of the IGW energy spectrum is commonly described by the GM model (Cairns and Williams 1976 and Munk 1981). The persistence of this characteristic spectral shape suggests the presence of a systematic redistribution of energy in the phase space from the regions of generation to those of dissipation. Such a transfer, or energy cascade, implies an active balance maintained through the interaction of IGWs with their changing environment, such as the mean flow, IGWs or other types of waves, boundaries like topography, etc. Building upon the observed regularity of the oceanic IGW spectrum, this thesis has explored whether, and if so how, wave-mean flow and wave-wave interactions affect this apparent universality of the IGW spectrum, i.e., a state that is close to or even in temporal equilibrium.

The route of an energy balance of the IGW field in the ocean is followed through the formulation of a radiative transfer equation – a kinetic equation describing the evolution of spectral energy density in physical, phase space and time. This approach provides a unifying description of the wave propagation and refraction, and the redistribution of IGW energy under the influence of background mean flow, stratification, and additional source terms (inter alia external forcing or internal nonlinear processes like wave-wave interactions). Throughout the thesis, various forms of kinetic equations have been derived and applied to characterize the evolution of the IGW spectrum. Chapter 2 focuses on linear processes – wave propagation, refraction, and wave-mean flow interations – that arise from large-scale variations in background stratification and mean flow. Chapters 3 and 4 examine nonlinear wave–wave interactions as a mechanism for energy transfer within the IGW field.

6.1. Synthesis and perspectives across the three main chapters

This chapter reviews and synthesizes the highlights from the three chapters of this thesis. Each chapter's synthesis is followed by a discussion of the limitations of the current work, perspectives, and possible avenues for future research. Together, this thesis provides a coherent and detailed picture of the dynamical pathways governed by wave-mean flow and wave-wave interactions that shape the IGW field in the ocean.

6.1.1. How do interactions between internal gravity waves and a mesoscale eddy shape the internal gravity wave spectrum?

Chapter 2 introduces the Internal Wave Energy Model (IWEM), a new numerical framework based on the radiative transfer equation. Using a six-dimensional radiative transfer equation, IWEM solves the ray tracing equations and separates key physical processes: wave propagation, refraction, explicit energy exchanges between IGWs and mean flow, and energy loss due to wave breaking and dissipation driven by vertical and horizontal refraction. Observations of a coherent mesoscale eddy in the Canary Current System are used to prescribe both the background environment as an idealized mean flow and a depth-varying stratification, and the initial IGW spectrum by the universal GM76 model. IWEM then models how this full IGW spectrum evolves in response to the background, specifically through wave–mean flow interactions and refraction by the stratification under the conditions that the wave's periods and wavelengths are much shorter compared to the ones from the mean flow (WKBJ approximation). The simulations presented in Chapter 2 are the first to comprehensively model the evolution of a complete IGW spectrum within a mesoscale eddy under the WKBJ approximation. The main highlights from Chapter 2 are:

- IGW energy decreases most strongly at the eddy rim and near the surface, while a small energy gain occurs at the eddy center. The spectral analysis from observations supports this finding. Within the limitations of the WKBJ approximation, we do not find any significant difference between the influences of a cyclonic compared to an anticyclonic eddy on the evolution of the IGW field.
- Vertical shear leads to a net energy loss from the wave field to the mean flow and leads to critical-layer-like dissipation: Wave packets are refracted to larger vertical wavenumbers until they cross the boundaries of the resolved wavenumber space, where they have become small enough such that they most likely become unstable and break. Vertical-shear-driven refraction and the resulting wave breaking dominate the energy loss and are strongest at the eddy rim.
- Lateral shear leads to wave energy gain from the mean flow outside the eddy once horizontal anisotropy in the wave spectrum is developed. Horizontal anisotropy develops in the first place by the effect of vertical refraction, energy transfer from the wave field to the mean flow by vertical shear, and wave energy dissipation by vertical shear. Lateral-shear-driven refraction only weakly contributes to dissipation.
- Diagnosed diapycnal diffusivities peak at the rim with estimates of $\kappa \sim 10^{-7}$ to $10^{-5}\,\mathrm{m^2\,s^{-1}}$, consistent with enhanced near-surface mixing driven by strong vertical shear and sharp stratification gradients.

The findings of Chapter 2 are indicative of the complex interplay between IGWs and mesoscale eddies in the ocean, where the IGW field is modified from the initial universal GM76 model. Fig. 6.1 shows the importance of the different terms in the radiative transfer equation to the energy changes relative to the initial IGW field. Each term is integrated over the simulation period, wavenumber space, and depth to provide a measure of the net effect of each process on the IGW energy budget locally. Fig. 6.1 (a) shows the overall change of energy in the IGW field after 6 days of simulation. This picture is the result of the combined effects of wave propagation shown in Fig. 6.1 (b), wave-mean flow interaction in Fig. 6.1 (c), and dissipation in Fig. 6.1 (d), which amount locally up to a change of maximal 50 % of the

initial IGW energy, respectively. Seemingly, propagation effects are the largest contributor, but only due to the consideration of open boundary conditions, which allows energy to leave the domain. Under consideration of cyclic boundary conditions, propagation effects integrate to less than 1 % energy loss relative to the initial IGW energy over the whole domain. On the contrary, wave-mean flow interaction and dissipation are internal processes, which do not depend on the boundary conditions. There is a net energy loss within the eddy and concentrated at the eddy rim by vertical wave-mean flow interaction and an energy gain outside the eddy by horizontal wave-mean flow interaction that can amount locally to 50 % of the initial IGW energy. In the overall integral, horizontal wave-mean flow interaction leads to an energy gain of 6.7 % of the initial IGW energy, while vertical wave-mean flow interaction leads to an energy loss of 5 %. Horizontal and vertical wave-mean flow interactions are almost in balance in the overall integral, however, they lead to significant local changes in the IGW energy budget. Wave dissipation by wave breaking leads only to a small energy loss of a few percent locally and 2.3 % in the overall integral. This small percentage of energy loss is, however, significant enough to provide diapycnal diffusivities of the order of $\kappa \approx 10^{-5}\,\mathrm{m^2 s^{-1}}$ locally. Such values for the diapycnal diffusivity are of the same order as local estimates from observations in the open ocean, e.g., from the North Atlantic Tracer Release Experiment (Ledwell et al., 1993, 1998).

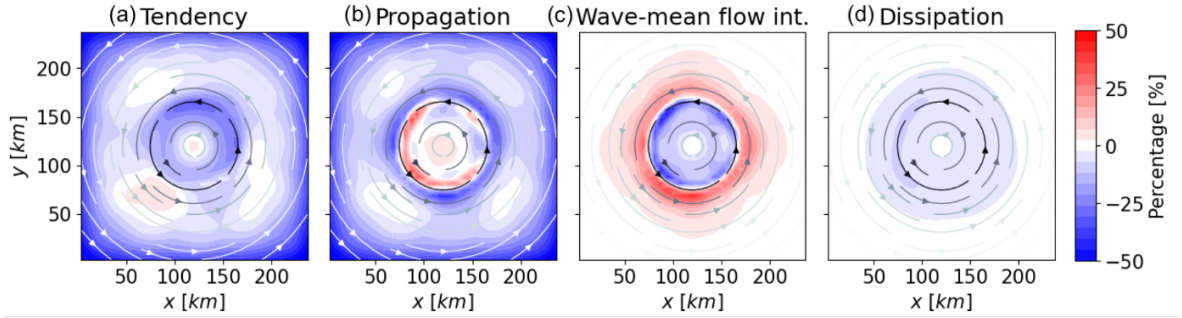

Figure 6.1: Integrated effects of different processes acting on the IGW field relative to the initial IGW energy after 6 days of simulation. (a) Overall change of IGW energy. (b) Contribution from wave propagation. (c) Contribution from wave-mean flow interactions. (d) Contribution from wave dissipation by wave breaking. Each term is integrated over the simulation period, wavenumber space, and depth and normalized by the initial wave energy to provide a measure of the net effect of each process on the IGW energy budget locally.

These findings show how the IGW field deviates from the initial GM76 model (see Fig. 2.10), which is believed to characterize the IGW field universally as a steady-state solution to the radiation balance. The results rather hint towards a picture of a dynamic equilibrium where the IGW spectrum is continuously reshaped by interactions with their surroundings, rather than a steady-state solution. As the IGW field experiences significant energy changes across the spectrum, one naturally wonders how these modifications influence the underlying surroundings. This is indeed one limitation of the current work, as the feedback of the modified IGW spectrum or induced mixing on the mean flow and stratification has not been considered. However, the energy gain and loss via wave-mean flow interactions are almost in balance in the overall integral, suggesting that the feedback on the mean flow might be small. Furthermore, the potential feedback on the mean flow can be estimated by knowing the energy transfers from the IGW field to the mean flow by vertical wave-mean flow interactions and turns out to be small. Assuming that the diagnosed energy transfer from the IGW field

to the mean flow by vertical wave-mean flow interactions is transferred to the mean flow as kinetic energy, one can estimate its change after the simulation period. By integrating the energy transfer over the simulation period, wavenumber, and physical space and comparing it to the total eddy kinetic energy, one finds that the energy transfer corresponds to about 0.01 % of the total eddy kinetic energy.

Outlook

The findings of Chapter 2 suggest that the feedback of the IGW field on the mean flow is overall negligible. However, over longer timescales, in regions with stronger IGW activity or more complex realistic eddying flows, this feedback could become more significant and warrants further investigation. A natural way to explore such scenarios is through frameworks that account for the evolution of wave characteristics in turbulent flows.

To better understand how such feedback might emerge, it is instructive to consider the work of Dong et al. (2023). Building on Bühler (2014) and consistent with the discussion in Chapter 2 of this thesis, they apply the ray-tracing framework to examine the evolution of near-inertial gravity waves in a quasigeostrophic turbulent flow with constant stratification and Coriolis parameter. In this case, wave refraction solely includes the terms related to the Doppler shift by the background flow. The tendency equations of the horizontal wavenumber components (k_x, k_y) become independent of the vertical wavenumber m and therefore form a closed system. It is thus sufficient to solve the initial value problem for (k_x, k_y), which delivers two eigenvalues $\lambda_\pm = \pm\sqrt{\partial_x U^2 + \frac{1}{4}(\partial_x V + \partial_y U)^2 - (\partial_x V - \partial_y U)^2}$, where a divergence-free flow has been assumed, i.e., $\partial_x U + \partial_y V = 0$, and the vorticity $\partial_x V - \partial_y U$ has been introduced. This simple calculation shows that the eigenvalue $\lambda_\pm$ can become imaginary as the vorticity becomes large or real as the vorticity becomes weak. In this form, the frequency changes governing the interactions follow exponential functions of the form $e^{\lambda_\pm t}$. If the eigenvalue is real, $\boldsymbol{K}(t)$ and thus $\omega(\boldsymbol{K}(t))$ grow or decay exponentially, leading to significant energy exchanges between the IGW field and the mean flow, and potentially to wave breaking and energy dissipation. If the eigenvalue is imaginary, $\boldsymbol{K}(t)$ and thus $\omega(\boldsymbol{K}(t))$ oscillate, which in turn limits the effective energy transfers between the IGW field and the mean flow. Within this framework, Dong et al. (2023) observe that energy spreads across frequencies, eventually forming a well-populated IGW energy spectrum. This process allows for energy exchange between IGWs and the mean flow, though over longer timescales than those considered by Kafiabad et al. (2019) in the context of wave scattering at geostrophic turbulence, which is addressed below. It is important to note, however, that Dong et al. (2023) report an approximate error of 10 % in absolute frequency conservation. Since ray propagation and refraction are sensitive to this, it may contribute to additional frequency spreading. However, identifying the conditions under which the eigenvalues are real or imaginary is crucial, as it determines which behaviors are most relevant for oceanic flows.

Recently, Kafiabad et al. (2019); Cox et al. (2023) in the diffusion regime and Savva et al. (2021) for the general case derive a kinetic equation for the non-hydrostatic Boussinesq system linearized about a background flow using the Wigner transform (see Ryzhik et al., 1996) and avoid the WKBJ assumption of slowly varying background conditions. Their kinetic equation takes a similar form to the radiative transfer equation used in this thesis, but they replace the refraction terms and wave-mean flow interactions by a scattering operator. The scattering operator describes a catalytic redistribution of wave energy, resembling a diffusion process, as previously observed in the diffusion limit by Kafiabad et al. (2019);

Cox et al. (2023). Their approach restricts wave–mean flow interactions – more specifically, wave scattering at the vortical mode described by steady and weak geostrophic turbulence – along constant-frequency cones by resonant triad interactions ($\omega_{\text{wave}} = \omega_{\text{wave}} \pm \omega_{\text{vortex}}$ where $\omega_{\text{vortex}} = 0$). This perspective effectively implies that there is no energy exchange between the IGW field and the mean flow, which are governed by the changes in frequency $\dot{\omega}$, see Eq. (1.6). In their simulations, Savva et al. (2021) initialize a horizontally isotropic IGW field along a single ring in wavenumber space with horizontal scales comparable to the mean flow. These scales are thus rather large, and the waves are thus stable compared to the GM spectrum considered in Chapter 2, which contains a wide range of scales down to the dissipation scale. Choosing such initial conditions, Savva et al. (2021) find that there is no net energy transfer between the IGW field and the mean flow. If wave breaking were to be considered, their spectrum would probably become anisotropic, and then wave-mean flow interactions could lead to energy exchanges, as is the case for the findings in Chapter 2. Furthermore, they limit their analysis to resonant interactions, while non-resonant interactions with finite frequency mismatch could also lead to energy exchanges once anisotropy kicks in, as has been shown in Chapter 3 of this thesis.

The contrasting views between Savva et al. (2021), Dong et al. (2023) and Chapter 2 of this thesis highlight that the significance of wave–mean flow interactions may be highly regime-dependent. The question therefore arises whether there is a regime in which both viewpoints, wave scattering within constant frequency cones and ray tracing leading to wave refraction and wave-mean flow interactions, are valid. More specifically, it remains to be investigated under which conditions the IGW field propagates in the real ocean and if they lead to energy exchanges between IGWs and mean flow. And if so, how significant the feedback of the IGW field on the mean flow is, when considering a random eddy field or more realistic scenarios rather than an isolated eddy as in this thesis.

Ray tracing seems to be able to match some of the dynamics captured by the scattering approach when the eigenvalue is imaginary, frequency changes oscillate, and energy exchanges between waves and mean flow are limited, while refraction by the mean flow acts as the catalytic interaction described by Savva et al. (2021). Furthermore, wave dissipation by wave breaking is straightforward to implement in the ray tracing framework and readily included in IWEM, which addresses a key process for the ocean's circulation, i.e., wave-induced mixing. IWEM is thus a powerful tool to address these questions by systematically investigating how the nature of wave-mean flow interactions changes in a more realistic setting and under which conditions energy exchanges with the mean flow become significant or negligible. Understanding these dynamics is crucial for accurately modeling not only the IGW field and its role in ocean mixing but also assessing the relevance of feedback mechanisms involved in energy redistribution between the IGW field and the mean flow. Future research could explore this two-way coupling, investigating how changes in the IGW field affect mesoscale eddy dynamics and vice versa.

Building upon the scattering of waves at geostrophic turbulence, it remains to be investigated how the complete IGW spectrum evolves in a random eddy field, rather than isolated waves at a single frequency ring as in Savva et al. (2021). Furthermore, non-resonant interactions have been largely neglected in previous studies, but as shown in Chapter 3 of this thesis, they may contribute to energy transfers once anisotropy develops in the IGW spectrum. For that, one could build upon the kinetic equation derived in Chapter 3 for the case of IGWs interacting with geostrophic turbulence.

6.1.2. How do nonlinear interactions among internal gravity waves govern energy transfers within the oceanic internal gravity wave field?

Chapter 3 revisits the kinetic equation for wave-wave interactions in a non-hydrostatic Boussinesq system with rotation and constant stability frequency. Stemming from over 50 years of research since the dissertation by Olbers (1974) and building upon the pioneering work from Hasselmann (1966) on the Lagrangian theory of ocean waves, wave-wave interactions have been a long-standing theoretical problem in wave turbulence theory. Since then, various forms of the kinetic equation have been derived under different approximations or limits, such as the hydrostatic approximation or neglecting rotation (see Chapter 3 for details). Furthermore, most of the derived kinetic equations are formulated under resonant conditions, where the frequency mismatch of the interacting waves vanishes, $\omega_0 - (\omega_1 \pm \omega_2) = 0$, while non-resonant interactions with finite frequency mismatch have been largely neglected. Despite the long history of research on this topic, systematic comparisons between different derivations have been lacking.

The main focus of Chapter 3 is to reconcile the derivations from two different frameworks: the Lagrangian as in Olbers (1974, 1976) and the Eulerian as in the lines of Eden et al. (2020). One might expect that the resulting kinetic equations should be identical under the same approximations, however, nonlinearities enter the Lagrange and Euler equations in different ways, resulting in differences in the kinetic equations. In the Lagrangian system, nonlinearities arise via the pressure gradient and the continuity equation, while in the Eulerian system, they enter through the advection terms in the momentum equation. The highlights of Chapter 3 are the following consequences of this difference:

- The different forms that nonlinearities take in the Lagrange and Euler equations lead to different definitions of wave amplitudes that carry different physical meanings. Consequently, the two frameworks yield different energies, interaction coefficients, and thus different kinetic equations in general.
- Despite these fundamental differences, the Lagrangian and Eulerian interaction coefficients and thus kinetic equations coincide under resonant conditions.
- For non-resonant interactions, the two frameworks differ. However, for horizontally isotropic spectra (GM-like), non-resonant interactions vanish, and the Lagrange and Euler frameworks become identical.

Outlook

Resonant interactions are generally considered the dominant mechanism for energy transfers in IGW fields. In the case of resonant interactions, the frequency mismatch $\Omega = \omega_0 \mp (\omega_1 + \omega_2)$ vanishes, leading to a time response function Eq. (3.48) that grows linearly in time and can amount to large energy transfers. Non-resonant interactions, on the other hand, are characterized by a finite frequency mismatch $\Omega \neq 0$, leading to an oscillatory time response function that in principle averages out over long timescales. This behavior has led to the common assumption that non-resonant interactions are negligible for IGW fields evolving over long timescales compared to wave periods. However, Chapter 3 reveals that this assumption may overlook energy transfers by non-resonant interactions, as the imaginary part of the time response function can still contribute a significant weighting to the kinetic equation. Fig. 6.2 (a) shows the real part of the time response function, while (b) shows the imaginary

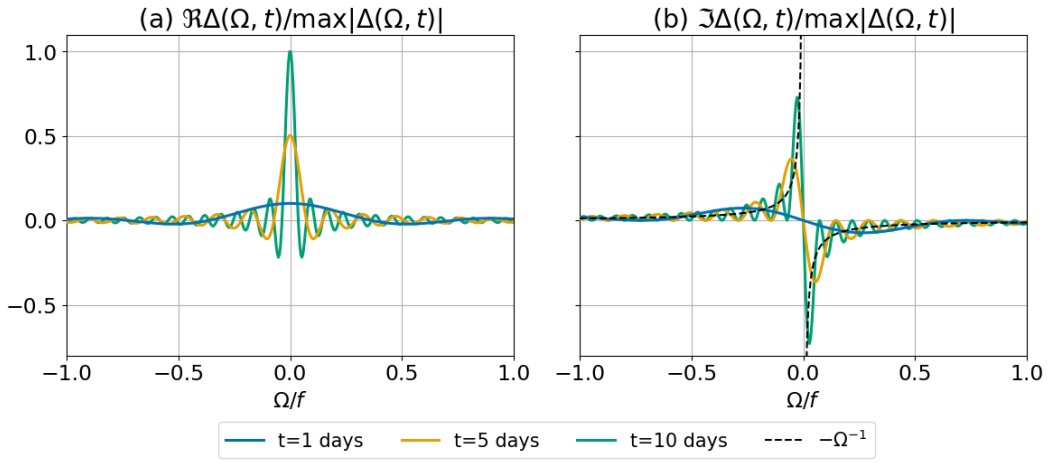

Figure 6.2: (a) Real and (b) imaginary parts of the time response function $\Delta(\Omega, t)$ as in Eqs. (3.49, 3.50) normalized by the maximum response as a function of the frequency mismatch $\Omega = \omega_0 \mp (\omega_1 + \omega_2)$ and time $t = (1, 5, 10)$ days. The abscissa is normalized by the Coriolis parameter $f = 10^{-4}\,\mathrm{s}^{-1}$, and the dashed black line shows $-\Omega^{-1}$ for reference.

part for different times as a function of the frequency mismatch $\Omega = \omega_0 \mp (\omega_1 + \omega_2)$. The weighting by the imaginary part is actually not small but even comparable to the real part that governs resonant interactions. Future research could build upon this finding and explore the significance of non-resonant interactions in more detail. In particular, their role once anisotropy develops in the IGW spectrum through, for example, wave-eddy interactions as demonstrated in Chapter 2.

6.1.3. How do interactions within the internal gravity wave field affect variations of the universal oceanic internal gravity wave spectrum?

In Chapter 4, the novel numerical framework ScINET[1] – Scattering Integral for Nonlinear Energy Transfers – is developed and used to evaluate spectral energy transfers due to wave-wave interactions in IGW fields. Building upon the theoretical foundations laid in Chapter 3 and the previous numerical methods in Olbers (1976); Eden et al. (2019c), five numerical methods (M1–M5) are developed to compute the scattering integral for both finite and infinite timescale separations of amplitude variations and wave oscillations. All methods are parallelized, providing a cost-effective framework capable of resolving multiscale interactions with unprecedented detail and accuracy. These methods account for both resonant and non-resonant interactions. Applied to GM-like spectra, the highlights of Chapter 4 are:

- Resonant triads dominate energy transfers; non-resonant interactions vanish for horizontally isotropic spectra. The contributions of inertial and buoyancy oscillations to the energy transfers within the IGW spectrum are negligible.
- The canonical GM76 model produces generally small Boltzmann rates – supporting the weak-interaction assumption – except at higher frequencies, see Fig. 4.3. The GM76 model fails to produce a convergent scattering integral, meaning the theory cannot

[1]The numerical framework ScINET can be accessed via the repository Sebastia Saez (2025). The numerical codes are implemented in Cython and Julia native languages.

predict finite energy transfers through wavenumber space. Prescribing steeper slopes in vertical wavenumber (e.g., −3) or introducing a smooth roll-off that mimics the transition from IGWs to turbulence results in a convergent scattering integral that is also consistent with the weak-interaction assumption.

- Non-local interactions govern the energy transfers and adopt the following roles when applied to the GM76 model: PSI is the primary driver of the inverse energy cascade toward near-inertial frequencies; ID is bidirectional in frequency but net-forward to small scales; ES provides weak forward transfers; newly identified TPG emerges as a principal driver of the forward cascade to high frequency and large vertical wavenumber; and HD extracts energy at the highest frequencies. Energy transfers by local interactions are negligible.
- The relative importance of the different triad interaction mechanisms depends on the spectral slope of the IGW energy spectrum: Shallower slopes enhance overall energy transfers, particularly through PSI and TPG. Steeper slopes weaken overall energy transfers and PSI, and diffusion-type processes gain relative importance. Local interactions remain consistently weak.

The numerical methods developed in Chapter 4 allow efficient, high-resolution computation of the scattering integral. This makes it possible to study how energy transfers within the IGW field are affected by environmental parameters and different spectral shapes, as has been observed by, for example, Pollmann (2020), who uses measurements from ARGO-floats to characterize the IGW field globally. Such parameter studies are needed to understand the regional variability in IGW dynamics, their dissipation, and their role in ocean mixing processes, which are crucial for improving parameterizations in ocean and climate models.

A common approach to represent the dissipation of IGWs in ocean models is the fine structure parameterization. The fine structure parameterization is based on early studies of the kinetic equation (Olbers, 1976; McComas and Müller, 1981) and later refined in Gregg (1989); Polzin et al. (2014). The fine structure parameterization relies on the idea that the energy transfers due to wave-wave interactions lead to a downscale energy cascade, ultimately resulting in wave breaking and small-scale turbulence. In other words, the fine structure parameterization can be interpreted as the negative energy transfers computed from the kinetic equation as the energy flux from the IGW field to small-scale turbulence.

Eden et al. (2019c) compare the fine structure parameterization and the negative energy transfers over the frequency range $2f < \omega < 3f$, computed from the scattering integral. They find a dependency of the energy transfers on the spectral slope and propose a refined fine structure parameterization that reads

$$D = \mu_0 f c^{*-2}(-t-1)^{-3} E_0^2 \tag{6.1}$$

where $\mu_0 = 0.6$ is a dimensionless constant, f is the Coriolis parameter, c^* is the parameter related to the spectral bandwidth (refer to Chapter 2 or Appendix A from Chapter 4), t is the spectral slope, and E_0 is the total energy level of the IGW spectrum. However, their comparison is limited to a small parameter space, where only one parameter is allowed to vary, while all others are kept fixed. Due to the complex variability in the spectral shape of the IGW field in the ocean (see Pollmann (2020)), a more systematic validation of the fine structure parameterization with the energy transfer rates computed from the scattering integral is needed, where multiple parameters are allowed to change simultaneously.

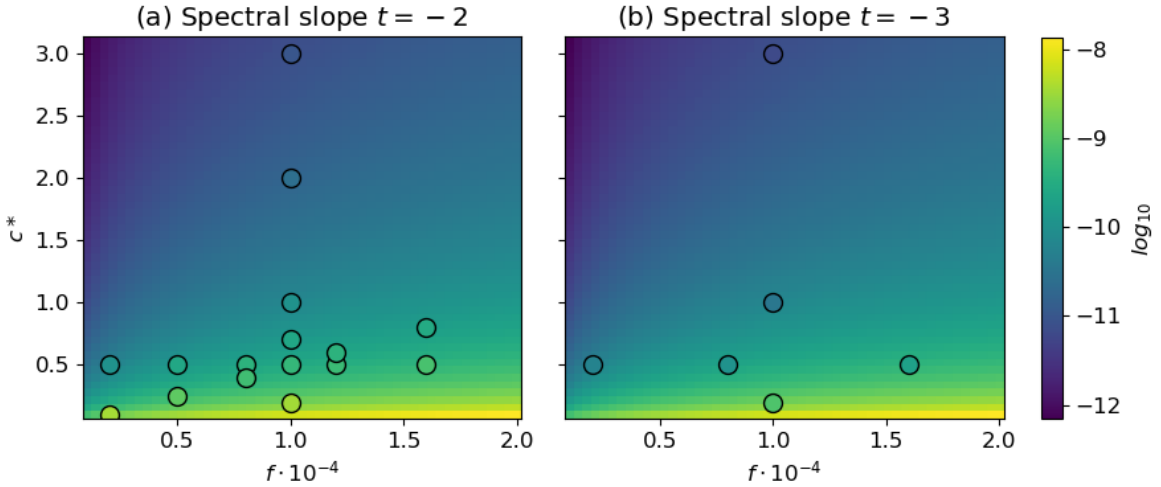

Figure 6.3: Preliminary results comparing the fine structure parameterization and the negative energy transfers over the frequency range $2f < \omega < 3f$ computed from the scattering integral with method M3 from Chapter 3. The colormap shows the parameterized energy transfers D as a function of Coriolis parameter f and spectral bandwidth parameter c^*. The overlaid circles show the negative energy transfers computed from the scattering integral as $\int |\partial_t E_{2f<\omega<3f}| d\boldsymbol{k} dm$ for different values of f and c^*. The results are shown in a logarithmic scale, in (a) for a slope in vertical wavenumber of $t = -2$ and in (b) for a slope of $t = -3$.

Preliminary results comparing the fine structure parameterization and the negative energy transfers over the frequency ranges $2f < \omega < 3f$ computed from the scattering integral reveal promising agreement. Fig. 6.3 shows the results from the fine structure parameterization for changes in f and c^* as the background colormap and the overlaid circles show the negative energy transfers computed from the scattering integral $\int |\partial_t E_{2f<\omega<3f}| d\boldsymbol{k} dm$. The results for a slope in vertical wavenumber of $t = -2$ are shown in (a) and for $t = -3$ in (b). The scattering integral is evaluated in a grid with $L_x = L_y = 75\,\text{km}$, $L_z = 6\,\text{km}$, and $401^2 \times 1001$ grid points in wavenumber space (with positive and negative wavenumbers), using method M3 from Chapter 4. The results show a good agreement between the fine structure parameterization and the scattering integral, although some discrepancies arise for the steeper slope of $t = -3$ in (b). Furthermore, the fine structure parameterization captures only the energy transfers in the frequency range $2f < \omega < 3f$. However, negative energy transfers can occur across the entire spectrum due to variations of the IGW spectral shape, as shown in Chapter 4. For example, Fig. 5.1 shows how energy transfers vary across the entire spectrum when changing the spectral slope in vertical wavenumber from $t = -2$ to $t = -3$. It becomes evident that the frequency range $2f < \omega < 3f$ captures only partly the total negative energy transfers occurring across the entire spectrum. This could lead to underestimations in the fine structure parameterization and, consequently, in the estimated dissipation rates.

Another relevant aspect concerns the role of vertically asymmetric IGW spectra. As discussed in the introduction, the IGW field finds its origin in various generation mechanisms, such as wind forcing at the surface and tidal interactions with topography at depth. These generation processes can lead to vertical asymmetries in the IGW spectrum, which may influence the energy transfers, raising the question of how external forcing at near-inertial and tidal frequencies modulates the energy transfers within the IGW field. Furthermore, it would be valuable to explore how vertical asymmetries in the IGW energy spectrum induced

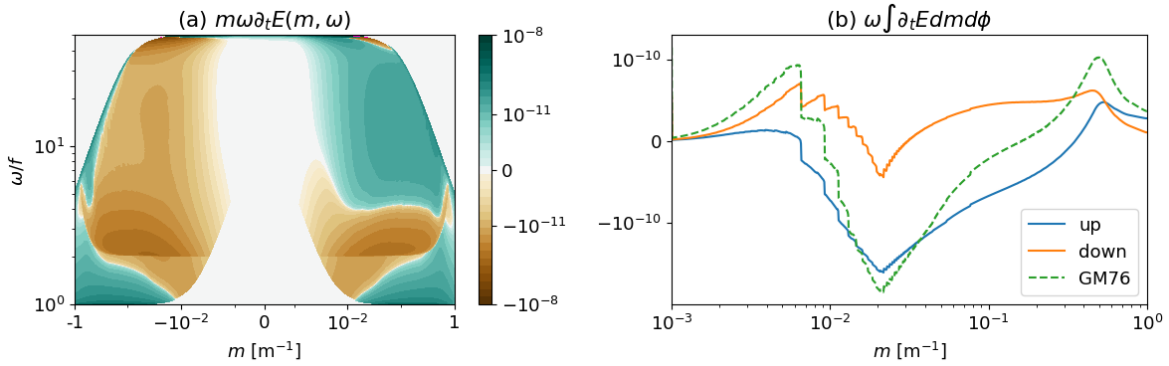

Figure 6.4: Preliminary results of the scattering integral computed for a vertically asymmetric IGW spectrum, where the spectra of both upward and downward propagating waves are prescribed by the GM76 model, but there is twice as much energy in upward propagating waves compared to downward propagating waves. (a) Content spectrum of energy transfers as a function of vertical wavenumber and frequency. (b) Content spectrum of energy transfers integrated over vertical wavenumber and wave angle as a function of frequency for the upward (in blue) and downward (in orange) propagating waves. For reference, the dashed green line shows the integrated energy transfers for the canonical vertically symmetric GM76 model for only half of the spectrum in the vertical direction.

by inhomogeneous forcings affect the scattering integral and the resulting energy transfers, potentially leading to a symmetrization of the IGW spectrum over time.

Fig. 6.4 shows preliminary results of the scattering integral computed with method M5 (with the resolution given in Tab. tab:methods under method M5) for a vertically asymmetric IGW spectrum, where the spectra of both upward and downward propagating waves are prescribed by the GM76 model, but there is twice as much energy in upward propagating waves compared to downward propagating waves. Fig. 6.4 (a) shows the energy transfers as a function of vertical wavenumber and frequency, and Fig. 6.4 (b) shows the energy transfers integrated over vertical wavenumber and angle ϕ as a function of frequency for upward (in blue) and downward (in orange) propagating waves, and for the canonical vertically symmetric GM76 model (in dashed green). This preliminary result suggests that wave-wave interactions tend to symmetrize the IGW spectrum over time by transferring energy from the more energetic upward propagating waves (negative vertical wavenumbers) to the weaker downward propagating waves (positive vertical wavenumbers).

Outlook

Looking forward, the developments presented in Chapter 4 establish a solid foundation for advancing our understanding of IGW–wave interactions and for improving how these processes are parameterized in ocean and climate models. Future research could leverage ScINET to systematically explore a wide range of spectral configurations by varying multiple parameters simultaneously. This approach facilitates more complete sampling of the parameter space and enables a robust validation of the fine structure parameterization. Extending the computation of the scattering integral across this expanded parameter space will be essential for assessing the generality and accuracy of the parameterization.

Incorporating vertically asymmetric spectra and more realistic forcing scenarios such as wind-generated near-inertial waves and internal tides could reveal how asymmetries evolve and whether scattering leads to a symmetrization of the IGW spectrum over time.

Future research could investigate the timescale at which this symmetrization occurs and its dependency on the initial degree of asymmetry and other environmental parameters. This line of research could provide valuable insights for understanding the long-term evolution of the IGW field in the ocean. Together, these research directions point toward a more comprehensive theoretical and modeling framework that links observed IGW spectral diversity to mixing rates, refines parameterizations that better capture the nuances of IGW dynamics across different oceanic regimes, and ultimately enhances the fidelity of ocean and climate simulations.

Alternatively to developing increasingly compact parameterizations of wave-wave interactions, an effort long hindered by the prohibitive cost of evaluating the high-dimensional scattering integral, future research may instead focus on numerical methods that fundamentally reduce the cost of computing the exact nonlinear energy transfer. Although the numerical methods developed in Chapter 4 of this thesis already provide a robust and cost-efficient framework, they remain insufficiently fast for direct use in operational wave models. Hasselmann and Hasselmann (1985) and Hasselmann et al. (1985) demonstrate the potential of such cost-reducing methods in the context of interactions of surface gravity waves, which may be equally well suited for efficient evaluation or approximation of nonlinear energy transfers in the IGW field.

Hasselmann and Hasselmann (1985) introduce a symmetrical treatment of resonant surface gravity wave quadruplets that reduces the computational burden of the exact scattering integral by nearly two orders of magnitude. This method exploits the intrinsic symmetry in the dynamics and energy cycle of a resonant wave quadruplet to compute the energy change of all four interacting waves simultaneously; because the energy gained by the generated wave equals that lost by the colliding waves, the method ensures exact energy conservation without the need for high spectral resolution, in contrast to the methods presented in Chapter 4 of this thesis. Building on this foundation, Hasselmann et al. (1985) propose the discrete interaction approximation, which replaces the full integral with a summation over a small set of optimally chosen points in wavenumber space that reproduce the dominant features of the exact transfer. The discrete interaction approximation is thus presented as the most practical and computationally efficient means of representing the scattering integral within discrete wave models.

6.2. An integrated picture

The concept of a universal IGW spectrum has been widely established, yet its origin, development, and apparent steadiness remain subtle and complex questions. A strictly universal spectrum implies a precise balance between energy generation by external forcings (e.g., winds, tides) and energy removal by dissipation (e.g., wave breaking) – a balance that would maintain the ocean's IGW field in a stationary state. Observations and regional studies (see Polzin and Lvov, 2011; Pollmann, 2020; Le Boyer and Alford, 2021), however, reveal significant departures from the canonical GM form, suggesting that the IGW field may not be in a strict steady-state. Most probably, forcing and dissipation are inhomogeneously distributed across the space and time, with unequivocally a balance of energy in wavenumber space, leading to a temporal rate of change of the initial energy spectrum. Consequently, time integration of the radiative transfer equation results in spectral states that deviate from the

initial distribution. This imbalance indicates that the IGW field is not strictly stationary but rather in a state of dynamic equilibrium maintained by ongoing, but approximately balanced, generation, transfer, and dissipation of wave energy.

The focus of the thesis lies in the redistribution of energy through wave-mean flow and wave-wave interactions, which can ultimately transfer energy injected at low frequencies and large scales toward higher wavenumbers, where dissipation removes energy from the system. The IGW field should therefore not be framed as a static equilibrium but as a dynamically evolving one, where apparent universality emerges from a persistent near-balance among energy generation, redistribution, and dissipation. Quantifying these processes over the global ocean collectively delineates the life cycle of IGWs as illustrated in Fig. 1.3.

As a concluding remark, let us revisit the IGW energy balance as described in Section 1.1. In a broad and integrated sense, the IGW energy budget is attempted to be closed by quantifying the contributions from wave-mean flow and wave-wave interactions to the total energy transfers that ultimately lead to energy dissipation. The work done through wave-mean flow interactions, wave-wave interactions, and dissipation can be estimated by integrating the respective energy changes over the resolved domain multiplied by the reference density $\rho = 1025\,\mathrm{kg/m^3}$ of the seawater. The estimates can be summarized as follows:

- The work done by the mean flow on the IGW field by horizontal wave-mean flow interaction amounts to around 4×10^{-5} TW over the whole simulation period. IGWs exert a total work of around 3×10^{-5} TW on the mean flow by vertical wave-mean flow interactions. The resulting amount of work done by IGWs to wave dissipation as a result of wave-mean flow interaction is around 1.4×10^{-5} TW. These values are estimates within the resolved domain ($250^2\,\mathrm{km}^2 \times 4\,\mathrm{km}$) over a period of 6 days.
- The work done to remove energy from the IGW spectrum by wave-wave interactions can be estimated by integrating the negative energy transfers computed from the scattering integral, which amount to around 2.8×10^{-5} TW, within the resolved domain ($75^2\,\mathrm{km}^2 \times 6\,\mathrm{km}$).

The contributions from wave-mean flow and wave-wave interactions to the dissipation of IGW energy can be assessed for the global ocean via scaling arguments in relation to the energy content of the mean flow and the IGW field considered in this thesis compared to the global eddy kinetic energy and IGW energy levels. The extrapolation metric related to the mean flow is based on the ratio

$$r_{\mathrm{EKE}} = \frac{\int_{-2000\,\mathrm{m}}^{-300\,\mathrm{m}} \mathrm{EKE}_{\mathrm{global}}\, dz}{\int_{-2000\,\mathrm{m}}^{-300\,\mathrm{m}} \overline{\mathrm{EKE}_{\mathrm{eddy}}}\, dz}, \tag{6.2}$$

where the denominator is the depth-integrated eddy kinetic energy $\mathrm{EKE}_{\mathrm{global}}$ from a $1/10°$ global ocean simulation from Dettmer and Eden (2025) and the enumerator is the averaged (denoted by the overbar) depth-integrated eddy kinetic energy $\mathrm{EKE}_{\mathrm{eddy}}$ within the resolved domain in Chapter 2.

The extrapolation metric related to IGWs is based on the ratios

$$r_{\text{IGW-Eddy}} = \frac{\sum_i^3 \mathrm{E}_{\mathrm{ARGO,i}} \Delta z_i}{\sum_i^3 \mathrm{E}_{\mathrm{IWEM,i}} \Delta z_i} \quad \text{and} \quad r_{\text{IGW-W}} = \frac{\sum_i^3 \mathrm{E}^2_{\mathrm{ARGO,i}} \Delta z_i}{\mathrm{E}_0^2 Z}. \tag{6.3}$$

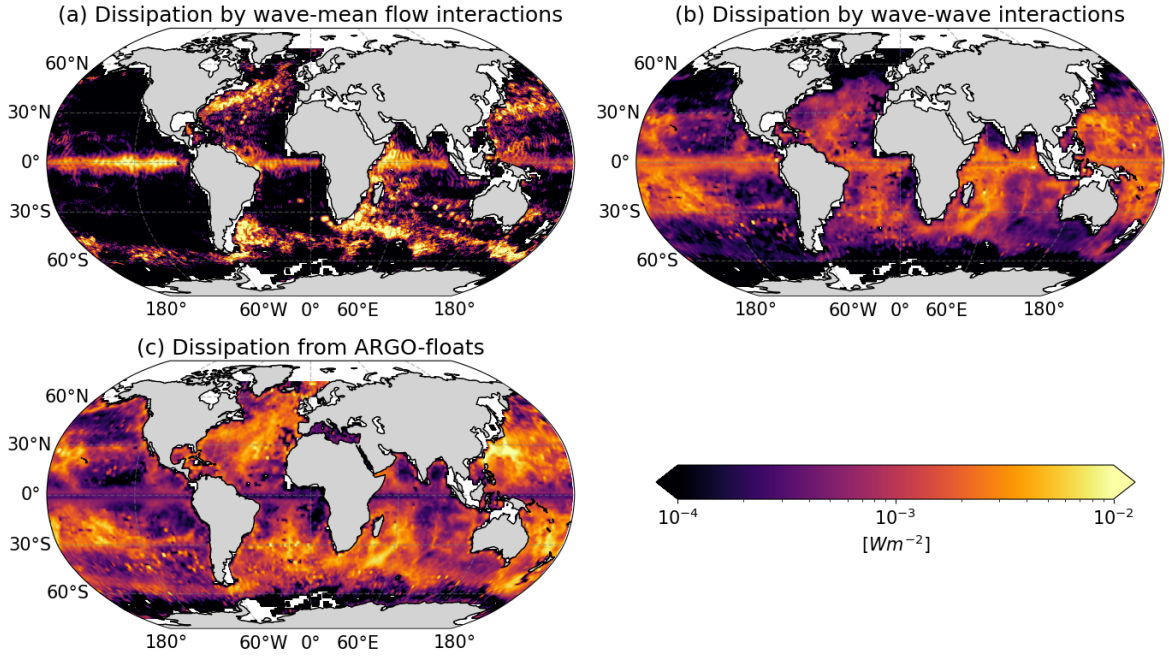

Figure 6.5: Global maps of the depth-integrated dissipation rates per unit area from: (a) wave-mean flow interactions scaled by the eddy kinetic energy ratio and the IGW energy ratio; and (b) wave-wave interactions scaled by the IGW energy ratio, and (c) from ARGO-float estimates in Pollmann et al. (2017). The scaling factors are based on a 1/10° global ocean simulation from Dettmer and Eden (2025) and IGW energy estimates from ARGO-float measurements from Pollmann et al. (2017) and Pollmann et al. (2023), as described in the main text. The dissipation rates are interpolated to 1/10° horizontal resolution for consistency, and the colorbar is in logarithmic scale.

Eq. (6.3) presents the ratios between the ARGO-float measurements binned into $1.5° \times 1.5°$ horizontal bins from Pollmann et al. (2017) and Pollmann et al. (2023) and the IGW energy within the resolved domains in Chapters 2 and 4 respectively. The dataset from Pollmann et al. (2017) includes global estimates of IGW energy levels obtained from hydrographic profiles collected by ARGO-float measurements in the ocean's upper 2000 m and built on the evaluation of the scattering integral for wave-wave interactions in GM-like spectra (e.g., Gregg, 1989; Kunze et al., 2006; Polzin et al., 2014). The IGW energy levels are averaged in three depth-ranges $z_1 = 300 - 500\,\mathrm{m}$, $z_2 = 500 - 1000\,\mathrm{m}$, and $z_3 = 1000 - 2000\,\mathrm{m}$. The depth-integrated IGW energy from the ARGO-float measurements is then defined by the sum over each energy level $E_{\mathrm{ARGO},i}$ weighted by the respective depth-range Δz_i where $i = (1, 2, 3)$. For the case of wave-mean flow interactions, Eq. (2.12) is averaged over each depth-range $E_{\mathrm{IWEM},i}$, weighted by the respective depth-range and summed, to calculate a comparable quantity. The dissipation terms related to wave-mean flow interaction, see Eqs. (2.6, 2.5), scale with the IGW energy level itself, thus the ratio $r_{\text{IGW-Eddy}}$ is appropriate. In contrast, the dissipation by nonlinear wave-wave interactions scales with IGW energy squared, see Eq. (3.47). For the case of wave-wave interactions, the IGW energy level $E_0 = 3 \times 10^{-3}\,\mathrm{m^2 s^2}$ is squared prior to weighting over the depth-range $Z = 1700\,\mathrm{m}$, and similarly for $E_{\mathrm{ARGO},i}$. All scaling fields and dissipation estimates are interpolated to 1/10° for consistency.

Fig. 6.5 (a) shows the dissipation rates per unit area associated with wave-mean flow interactions, scaled by r_{EKE} and $r_{\text{IGW-Eddy}}$. Dissipation is spatially intermittent and is largely

confined to dynamical "hotspots" where strong mesoscale or large-scale currents generate substantial shear. Elevated dissipation is evident along the equatorial waveguide, within major western boundary current systems, and throughout the Southern Ocean frontal systems. Although these regions host locally enhanced rates approaching 10^{-3} to $10^{-2}\,\mathrm{Wm}^{-2}$, much of the global ocean is characterized by significantly weaker dissipation, typically nearer $10^{-4}\,\mathrm{Wm}^{-2}$ or lower. Globally integrated, this pathway accounts for approximately 0.3 TW of work on IGW energy loss.

Fig. 6.5 (b) shows the dissipation rates per unit area associated with wave-wave interactions, scaled by $r_{\text{IGW-W}}$. In contrast to the localized structure of Fig. 6.5 (a), dissipation by wave–wave interactions is broad and pervasive, with elevated rates throughout the midlatitudes, the Antarctic Circumpolar Current, and the subtropical and subpolar gyres. Although the energy transfers from the scattering integral do not include explicit tidal forcing, the dissipation rates nonetheless intensify near the latitude where the local Coriolis frequency equals one-half of the semidiurnal M_2-tide. This feature reflects elevated IGW energy estimates from ARGO-float measurements, which scale the energy transfers in the denominator of $r_{\text{IGW-W}}$ in Eq. (6.3). This enhanced dissipation is consistent with the expectations of PSI, a resonant triad process in which the parent internal tide at frequency $\omega = \omega_{M_2}$ transfers energy to two daughter waves of frequency $\omega = \omega_{M_2}/2$. The alignment strongly supports PSI as a primary driver of nonlinear energy transfer in these regions (Olbers et al., 2020b). The globally integrated dissipation via this pathway is 0.3 TW.

Fig. 6.5 (c) shows fine structure dissipation estimates from Pollmann et al. (2017), which are based on evaluation of the scattering integral for wave-wave interactions in GM-like spectra. The spatial pattern partially resembles Fig. 6.5 (b), notably in the PSI band and in western boundary sectors of subtropical and subpolar gyres. However, magnitudes in Fig. 6.5 (c) are generally higher and more widespread. Unlike Fig. 6.5 (b), these estimates capture enhanced dissipation at the sites of IGW generation by the M_2-tidal component (e.g., Southwestern Indian Ridge, Walvis Ridge, Mid-Atlantic Ridge, or along the west coast of the North and South Pacific Oceans, see Nycander (2005)), which are absent in Fig. 6.5 (b) due to the lack of explicit forcing. Furthermore, Fig. 6.5 (c) uses an empirical correction factor to reduce wave-driven dissipation at the Equator, which leads to a significant difference from the relatively large dissipation rates from Fig. 6.5 (b). Enhanced dissipation in western boundary currents also resembles the mean-flow signature seen in Fig. 6.5 (a), suggesting that fine structure estimates may conflate contributions from wave–wave and wave–mean flow interactions. Although Fig. 6.5 (c) includes a correction factor for non-wave-driven mixing, separating mechanisms remains nontrivial and warrants further study.

The combined estimates of IGW energy dissipation by wave-mean flow and wave-wave interactions in this thesis amount to around 0.6 TW within the upper ocean (between $300 - 2000$ m depth). While lower than the canonical 2 TW required to sustain abyssal mixing (Munk, 1966), the canonical estimate pertains to the full ocean volume, making direct comparison imperfect. Notably, fine structure dissipation estimates from ARGO-observations yield 0.56 TW, although the comparison is non-trivial and the similar magnitude is not necessarily attributable to the same processes. The remaining order-(1 TW) is likely to arise from a suite of additional processes not explicitly quantified in this work. These include external forcing and boundary-related mechanisms such as the generation and dissipation of Lee waves and tidally generated IGWs, which enhance mixing both near topographic features and within the ocean interior. Wind-forced near-inertial motions also represent

a significant global energy input, particularly in regions of strong atmospheric variability. Further contributions are likely associated with boundary-layer turbulence, wave–topography scattering, and elevated dissipation over rough abyssal terrain, as well as from processes that remain poorly constrained, such as secondary wave generation accompanying wave breaking. Taken together, these considerations highlight that the mechanisms examined here form only part of a wider and still incompletely resolved IGW energy budget. This broader context naturally motivates a final reflection on the implications of the present findings for our understanding of the IGW field.

In summary, this thesis sheds light on the pathways through which IGWs transport and redistribute energy, connecting processes across scales from the vast oceanic currents to the smallest wave motions. While advances in high-resolution numerical models and satellite observations are opening new frontiers in oceanography, the full dynamics of the IGW field remain beyond the reach of current models. As a result, IGWs and their interactions must still be largely parameterized in ocean and climate simulations, and the complexity of their interactions ensures they will remain challenging to resolve for the foreseeable future. Perhaps, as the ancients once gazed upon the silent sea, we may never fully master its secrets – but we can continue to marvel at the subtle forces that have always moved, unseen, beneath the surface.

Acknowledgement

First and foremost, I would like to thank my supervisor, Prof. Dr. Carsten Eden. I owe him my deepest gratitude for his continuous support throughout my PhD studies, for his patience, motivation, and immense knowledge. He not only encouraged me to pursue my research interests by providing the freedom to explore various topics independently, but also guided me in the right direction whenever I felt stuck. I am deeply grateful for the countless opportunities, conferences, and adventures that he made possible.

I would also like to express my sincere gratitude to my second supervisor, Dr. Manita Chouksey, for her insightful comments and constructive suggestions, which consistently pushed me to sharpen my thinking. Throughout all the ups and downs of these past years, she always had an open ear for my questions and offered steady moral support. My heartfelt thanks also go to Prof. Dr. Dirk Olbers, who, without officially being my supervisor, felt very much like one. He always took the time to answer my questions and generously shared his expertise in physical oceanography. His valuable feedback and the inspiring ongoing work on his new book Oceanic Internal Gravity Waves greatly improved the quality of this thesis.

Their enthusiasm for science has been both contagious and inspiring. Thank you, Carsten. Thank you, Manita. Thank you, Dirk. You have been my inspiration.

I would like to thank the members of my advisory panel. To my panel chair, Prof. Dr. Kevin Lamb, I am grateful for his constructive feedback and insightful comments, which significantly helped to improve this thesis. I also thank Prof. Dr. Hossein Kafiabad for his valuable suggestions and thoughtful remarks. I sincerely appreciate the time they dedicated to my work and their patience in helping to organize our intercontinental panel meetings.

I gratefully acknowledge the Collaborative Research Center TRR181 "Energy Transfers in Atmosphere and Ocean", funded by the German Research Foundation, through which I received financial support. Within the PhD School, I had the opportunity to participate in many courses, meet PhD students from diverse disciplines, and realize my research stay. Thanks to Prof. Dr. William Young for hosting me during my research stay at Scripps, the opportunity to share my work, and our in-depth, enlightening discussions. Special thanks go to Jennifer and Lea, the project coordinators, for their continuous and tireless support.

I would also like to thank my colleagues, everyone on the fourth floor, for the friendly atmosphere and the countless scientific discussions. For all the small moments of our everyday life, enjoying mensa delights, sharing an after-lunch espresso, and meeting after work, I thank you: Johannes, Lars, Alexa, Julia, Han, Josh, Jabeen, Belal, Genevieve, Philomene, Che, and Simon. I am particularly grateful to Friederike, Moritz, Yang, Silvano, and Jan for their critical reading of my thesis. Thanks to Ankit and Mariana, my office mates and friends – being so far away from my family, you made me feel at home.

Many thanks to my friends outside academia for bringing balance into my life. Cheers to my flatmates, and to Kubi, Christine and Conni for enduring me throughout this journey. To my dearest friends, the few, the many: Miguel, Adolfo, Herby, and Albert, thank you for your friendship and constant support. And thank you, Alicja, for your kindness, your encouragement, and for being my sunshine during the darkest moments.

And last but certainly not least, I thank my loving family, my brother, my parents, and my grandparents. I feel incredibly fortunate to have received your unwavering support.

There was a kid with an odd dream: "Quiero ser inventor."

Mom, Dad, I did it!

Bibliography

Alford, M., 2001: Internal swell generation: The spatial distribution of energy flux from the wind to mixed layer near-inertial motions. *J. Phys. Oceanogr.*, **31 (8)**, 2359–2368, doi: 10.1175/1520-0485(2001)031<2359:ISGTSD>2.0.CO;2.

Bartello, P., 1995: Geostrophic adjustment and inverse cascades in rotating stratified turbulence. *Journal of Atmospheric Sciences*, **52 (24)**, 4410 – 4428, doi: 10.1175/1520-0469(1995)052<4410:GAAICI>2.0.CO;2.

Bel, G., and E. Tziperman, 2023: Is the resonant wave interaction approximation consistent with the dynamics of internal wave fields?, 10.48550/arxiv.2207.02758. URL 10.48550/arXiv.2207.02758.

Bell, T., 1973: Internal wave generation by deep ocean flows over abyssal topography. Ph.D. thesis, Johns Hopkins University.

Bell, T. H., 1978: Radiation damping of inertial oscillations in the upper ocean. *Journal of Fluid Mechanics*, **88 (2)**, 289–308, doi: 10.1017/S0022112078002116.

Borchert, S., U. Achatz, and M. D. Fruman, 2014: Gravity wave emission in an atmosphere-like configuration of the differentially heated rotating annulus experiment. *Journal of Fluid Mechanics*, **758**, 287–311, doi: 10.1017/jfm.2014.528.

Bretherton, F. P., 1964: Resonant interactions between waves. the case of discrete oscillations. *Journal of Fluid Mechanics*, **20 (3)**, 457–479, doi: 10.1017/S0022112064001355.

Briscoe, M. G., 1975: Internal waves in the ocean. *Rev. Geophys.*, **13 (3)**, 591–598, doi: 10.1029/RG013i003p00591.

Browning, T., A. Al-Hashem, M. Hopwood, A. Engel, I. Belkin, E. Wakefield, T. Fischer, and E. Achterberg, 2021: Iron regulation of North Atlantic eddy phytoplankton productivity. *Geophysical Research Letters*, **48**, doi: 10.1029/2020GL091403.

Bryan, K., 1979: Models of the world ocean. *Dynamics of Atmospheres and Oceans*, **3 (2)**, 327–338, doi: 10.1016/0377-0265(79)90016-2.

Bühler, O., 2014: *Waves and mean flows*. Cambridge University Press, doi: 10.1017/CBO9781107478701.

Bühler, O., and M. E. McIntyre, 2005: Wave capture and wave–vortex duality. *Journal of Fluid Mechanics*, **534**, 67–95, doi: 10.1017/S0022112005004374.

Caillol, P., and V. Zeitlin, 2000: Kinetic equations and stationary energy spectra of weakly nonlinear internal gravity waves. *Dynamics of Atmospheres and Oceans*, **32 (2)**, 81–112, doi: 10.1016/S0377-0265(99)00043-3.

Cairns, J. L., and G. O. Williams, 1976: Internal wave observations from a midwater float, 2. *Journal of Geophysical Research (1896-1977)*, **81 (12)**, 1943–1950, doi: 10.1029/JC081i012p01943.

Castelão, G. P., and W. E. Johns, 2011: Sea surface structure of North Brazil Current rings derived from shipboard and moored acoustic Doppler current profiler observations. *Journal of Geophysical Research: Oceans*, **116 (C1)**, doi: 10.1029/2010JC006575.

Chouksey, M., C. Eden, and N. Brüggemann, 2018: Internal gravity wave emission in different dynamical regimes. *Journal of Physical Oceanography*, **48**, doi: 10.1175/JPO-D-17-0158.1.

Chouksey, M., C. Eden, G. T. Masur, and M. Oliver, 2023: A comparison of methods to balance geophysical flows. *Journal of Fluid Mechanics*, **971**, A2, doi: 10.1017/jfm.2023.602.

Chouksey, M., C. Eden, and D. Olbers, 2022: Gravity wave generation in balanced sheared flow revisited. *Journal of Physical Oceanography*, **52 (7)**, 1351–1362, doi: 10.1175/JPO-D-21-0115.1.

Cox, M. R., H. A. Kafiabad, and J. Vanneste, 2023: Inertia-gravity-wave diffusion by geostrophic turbulence: the impact of flow time dependence. *Journal of Fluid Mechanics*, **958**, A21, doi: 10.1017/jfm.2023.83.

Crawford, G., and W. Large, 1996: A numerical investigation of resonant inertial response of the ocean to wind forcing. *J. Phys. Oceanogr.*, **26 (6)**, 873–891, doi: 10.1175/1520-0485(1996)026<0873:ANIORI>2.0.CO;2.

Cummins, P. F., G. Holloway, and E. Gargett, 1990: Sensitivity of the GFDL ocean general circulation model to a parameterization of vertical diffusion. *Journal of Physical Oceanography*, **20 (6)**, 817–830, doi: 10.1175/1520-0485(1990)020<0817:SOTGOG>2.0.CO;2.

D'Asaro, E. A., 1985: The energy flux from the wind to near-inertial motions in the surface mixed layer. *J. Phys. Oceanogr.*, **15 (8)**, 1043–1059, doi: 10.1175/1520-0485(1985)015<1043:TEFFTW>2.0.CO;2.

Davidson, R. C., 1967: The evolution of wave correlations in uniformly turbulent, weakly nonlinear systems. *Journal of Plasma Physics*, **1 (3)**, 341–359, doi: 10.1017/S0022377800003342.

Dematteis, G., A. Le Boyer, F. Pollmann, K. Polzin, M. Alford, C. Whalen, and Y. Lvov, 2024: Interacting internal waves explain global patterns of interior ocean mixing. *Nature Communications*, **15**, doi: 10.1038/s41467-024-51503-6.

Dematteis, G., K. Polzin, and Y. V. Lvov, 2022: On the origins of the oceanic ultraviolet catastrophe. *Journal of Physical Oceanography*, **52 (4)**, 597 – 616, doi: 10.1175/JPO-D-21-0121.1.

Dettmer, J., and C. Eden, 2025: Mechanisms of baroclinic eddy damping on large scales. *Journal of Physical Oceanography*, **55 (10)**, 1751 – 1769, doi: 10.1175/JPO-D-24-0253.1.

Dong, W., O. Bühler, and K. S. Smith, 2023: Geostrophic eddies spread near-inertial wave energy to high frequencies. *Journal of Physical Oceanography*, **53 (5)**, 1311 – 1322, doi: 10.1175/JPO-D-22-0153.1.

Duda, T. F., and C. S. Cox, 1989: Vertical wave number spectra of velocity and shear at small internal wave scales. *Journal of Geophysical Research: Oceans*, **94 (C1)**, 939–950, doi: 10.1029/JC094iC01p00939.

Eden, C., M. Chouksey, and D. Olbers, 2019a: Gravity wave emission by shear instability. *Journal of Physical Oceanography*, **49 (9)**, 2393 – 2406, doi: 10.1175/JPO-D-19-0029.1.

Eden, C., M. Chouksey, and D. Olbers, 2019b: Mixed rossby–gravity wave–wave interactions. *Journal of Physical Oceanography*, **49 (1)**, 291 – 308, doi: 10.1175/JPO-D-18-0074.1.

Eden, C., and A. Iske, 2019: *Energy Transfers in Atmosphere and Ocean*. doi: 10.1007/978-3-030-05704-6.

Eden, C., and D. Olbers, 2017: A closure for internal wave–mean flow interaction. Part II: Wave drag. *Journal of Physical Oceanography*, **47**, 1403–, doi: 10.1175/JPO-D-16-0056.1.

Eden, C., F. Pollmann, and D. Olbers, 2019c: Numerical evaluation of energy transfers in internal gravity wave spectra of the ocean. *Journal of Physical Oceanography*, **49 (3)**, 737–749, doi: 10.1175/JPO-D-18-0075.1.

Eden, C., F. Pollmann, and D. Olbers, 2020: Towards a global spectral energy budget for internal gravity waves in the ocean. *Journal of Physical Oceanography*, **50 (4)**, 935 – 944, doi: 10.1175/JPO-D-19-0022.1.

Egbert, G., and R. Ray, 2000: Significant dissipation of tidal energy in the deep ocean inferred from satellite altimeter data. **405 (6788)**, 775–778, doi: 10.1038/35015531.

Ekman, V. W., 1904: On dead water. norwegian north polar expedition 1893 - 1896: scientific results.

Falahat, S., J. Nycander, F. Roquet, and M. Zarroug, 2014: Global calculation of tidal energy conversion into vertical normal modes. *Journal of Physical Oceanography*, **44 (12)**, 3225–3244, doi: 10.1175/JPO-D-14-0002.1.

Fer, I., A. Bosse, B. Ferron, and P. Bouruet-Aubertot, 2018: The dissipation of kinetic energy in the lofoten basin eddy. *Journal of Physical Oceanography*, **48 (6)**, 1299–1316, doi: 10.1175/JPO-D-17-0244.1.

Fofonoff, N., 1969: Spectral characteristics of internal waves in ocean. *Deep-Sea Res.*, 59.

Fourdrinoy, J., J. Dambrine, M. Petcu, M. Pierre, and G. Rousseaux, 2020: The dual nature of the dead-water phenomenology: Nansen versus ekman wave-making drags. *Proceedings of the National Academy of Sciences*, **117 (29)**, 16 770–16 775, doi: 10.1073/pnas.1922584117.

Furuichi, N., T. Hibiya, and Y. Niwa, 2008: Model-predicted distribution of wind-induced internal wave energy in the world's oceans. *J. Geophys. Res.*, **113 (C9)**, doi: 10.1029/2008JC004768.

Gallmeier, K., J. X. Prochaska, P. Cornillon, D. Menemenlis, and M. Kelm, 2023: An evaluation of the llc4320 global-ocean simulation based on the submesoscale structure of modeled sea surface temperature fields. *Geoscientific Model Development*, **16 (23)**, 7143–7170, doi: 10.5194/gmd-16-7143-2023.

Garanaik, A., and S. K. Venayagamoorthy, 2019: On the inference of the state of turbulence and mixing efficiency in stably stratified flows. *Journal of Fluid Mechanics*, **867**, 323–333, doi: 10.1017/jfm.2019.142.

Gargett, A. E., P. J. Hendricks, T. B. Sanford, T. R. Osborn, and A. J. Williams, 1981: A composite spectrum of vertical shear in the upper ocean. *Journal of Physical Oceanography*, **11 (9)**, 1258–1271, doi: 10.1175/1520-0485(1981)011<1258:ACSOVS>2.0.CO;2.

Garrett, C., and W. Munk, 1972: Space-timescales of internal waves. *Geophysical and Astrophysical Fluid Dynamics*, **3**, 225–264, doi: 10.1080/03091927208236082.

Garrett, C., and W. Munk, 1979: Internal waves in the ocean. *Annual Review of Fluid Mechanics*, **11 (1)**, 339–369, doi: 10.1146/annurev.fl.11.010179.002011.

Garrett, C. J. R., and W. H. Munk, 1975: Space-time scales of internal waves' a progress report. *Journal of Geophysical Research*, **80**, 291–297, doi: 10.1029/JC080i003p00291.

Goldstein, H., 1972: *Klassische Mechanik*. Akademische Verlagsgesellschaft, Frankfurt am Main.

Gregg, M. C., 1987: Diapycnal mixing in the thermocline: A review. *Journal of Geophysical Research: Oceans*, **92 (C5)**, 5249–5286, doi: 10.1029/JC092iC05p05249.

Gregg, M. C., 1989: Scaling turbulent dissipation in the thermocline. *Journal of Geophysical Research*, **94**, 9686–9698, doi: 10.1029/JC094iC07p09686.

Hasselmann, K., 1962: On the non-linear energy transfer in a gravity-wave spectrum part 1. general theory. *Journal of Fluid Mechanics*, **12 (4)**, 481–500, doi: 10.1017/S0022112062000373.

Hasselmann, K., 1963a: On the non-linear energy transfer in a gravity wave spectrum part 2. conservation theorems; wave-particle analogy; irrevesibility. *Journal of Fluid Mechanics*, **15 (2)**, 273–281, doi: 10.1017/S0022112063000239.

Hasselmann, K., 1963b: On the non-linear energy transfer in a gravity-wave spectrum. part 3. evaluation of the energy flux and swell-sea interaction for a Neumann spectrum. *Journal of Fluid Mechanics*, **15 (3)**, 385–398, doi: 10.1017/S002211206300032X.

Hasselmann, K., 1966: Feynman diagrams and interaction rules of wave-wave scattering processes. *Reviews of Geophysics*, **4 (1)**, 1–32, doi: 10.1029/RG004i001p00001.

Hasselmann, K., 1970: Wave-driven inertial oscillations. *Geophysical Fluid Dynamics*, **1 (3-4)**, 463–502, doi: 10.1080/03091927009365783.

Hasselmann, S., and K. Hasselmann, 1985: Computations and parameterizations of the nonlinear energy transfer in a gravity-wave spectrum. Part I: A new method for efficient computations of the exact nonlinear transfer integral. *Journal of Physical Oceanography*, **15 (11)**, 1369 – 1377, doi: 10.1175/1520-0485(1985)015<1369:CAPOTN>2.0.CO;2.

Hasselmann, S., K. Hasselmann, J. Allender, and T. Barnett, 1985: Computations and parameterizations of the nonlinear energy transfer in a gravity-wave specturm. Part II: Parameterizations of the nonlinear energy transfer for application in wave models. *Journal of Physical Oceanography*, **15 (11)**, 1378–1391, doi: 10.1175/1520-0485(1985)015<1369:CAPOTN>2.0.CO;2.

Henyey, F., J. Wright, and S. M. Flatté, 1986: Energy and action flow through the internal wave field: An eikonal approach. *J. Geophys. Res.*, **91**, 8487–8495, doi: 10.1029/JC091iC07p08487.

Hibiya, T., Y. Niwa, and K. Fujiwara, 1998: Numerical experiments of nonlinear energy transfer within the oceanic internal wave spectrum. *Journal of Geophysical Research: Oceans*, **103 (C9)**, 18 715–18 722, doi: 10.1029/98JC01362.

Holloway, G., 1978: On the spectral evolution of strongly interacting waves. *Geophysical & Astrophysical Fluid Dynamics*, **11 (1)**, 271–287, doi: 10.1080/03091927808242670.

Holloway, G., 1980: Oceanic internal waves are not weak waves. *Journal of Physical Oceanography*, **10 (6)**, 906 – 914, doi: 10.1175/1520-0485(1980)010<0906:OIWANW>2.0.CO;2.

Holloway, G., 1981: Theoretical approaches to interactions among internal waves, turbulence and finestructure. *AIP Conference Proceedings*, **76 (1)**, 47–77, doi: 10.1063/1.33197.

Holloway, G., 1982: On interaction time scales of oceanic internal waves. *Journal of Physical Oceanography*, **12 (3)**, 293 – 296, doi: 10.1175/1520-0485(1982)012<0293:OITSOO>2.0.CO;2.

Kafiabad, H. A., M. A. C. Savva, and J. Vanneste, 2019: Diffusion of inertia-gravity waves by geostrophic turbulence. *Journal of Fluid Mechanics*, **869**, R7, doi: 10.1017/jfm.2019.300.

Korn, P., and Coauthors, 2022: Icon-o: The ocean component of the icon earth system model—global simulation characteristics and local telescoping capability. *Journal of Advances in Modeling Earth Systems*, **14 (10)**, e2021MS002 952, doi: 10.1029/2021MS002952.

Kraichnan, R. H., 1973: Helical turbulence and absolute equilibrium. *Journal of Fluid Mechanics*, **59 (4)**, 745–752, doi: 10.1017/S0022112073001837.

Kunze, E., E. Firing, J. M. Hummon, T. K. Chereskin, and A. M. Thurnherr, 2006: Global abyssal mixing inferred from lowered adcp shear and ctd strain profiles. *Journal of Physical Oceanography*, **36 (8)**, 1553 – 1576, doi: 10.1175/JPO2926.1.

Kunze, E., and S. Smith, 2004: The role of small-scale topography in turbulent mixing of the global ocean. *Oceanography*, **17**, 55–64, doi: 10.5670/oceanog.2004.67.

Labarre, V., N. Lanchon, P.-P. Cortet, G. Krstulovic, and S. Nazarenko, 2024: On the kinetics of internal gravity waves beyond the hydrostatic regime. *Journal of Fluid Mechanics*, **998**, A17, doi: 10.1017/jfm.2024.802.

Le Boyer, A., and M. H. Alford, 2021: Variability and sources of the internal wave continuum examined from global moored velocity records. *Journal of Physical Oceanography*, **51 (9)**, 2807 – 2823, doi: 10.1175/JPO-D-20-0155.1.

Ledwell, J., A. Watson, and C. Law, 1993: Evidence for slow mixing across the pycnocline from an open-ocean tracer-release experiment. *Nature*, **364**, 701–703, doi: 10.1038/364701a0.

Ledwell, J. R., A. J. Watson, and C. S. Law, 1998: Mixing of a tracer in the pycnocline. *Journal of Geophysical Research*, **103**, 21 499–21 529, doi: 10.1029/98JC01738.

Lvov, Y., and E. Tabak, 2001: Hamiltonian formalism and the Garrett-Munk spectrum of internal waves in the ocean. *Physical Review Letters*, **87 (16)**, 168 501, doi: 10.1103/PhysRevLett.87.168501.

Lvov, Y. V., K. L. Polzin, E. G. Tabak, and N. Yokoyama, 2010: Oceanic internal-wave field: Theory of scale-invariant spectra. *Journal of Physical Oceanography*, **40 (12)**, 2605 – 2623, doi: 10.1175/2010JPO4132.1.

Lvov, Y. V., K. L. Polzin, and N. Yokoyama, 2012: Resonant and near-resonant internal wave interactions. *Journal of Physical Oceanography*, **42 (5)**, 669 – 691, doi: 10.1175/2011JPO4129.1.

Masur, G. T., and M. Oliver, 2020: Optimal balance for rotating shallow water in primitive variables. *Geophysical & Astrophysical Fluid Dynamics*, **114 (4-5)**, 429–452, doi: 10.1080/03091929.2020.1745789.

McComas, C. H., and F. P. Bretherton, 1977: Resonant interaction of oceanic internal waves. *Journal of Geophysical Research (1896-1977)*, **82 (9)**, 1397–1412, doi: 10.1029/JC082i009p01397.

McComas, C. H., and P. Müller, 1981: The dynamic balance of internal waves. *Journal of Physical Oceanography*, **11 (7)**, 970 – 986, doi: 10.1175/1520-0485(1981)011<0970:TDBOIW>2.0.CO;2.

Munk, W., and C. Wunsch, 1998: Abyssal recipes ii: energetics of tidal and wind mixing. *Deep Sea Research Part I: Oceanographic Research Papers*, **45 (12)**, 1977–2010, doi: 10.1016/S0967-0637(98)00070-3.

Munk, W. H., 1966: Abyssal recipes. *Deep Sea Research and Oceanographic Abstracts*, **13 (4)**, 707–730, doi: 10.1016/0011-7471(66)90602-4.

Munk, W. H., 1981: Internal waves and small-scale processes. 264–269.

Muraschko, J., M. D. Fruman, U. Achatz, S. Hickel, and Y. Toledo, 2015: On the application of Wentzel–Kramer–Brillouin theory for the simulation of the weakly nonlinear dynamics of gravity waves. *Quarterly Journal of the Royal Meteorological Society*, **141 (688)**, 676–697, doi: 10.1002/qj.2381.

Musgrave, R., F. Pollmann, S. Kelly, and M. Nikurashin, 2022: *The lifecycle of topographically-generated internal waves*, 117–144. doi: 10.1016/B978-0-12-821512-8.00013-X.

Müller, M., 2013: On the space- and time-dependence of barotropic-to-baroclinic tidal energy conversion. *Ocean Modelling*, **72**, 242–252, doi: 10.1016/j.ocemod.2013.09.007.

Müller, P., and M. Briscoe, 2000: Diapycnal mixing and internal waves. *Oceanography*, **13**, doi: 10.5670/oceanog.2000.40.

Müller, P., G. Holloway, F. Henyey, and N. Pomphrey, 1986: Nonlinear interactions among internal gravity waves. *Reviews of Geophysics*, **24 (3)**, 493–536, doi: 10.1029/RG024i003p00493.

Müller, P., and D. J. Olbers, 1975: On the dynamics of internal waves in the deep ocean. *Journal of Geophysical Research (1896-1977)*, **80 (27)**, 3848–3860, doi: 10.1029/JC080i027p03848.

Müller, P., D. J. Olbers, and J. Willebrand, 1978: The IWEX spectrum. *Journal of Geophysical Research: Oceans*, **83 (C1)**, 479–500, doi: 10.1029/JC083iC01p00479.

Nansen, F., 1902: *The Oceanography of the North Polar Basin*. Norwegian North Polar Expedition 1893 - 1896 : scientific results, Longmans, Green, and Company.

Natarov, A., and P. Müller, 2005: A dissipation function for internal wave radiative balance equation. *Journal of Atmospheric and Oceanic Technology*, **22**, doi: 10.1175/JTECH1788.1.

Nazarenko, S., 2011: *Wave turbulence*. Springer Science & Business Media, doi: 10.1007/978-3-642-15942-8, lecture Notes in Physics 825.

Nikurashin, M., and R. Ferrari, 2011: Global energy conversion rate from geostrophic flows into internal lee waves in the deep ocean. *Geophysical Research Letters*, **38**, doi: 10.1029/2011GL046576.

Nycander, J., 2005: Generation of internal waves in the deep ocean by tides. *Journal of Geophysical Research: Oceans*, **110 (C10)**, doi: 10.1029/2004JC002487.

Olbers, D., 1974: On the energy balance of small-scale internal waves in the deep-sea. Ph.D. thesis, Hamburg, Univ., Fachbereich Geowissenschaften, Diss., 1974 (Nur beschr. f. d. Austausch).

Olbers, D., 1976: Non-linear energy transfer and the energy balance of the internal wave in the deep ocean. *Journal of Fluid Mechanics*, **74**, 375 – 399, doi: 10.1017/S0022112076001857.

Olbers, D., 1983: Models of the oceanic internal wave field. *Reviews of Geophysics and Space Physics*, doi: 10.1029/RG021i007p01567.

Olbers, D., 1986: *Internal gravity waves*, 37–82. Springer Verlag, Berlin.

Olbers, D., and C. Eden, 2013: A global model for the diapycnal diffusivity induced by internal gravity waves. *Journal of Physical Oceanography*, **43**, doi: 10.1175/JPO-D-12-0207.1.

Olbers, D., and C. Eden, 2017: A closure for internal wave–mean flow interaction. Part I: Energy conversion. *Journal of Physical Oceanography*, **47**, 1389–, doi: 10.1175/JPO-D-16-0054.1.

Olbers, D., C. Eden, E. Becker, F. Pollmann, and J. Jungclaus, 2019: *The IDEMIX Model: Parameterization of internal gravity waves for circulation models of ocean and atmosphere*, 87–125. Springer International Publishing, Cham, doi: 10.1007/978-3-030-05704-6_3.

Olbers, D., P. Jurgenowski, and C. Eden, 2020a: A wind-driven model of the ocean surface layer with wave radiation physics. *Ocean Dynamics*, **70 (8)**, 1067–1088, doi: 10.1007/s10236-020-01376-2.

Olbers, D., F. Pollmann, and C. Eden, 2020b: On psi interactions in internal gravity wave fields and the decay of baroclinic tides. *Journal of Physical Oceanography*, **50 (3)**, 751 – 771, doi: 10.1175/JPO-D-19-0224.1.

Olbers, D., J. Willebrand, and C. Eden, 2012: *Ocean Dynamics*. Springer, Heidelberg, doi: 10.1007/978-3-642-23450-7.

Olbers, D. J., and K. Herterich, 1979: The spectral energy transfer from surface waves to internal waves. *Journal of Fluid Mechanics*, **92 (2)**, 349–379, doi: 10.1017/S0022112079000653.

Onuki, Y., and T. Hibiya, 2018: Decay rates of internal tides estimated by an improved wave-wave interaction analysis. *J. Phys. Oceanogr.*, 2689–2701, doi: 10.1175/JPO-D-17-0278.1.

Osborn, T. R., 1980: Estimates of the local rate of vertical diffusion from dissipation measurements. *Journal of Physical Oceanography*, **10 (1)**, 83 – 89, doi: 10.1175/1520-0485(1980)010<0083:EOTLRO>2.0.CO;2.

Osborn, T. R., and C. S. Cox, 1972: Oceanic fine structure. *Geophysical Fluid Dynamics*, **3 (4)**, 321–345, doi: 10.1080/03091927208236085.

Phillips, O. M., 1968: The interaction trapping of internal gravity waves. *Journal of Fluid Mechanics*, **34 (2)**, 407–416, doi: 10.1017/S0022112068001977.

Pollmann, F., 2020: Global characterization of the ocean's internal wave spectrum. *Journal of Physical Oceanography*, **50 (7)**, 1871 – 1891, doi: 10.1175/JPO-D-19-0185.1.

Pollmann, F., C. Eden, and D. Olbers, 2017: Evaluating the global internal wave model idemix using finestructure methods. *Journal of Physical Oceanography*, **47 (9)**, 2267 – 2289, doi: 10.1175/JPO-D-16-0204.1.

Pollmann, F., C. Eden, and D. Olbers, 2023: Global finestructure estimates of internal wave energy levels and wave-induced mixing from argo float profiles. SEANOE, doi: 10.17882/95327.

Polzin, K., 2004: Idealized solutions for the energy balance of the finescale internal wave field. *Journal of Physical Oceanography*, **34**, doi: 10.1175/1520-0485(2004)034<0231:ISFTEB>2.0.CO;2.

Polzin, K., 2009: An abyssal recipe. *Ocean Modelling*, **30**, 298–309, doi: 10.1016/j.ocemod.2009.07.006.

Polzin, K. L., and Y. V. Lvov, 2011: Toward Regional Characterizations of the Oceanic Internal Wavefield. *Reviews of Geophysics*, **49 (4)**, RG4003, doi: 10.1029/2010RG000329, 1007.2113.

Polzin, K. L., A. C. Naveira Garabato, T. N. Huussen, B. M. Sloyan, and S. Waterman, 2014: Finescale parameterizations of turbulent dissipation. *Journal of Geophysical Research: Oceans*, **119 (2)**, 1383–1419, doi: 10.1002/2013JC008979.

Pomphrey, N., J. D. Meiss, and K. M. Watson, 1980: Description of nonlinear internal wave interactions using langevin methods. *Journal of Geophysical Research: Oceans*, **85 (C2)**, 1085–1094, doi: 10.1029/JC085iC02p01085.

REEBUS: Role of eddies in the carbon pump of the eastern boundary upwelling systems, 2019: The importance of climate change in coastal upwelling areas. GEOMAR, UHH.

Remmel, M., and L. Smith, 2009: New intermediate models for rotating shallow water and an investigation of the preference for anticyclones. *Journal of Fluid Mechanics*, **635**, 321–359, doi: 10.1017/S0022112009007897.

Richardson, L. F., 2007: *Weather Prediction by Numerical Process*. 2nd ed., Cambridge Mathematical Library, Cambridge University Press, doi: 10.1017/CBO9780511618291.

Rimac, A., J.-S. von Storch, C. Eden, and H. Haak, 2013: The influence of high-resolution wind stress field on the power input to near-inertial motions in the ocean. *Geophys. Res. Lett.*, **40 (18)**, 4882–4886, doi: 10.1002/grl.50929.

Ryzhik, L., G. Papanicolaou, and J. B. Keller, 1996: Transport equations for elastic and other waves in random media. *Wave Motion*, **24 (4)**, 327–370, doi: 10.1016/S0165-2125(96)00021-2.

Salmon, R., 1998: *Lectures on Geophysical Fluid Dynamics*. Oxford University Press, doi: 10.1093/oso/9780195108088.001.0001.

Salmon, R., 2013: An alternative view of generalized Lagrangian mean theory. *Journal of Fluid Mechanics*, **719**, 165–182, doi: 10.1017/jfm.2012.638.

Savva, M., H. Kafiabad, and J. Vanneste, 2021: Inertia-gravity-wave scattering by three-dimensional geostrophic turbulence. *Journal of Fluid Mechanics*, **916**, A6, doi: 10.1017/jfm.2021.205.

Sebastia Saez, P., 2025: pablosebastiasaez/ScINET: Scattering Integral for Nonlinear Energy Transfers. doi: 10.5281/zenodo.17367456.

Sebastia Saez, P., M. Chouksey, C. Eden, and D. Olbers, 2025a: Wave-wave interactions of internal gravity waves Part A - Comparison of wave-wave triad interactions from Eulerian and Lagrangian frameworks. *Submitted to Journal of Physical Oceanography*.

Sebastia Saez, P., M. Chouksey, C. Eden, and D. Olbers, 2025b: Wave-wave interactions of internal gravity waves Part B: Spectral energy transfers within a typical internal gravity wave field in the ocean. *Submitted to Journal of Physical Oceanography*.

Sebastia Saez, P., C. Eden, and M. Chouksey, 2024: Evolution of internal gravity waves in a mesoscale eddy simulated using a novel model. *Journal of Physical Oceanography*, **54 (4)**, 985 – 1002, doi: 10.1175/JPO-D-23-0095.1.

Serrin, J., 1959: *Mathematical Principles of Classical Fluid Mechanics*, 125–263. Springer Berlin Heidelberg, Berlin, Heidelberg, doi: 10.1007/978-3-642-45914-6_2.

Sherman, J. T., 1989: Observations of fine-scale vertical shear and strain in the upper ocean. Ph.D. thesis, University of California, San Diego.

Sherman, J. T., and R. Pinkel, 1991: Estimates of the vertical wavenumber–frequency spectra of vertical shear and strain. *Journal of Physical Oceanography*, **21 (2)**, 292 – 303, doi: 10.1175/1520-0485(1991)021<0292:EOTVWS>2.0.CO;2.

Staquet, C., 2004: Gravity and Inertia-Gravity Internal Waves: Breaking Processes and Induced Mixing. *Surveys in Geophysics*, **25 (3)**, 281–314, doi: 10.1007/s10712-003-1280-8.

Susanto, R., L. Mitnik, and Q. Zheng, 2005: Ocean internal waves observed in the lombok strait. *Oceanography*, **18**, 80–87, doi: 10.5670/oceanog.2005.08.

Talley, L. D., 2013: Closure of the global overturning circulation through the indian, pacific, and southern oceans: Schematics and transports. *Oceanography*, doi: 10.5670/oceanog.2013.07.

Walter, M., C. Mertens, J. Köhler, J. Löb, and M. Rhein, 2020: Current meter and temperature time series (2017/2018) from mooring ET1 south of Azores. PANGAEA, doi: 10.1594/PANGAEA.918730.

Watanabe, M., and T. Hibiya, 2002: Global estimates of the wind-induced energy flux to inertial motions in the surface mixed layer. *Geophys. Res. Lett.*, **29 (8)**, 1239, doi: 10.1029/2001GL014422.

Webster, F., 1972: Estimates of the coherence of ocean currents over vertical distances. Elsevier, Vol. 19, 35–44, doi: 10.1016/0011-7471(72)90071-X.

Wright, C. J., R. B. Scott, P. Ailliot, and D. Furnival, 2014: Lee wave generation rates in the deep ocean. *Geophys. Res. Lett.*, **41 (7)**, 2434–2440, doi: 10.1002/2013GL059087.

Wu, Y., and Y. Pan, 2023: Energy cascade in the Garrett–Munk spectrum of internal gravity waves. *Journal of Fluid Mechanics*, **975**, A11, doi: 10.1017/jfm.2023.862.

Wunsch, C., and R. Ferrari, 2003: Vertical mixing, energy, and the general circulation of the oceans. *Annu. Rev. Fluid Mech*, **18**, 281–314, doi: 10.1146/annurev.fluid.36.050802.122121.

Zakharov, V. E., V. S. L'Vov, and G. Falkovich, 1992: *Kolmogorov spectra of turbulence I. Wave turbulence.* Springer-Verlag, doi: 10.1007/978-3-642-50052-7.